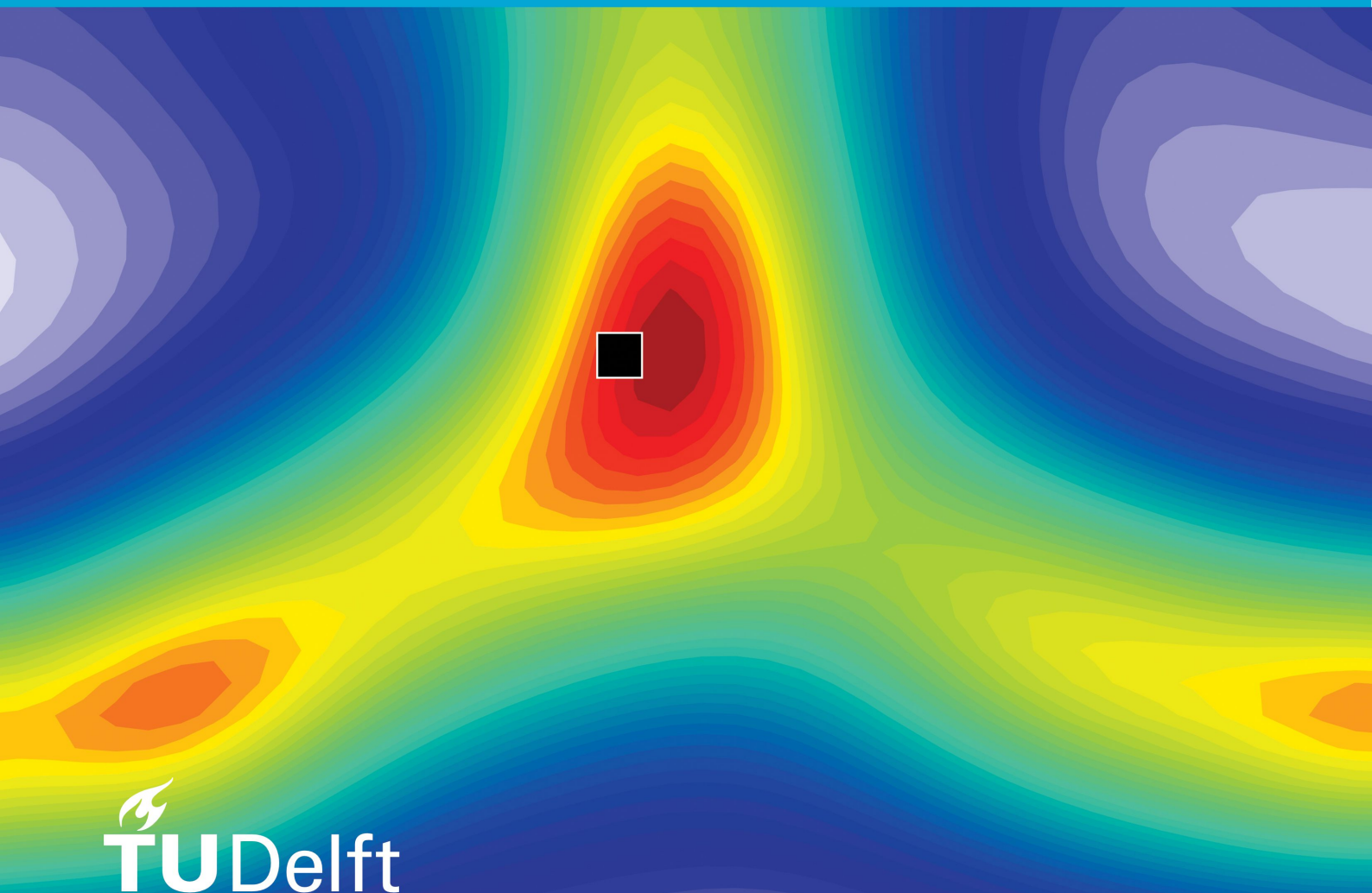


MSc Thesis in Materials Science and Engineering

Investigation of crystallographic disorientation topology in simulation of rolling textures with the ALAMEL model

Aleem Pirani
2021



INVESTIGATION OF CRYSTALLOGRAPHIC DISORIENTATION
TOPOLOGY IN SIMULATION OF ROLLING TEXTURES WITH THE
ALAMEL MODEL

A thesis submitted to the Delft University of Technology in partial fulfilment
of the requirements for the degree of

Master of Science in Material Science and Engineering

by

Aleem Pirani

February 2021

Aleem Pirani: Investigation of crystallographic disorientation topology in simulation of rolling textures with the ALAMEL model (2021)

The work in this thesis was made in the:

Mechanical Behaviour group
Department of Materials Science & Engineering
Faculty of Mechanical, Maritime & Materials Engineering
Delft University of Technology

Supervisors: Prof.dr. Leo Kestens
ir. Jhon Ochoa-Avendaño
Prof.dr.ing. Victor Scholten

ABSTRACT

The crystallographic texture of a material has a direct impact on its mechanical and functional properties. As a result, texture control is an imperative part of manufacturing processes, especially those involving plastic deformation, such as rolling, which significantly impact crystallographic texture. The exact mechanisms and underlying causes behind such texture evolution's are not well understood.

This study investigates the effect of initial disorientation topology on plastically deformed texture, with the help of mean field crystal plasticity simulations performed using the ALAMEL model. The simulated textures are compared to experimentally measured textures of IF steel samples with symmetric rolling reductions of 55 % and 83 %. The results indicate a clear distinction between low **disorientation topologies** and high disorientation topologies, most evident at high rolling reductions.

The study aims to incorporate the disorientation information into the ALAMEL simulations, by re-ordering textural input orientations. The Monte Carlo algorithm is used in addition to the Hungarian Algorithm to re-order orientations on the basis of preset disorientation angles.

A comparison between the two re-ordering algorithms is also performed, and the Hungarian algorithm is found to have a disorientation distribution closer the ideal result. A comparison between the two yields minimal differences, with the difference between the two results being the error index local minima for minimum disorientation evolved textures and average disorientation (between 35° . Local maxima for error index comparisons are observed for very high disorientation values of over 60° .

In the present study, we also result spread for similar disorientation topologies orders to discount the randomness associated with such a process. Thus, multiple files are created with largely similar disorientation characteristics but different grain orders. An overlap is observed for high disorientation simulations, at a higher frequency for lower rolling reductions. The deviation of obtained results is also highest for a disorientation angle average of 15° .

The simulated texture comparisons between textures with modified and unmodified texture disorientation topology also indicate a higher disparity with minimum disorientation modified texture. A convergence is observed at a disorientation value between 35° and 40° , close to the disorientation average of the unmodified texture, and an overlap is observed at higher disorientation values.

The valorisation of such a technology is also considered in this study. The current study precedes applied research and is assessed as a level 2 on the technology readiness scale, in danger of facing the 'valley of death'. This is owing to fading interest and funding unless the private sector see's value in the technology. The domain most aligned for the application of such technology is electrical steels, which is set to see a large increase in demand and will play a significant role in the energy transition and move towards electrical mobility.

The high cost of development and price sensitive market serve as barriers of entry, and entry into the niche beachhead market of DC converters for next generation 'more electrified aircraft' is determined to be an appropriate valorisation strategy. The study also proposes a 'way to market' strategy, drawing parallels with other high tech and high value material industries, to determine 'critical partnerships' with high levels of integration in addition to leadership in materials and manufacturing development as key factors for a successful entry.

ACKNOWLEDGEMENTS

I would like to express my gratitude towards my research supervisor, Dr. Leo Kestens, for giving me the freedom and guidance I needed, to embark on this adventurous journey. A year working with you has made me appreciate the value of strong fundamentals, and that innovation is much more than adopting to the bleeding edge. I appreciate your support for trying some of our more ridiculous ideas, and frank reflection when some of them failed spectacularly.

I would like to thank Dr. Victor Schloten, for teaching me the Dutch way of looking at Entrepreneurship. Thanks for taking time out of your busy schedule to work with me (and deal with the many many emails). I find your method and thought process inspiring and fiendishly objective. The focus on collaborative partnerships and due diligence in fundamental value is something I will take away fondly.

I would also like to thank my supervisor Jhon, for guiding me through this esoteric field of study, teaching me the ropes and mentoring me when things got tough. Thanks for painstakingly and critically analysing my work, especially as the pandemic has affected our traditional communications immensely. Thanks for putting in the time and effort, beyond what was asked of you.

I would also like to thank my friends, of whom there are many to mention. Thanks for keeping the spirits up and offering me camaraderie, humour and a place to vent. I found you by my side at my lowest lows, bunched up below my stove. It is cruel irony that we have grown closer when we are forced to be the most apart. While we missed out on barbecues, card games and travel in the past year, you can probably take solace in the fact that you missed out on my excellent taste in music, dark humour and stories following the current set of unfortunate events taking place. Thanks Aniruddh for bearing with me since the day I pushed you off a banyan tree in Kinder-garden, looks like you didn't learn anything since that day. I am sure head injuries are why you're still a dear friend (and why you have eventually chosen to move to specialise in Industrial design).

I am also extremely thankful to Mr. Pinaki Das and Ms. Vijay Lakshmi, my high-school Physics and Chemistry teachers. You were definitely not paid enough to deal with my classmates and me. Thanks for an excellent education and mentorship, the times where we shared books on UFO conspiracy theories and shared rosgulla while discussing 'e' have helped shape how I think.

Lastly, and most importantly, I would also like to thank my family for all they have done, especially in the past few months, offering me only support and reassurance in the past few isolating months. Thanks mum, dad and Alifia for the tons of love and patience you showed, even after being thousands of kilometres away. In a better world we would have been able to share our joy in person, but alas, it was not to be.

Jared diamond wrote a book on how human history has been determined by guns, germs and steel. My work is but a fold within Damsascus steel, tempered and forged by countless others before and after. The time in a bubble has brought us more silicon, and shown us what lightning does to the grid. The new hope that I take with me is the knowledge on the steel going into the system, and knowing the anvil is alive.

CONTENTS

| | | |
|-------|--|----|
| 1 | CRYSTALLOGRAPHIC TEXTURE | 1 |
| 1.0.1 | Texture research | 1 |
| 1.0.2 | Texture Orientation | 2 |
| 1.1 | Orientation Matrix | 3 |
| 1.1.1 | Misorientation and Mesotexture | 3 |
| 1.1.2 | Disorientation | 4 |
| 1.1.3 | Crystal Symmetry | 4 |
| 1.1.4 | Disorientation and symmetry | 4 |
| 1.1.5 | Euler angles and Euler space | 4 |
| 1.1.6 | Texture Representation | 5 |
| 1.1.7 | Texture measurement | 7 |
| 2 | ELECTRICAL STEELS | 9 |
| 2.1 | History and Evolution of Electrical Steels | 10 |
| 2.1.1 | Early developments | 10 |
| 2.1.2 | GOSS and 'textured electrical steels' | 11 |
| 2.1.3 | Magnetic Domain refinement and the present | 12 |
| 2.2 | Crystallographic Texture and Electrical Steels | 12 |
| 2.2.1 | Texture control | 14 |
| 2.3 | Disorientation and grain growth | 15 |
| 2.3.1 | Macro-structure of electrical steel | 15 |
| 2.3.2 | Production of Electrical Steels | 16 |
| 2.3.3 | Electrical Steel Innovations | 17 |
| 3 | ELECTRICAL STEEL MARKETS | 19 |
| 3.1 | Electrical steel market | 19 |
| 3.1.1 | Prospective applications and User gains | 19 |
| 3.2 | Commercialisation Strategy | 20 |
| 3.2.1 | Lead User | 21 |
| 3.2.2 | Opportunities and strategies | 21 |
| 3.2.3 | Planar Magnetic Component systems | 22 |
| 3.2.4 | DC-DC converter system market | 23 |
| 3.2.5 | Way to market | 24 |
| 4 | MANUFACTURE AND PROCESSING OF ELECTRICAL STEELS | 25 |
| 4.1 | Rolling of Electrical Steels | 26 |
| 4.1.1 | Cold Rolling | 26 |
| 4.1.2 | Hot Rolling | 26 |
| 4.1.3 | Asymmetric Rolling | 26 |
| 4.1.4 | Shear stress characteristics of asymmetric rolling | 27 |
| 4.2 | Severe Plastic deformation | 29 |
| 4.3 | Cross Rolling | 30 |
| 5 | COMPUTATIONAL MODELLING | 31 |
| 5.1 | Crystal Plasticity modelling | 31 |
| 5.1.1 | Multi-level Scaling | 31 |
| 5.1.2 | Taylor model | 32 |
| 5.1.3 | Relaxed Constraint Taylor Model | 33 |
| 5.1.4 | Multigrain Relaxed Constraint models | 34 |
| 5.2 | LAMEL | 34 |
| 5.2.1 | ALAMEL | 35 |
| 5.2.2 | Implementation of the ALAMEL model | 36 |
| 5.2.3 | ALTAY software system | 36 |
| 6 | DISORIENTATION REORDERING | 39 |
| 6.1 | Problem Definition | 39 |

| | | |
|-------|--|-----|
| 6.2 | Model Validity | 40 |
| 6.3 | Monte Carlo method | 40 |
| 6.3.1 | Implementation of the Monte Carlo Model | 41 |
| 6.3.2 | Drawbacks of the current methodology | 42 |
| 6.3.3 | Verification of Monte Carlo model | 43 |
| 6.4 | Hungarian Algorithm | 44 |
| 6.4.1 | Definition of problem | 44 |
| 6.4.2 | Modes for solution | 45 |
| 6.4.3 | Implementation of Hungarian Algorithm | 47 |
| 6.4.4 | Verification of Hungarian Algorithm | 50 |
| 6.4.5 | Validation of Hungarian Algorithm | 50 |
| 7 | RESULTS | 53 |
| 7.1 | Texture Index | 53 |
| 7.2 | Error Index | 53 |
| 7.3 | Monte Carlo and Experimental result Variance | 54 |
| 7.3.1 | Error Index values and Rolling reduction curve variations of Monte Carlo results | 54 |
| 7.3.2 | Texture Index values and Rolling reduction curve variations of Monte Carlo results | 56 |
| 7.3.3 | Error Index values and Rolling reduction curve variations of Monte Carlo results | 58 |
| 7.4 | Standard deviation properties of Monte Carlo results | 61 |
| 7.4.1 | Standard deviation properties of Monte Carlo Error Index Value results, plotted against disorientation angle | 62 |
| 7.4.2 | Standard deviation properties of Monte Carlo Texture Index Value results, plotted against disorientation angle | 63 |
| 7.4.3 | Standard deviation properties of Monte Carlo Error Index Value results, plotted against rolling reduction | 64 |
| 7.4.4 | Standard deviation properties of Monte Carlo texture index results, plotted against rolling reduction | 65 |
| 7.5 | Monte Carlo results compared to Default evolved texture | 66 |
| 7.5.1 | Monte Carlo and Default texture ODFs, variation with rolling reduction | 69 |
| 7.6 | Hungarian Results and Experimental texture comparison | 71 |
| 7.6.1 | Hungarian Output rolling reduction results | 71 |
| 7.6.2 | Hungarian Texture index Result | 73 |
| 7.7 | Comparison between Hungarian Results and original texture evolution | 74 |
| 7.8 | Comparison of Ordering methodology | 76 |
| 8 | CONCLUSIONS | 79 |
| A | ERROR INDEX VARIATION WITH EXPERIMENTAL RESULTS | 89 |
| A.1 | Series 1: Monte Carlo Rolling Reduction vs Error Index for 55 percent sample | 89 |
| A.2 | Series 2. Monte Carlo disorientation angle vs Error index for 55 percent experimental sample | 90 |
| A.3 | Series 3. Monte Carlo Rolling Reduction vs Error index for 83 percent experimental sample | 91 |
| A.4 | Series 4. Monte Carlo Disorientation angle vs Error index for 83 percent experimental sample | 91 |
| B | TEXTURE INDEX VALUES OF MONTE CARLO SAMPLES | 97 |
| B.1 | Series 1. Monte Carlo Disorientation vs Texture index | 97 |
| B.2 | Series 2. Monte Carlo Rolling reduction vs Texture index | 98 |
| C | MONTE CARLO ERROR INDEX VARIATION WITH SIMULATED ORIGINAL TEXTURE RESULTS | 101 |
| C.1 | Series 1. Monte Carlo Rolling reduction vs Error Index | 101 |
| C.2 | Series 2. Monte Carlo Disorientation angle vs Error Index | 102 |

| | | |
|-----|---|-----|
| D | HUNGARIAN ERROR INDEX VARIATION WITH EXPERIMENTALLY OBTAINED 55 PERCENT REDUCTION RESULTS | 105 |
| D.1 | Series 1. Error Index variation for 55 percent sample | 105 |
| D.2 | Series 2. Error Index variation for 83 percent sample | 106 |
| E | HUNGARIAN ALGORITHM TEXTURE INDEX VARIATION | 107 |
| E.1 | Series 1. Error Index variation for 55 percent sample | 107 |
| F | HUNGARIAN ERROR INDEX VARIATION WITH SIMULATED ORIGINAL TEXTURE SOLUTION | 109 |
| G | ERROR INDEX COMPARISON BETWEEN HUNGARIAN AND MONTE CARLO SOLUTIONS | 111 |
| G.1 | Series 1. Rolling reduction vs Error Index Comparison | 111 |
| G.2 | Series 2. Disorientation angle vs Error Index Comparison | 112 |
| H | MONTE CARLO ODF FIGURES FOR MAXIMUM STANDARD DEVIATION, 50 DEGREE DISORIENTATION AND 50 PERCENT ROLLING REDUCTION | 115 |
| I | VARIATION OF ODF WITH ROLLING REDUCTION WITH DISORIENTATION ANGLE | 117 |
| I.1 | Series 1. 30 percent rolling | 117 |
| I.2 | Series 2. 50 percent rolling | 118 |
| I.3 | Series 3. 80 percent rolling | 119 |
| J | VARIATION OF ODF WITH DISORIENTATION ANGLE | 127 |
| J.1 | Series 1: Minimum Disorientation Angle | 127 |
| J.2 | Series 1: 20 Degree Disorientation Angle | 128 |
| J.3 | Section 3 : 55 Degree Disorientation | 128 |

LIST OF FIGURES

| | | |
|-------------|---|----|
| Figure 1.1 | Undesirable 'Earrings' formed during deep drawing processes | 2 |
| Figure 1.2 | Relationship between specimen (given by RD,TD and ND or X,Y,Z) and crystal co-ordinate sytem (given by crystal miller indices) | 2 |
| Figure 1.3 | Relationship between orientation matrix and common orientation descriptors | 3 |
| Figure 1.4 | Distribution of minimum disorientation of random orientations (Mackinzie distribution) | 5 |
| Figure 1.5 | Visual representation of Euler Angles | 6 |
| Figure 1.6 | Projection of a pole figure into two dimensions by (a) projecting the crystal poles on a unit sphere, (b) projection of poles on equitorial planes and (c) representation of pole figures and pole figure angles | 6 |
| Figure 2.1 | Comparative response of Ferromagnets and air to an external magnetic field | 9 |
| Figure 2.2 | Variation of Eddy current loss with lamination thickness and number of segments | 10 |
| Figure 2.3 | Early (left) and later (right) historical development of electrical steel on the basis of core loss per unit weight | 11 |
| Figure 2.4 | Illustration of technology lifecycle stages | 12 |
| Figure 2.5 | Magnetic Domain structure of grain oriented silicon steel . . . | 13 |
| Figure 2.6 | Goss texture visualisation (left), magnetic crystalline anisotropy (Ease of magnetisation) for major axes, BCC crystal structure | 13 |
| Figure 2.7 | Illustration of the concept of A_θ (left) and A_θ values for common textures (table on the right) | 14 |
| Figure 2.8 | Average grain area as a function of time during grain growth from a random initial texture for different disorientation angles | 15 |
| Figure 2.9 | Macrostructure and texture of grain oriented steel | 16 |
| Figure 2.10 | Distribution of deviation angle from ideal Goss orientation in grain Oriented Steel | 16 |
| Figure 2.11 | Production Schedule for Grain Oriented Steel | 17 |
| Figure 2.12 | Core Loss v/s grade | 18 |
| Figure 3.1 | Breakdown of Electrical Steel Losses | 21 |
| Figure 3.2 | Trends of More Electrified Aircraft (MEA) throughout the ages | 22 |
| Figure 3.3 | Illustration of technological readiness level with associated actors and funding | 23 |
| Figure 4.1 | Production Schedule for Grain Oriented Steel | 25 |
| Figure 4.2 | Change in inclination profiles for pins parallel to the normal direction at different asymmetric rolling ratios for 65 and 75 % reduction, and Sections of $\Phi_{12} = 45$ ODF for rolling reductions between 20 and 75 % | 28 |
| Figure 4.3 | Obtained orientation densities along the alpha and gamma fibres for different layers in the cold rolled non oriented silicon steel sheets a) $S = 1$, b) $S = -1$, c) $D = 0.5$, d) $S = -0.5$, e) $S = 0$. Square datapoints indicate symmetric rolling and triangular datapoints indicate asymmetrical rolling | 29 |
| Figure 4.4 | distribution of texture concentration of A- ζ Asymmetric rolling B- ζ Conventional rolling at different cross sections | 30 |

| | | |
|-------------|---|----|
| Figure 5.1 | Representation of an elongated grain, with x_1 indicating rolling direction and x_3 normal direction. For lath relaxed constraint models, l_{13} is relaxed | 33 |
| Figure 5.2 | Modes of relaxation considered for the LAMEL model | 35 |
| Figure 5.3 | Illustration of polycrystal and grain boundary structure for ALAMEL model | 36 |
| Figure 6.1 | Procedure of ALAMEL pair assignment modification, illustrating the original unmodified pair assignment (left), and disorientation sorted modified pair assignment (right) —Need to include credit— | 39 |
| Figure 6.2 | Random orientation distribution in Euler space without invariance (left) and after invariant transformation (right) which takes into account the distortion of Euler space | 41 |
| Figure 6.3 | Monte Carlo convergence of the Hanging chain problem, indicating the variation in sum of potential and kinetic energy (subplot 1), bending energy (subplot 3) and fraction of bending energy (subplot 4) with number of iterations and steady state chain shape (subplot 2) | 42 |
| Figure 6.4 | Histogram for obtained disorientation distribution and pairwise variation of disorientation | 43 |
| Figure 6.5 | Obtained results for variation of average disorientation for target angle values of 60° disorientation (top left), 35° disorientation (top right) and standard deviation for target angles of 60° (bottom left) and 30° (bottom right) v/s number of iterations | 45 |
| Figure 6.6 | Hungarian problem definition according to Kuhn | 46 |
| Figure 6.7 | Hungarian routine for solution optimisation | 47 |
| Figure 6.8 | Routine 1 or the Kuhn algorithm | 48 |
| Figure 6.9 | Hungarian Method Implementation visualisation with input and output files | 49 |
| Figure 6.10 | Histogram for obtained disorientation, using the LAPJV algorithm with a 35° disorientation goal | 50 |
| Figure 6.11 | Pairwise disorientation obtained, using the LAPJV algorithm with a 35° disorientation goal | 50 |
| Figure 6.12 | Variation of obtained mean disorientation value with input disorientation specification | 51 |
| Figure 6.13 | Variation of obtained disorientation standard deviation values with input disorientation specification | 51 |
| Figure 6.14 | Variation of obtained disorientation variance with input disorientation specification | 51 |
| Figure 7.1 | Rolling Reduction v/s Error Index, comparison between 55 % rolled experimental samples and Monte Carlo evolved texture, with Error bars | 54 |
| Figure 7.2 | Rolling Reduction v/s Error Index, comparison between 83 % rolled experimental samples and Monte Carlo evolved texture, with Error bars | 55 |
| Figure 7.3 | Rolling Reduction v/s Texture Index, Monte Carlo evolved texture, with Error bars | 56 |
| Figure 7.4 | ODF plot for Run Number 5, Monte Carlo simulation, with an input disorientation of 10° and rolling reduction of 70 % | 57 |
| Figure 7.5 | ODF plot for Run Number 5, Monte Carlo simulation, with a minimum input disorientation and rolling reduction of 70 % | 57 |
| Figure 7.6 | ODF difference plot between obtained experimental 55 % rolling reduction and Run Number 5, Monte Carlo simulation, with an input disorientation of 10° and rolling reduction of 70 % | 58 |

| | | |
|-------------|--|----|
| Figure 7.7 | ODF difference plot between obtained experimental 55 % rolling reduction and Run Number 5, Monte Carlo simulation, with minimum input disorientation and rolling reduction of 70 % | 58 |
| Figure 7.8 | Rolling Reduction v/s Error Index, comparison between 55 % rolled experimental samples and Monte Carlo evolved texture, with Error bars | 59 |
| Figure 7.9 | Rolling Reduction v/s Error Index, comparison between 83 % rolled experimental samples and Monte Carlo evolved texture, with Error bars | 59 |
| Figure 7.10 | Rolling Reduction v/s Texture Index, Monte Carlo evolved texture, with Error bars | 60 |
| Figure 7.11 | ODF plot for Run Number 3, Monte Carlo simulation, with an input disorientation of 55° and rolling reduction of 70 % | 61 |
| Figure 7.12 | ODF plot for Run Number 3, Monte Carlo simulation, with a maximum input disorientation and rolling reduction of 70 % | 61 |
| Figure 7.13 | ODF difference plot between obtained experimental 55 % rolling reduction and Run Number 3, Monte Carlo simulation, with an input disorientation of 55° and rolling reduction of 70 % | 61 |
| Figure 7.14 | ODF difference plot between obtained experimental 55 % rolling reduction and Run Number 3, Monte Carlo simulation, with maximum input disorientation and rolling reduction of 70 % | 62 |
| Figure 7.15 | Disorientation Angle v/s Error Index Standard deviation, comparison between 55 % rolled experimental samples and Monte Carlo evolved texture | 62 |
| Figure 7.16 | Disorientation Angle v/s Error Index Standard deviation, comparison between 83 % rolled experimental samples and Monte Carlo evolved texture | 63 |
| Figure 7.17 | Disorientation Angle v/s Texture Index Standard deviation, Monte Carlo evolved texture | 63 |
| Figure 7.18 | Rolling Reduction v/s Error Index Standard deviation, comparison between 55 % rolled experimental samples and Monte Carlo evolved texture | 64 |
| Figure 7.19 | Rolling Reduction v/s Error Index Standard deviation, comparison between 83 % rolled experimental samples and Monte Carlo evolved texture | 65 |
| Figure 7.20 | Rolling Reduction v/s Texture Index Standard deviation, Monte Carlo evolved texture | 65 |
| Figure 7.21 | ODF plot for Run Number 1, Monte Carlo simulation, with a 20° input disorientation and rolling reduction of 45 % | 66 |
| Figure 7.22 | ODF plot for Run Number 2, Monte Carlo simulation, with a 20° input disorientation and rolling reduction of 45 % | 66 |
| Figure 7.23 | ODF plot for Run Number 3, Monte Carlo simulation, with a 20° input disorientation and rolling reduction of 45 % | 67 |
| Figure 7.24 | ODF plot for Run Number 4, Monte Carlo simulation, with a 20° input disorientation and rolling reduction of 45 % | 67 |
| Figure 7.25 | ODF plot for Run Number 5, Monte Carlo simulation, with a 20° input disorientation and rolling reduction of 45 % | 67 |
| Figure 7.26 | Disorientation Angle v/s Error Index, comparison between Original evolved texture and Monte Carlo evolved texture, with Error bars | 68 |
| Figure 7.27 | Disorientation Angle v/s Error Index Standard deviation, comparison between Original evolved texture and Monte Carlo evolved texture | 68 |

| | | |
|-------------|--|----|
| Figure 7.28 | Rolling Reduction v/s Error Index, comparison between Original evolved texture and Monte Carlo evolved texture, with Error Index | 69 |
| Figure 7.29 | Rolling Reduction v/s Error Index Standard Deviation, comparison between Original evolved texture and Monte Carlo evolved texture | 70 |
| Figure 7.30 | ODF plot for Run Number 4, Monte Carlo simulation, with a 40° input disorientation and rolling reduction of 30 % . . . | 70 |
| Figure 7.31 | ODF plot for Run Number 4, Monte Carlo simulation, with a 40° input disorientation and rolling reduction of 80 % . . . | 70 |
| Figure 7.32 | ODF difference plot between obtained experimental 83 % rolling reduction and Run Number 4, Monte Carlo simulation, with an input disorientation of 40° and rolling reduction of 30 % | 71 |
| Figure 7.33 | ODF difference plot between obtained experimental 83 % rolling reduction and Run Number 4, Monte Carlo simulation, with an input disorientation of 40° and rolling reduction of 80 % | 71 |
| Figure 7.34 | Rolling Reduction v/s Error Index, comparison between 55 % rolled experimental samples and Hungarian evolved texture | 72 |
| Figure 7.35 | Rolling Reduction v/s Error Index, comparison between 83 % rolled experimental samples and Hungarian evolved texture | 72 |
| Figure 7.36 | Disorientation Angle v/s Error Index, comparison between 55 % rolled experimental samples and Hungarian evolved texture | 73 |
| Figure 7.37 | Disorientation Angle v/s Error Index, comparison between 83 % rolled experimental samples and Hungarian evolved texture | 73 |
| Figure 7.38 | Disorientation Angle v/s Texture Index, Hungarian evolved texture | 74 |
| Figure 7.39 | Rolling Reduction v/s Texture Index, Hungarian evolved texture | 74 |
| Figure 7.40 | Rolling Reduction v/s Error Index, comparison between original evolved texture and Hungarian evolved texture | 75 |
| Figure 7.41 | Disorientation Angle v/s Error Index, comparison between original evolved texture and Hungarian evolved texture . . . | 75 |
| Figure 7.42 | Disorientation Angle v/s Error Index, comparison between Hungarian evolved texture and Monte Carlo evolved texture, with Error bars | 76 |
| Figure 7.43 | Rolling Reduction v/s Error Index, comparison between Hungarian evolved texture and Monte Carlo evolved texture, with Error bars | 77 |
| Figure A.1 | Disorientation Angle v/s Error Index : 55 percent reduction sample, Monte Carlo, 5 trials | 89 |
| Figure A.2 | Disorientation Angle v/s Error Index mean : 55 percent reduction sample, Monte Carlo | 89 |
| Figure A.3 | Disorientation Angle v/s Error Index Standard Deviation : 55 percent reduction sample, Monte Carlo | 90 |
| Figure A.4 | Disorientation Angle v/s Error Index : 83 percent reduction sample, Monte Carlo, 5 trials | 90 |
| Figure A.5 | Disorientation Angle v/s Error Index mean : 83 percent reduction sample, Monte Carlo | 91 |
| Figure A.6 | Disorientation Angle v/s Error Index Standard Deviation : 83 percent reduction sample, Monte Carlo | 92 |
| Figure A.7 | Rolling Reduction v/s Error Index : 83 percent reduction sample, Monte Carlo, 5 trials | 92 |

| | | |
|-------------|---|-----|
| Figure A.8 | Rolling Reduction v/s Error Index mean : 83 percent reduction sample, Monte Carlo | 93 |
| Figure A.9 | Rolling Reduction v/s Error Index Standard Deviation : 83 percent reduction sample, Monte Carlo | 93 |
| Figure A.10 | Rolling Reduction v/s Error Index : 55 percent reduction sample, Monte Carlo, 5 trials | 94 |
| Figure A.11 | Rolling Reduction v/s Error Index mean : 55 percent reduction sample, Monte Carlo | 94 |
| Figure A.12 | Rolling Reduction v/s Error Index Standard Deviation : 55 percent reduction sample, Monte Carlo | 95 |
| Figure B.1 | Disorientation Angle v/s Texture Index : Monte Carlo All runs | 97 |
| Figure B.2 | Disorientation Angle v/s Texture Index : Monte Carlo, mean value | 97 |
| Figure B.3 | Disorientation Angle v/s Texture Index : Monte Carlo, standard deviation value | 98 |
| Figure B.4 | Rolling Reduction v/s Texture Index : Monte Carlo All runs . | 98 |
| Figure B.5 | Rolling Reduction v/s Texture Index : Monte Carlo, mean value | 99 |
| Figure B.6 | Rolling Reduction v/s Texture Index : Monte Carlo, standard deviation value | 99 |
| Figure C.1 | Rolling Reduction v/s Error Index between Monte Carlo and original simulated results, All trials | 101 |
| Figure C.2 | Rolling Reduction v/s Error Index between Monte Carlo and original simulated results, mean values | 101 |
| Figure C.3 | Rolling Reduction v/s Error Index between Monte Carlo and original simulated results, Standard deviation values | 102 |
| Figure C.4 | Disorientation Angle v/s Error Index between Monte Carlo and original simulated results, All trials | 102 |
| Figure C.5 | Disorientation Angle v/s Error Index between Monte Carlo and original simulated results, mean values | 103 |
| Figure C.6 | Disorientation Angle v/s Error Index between Monte Carlo and original simulated results, Standard deviation values . . . | 103 |
| Figure D.1 | Disorientation Angle v/s Error Index between 55 Percent Experimental Texture and Hungarian Result | 105 |
| Figure D.2 | Rolling Reduction v/s Error Index between 55 Percent Experimental Texture and Hungarian Result | 105 |
| Figure D.3 | Disorientation Angle v/s Error Index between 83 Percent Experimental Texture and Hungarian Result | 106 |
| Figure D.4 | Rolling Reduction v/s Error Index between 83 Percent Experimental Texture and Hungarian Result | 106 |
| Figure E.1 | Disorientation Angle v/s Texture Index, Hungarian Algorithm | 107 |
| Figure E.2 | Rolling Reduction v/s Texture Index, Hungarian Algorithm . | 107 |
| Figure F.1 | Rolling Reduction v/s Error Index for difference between original texture evolution and Hungarian Evolution | 109 |
| Figure F.2 | Disorientation Angle v/s Error Index for difference between original texture evolution and Hungarian Evolution | 109 |
| Figure G.1 | Rolling Reduction v/s Error Index comparison between Hungarian and Monte Carlo results, All runs | 111 |
| Figure G.2 | Rolling Reduction v/s Error Index comparison between Hungarian and Monte Carlo results, Mean value | 111 |
| Figure G.3 | Rolling Reduction v/s Error Index comparison between Hungarian and Monte Carlo results, Standard Deviation | 112 |
| Figure G.4 | Disorientation Angle v/s Error Index comparison between Hungarian and Monte Carlo results, All runs | 112 |
| Figure G.5 | Disorientation Angle v/s Error Index comparison between Hungarian and Monte Carlo results, mean value | 113 |

| | | |
|-------------|---|-----|
| Figure G.6 | Disorientation Angle v/s Error Index comparison between Hungarian and Monte Carlo results, Standard Deviation . . . | 113 |
| Figure H.1 | ODF 50 degree disorientation and 50 percent rolling reduction Run 1 | 115 |
| Figure H.2 | ODF 50 degree disorientation and 50 percent rolling reduction Run 2 | 115 |
| Figure H.3 | ODF 50 degree disorientation and 50 percent rolling reduction Run 3 | 115 |
| Figure H.4 | ODF 50 degree disorientation and 50 percent rolling reduction Run 4 | 116 |
| Figure H.5 | ODF 50 degree disorientation and 50 percent rolling reduction Run 5 | 116 |
| Figure I.1 | ODF Plot, Monte Carlo Run 1 30 percent rolling, min disorientation | 117 |
| Figure I.2 | ODF Plot, Monte Carlo Run 1 30 percent rolling, 10 degree disorientation | 117 |
| Figure I.3 | ODF Plot, Monte Carlo Run 1 30 percent rolling, 15 degree disorientation | 117 |
| Figure I.4 | ODF Plot, Monte Carlo Run 1 30 percent rolling, 20 degree disorientation | 118 |
| Figure I.5 | ODF Plot, Monte Carlo Run 1 30 percent rolling, 25 degree disorientation | 118 |
| Figure I.6 | ODF Plot, Monte Carlo Run 1 30 percent rolling, 30 degree disorientation | 118 |
| Figure I.7 | ODF Plot, Monte Carlo Run 1 30 percent rolling, 35 degree disorientation | 118 |
| Figure I.8 | ODF Plot, Monte Carlo Run 1 30 percent rolling, 40 degree disorientation | 119 |
| Figure I.9 | ODF Plot, Monte Carlo Run 1 30 percent rolling, 45 degree disorientation | 119 |
| Figure I.10 | ODF Plot, Monte Carlo Run 1 30 percent rolling, 50 degree disorientation | 119 |
| Figure I.11 | ODF Plot, Monte Carlo Run 1 30 percent rolling, 55 degree disorientation | 119 |
| Figure I.12 | ODF Plot, Monte Carlo Run 1 30 percent rolling, 60 degree disorientation | 120 |
| Figure I.13 | ODF Plot, Monte Carlo Run 1 30 percent rolling, max disorientation | 120 |
| Figure I.14 | ODF Plot, Monte Carlo Run 1 50 percent rolling, min disorientation | 120 |
| Figure I.15 | ODF Plot, Monte Carlo Run 1 50 percent rolling, 10 degree disorientation | 120 |
| Figure I.16 | ODF Plot, Monte Carlo Run 1 50 percent rolling, 15 degree disorientation | 121 |
| Figure I.17 | ODF Plot, Monte Carlo Run 1 50 percent rolling, 20 degree disorientation | 121 |
| Figure I.18 | ODF Plot, Monte Carlo Run 1 50 percent rolling, 25 degree disorientation | 121 |
| Figure I.19 | ODF Plot, Monte Carlo Run 1 50 percent rolling, 30 degree disorientation | 121 |
| Figure I.20 | ODF Plot, Monte Carlo Run 1 50 percent rolling, 35 degree disorientation | 122 |
| Figure I.21 | ODF Plot, Monte Carlo Run 1 50 percent rolling, 40 degree disorientation | 122 |
| Figure I.22 | ODF Plot, Monte Carlo Run 1 50 percent rolling, 45 degree disorientation | 122 |

| | | |
|-------------|--|-----|
| Figure I.23 | ODF Plot, Monte Carlo Run 1 50 percent rolling, 50 degree disorientation | 122 |
| Figure I.24 | ODF Plot, Monte Carlo Run 1 50 percent rolling, 55 degree disorientation | 123 |
| Figure I.25 | ODF Plot, Monte Carlo Run 1 50 percent rolling, 60 degree disorientation | 123 |
| Figure I.26 | ODF Plot, Monte Carlo Run 1 50 percent rolling, max disorientation | 123 |
| Figure I.27 | ODF Plot, Monte Carlo Run 1 80 percent rolling, min disorientation | 123 |
| Figure I.28 | ODF Plot, Monte Carlo Run 1 80 percent rolling, 10 degree disorientation | 124 |
| Figure I.29 | ODF Plot, Monte Carlo Run 1 80 percent rolling, 15 degree disorientation | 124 |
| Figure I.30 | ODF Plot, Monte Carlo Run 1 80 percent rolling, 20 degree disorientation | 124 |
| Figure I.31 | ODF Plot, Monte Carlo Run 1 80 percent rolling, 25 degree disorientation | 124 |
| Figure I.32 | ODF Plot, Monte Carlo Run 1 80 percent rolling, 30 degree disorientation | 125 |
| Figure I.33 | ODF Plot, Monte Carlo Run 1 80 percent rolling, 35 degree disorientation | 125 |
| Figure I.34 | ODF Plot, Monte Carlo Run 1 80 percent rolling, 40 degree disorientation | 125 |
| Figure I.35 | ODF Plot, Monte Carlo Run 1 80 percent rolling, 45 degree disorientation | 125 |
| Figure I.36 | ODF Plot, Monte Carlo Run 1 80 percent rolling, 50 degree disorientation | 126 |
| Figure I.37 | ODF Plot, Monte Carlo Run 1 80 percent rolling, 55 degree disorientation | 126 |
| Figure I.38 | ODF Plot, Monte Carlo Run 1 80 percent rolling, 60 degree disorientation | 126 |
| Figure I.39 | ODF Plot, Monte Carlo Run 1 80 percent rolling, max disorientation | 126 |
| Figure J.1 | ODF Plot, Monte Carlo Run 1 30 percent rolling, min disorientation | 127 |
| Figure J.2 | ODF Plot, Monte Carlo Run 1 35 percent rolling, min disorientation | 127 |
| Figure J.3 | ODF Plot, Monte Carlo Run 1 40 percent rolling, min disorientation | 127 |
| Figure J.4 | ODF Plot, Monte Carlo Run 1 45 percent rolling, min disorientation | 128 |
| Figure J.5 | ODF Plot, Monte Carlo Run 1 50 percent rolling, min disorientation | 128 |
| Figure J.6 | ODF Plot, Monte Carlo Run 1 55 percent rolling, min disorientation | 128 |
| Figure J.7 | ODF Plot, Monte Carlo Run 1 60 percent rolling, min disorientation | 128 |
| Figure J.8 | ODF Plot, Monte Carlo Run 1 65 percent rolling, min disorientation | 129 |
| Figure J.9 | ODF Plot, Monte Carlo Run 1 70 percent rolling, min disorientation | 129 |
| Figure J.10 | ODF Plot, Monte Carlo Run 1 75 percent rolling, min disorientation | 129 |
| Figure J.11 | ODF Plot, Monte Carlo Run 1 80 percent rolling, min disorientation | 129 |

| | | |
|-------------|--|-----|
| Figure J.12 | ODF Plot, Monte Carlo Run 1 30 percent rolling, 20 degree disorientation | 130 |
| Figure J.13 | ODF Plot, Monte Carlo Run 1 35 percent rolling, 20 degree disorientation | 130 |
| Figure J.14 | ODF Plot, Monte Carlo Run 1 40 percent rolling, 20 degree disorientation | 130 |
| Figure J.15 | ODF Plot, Monte Carlo Run 1 45 percent rolling, 20 degree disorientation | 130 |
| Figure J.16 | ODF Plot, Monte Carlo Run 1 50 percent rolling, 20 degree disorientation | 131 |
| Figure J.17 | ODF Plot, Monte Carlo Run 1 55 percent rolling, 20 degree disorientation | 131 |
| Figure J.18 | ODF Plot, Monte Carlo Run 1 60 percent rolling, 20 degree disorientation | 131 |
| Figure J.19 | ODF Plot, Monte Carlo Run 1 65 percent rolling, 20 degree disorientation | 131 |
| Figure J.20 | ODF Plot, Monte Carlo Run 1 70 percent rolling, 20 degree disorientation | 132 |
| Figure J.21 | ODF Plot, Monte Carlo Run 1 75 percent rolling, 20 degree disorientation | 132 |
| Figure J.22 | ODF Plot, Monte Carlo Run 1 80 percent rolling, 20 degree disorientation | 132 |
| Figure J.23 | ODF Plot, Monte Carlo Run 1 30 percent rolling, 55 degree disorientation | 132 |
| Figure J.24 | ODF Plot, Monte Carlo Run 1 35 percent rolling, 55 degree disorientation | 133 |
| Figure J.25 | ODF Plot, Monte Carlo Run 1 40 percent rolling, 55 degree disorientation | 133 |
| Figure J.26 | ODF Plot, Monte Carlo Run 1 45 percent rolling, 55 degree disorientation | 133 |
| Figure J.27 | ODF Plot, Monte Carlo Run 1 50 percent rolling, 55 degree disorientation | 133 |
| Figure J.28 | ODF Plot, Monte Carlo Run 1 55 percent rolling, 55 degree disorientation | 134 |
| Figure J.29 | ODF Plot, Monte Carlo Run 1 60 percent rolling, 55 degree disorientation | 134 |
| Figure J.30 | ODF Plot, Monte Carlo Run 1 65 percent rolling, 55 degree disorientation | 134 |
| Figure J.31 | ODF Plot, Monte Carlo Run 1 70 percent rolling, 55 degree disorientation | 134 |
| Figure J.32 | ODF Plot, Monte Carlo Run 1 75 percent rolling, 55 degree disorientation | 135 |
| Figure J.33 | ODF Plot, Monte Carlo Run 1 80 percent rolling, 55 degree disorientation | 135 |

ACRONYMS

| | |
|--------------|--|
| RD | Rolling Direction |
| ND | Normal Direction |
| TD | Transverse Direction |
| BCC | Body Centered Cubic |
| FCC | Face Centered Cubic |
| FE | Finite Element |
| FEM | Finite Element Modelling |
| CSL | Coincident Site Lattice |
| MC | Monte Carlo |
| ODF | Orientation Distribution Function |
| GOSS | Grain Oriented Silicon Steel |
| GOES | Grain Oriented Electrical Steel |
| Mt | Mega tonnes |
| DC | Direct Current |
| MEA | More Electrified Aircraft |
| PMC | Planar Magnetic Component |
| EV | Electric Vehicles |
| TSMC | Taiwan Semiconductor Manufacturing Company |
| OECD | Organisation for Economic Co-operation and Development |
| EU | European Union |
| FRT | Finish Rolling Temperature |
| FC | Full Constraint |
| SPD | Severe Plastic Deformation |
| CPFEM | Crystal Plasticity Finite Element Modelling |
| RVE | Representative Volume Element |
| RC | Relaxed Constraint |
| LAPJV | Linear Assignment Problem using Jonker-Volgenant Algorithm |
| EIV | Error Index Value |
| TI | Texture Index |

1

CRYSTALLOGRAPHIC TEXTURE

Most natural and technological materials derive their material properties from fundamental units and the structure of those fundamental units. The vast difference between the different allotropes of Carbon highlight the role of atomic structure on the material properties made from an otherwise homogenous group of atoms. In the same manner, the structure and orientation of component units is an important aspect of material properties of most natural and technological materials.

Many solid materials conform to a crystalline structure, including most metals, ceramics, minerals and even semiconductors. The structure of these crystalline materials is highly ordered, forming a crystal lattice that extends in all directions [AM⁺76]. Additionally, most crystalline materials comprise many crystals or 'grains', and are referred to as polycrystalline materials (in contrast to mono or bi-crystalline materials).

The orientation of atomic planes within a monocrystal or a grain is largely homogenous. However, the distribution of grain orientations with respect to a common reference is seldom equal. The occurrence of randomly distributed grain orientations in nature is also quite rare (the compression of a powder tends to yield a poly-crystal with random orientation distribution), and most commonly, the distribution of orientations follows a preference for a specific orientation, or a set of orientations. This distribution of these crystallographic orientations for a polycrystalline sample is also referred to as its crystallographic texture and is sometimes also simply referred to as texture.

The cause for a specific crystallographic texture of a material tends to be thermochemical, caused by processes such as deformation, recrystallisation and phase transformation.

Material texture has been found to influence mechanical, thermal and electromagnetic properties of materials. The quantum of influence of texture on material properties has been found to be, in many cases between 20 and 50 % of the property values [Bun13]. The exact mechanisms in which texture influences material properties is not always known, and empirical practices are utilized to establish production processes and mechanisms in manufacturing [AM⁺76].

1.0.1 Texture research

A better understanding of texture evolution is carried out based on two related fronts, the control of material processing, and understanding of material science processes. An example of the former is the use of texture control in the context of deep drawing cups from heavily textured rolled sheets, which result in the presence of undesirable 'earings' in specific directions (0° and 90° to the rolling direction), and is illustrated in Figure 1.1.

In the aforementioned scenario, an anisotropic sheet is desired, and thus, the modification of material processing would serve to reduce the undesirable effect.



Figure 1.1: Undesirable 'Earrings' formed during deep drawing processes
[Rano6]

1.0.2 Texture Orientation

When describing crystallographic orientation, two reference systems are required, related to both the specimen and the grain in question [KTW98]. Both the reference systems are Cartesian in nature (and preferable right handed), while each of them is known as a co-ordinate system. The axes of these co-ordinate system are chosen according to the important directions or surfaces of the specimen in question

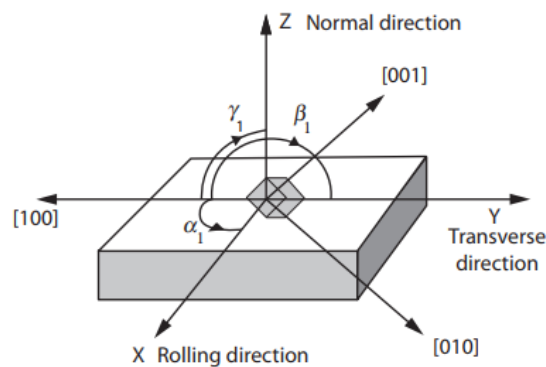


Figure 1.2: Relationship between specimen (given by RD,TD and ND or X,Y,Z) and crystal co-ordinate system (given by crystal miller indices)

[Ran70]

The co-ordinate systems of rolled products, for example, are described in terms of rolling direction (RD), normal direction (ND) and transverse direction (TD). Figure 1.2 illustrates the use of miller indices as reference axes for specimen reference axes and the aforementioned rolling specimen axes. In a case where there are no apparent specimen reference system, an arbitrary system can be used.

The use of crystal axes to describe grain specimen systems is convenient (though another system may be used if desired), as orthogonal structures form an orthogonal frame (and other crystal structures may be adopted to form such a frame by using orthonormal transformations).

1.1 ORIENTATION MATRIX

The crystallographic orientation is described as the position of the crystal reference system with the sample reference system. This can be described in a number of ways, most simply as the rotation matrix, which describes the rotation of the specimen reference to the sample reference, and is given as $C_C = g.C_S$, where C_C and C_S are the crystal/grain and sample reference axes and g is the orientation matrix.

The orientation matrix is closely related to the most common mathematical parameters (or descriptors) used to calculate texture properties. The relationship between the orientation matrix and the common mathematical parameters is given in figure 1.3

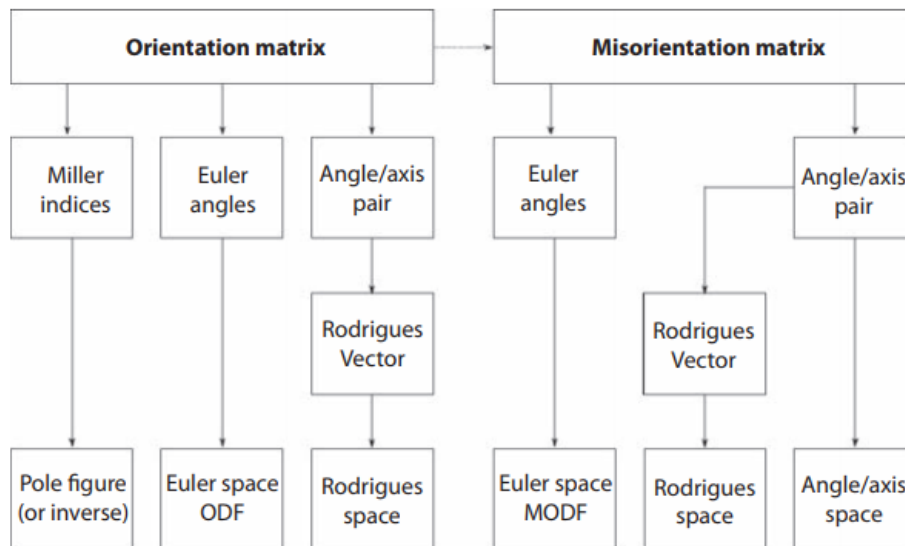


Figure 1.3: Relationship between orientation matrix and common orientation descriptors [Ran70]

1.1.1 Misorientation and Mesotexture

The individual orientation data can also be used to calculate the orientation difference between two different grains, which is also known as misorientation. This is given by $R_{12} = A_1^{-1}A_2$, where A_1 and A_2 are absolute orientations of two neighboring grains and expressed as an orientation matrix.

When this misorientation is calculated for a contiguous set of grains, a ‘mesotexture’ is obtained. The misorientation distribution in a texture also follows a non-random distribution [Ran70]. The mesostructured properties can be studied to relate grain boundary characteristics to material property,

The characterization of mesotexture is carried out in the basis of angle misorientation (into high angle or low angle misorientations), axis misorientation (a high

density of low index or high index axes) or combined angle and axes mesotexture, which is classified on the bases of Coincident Site Lattice (CSL) parameters.

1.1.2 Disorientation

The angle of disorientation is described as the minimum angle of rotation to rotate a crystal into the same orientation as that of its neighbour. This function depends on both the texture of a material, and crystal symmetry. The angle of rotation between two orientations is often described using an axes, as an 'axis angle pair'. Rotation operations may be described using a multitude of axes, but only the smallest angle of rotation is considered in this scenario.

1.1.3 Crystal Symmetry

Crystal symmetry is a property of a crystal, whereby the rotation of a crystal orientation about an axis, or reflection about a mirror plane, or translation by an angle, or even a combination of the above results in an atomic configuration similar to its original configuration. [Rano06]. If a crystal is symmetric for every 90° of rotation about a specific axis, it has a four-fold ($360^\circ/90^\circ$) symmetry about the axis.

Crystal symmetry is derived from the symmetry of its lattice. Crystal systems are groupings of structures according to the axial systems used to describe crystal lattices. Seven crystal systems are used to describe three dimensional lattices, which satisfy the criteria of each lattice point having a symmetric environment. In combination with various lattice centring's, they make up the 14 'bravais' lattices. The crystal system with the lowest symmetry is the triclinic system, and the system with the highest symmetry is the cubic system, which has four threefold rotation axes of symmetry. Monoclinic crystal systems have one twofold mirror axes of symmetry. Most metals follow cubic or hexagonal symmetry.

1.1.4 Disorientation and symmetry

For two neighbours, the angle of disorientation is calculated as the angle between the two orientations, for each application of the aforementioned symmetry operations. Iron, and its alloys, have a body centred cubic crystal structure, for which 24 symmetric pairs are analysed for a set of grains. For a random cubic texture, the frequency function of the minimum angle of disorientation is given by the Mckinzie distribution, as illustrated in figure 1.4 [Mac58]. It is named so after J K Mackinzie, who estimated the same using the Monte Carlo method [MT57]. The maximum angle of disorientation for cubic crystals was first proposed by FC Frank, as a rotation of 90° about any of the $\langle 110 \rangle$ axes, with an angle of rotation of 62.8° , as is observed in figure 1.4

1.1.5 Euler angles and Euler space

Another method to describe orientation is Euler angles, which describe orientation as a series of three rotations. If these rotations are performed in the correct order, transform the crystal reference to the sample reference. There are numerous notations describing Euler transformation, but the most common notation, Bunge notation, is used for this study [Bun13].

Figure 1.5 describes the Bunge rotations performed, which is a rotation by angle ϕ_1 about the normal axes (represented by Z in the image), followed by a rotation by angle Φ about the new rolling direction (represented by X') and rotation by an angle ϕ_2 about new normal axes (represented by Z'). Each transformation alters the

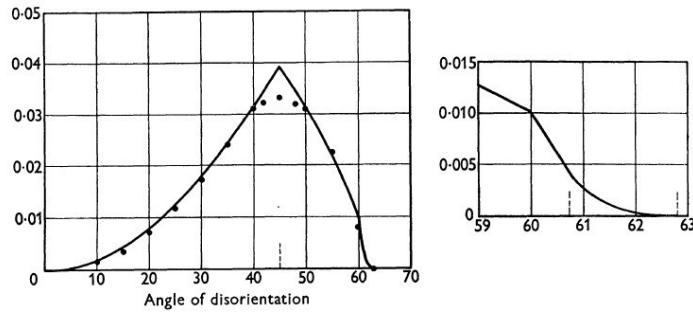


Figure 1.4: Distribution of minimum disorientation of random orientations (Mackinzie distribution)

[Mac58]

subsequent axes of rotation.

Euler angles operate in Euler space, which operates within limits of $0^\circ \leq \phi_1, \phi_2 \leq 360^\circ$. $0^\circ \leq \Phi \leq 180^\circ$ though for crystal structures with a high degree of symmetry, can be defined in the range $-90^\circ \leq \phi_1, \phi_2, \Phi \leq 90^\circ$

Angle Axis pair

The crystallographic orientation can also be described as a single rotation around a specific axes, where the axis is referred to as the axis of rotation, and the angle is known as the angle of rotation, with the notation being referred to as an angle axis pair. The notation specifies a single direction, and is usually denoted in the format $\langle uvw \rangle \theta^\circ$, where $\langle uvw \rangle$ denotes the axes and θ° the angle.

The angle axis pair may not be an important representation of orientation for crystallographic orientation as does not convey the relationship between orientation and important physical axes but is an invaluable tool in the study of misorientation characteristics. The angle axis pair notation can be used to describe misorientation relationships between two grains by simply substituting either reference to represent the pair of grains whose misorientation is to be calculated. The misorientation angle axis pair is thus given by $M_{12} = g_1^{-1}g_2$.

1.1.6 Texture Representation

The representation of crystallographic texture distribution is not only carried out in a qualitative manner as indicated by preferred orientation(s) of the specimen, and also in a quantitative manner (which describe the exact distribution of texture).

Orientation Distribution Function

The orientation distribution function (ODF) aims to describe the exact orientation distribution within a specimen. Instead of representing orientation distribution as a set of discrete homogenous crystals, this function analyses the orientation distribution at every point. A complete description is formed by specifying the orientation of every point, and given as $g = g(x, y, z)$ [Bun13].

The description of the same in terms of Euler angles results in three mathematical functions spread in Cartesian and Euler space. For simpler mathematical treatment, $\frac{dV}{V} = f(g)dg$ used. Additionally, as this function requires a 3 dimensional function, it is most commonly represented in constant section of PHI . Appendix H illustrates a common representation of ODF figures.

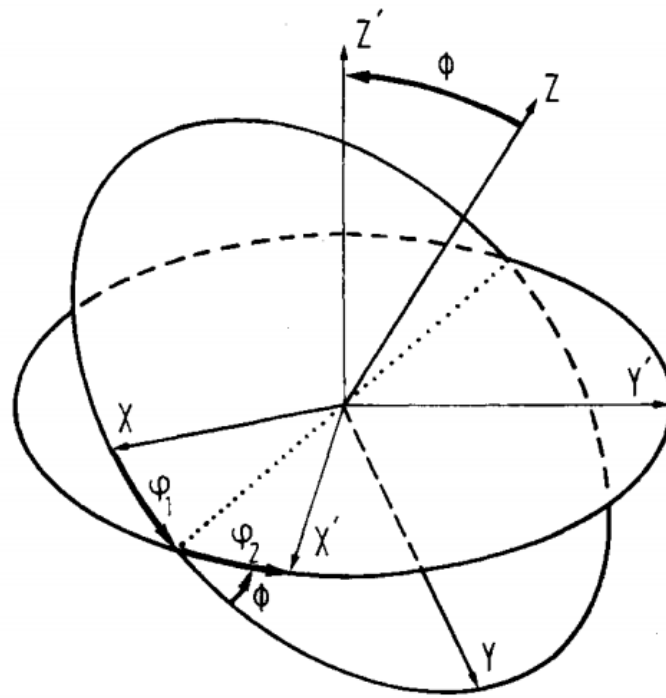


Figure 1.5: Visual representation of Euler Angles
[Bun13]

The orientation distribution function is not directly accessible from X-ray specimen measurements but is rather processed from another texture representation (pole figures) by using mathematical methods such as series expansion of spherical harmonics. Modern laboratory software suites include such functionality within their software systems, and third-party software suites also provide the same functionalities [Ran70].

Pole Figures and Inverse Pole figures Pole figures and inverse pole figures are a method of representation of orientation. A pole figure describes an orientation as a point in the unit reference sphere, described as the intersection of normal to atomic plane with the reference sphere. This is projected to a 2 dimensional plane using stereographic projection (or Lambert projection) of the poles in the equatorial plane as shown in figure 1.6.

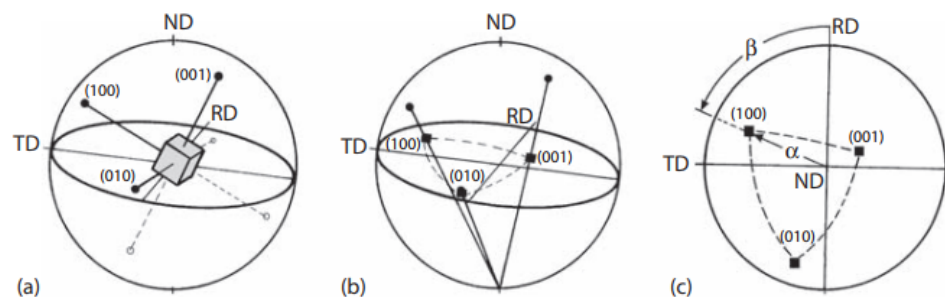


Figure 1.6: Projection of a pole figure into two dimensions by (a) projecting the crystal poles on a unit sphere, (b) projection of poles on equatorial planes and (c) representation of pole figures and pole figure angles

[Ran70]

Each pole figure describes the normal for a family of atomic planes, and thus, multiple pole figures are required to adequately describe the texture of a specimen. The number of poles required is dependent on the crystal symmetry, and can extend to 24 for certain cases.

Another way to represent this orientation data is in the form of an inverse pole figure. An inverse pole figure projects orientation of specimen co-ordinate system into the crystal co-ordinate system. The reference system of inverse pole figures are thus the crystal co-ordinate system and the orientation, the specimen co-ordinate system.

1.1.7 Texture measurement

The most common techniques to measure texture are X-ray diffraction and neutron diffraction. Early evaluations of texture measurement relied on the intensity distribution in Debye-Scherrer rings to evaluate preferred orientation. The use of texture goniometers began in the late 1940s, with instruments capable of directly measuring the pole figure of a specimen.

2 | ELECTRICAL STEELS

Electric machines are the backbone of modern civilisation, delegating much of the manual labour required for the production of goods to machines. The conversion of electrical energy into mechanical energy is dependant on magnetic materials. Iron, and some of its oxides, make for excellent magnetic materials because of their inherent magnetic properties, which are a result of their atomic electronic configuration.

Magnets are classified into hard magnets, which have their own magnetic field, examples of which include common fridge magnets and bar magnets, and soft magnets, which magnify a magnetic field acting on them, examples of which include electromagnets. Soft magnetic materials do not retain a magnetic field but magnify the magnetic flux, or magnetic force passing through them by a factor of up to 1 million [Beco2], and their effect on an applied magnetic field can be observed from figure 2.1.

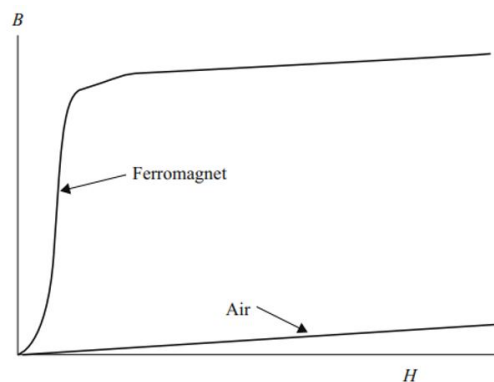


Figure 2.1: Comparative response of Ferromagnets and air to an external magnetic field [Beco2]

Silicon rich steels are often used as such soft magnetic steel, owing to Silicons high electrical resistivity and its effect on the magnetic properties of steel (the addition of silicon reduces magnetic anisotropy and magnetostriction of electrical steels) [Che14]. Production of electric steel accounts for 1 % of the total world steel production [Pet10], at over 12 million tonnes per year[Mos12] . Over 97% of soft magnetic materials produced are electrical steels [Mos02]. Electrical steels are further classified into grain oriented and non-grain oriented electrical steels based on their 'texture' orientation.

Electric steel producers have made only very small changes to the basic chemistry of electrical steel used for most commercial grades[Pet10]. Most research in the past 70 years has focused on improving the crystallographic texture, development of thinner grades, and magnetic domain refinement [XKW08].

There are two applications of electrical steels, use in transformers and use in rotating machines. Electrical steels used in transformers derive their benefit from the flux magnification properties of electrical steels, while those used in rotating ma-

chines are designed for optimum force magnification properties around a complete rotation.

2.1 HISTORY AND EVOLUTION OF ELECTRICAL STEELS

The development of electrical steels began with its use to enhance the power of a lifting magnets, with the use of solid iron cores. Cast irons were initially used before the advent of higher permeability steels [Beco2]. The use of a solid iron core is inefficient as it results in significant losses due to eddy currents, and its associated thermal limitations (machines of this era tended to run hot). The use of laminated sheets addressed this problem, as the associated eddy currents reduce with the reduction of lamination sheet thickness, as demonstrated by figure 2.2. Total core losses include eddy current losses and magnetic hysteresis losses and may be described using Steinmetz's equations [KS10] [531].

2.1.1 Early developments

Early refinements in this area focused on increasing resistivity and improving purity of silicon steels as a mode of reducing eddy currents and improving efficiency [Pry59]. An increase in purity resulted in more efficient machines, and the developments of the time aimed to balance the increase in cost of higher purity steel with the savings made by increased efficiency. Interestingly the mechanisms and specific relationships linking purity to magnetic performance were not known well into the 1950s. The increase in concentration of silicon was traditionally limited to an upper limit of 4.5% Silicon by weight, above which the brittleness of the resulting steels prevented their use. Heat treatment processes such as annealing can allow for a 'critical limit' of 5.487% by weight [YSB⁺01] above which it becomes impossible to suppress the B2 ordered phase, responsible for the brittleness.

Figure 2.12 illustrates the early development of electrical steels.

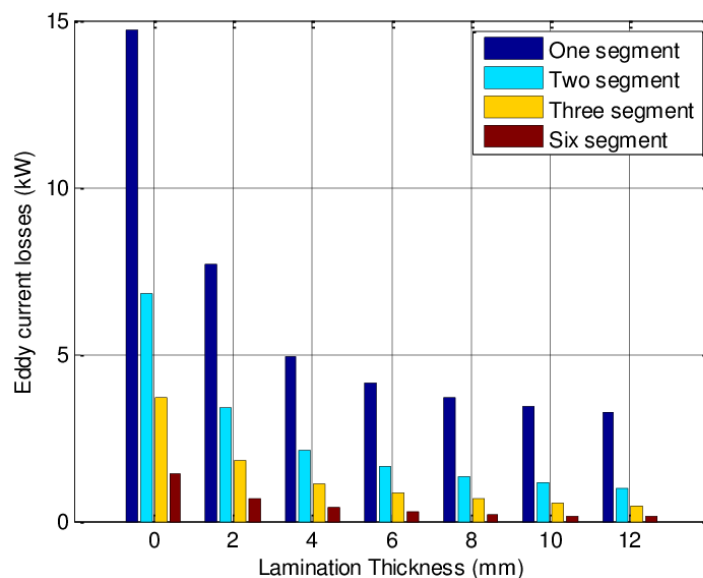


Figure 2.2: Variation of Eddy current loss with lamination thickness and number of segments [JLT⁺16]

2.1.2 GOSS and 'textured electrical steels'

The electrical steels used until the mid 1930s were manufactured using hand fed mills largely using hot rolling methods, and processed by annealing electrical steels prior to, or after punching operations [CT35]. This was performed to reduce 'surface scale' and warping, which affected magnetic and hysteresis properties adversely. The result of these processes is anisotropic steel, whose properties are in dependant on the direction of the axes of measurement. In the mid 1930s, the first method for aligning the directions of grains was patented by Goss [Gos34], which marked the beginning of the development of 'textured' electrical steels.

Textured alloys have a higher magnetic permeability and lower electrical energy loss than previous anisotropic electrical steels. The development of electrical steels after the advent of 'textured electrical steels' is illustrated in the image on the right in figure 2.12.

There has been a significant decrease in core energy loss per unit mass (and thus, increase in efficiency) following the implementation of texture control in electrical steels. The core energy loss reduced by nearly half with the implementation of texture control technologies in just over a decade between 1955 and 1965. The introduction of high permeability grades of electrical steel had also helped in reducing core loss by close to 25% in a span of just over 15 years. The core loss of electrical steels has reduced to a seventh of its value in just 40 years of implementing manufacturing technologies relating to texture control, and continues to reduce with the induction of new technologies. Additional parameters responsible for the increasing efficiency of electrical steels are ever decreasing gauge sizing and spacing fractions.

Rolled alloys may display isotropic behaviour in off-axis magnetic properties. The properties are dependant on rolling parameters. Thus, the tight control of associated rolling processes and heat treatment processes may be used to 'control' texture, and by extension, isotropic magnetic properties.

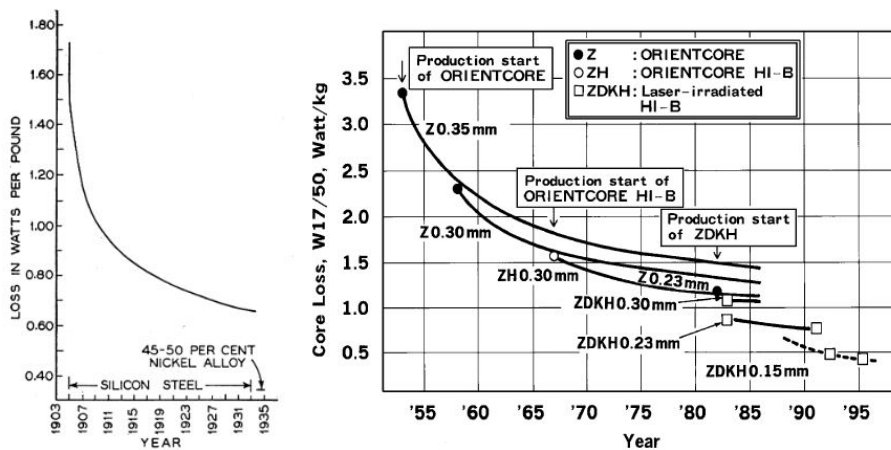


Figure 2.3: Early (left) and later (right) historical development of electrical steel on the basis of core loss per unit weight

[XKW08] [CT35]

Technology lifecycle

As discussed in section 2.1.2, the development of electrical steel material technologies have seen a continuous technology development lifecycle. The implementation of new technologies at first yields only marginal benefits for early adopters, as illustrated in figure ???. A more widespread increase in efficiency is seen after adoption

by the early majority, and subsequent investment by infrastructure buyers. The technology lifecycle is illustrated in figure 2.4

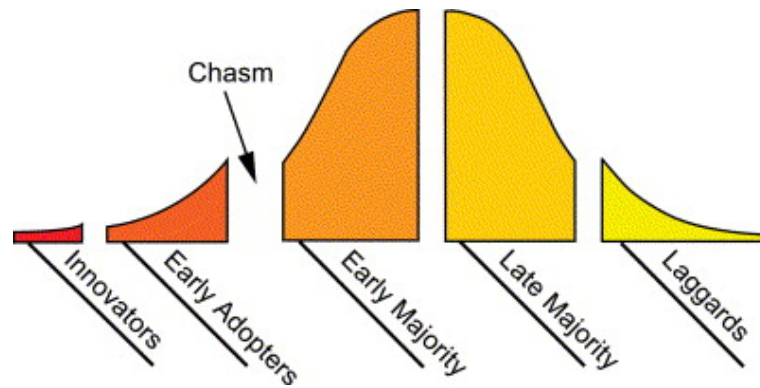


Figure 2.4: Illustration of technology lifecycle stages
[MR04]

2.1.3 Magnetic Domain refinement and the present

The image on the right in figure 2.12 cites the progress of isotropic steels grades or 'grain oriented electrical steels'. These electric steels have very large grains, and as a result, all sections within the grains may not align their magnetic domain. Ideally, when the polarisation of an applied field is reversed, the magnetic domain walls may be assumed to homogeneously move 180° during each cycle.

However, upon observation, this is not the case. The work of Nozawa et. al. [NMMM94] demonstrates that the dynamic wall movement is not homogeneous. When the process of magnetisation takes place, even if average magnetisation rates are constant, there is a variation between magnetic domains. Some domain walls move rapidly, while others move slowly. The cause of this heterogeneity are magnetic defect structures, consisting of surface closure domains perpendicular to the axis of magnetisation and pinned wall movements parallel to the axis of magnetisation. This is illustrated in figure 2.5

This domain wall movement causes 'anomalous' or unexpected eddy current losses. These losses can be reduced by carrying out domain wall refinement, using techniques such as laser irradiation [YI⁺82], application of tensile stress or even mechanical scratching.[UMF⁺03]. Magnetic domain refinement has led to an increase in efficiency from the 1980s., as can be seen from figure 2.12, where a reduction in loss can be observed between laser irradiated and standard samples.

2.2 CRYSTALLOGRAPHIC TEXTURE AND ELECTRICAL STEELS

The 'microstructure' of electrical steel comprises of an aggregate of single phase polycrystallines. The arrangement of these polycrystallines may represent a likening or increased probability of alignments to certain directions or orientations [KJ08]. Magnetic properties are also anisotropic, which are influenced by the alignment of these polycrystalline aggregates.

A divergence in Electrical steel manufacturing and application also resulted after the advent of texture control in the mid 1930s. Anisotropic electrical steels had excellent magnetic properties in specific directions, but poor magnetic properties in non-aligned directions. Electrical Steels used for flux magnification in static machines such as transformers benefited from anisotropic magnetic properties, while

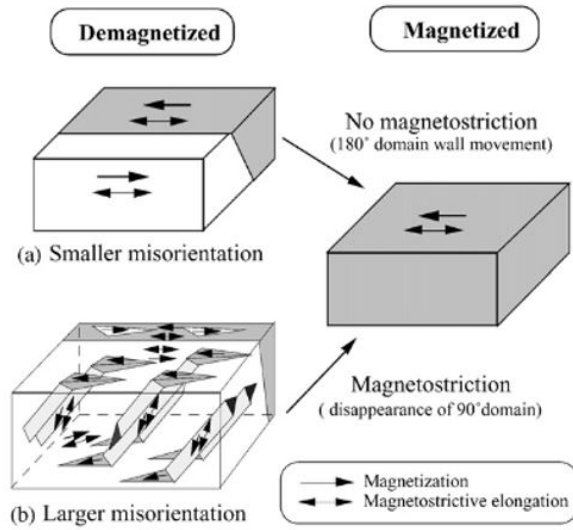


Figure 2.5: Magnetic Domain structure of grain oriented silicon steel [Hay17]

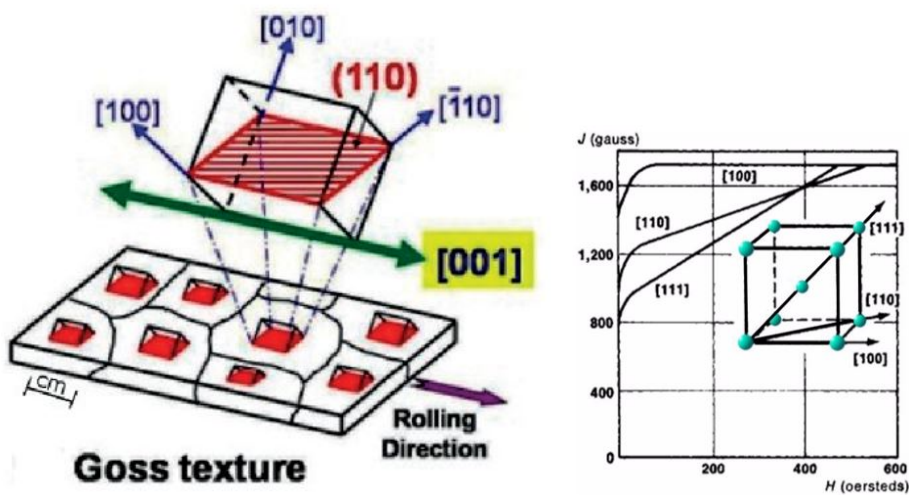


Figure 2.6: Goss texture visualisation (left), magnetic crystalline anisotropy (Ease of magnetisation) for major axes, BCC crystal structure [McHo1][FZL+08]

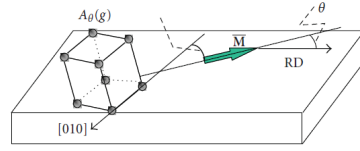


TABLE 1: Direction-averaged A values (in deg) of a number of texture components and fibres which are present in the typical texture of NO electrical steels (random refers to a random texture).

| | θ fibre | α fibre | γ fibre |
|------------|----------------|----------------|----------------|
| {001}<110> | 22.5 | 30.1 | 38.7 |
| {110}<001> | {001}<001> | {112}<110> | random |
| 33.8 | 22.5 | 36.1 | 31.9 |

Figure 2.7: Illustration of the concept of A_θ (left) and A_θ values for common textures (table on the right)

[KJ08]

those used in rotating machines were not suited for these grades of steel. Thus, two categories of electrical steels emerged, grain oriented steels, which are so named because their macro-structural 'grains' are aligned (these are the aforementioned anisotropic electrical steels), and non-grain oriented steels [McH01]. The list of desirable properties for non grain oriented electrical steels also include rotational losses [AMHP15], and are closely linked to magnetic isotropy [Mos92]. Grain oriented electrical steels make up 20 % of annual electrical steel production with non grain oriented steels making up the remainder [Mos12].

Figure 2.6 depicts the ease of magnetisation along various axes for a BCC crystal (signifying the properties of most forms of Iron at room temperature). The texture with the easiest axis of crystallisation is the axis denoted by the miller indices (1 0 0) — Rolling direction (Also known as a 'cubic texture') [FZL+08] for non grain oriented steels, and miller indices (1 1 0) — Rolling Direction for grain oriented steels (also known as a cube on edge or GOSS orientation) [Gos34]. This can be also seen in figure 2.6.

2.2.1 Texture control

Material properties are dependent on its structure. Electrical steels are comprised of a polycrystalline aggregate, as all steels, and most metals and many other solids comprise of. Single phase polycrystalline materials are made from a large number of microscopic (or in the case of grain oriented electrical steels, macroscopic) crystals, which are known as 'grains'. The structure of a polycrystalline material is of inherent importance to the material properties of the polycrystalline aggregate [ER09].

Kestens and Jacobs [KJ08] offer a fundamental insight into the relationship of texture and magnetic properties. They characterise the texture in terms of a texture parameter A_θ , which is the angle between the direction of the magnetisation vector and the nearest direction of the crystal. A_θ lower texture parameter would indicate a higher quality magnetic sample. Cubic textures were found to have the lowest values, and are thus best suited for non grain oriented applications.

For non oriented electrical steels, this value is averaged over a complete spherical range, as rotating machines have distributed magnetization axes. Thus, for every value of crystal orientation, the output is integrated over the entire spherical range values. The use of linear regression methods is made to account for the differences in grain size. The study also estimates an average A value, taking into account the effect of grain size on magnetic properties using linear regression methods. The value of A_θ is also estimated from the results of the 0° , 45° and 90° sample orientation values.

The conclusions of the aforementioned study are that wide variety of steel manufacturing methods result in a wide range of electrical steel quality. The obtained

results from hot rolling are more desirable when compared to cold rolling, but the required thicknesses (0.65 mm and below) cannot be obtained in even state of the art cold rolling mills.

2.3 DISORIENTATION AND GRAIN GROWTH

As discussed in earlier sections, texture has roots in thermochemical processes, whose knowledge and relationships are imperative in understanding texture control. Grain size control is also of importance, as grain size directly influences both mechanical and magnetic properties. The relationship between texture evolution and boundary energy and mobility are discussed in a study by Hore and Das [HD19], which aims to investigate the effect of anisotropic grain boundary energy and mobility on grain growth kinetics. The material used in this study is non oriented silicon steel produced by strip cast method and having a cubic texture. The initial entry in this model is the random/experimental results that include a grain identifier and orientation angles, which is used to calculate the final result, using the inputs and the read Shockley functions by the Monte Carlo method.

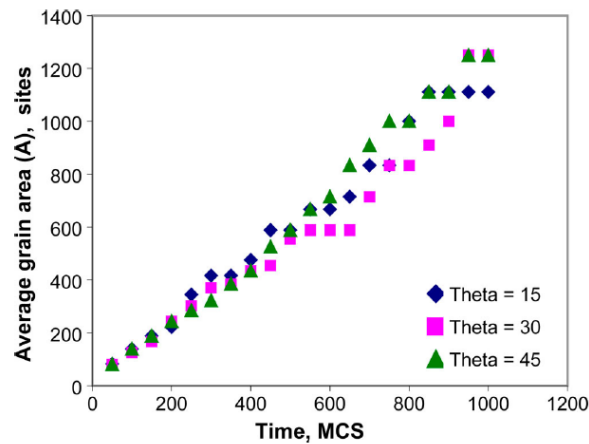


Figure 2.8: Average grain area as a function of time during grain growth from a random initial texture for different disorientation angles [HD19]

The results from this study indicate that the grain growth rates are independent of disorientation angles, and is cited as similar to actual results. (the steady grain growth rate is estimated to be 0.96 against an actual value of 1). Additionally, the kinetics of grain growth with anisotropy is lower than that of grains with isotropy. This is because the average mobility is less as a result of similar energy levels.

2.3.1 Macro-structure of electrical steel

The loss characteristics of electrical steel are closely related to its texture [LYS⁺15]. The obtained macro-structure of grain oriented electrical steel is depicted in figure 2.9. The most striking feature of the macro-structure of electrical steel is that it is visible without using a microscope. For ordinary varieties of steel, the microstructure of the steel is in the order of nanometers or micrometers [Hay17]. The figure 2.9 (ref to fig) also depicts a 'pole diagram' of the steel. A pole figure demonstrates the average orientation concentration. The pole figures depict a 'sharp' texture, with grain pole orientations being hundreds of times more concentrated along one direction than the average. This pole figure is indicative of a low deviation angle. Figure 2.10

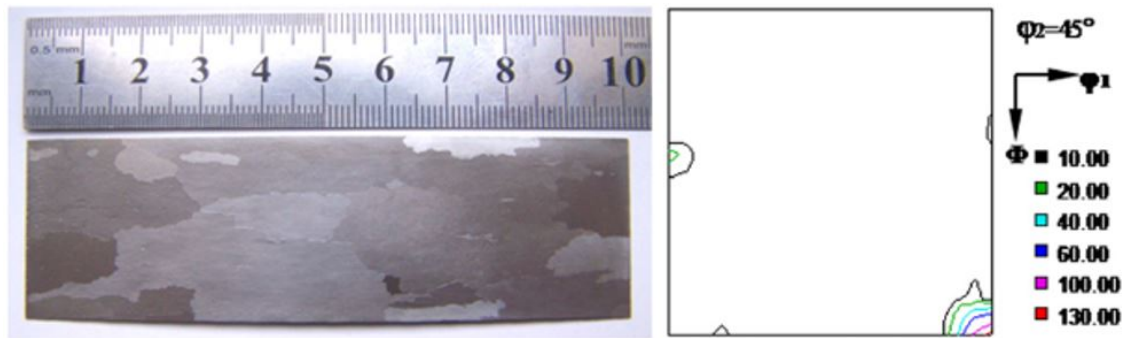


Figure 2.9: Macrostructure and texture of grain oriented steel
[LYS⁺15]

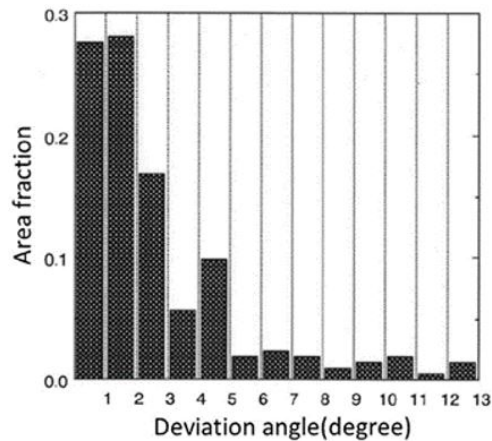


Figure 2.10: Distribution of deviation angle from ideal Goss orientation in grain Oriented Steel

[Hay17]

illustrates the angle of misorientation within the grain. As can be observed from the figure, a very small fraction has a misorientation of over 5°, which contributes to the high efficiency of electrical steel [UMF⁺03].

2.3.2 Production of Electrical Steels

Grain oriented steels are produced by a complex manufacturing process, consisting of more than 20 distinct heating steps. Grain oriented electrical steels are produced by the phenomenon of secondary re-crystallisation, and is the only product manufactured in the steel industry that uses such a process [XKW08]. It is manufactured through a complicated process, which is not fully understood, and is therefore often referred to as the 'artistic product of Iron'. Development of the aforementioned sharp Goss texture is a result of preferential 'abnormal growth' of the favourably oriented grains in the primary recrystallised matrix, whose development is characterised by the presence of fine precipitates (inhibitors)[HS90]. During the process of secondary re-crystallisation, Goss grains are estimated to consume in the order of a million grains [GAFLo5]. The conventional production schedule for Grain oriented silicon steel is illustrated in figure 4.1.

From the figure, the role of inhibitors may be highlighted as essential to the production of such steel. They are responsible for grain size after primary crystallisation being small, on average they vary between 100 to 200 nm, which allows for abnormal growth of Goss grains. The production of electrical steel is also sensitive to the concentration of elements such as Carbon and Nitrogen. The maximum

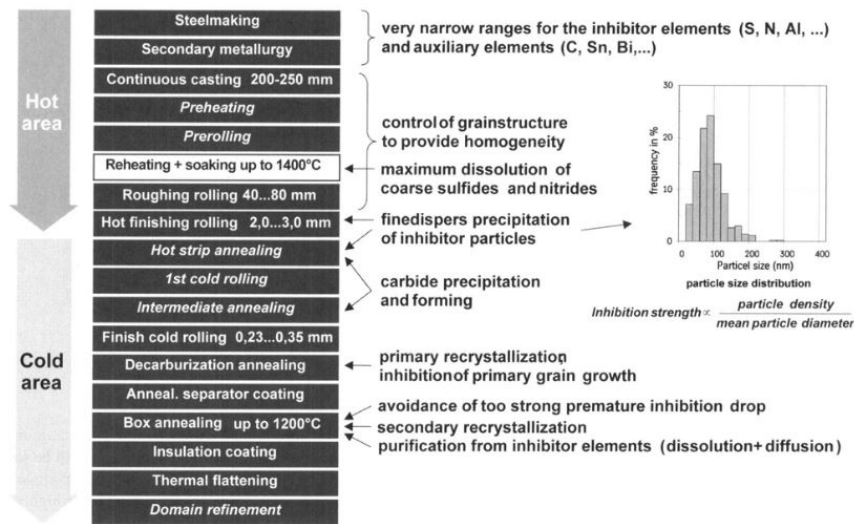


Figure 2.11: Production Schedule for Grain Oriented Steel
[GAFL05]

concentration of Carbon in electrical steel is 0.1%, which is lower than most steels. This also makes grain oriented electrical steel the low carbon steel with the highest added value. Thus, decarburisation and denitriding processes are also carried out prior to the primary crystallisation.

2.3.3 Electrical Steel Innovations

Newer methods of production such as low temperature slab reheating and thin strip casting have gained popularity in recent years over their lower energy consumption and simplified production process. There is a lack of quantitative models, as a result much of electrical steel research is carried out by industrial trials, which are expensive trials. Thinner gauge steels have a lower core loss than thicker gauge steels, and as a result, the thickness of electrical steel gauge has seen a sustained decrease in recent years, as is observed in figure 2.12. Older electrical steels (steels produced prior to the 1980s) are usually 0.35 mm or 0.30 mm thick, whereas newer variants have a thickness of 0.23 or 0.21 mm, with newer flagship grades having a thickness of 0.18 mm or less. A reduction of thickness is also accompanied by a reduction of spacing factor, a deterioration of shape and appearance and an reduction of stability of the secondary re-crystallisation, which result in limitations on the thickness [XKW08].

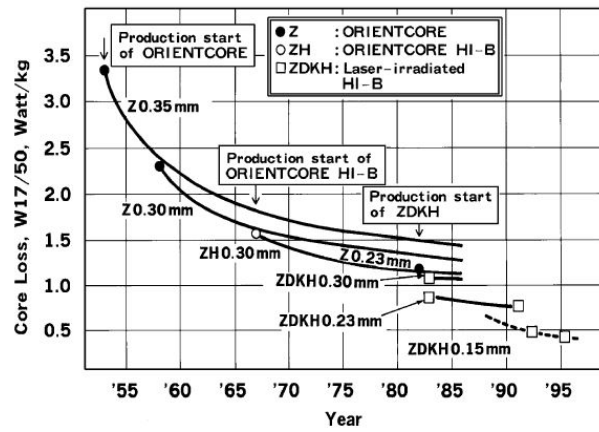


Figure 2.12: Core Loss v/s grade
[XKW08]

3

ELECTRICAL STEEL MARKETS

3.1 ELECTRICAL STEEL MARKET

Electrical steel is one of the fastest growing steel commodities, with an annual growth rate of over 7 %, driven by increasing demand in Western Europe and emerging markets in Asia [Ele], with a majority of such electrical steel being grain oriented or 'transformer steel'. A situation with oversupply is estimated to exist until the year 2025 [lm19]. The increasingly stringent regulations surrounding transformer efficiency, and the energy transition is also predicted to push demand for high-performance grades [Gro20].

Electrical Steels form a niche segment of the market and over the past decade have seen renewed interest owing to the energy transition away from fossil fuels [Ste18]. As electrical steels are a specialised niche, they command a high margin, in contrast to conventional steel manufacturing. As a consequence, steel giants such as Nippon are investing in the domain, especially as they face harsh competition and protectionism [Nip20].

Over the past two years, the international steel market has seen challenges, driven by international trade tensions and volatile oil prices, which have led to an increase in finished prices [MM20]. There is thus, an incentive to expand domestic manufacturing in countries such as the United States and India [Dil20]. Vos [Vos] expands on the area in detail, illustrating the probable effects on industry competitiveness, production and the effect of political administrations. The conclusion of the study predicts a reduction in steel production on the back of lower competitiveness.

The industry also faces challenges with technological development. [MECP19] relates common production methodologies to output texture and performance. The ever-improving standards and technologies require significant investment into research and innovation. This has resulted in greater consolidation in recent years [Had19]. Currently, only twelve companies across the globe produce 95% of all grain oriented electrical steel [Mar]

The medium and long term projections of electrical steel demand predict the largest gain to be in the domain of electrical mobility. The transition to electric mobility has the potential to increase demand by as much as 8 Mt (Mega Tonnes) per year [NF], which is 50% of the current market. An important point to note is that the grades of steel used in the electric mobility space differ from more traditional grades, as they operate at higher frequencies, and would require adaptation in the magnetic domain refinement space [SUYO18].

3.1.1 Prospective applications and User gains

One of the most promising areas of applications for next generation grain oriented electrical steels is in the domain of smart grids. Smart grids are an important challenge and key component of the energy transition away from fossil fuels [WD17]. Smart grids allow for intelligent decentralised distribution of power, resulting in

lower distribution and transformation losses, in addition to better quality of support to renewable energy [ML16]. Electrical steels form the backbone of renewable energy production methods such as Wind energy. Grain oriented electrical steels act as an important agent of smart grids, with next generation Direct Current (DC) grids being capable of smart DC grids paving the way for next generation power decentralisation [Jan18].

Another application of grain oriented steels is in the domain of charging infrastructure, where material benefits, including increased efficiency and reduced charging time [Jan18]. Effective charging time for electric vehicles is an important metric, and plays an important role in the purchasing intention of electrical vehicles [JM6]. The marginal utility of reduced charging time is found to be positive, and a study analysing effective charging times and charging cost points to heterogeneity depending on transport schedules and delays, supporting the case for speed-dependent electrical charging infrastructure [DSP17].

The sector most likely to benefit from the next generation of non-oriented electrical steels is electric mobility. The use of next generation non-oriented steels would allow for operations at higher frequencies, along with more efficient transformers, resulting in smaller and lighter components [Jan18]. The effect of smaller and lighter electrical components translates directly to benefits in initial costs, efficiency improvements due to lower weights and increased range/economy [BWW13]. In the context of electrical vehicles, this would result in a lighter cheaper vehicle, with a longer range [Inc20].

Frequency based losses

The use of electrical steels in high frequency applications allows for a small and light core to transmit the same power flows [Bec02]. This increased 'capacity' is accompanied by increased system reactance and raised losses. The loss characteristics of such as motor is described in figure 3.1. The figure illustrates the breakdown of electrical power and losses, with iron loss (which relates to material loss) being further divided into component losses. As illustrated, for the same material, an increased Iron loss is observed for a higher frequency (the frequency is given by f).

This increased loss is justified for applications related to mobility, where system weight directly impacts efficiency. Oftentimes specialised grades of electrical steels are used, which have different structural properties, and are designed keeping in mind stator assemble and operational environments (temperature, vibrations and coatings) [Div14] [SUYO18].

3.2 COMMERCIALISATION STRATEGY

Interestingly, the commercialisation strategy best suited for such materials may resemble the strategy adopted by many of the disruptors of the domain where it sees its largest potential, Electric Vehicles. The attacker's advantage strategy popularised by automaker Tesla. As Thomas [TM19] points out, Tesla took advantages of their competitors limited architectural innovations to introduce a product with superior capabilities. This strategy also revolved around the successful development of key performance attributes such as acceleration and range, which traditionally limited the use of such vehicles to micro-car segments. The strategy also requires strategic tradeoffs to be made, in domains with a lower priority for the market, consciously chosen to be domains that have a low priority for the lead users.

$$P_{el} = P_{mec} + L_{mec} + L_{Wires} + L_{Iron}$$

$$L_{Iron} = L_h f + \frac{\pi d^2}{6 \rho} (B_{max} f)^2 + 8(B_{max} f)^{3/2} \sqrt{\frac{GSV_0}{\rho}}$$

Losses for hysteresis
Classic dynamic losses
Anomalous losses

Figure 3.1: Breakdown of Electrical Steel Losses
[NF]

The strategic selection of a lead user is necessary, as the development of technology and processing methodology is a capital intensive process. There is a lack of quantitative models describing processes and states, as a result of which much of electrical steel research is carried out by industrial trials, which are expensive trials [XKW08]. Additionally, there is only a marginal increase in efficiency to be obtained for standard use case scenarios [Jan18]. The effect of efficiency is most acutely felt in mobility use case scenarios, where the impact of losses are amplified [NF].

3.2.1 Lead User

The most compelling lead user would be components used in aerospace transformers/power converters. Air-plane transformers and power converters are subject to heavy loads, for a diverse range of electrical systems D.S.Stephans. Aerospace components carry with them a Significant penalty for additional weight, and thus have some of the most extreme cost/weight ratios (and subsequently employ some of the most cutting edge and expensive alloys) [KZW10]. As a result, common designs involve the use of aforementioned compact high frequency (and high loss) electrical systems [NBM⁺17].

While the aforementioned arguments paint a compelling argument for the necessitation of deployment in the domain of aerospace transformers and power converters, the pièce de résistance of the argument lies in the medium to long term development of the aerospace sector, which is predicted to see increased electrification (such as the adoption of electric de-icing systems), and nascent developments of all-electric aircraft [WT18]. Figure 3.2 illustrates the increasing trend of electrification of modern aircraft systems.

Lastly, the adoption of the aforementioned technology, would benefit the most important ancillary of aerospace, safety. This would be due to a combination of smaller battery capacities required, and reduced insulation requirements. Both of the aforementioned properties reduce the risk of electrical fires, which are some of the most dangerous failures, and have even plagued modern platforms such as the 787 dreamliner [GS91] [WHHP13].

3.2.2 Opportunities and strategies

The electrical steel industry is characterised by a high barrier to entry, but in recent years, the market has seen fragmentation and closure of many players, such as AK steel, Essar Steel and ORB [MZ19] [Had19]. The global oversupply and uncertainty

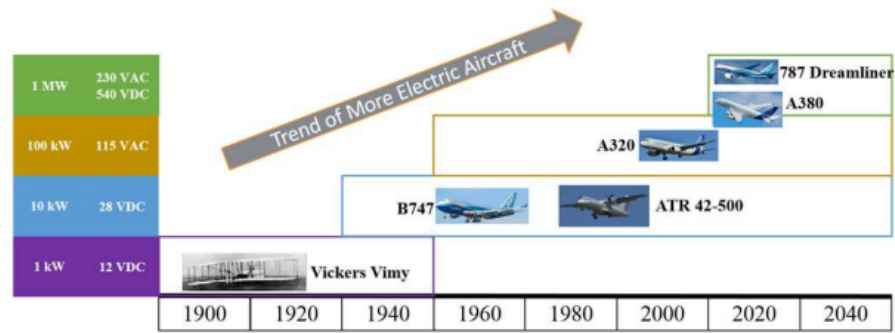


Figure 3.2: Trends of More Electrified Aircraft (MEA) throughout the ages
[NBM⁺17]

caused by trade disputes and the coronavirus have delayed consolidation. The cost of entry into these markets would thus only include the discounted price of the assets and a retrofitting cost. For the ORB electrical steel plant in Wales, the cost of retrofit for production of automotive grade electrical steels has been calculated to be close to 50 million Pounds.

The 'green recovery plan' brought proposed by the Organisation for Economic Co-operation and Development (OECD) and European Union (EU) also serves as an opportunity for development of technology and overcoming entry barriers [OEC]. The biggest threat facing this technology is the 'valley of death' described in section 3.2.2. Development of the current technology with government funding, or in government labs would counter the threat of they valley of death, and also help fulfil the green energy targets of the aforementioned groups.

Technological Feasibility and technology transfer

From the point of view of technological readiness, the current technology is assessed to be at the cusp of applied research. The goal of the current study is closely linked to proving domain feasibility. This phase of development is often succeeded by the 'valley of death', characterised by a gap between academic research and industrial commercialisation [Gul09]. Figure 3.3 illustrate the funding and actors associated with Technology readiness levels, with the curve in the figure illustrating resources invested and minima of the curve indicating the region associated with the 'Valley of death'

3.2.3 Planar Magnetic Component systems

DC-DC converter systems are power distribution electronics first introduced in the domain of avionics to efficiently and effectively supply diverse critical electrical systems with power. The past three decades has seen the development of more electrified aircraft, driven by concerns of sustainability and increasing fuel prices [Hea91]. This increasing electrification has driven developments in durability and compactness in the domain of power distribution electronics [Kel01].

The integration of power converters into increasingly electrified airplanes is limited by magnetic components, transformers and inductors [BAE15]. The consequence of increased electrification is linked to many positive outcomes for aircraft, such as reduced fuel consumption, reduced emissions and reduced noise [NBM⁺17]. Additionally, these systems offer greater energy rationalization and reduced maintenance costs [RSA12].

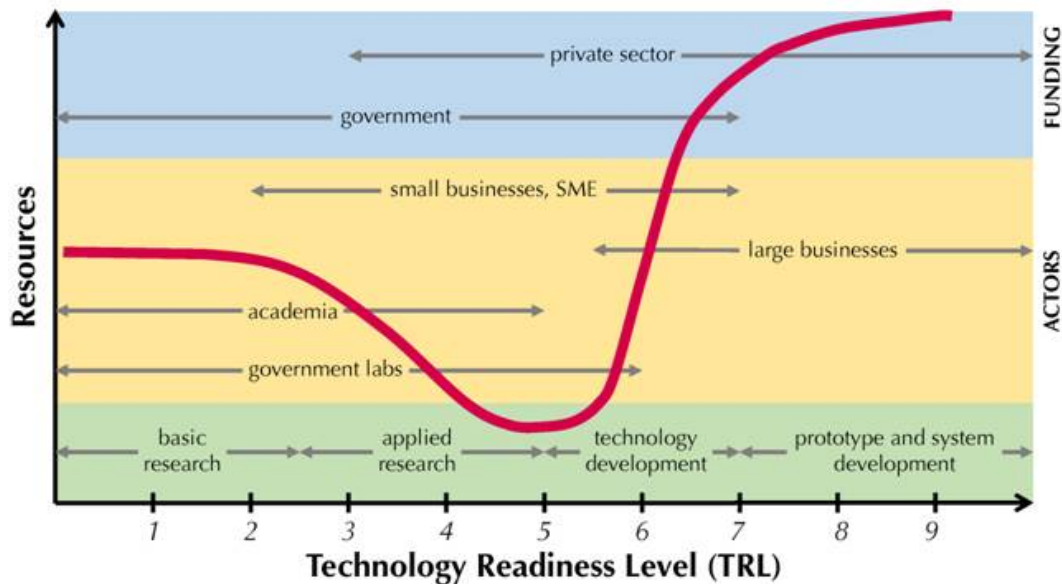


Figure 3.3: Illustration of technological readiness level with associated actors and funding [HLAK15]

The adoption of planar magnetic components is a result of increasing demand for high efficiency, high frequency and high energy density power supplies, where it outperforms traditional wire-wound magnetic components. Recent developments in the domain of Printed Circuit Board (PCB) technology have contributed to the reduction of size, weight and cost for such systems [OA14]. Ouyang [OA14] in his work details the recent developments, advantages and tradeoffs of such Planar Magnetic Component (PMC) systems. The use of PMC systems brings with it many fundamental advantages, especially in the domain of magnetic design, but also some tradeoffs, which the author is hopeful that the development and maturing of the domain will iron out.

The highly specialized Planar Magnetic Components (PMC) includes in addition to magnetic components, specialized electronic components such as transistors, capacitors and inductors. Additional requirements on operating conditions, and optimizations based on power density and efficiency result in a highly integrated design. The magnetic core designs are limited to specialized geometries, limited by winding requirements [McL88]. The dimensions of some magnetic cores designed by Magambo [BAE15] fall within the criteria of newer and more experimental electrical steel manufacturing methods [GAFL05].

3.2.4 DC-DC converter system market

The application domains of such converter systems include Aerospace, avionics, communications, server storage and networking, automotive applications and Industrial Electronic systems. The largest markets for such systems is in the domain of communication systems, though emerging domains such as automotive vehicles and industrial robotics offer higher growth potentials. The size of the market is estimated to be close to 10 billion dollars, and estimated to grow at close to 15

The product lineup of such system is specialized by its vertical, and classified on the basis of power, voltage and channel specific properties. The largest players in the market include electronics giants such as general electric, Ericsson and Texas Instruments. In the near term, the largest proportioning of growth is expected to take

place in the Asia Pacific region, driven by the installation of 5G infrastructure. The market share of newer systems such as those making use of PMC systems is unknown [MM18b].

The PMCs also find applications in the domain of Electric Vehicles (EVs), the largest sector for such materials. This sunrise sector is estimated to be responsible for the largest increase in electrical steel demand over the next decade. The sector has traditionally been dominated by high frequency transformers, though disruptive innovations such as PMCs are increasing their market share [BAE15] [RSA12].

A classification on the basis of PMC transformers cannot be made as data on the same is not publically available. PMC's are integrated into larger distribution systems, and the concentration of such systems is highly dependant on the specific model and manufacturers.

3.2.5 Way to market

The way to market for such materials is undoubtedly through partnerships with larger DC-DC converter manufacturers, as component manufacturers within their supply chains. The route to market strategy would thus be dependent on the ability to construct strategic alliances, in the face of expensive research and development of proprietary materials and manufacturing methods for both partners.

On examining the work of Yasuda [YI05], the aforementioned market environment closely resembles that of the semiconductor industry. Both the industries manufacture highly specialized materials for a diverse range of proprietary electronic components spread across different industries, and require large capital investments to upgrade manufacturing architecture and research, limited to short lifecycles.

The aforementioned study makes use of resource-based theory and social-exchange theory to draw attention to the importance of value chain integration. This is also reflected in the strategy of the market leader Taiwan Semiconductor Manufacturing Company (TSMC), which highlight Materials development, manufacturing technology and customer partnership as their largest strengths [Ind11].

A further analysis of the industry also highlights potential areas and requirements for establishing manufacturing plants. The establishment of semiconductor fabrication plants has a net positive effect on the entire industries innovation capability and performance due to Research and Development clustering [SY05]. Thus, in addition to generous incentives, some local city governments have also infused capital into such projects [Sho20] [Li16][MM18a]. However, the 'clustering' effect of the semiconductor industry is a topic of debate as it may be partially a result of its 'non-globalised' and 'learn by action' characteristics, though a weaker co-relation is still seen in low added-value steel products [HM98] [SVGW10].

The go-to market strategy is concentrated on high efficiency and power density PMC components for DC DC converter systems, developed and manufactured with specialized giants, with research and development conducted along traditional hotspots, which for electrical steel are concentrated along the Rhine region and Japan. The core strengths of this strategy are leadership in material development, manufacture and customer partnerships. This market leadership in development and specialized nature of product is part of a long-term trickle down innovation strategy.

4

MANUFACTURE AND PROCESSING OF ELECTRICAL STEELS

Material properties, such as magnetic properties are largely influenced by metallurgical properties such as material chemistry and texture [GCVK14][CKV+07][Mos90]. Some material properties have a clear and independent relationship to specific metallurgical properties, but for most material properties, the relationship between material and metallurgical properties are not simple and independent, but complex and dependant on a host of metallurgical properties. It is hard to isolate the exact relationship between specific material properties, such as magnetic properties, and metallurgical properties. So much so that isolating the individual relationships has proven a challenging endeavour [KJo8].

As a result, the production of modern grades of electrical steel is a complex and challenging endeavour. The manufacturing of grain oriented electrical steels is a complex affair, comprising of more than 20 distinct heating steps, and is the only low carbon steel product that incorporates the 'secondary recrystallisation process' in its manufacturing methodology. As a result of this complex manufacturing method, grain oriented electrical steels are often called 'the artistic product of Iron', and only produced by a dozen major manufacturers (even though its one the highest value added steel product made from low carbon steel). [LRB86]

Figure 4.1 details the steps involved in the manufacture of grain oriented silicon steel. The desired crystallographic texture for grain oriented steel includes large grains aligned in the GOSS orientation. The size of grain oriented silicon steels is controlled by adding an exact concentration of inhibitor elements, which inhibit grain growth during primary recrystallisation, but allow for the selective anomalous growth of GOSS grains during secondary recrystallisation [GAFL05].

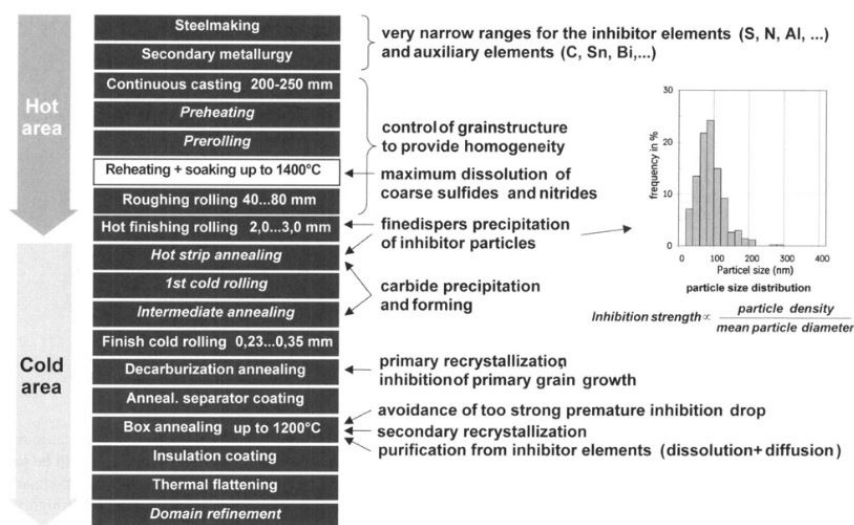


Figure 4.1: Production Schedule for Grain Oriented Steel [GAFL05]

4.1 ROLLING OF ELECTRICAL STEELS

The texture most suitable to applications making use of non oriented electrical steels is the cubic texture, or the $\langle 100 \rangle \parallel$ to Normal Direction fibre texture. This texture is challenging to develop, as the natural end texture after cold rolling and annealing for BCC materials like electrical steels are the gamma fibre or $\langle 111 \rangle \parallel$ Normal Direction fibre textures [Che13] (Incidentally, the $\langle 100 \rangle \parallel$ to Normal Direction fibre texture is obtained with relative ease for FCC polycrystalline materials with the application of plane strain deformation and recrystallisation) [PPD⁺10].

4.1.1 Cold Rolling

During recrystallisation, a cold rolled sheet transforms into a completely new texture [CBM14]. Various processes such as cold rolling, two stage rolling, or surface annealing are commonly used to enhance the $\langle 100 \rangle$ (cube or theta texture), in addition to processes such as severe plastic deformation.

4.1.2 Hot Rolling

As discussed in earlier sections, the finish rolling temperature (FRT) has a consequential effect on the final texture. Hot rolled products have a high FRT, and although this may result in predictable deviations in final texture, the final texture of hot rolled steels is also dependent on the gradients of temperature, in addition to the shear stress gradients. For low carbon steels such as silicon steel and chromium steels, Raab and Lucke [RL92] showed that gradients of shear and temperature lead to inhomogenities of texture and microstructure of hot rolled bands through the sample thickness.

Water was sprayed on the surface of the sample to enable high temperature gradients, which in turn reduced the dynamic recovery, and resulted in a higher comparative stored deformation energy in the centre. The observed differences were retained even after phase transformations took place [RL92].

4.1.3 Asymmetric Rolling

Asymmetric rolling is a rolling technique which aims to introduce a larger shear uniformly throughout when compared to conventional rolling [VSV⁺08]. This is realised by maintaining a high degree of friction between the rolls of the rolling apparatus, and the rolled sheet. Asymmetrical rolling introduces a shear stress distribution that doesn't only act on the surface, but also deep in the samples [FKK17].

This effect is achieved by changing the diameter of rolling or changing the velocity of rolling of one of the rolls [SVG⁺12]. The use of asymmetric rolling is noted by both surfaces of rolling undergo different shear stress characteristics. The use of techniques such as single roll drive (wherein only a single roll is driven and the other roll is disconnected to the driveshaft) are also modes of performing asymmetrical rolling.

The works of Lee and Nyung [LLo1a] also look at the deformation texture of asymmetrically rolled steel sheets in BCC and FCC materials [HT97][Ric97]. The aforementioned work utilizes FEM methods and the Full constraint Taylor model to calculate the crystal rotation and predict its deformation texture.

4.1.4 Shear stress characteristics of asymmetric rolling

Asymmetrical rolling decreases the normal pressure on rolled steel, and increases the cross shear region (which refers to the region between the neutral point of the upper layer and lower layer). The area of cross shear region is deformed in a unidirectional manner. Thus, while symmetric rolling provides ideal texture near the surface, asymmetrical rolling provides ideal texture through the thickness of the sample. The work of Nyung and Lee [LLo1a] observed a normal pressure reduction from 700 MPa to 300 MPa [Gho89].

Dhinwal and Toth [SDT⁺19] studies the behavior of single pass rolls of symmetric and asymmetric rolling for various rolling percentages. The image at the top of figure 4.2 details the obtained inclination profiles for symmetric and asymmetric rolling (which were parallel to the normal direction before rolling), while the image at the bottom of figure 4.2 detail the evolution of texture for symmetric and asymmetrical rolling.

As can be observed from Figure 4.2, an increase in rolling percent is linked to an increase in the sharpness of alpha and gamma fibres for symmetric rolling, while the texture for asymmetrical rolling goes towards a shear texture, which indicates a loss of symmetry. This has led some studies to indicate that the mid-section texture would be the same for symmetrical and asymmetrical rolling, and that a simple rigid body rotation would change the symmetric texture to an asymmetric texture [LLo1b]. This indicates that the phenomenon behind this transition may be caused because orientations that are the stable end orientations become unstable under asymmetrical rolling, leading to additional rotation beyond these stable end orientation [HRL91].

Additional studies also indicate that the magnitude of shear strain and uniformity are higher for asymmetrical rolls. An increase in shear strain also results in grain size refinement, tensile strength improvement and tilt/rotation of texture.

Asymmetric Cold rolling

Cold rolling textures for asymmetrically rolled non oriented silicon steels were studied by Pei and Shah [PSY⁺09], which investigated the through texture evolution of 2.1 % non oriented hot band silicon steel. Hot bands were normalised at 1000°C for 5 minutes, after which 80% cold rolled reduction is performed. The velocity ratio for this study is 1.125, while that of most other asymmetric rolling studies listed in this chapter is 1.5 (The velocity ratio refers to the ratio between the velocity of the upper and lower roll).

Figure 4.3 depicts the obtained results. The ODF functions are obtained using series expansion method, and are depicted in the Roe notation. Asymmetric rolling has a distinct effect on through thickness textures, with a weakened alpha fibre, most prominent at $112 < 110 >$, weakened $111 < 110 >$ and enhanced $111 < 112 >$, with the only exception being the topmost layer, where both alpha and gamma fibre are weakened. Cold rolling of silicon steel leads to a maxima of $001 < 110 >$ at 70 % reduction, with further rolling leading to the formation of $112 < 110 >$ and $111 < 110 >$ texture [BTN07].

Asymmetric rolling with a velocity ratio of 1.125 can produce uniform shear strain throughout the thickness. Thus, for this situation, the effects of asymmetric rolling at 80% reduction cold rolling are qualitatively similar to $S = -1$ (which denotes the bottom layer). Additionally, the final texture depends on the initial texture (in addition to the shear stress distribution) [SHL89]

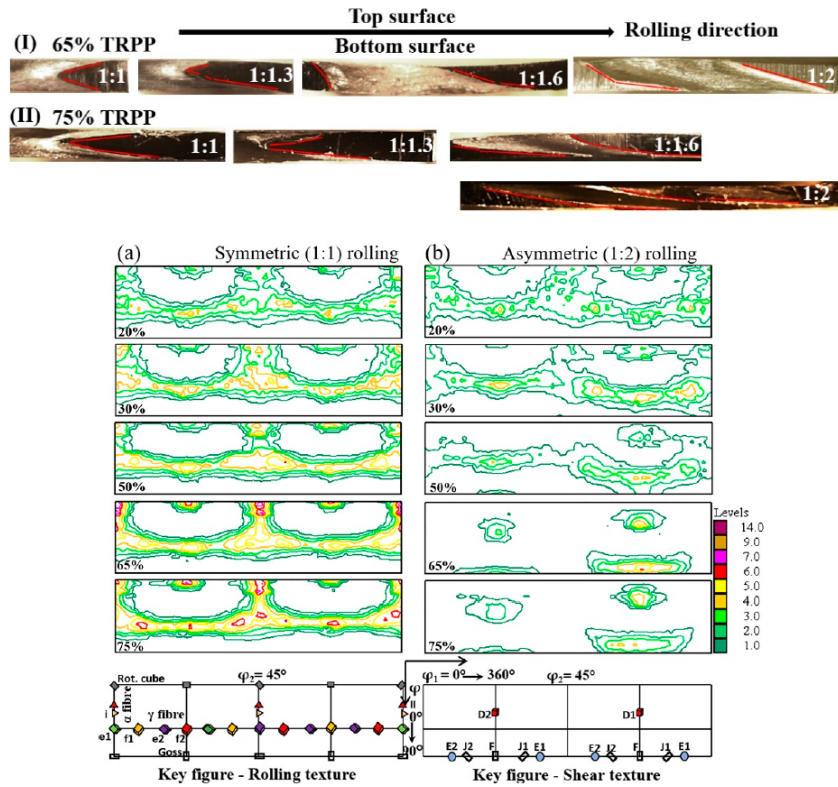


Figure 4.2: Change in inclination profiles for pins parallel to the normal direction at different asymmetric rolling ratios for 65 and 75 % reduction, and Sections of $\Phi_{12} = 45$ ODF for rolling reductions between 20 and 75 %

[SDT⁺19]

Asymmetric Hot rolling

The work of Chen and Butler [CBM14] investigates the effects of asymmetrical hot rolling, as compared to conventional hot rolling. The study aims to investigate its effect on non grain oriented steel, and describes a favourable Non grain orientated electrical steel texture for asymmetrical hot rolling samples, compared to conventional hot rolling samples. A higher concentration of theta fibre and lower concentration of gamma fibre is obtained for steels produced using hot band strip techniques, although much of this texture is eliminated after cold rolling processes are performed. An increase in the undesirable gamma fibre texture is also observed after cold rolling and annealing are performed.

On observing the texture of the samples at different section depths, a better understanding of the underlying causes for the results can be determined. Figure 4.4 depicts the obtained texture at different section thicknesses. The difference in obtained texture at the surface and mid-thickness sections point to the role of recovery and recrystallisation at the sections. For low carbon steels such as those used in electrical steel applications (and the ones used in this research), recrystallisation is possible in the ferritic region when hot rolling is performed, as long as the reduction or strain imposed is larger than a critical value. Thus, as fig. 4.4 illustrates, a Strong alpha fibre is observed in the mid-thickness section of the sample. This critical strain is temperature dependant. For higher temperatures a higher dynamic recovery rate and a smaller driving force is required. Thus, as the surface temperature of hot rolled steel is lower than the temperature at the centre of the sheet, recrystallisation is promoted at the surface, while recovery is promoted at the centre.

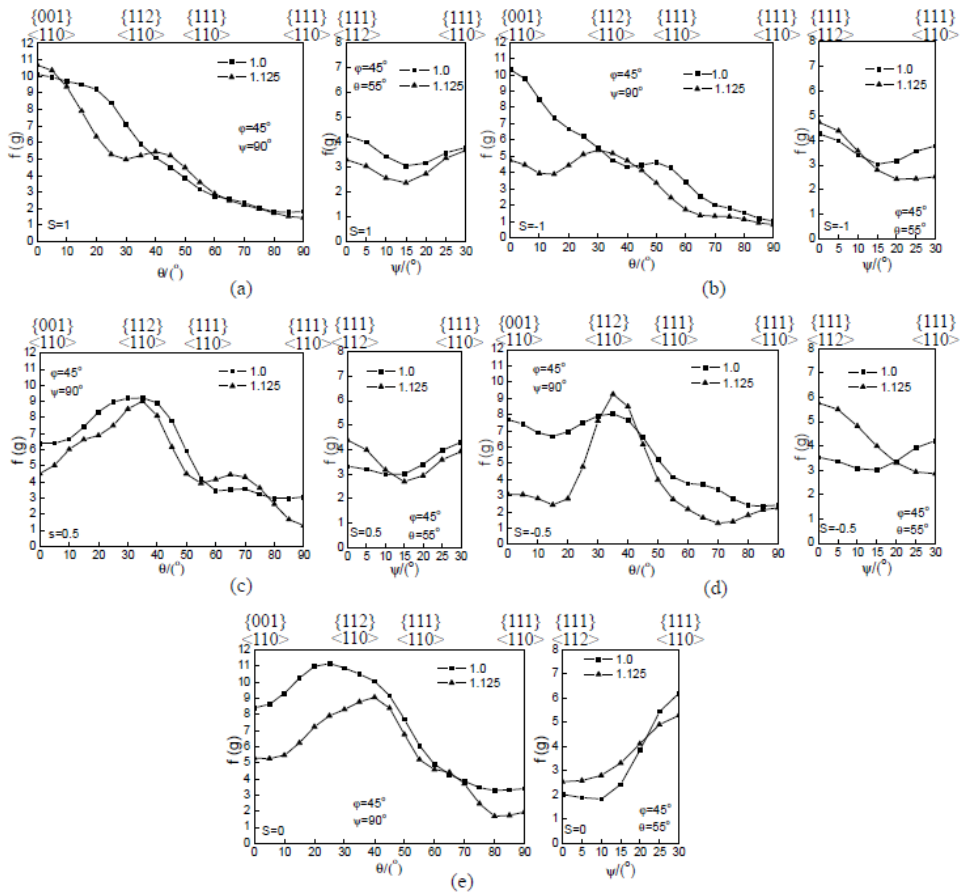


Figure 4.3: Obtained orientation densities along the alpha and gamma fibres for different layers in the cold rolled non oriented silicon steel sheets a) $S = 1$, b) $S = -1$, c) $D = 0.5$, d) $S = -0.5$, e) $S = 0$. Square datapoints indicate symmetric rolling and triangular datapoints indicate asymmetrical rolling

[PSY⁺09]

4.2 SEVERE PLASTIC DEFORMATION

[PPD⁺10] looks at Severe Plastic deformation as a method to reduce the concentration of the undesirable Gamma fibre texture (the gamma fibre texture is the fibre texture that denotes the $\langle 111 \rangle \parallel \text{ND}$ orientation). Five passes of 50 % reduction are made (for a cumulative reduction of 96.9 %), after which surface annealing is carried out, with an expectation to obtain the $\langle h11 \rangle \{1/h12\}$ texture, which was first carried out by Homma et al [HNY04].

The findings of the aforementioned research include a higher than expected concentration of gamma fibre, along with a strong rotated cube texture. Additionally, other textures were observed during the reduction steps, with a rotation only being observed in the last pass. Other variables playing a role in the final texture include the size of the grain prior to recrystallisation, with larger grain sizes being associated with identified texture, and smaller initial grain sizes being associated with gamma fibre textures.

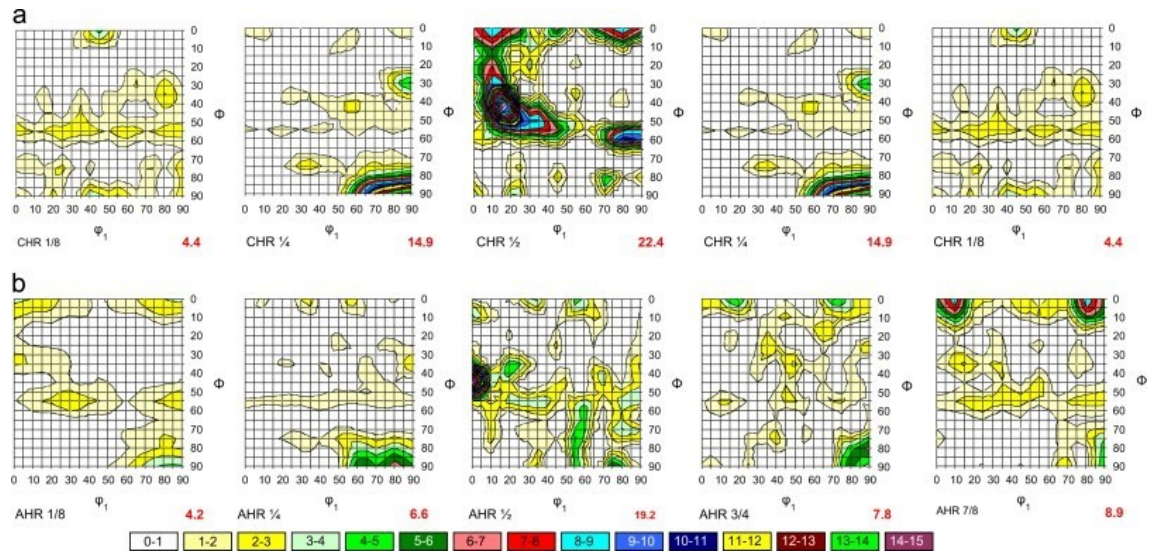


Figure 4.4: distribution of texture concentration of A- γ Asymmetric rolling B- γ Conventional rolling at different cross sections

[CBM14]

4.3 CROSS ROLLING

Cross rolling is a method of rolling in which the orientation of the rolling mill rolls with respect to the sample sheet are rotated. The aim of cross rolling is to change the orientation flow during plastic deformation [WWBW13]. Under laboratory conditions, cross rolling may lead to strong rotated cube component texture, with texture concentrations as high as 150x random intensity. Additionally, alpha and gamma fibres are not produced during cold reduction, although the strong rotated cube texture is much weaker then [KJo8].

The aforementioned study by Kestens and Jacobs [KJo8] also finds that when the material is cold rolled to a reduction of between 4 and 8 %, and is submitted to additional annealing treatment (comparable to what is applied on semi processed products), the rotated cube component re-appears. Other components, including components of the undesirable gamma fibre texture are formed as well [KJo8]. The main drawback of this technique is that it may nit be implemented on a traditional continuous line manufacturing process.

5

COMPUTATIONAL MODELLING

Physically based computational modelling is an integral tool in not only better understanding the relationship between microstructures and properties, but also serve as contributors to design of materials and processing. Computational modelling has long been restricted by the complexity associated with deformation mechanisms and limited computational power, to serve as indicators of qualitative trends and complement existing phenomenological designs by accounting for minor variations.

In recent years, there has been an exponential increase in computational power and has seen the development of increasingly sophisticated algorithms to describe the aforementioned physical relationships, which serve to broaden the scope, accuracy and adoption of computational modelling. Computational modelling for the development and optimisation of materials offer significant advantages in both the developmental timeline and economic costs associated.

5.1 CRYSTAL PLASTICITY MODELLING

The importance of texture and its applications have been discussed in earlier sections. Obtaining a desirable texture would favourably influence material performance. The processes involved in imparting texture are influenced by the thermo-mechanical processes, such as the forming processes. Forming processes involve the application of complex stresses and strain, and are modelled using techniques such as Finite Element (FE) analysis.

Crystal plasticity models aim to describe the behaviour of individual crystals within a polycrystalline aggregate, under plastic deformation. There are innumerable models describing this behaviour, and the use of a specific model determines the assumptions on which relationships between microstructural (including properties such as stresses on individual grains) and macro-structural parameters (which include properties such as average flow stress and average plastic strain) are determined. These models make use of a representative sample set as an input. The aggregate mechanical behaviour of input texture crystals is taken to be representative of texture evolution.

There are two types of crystal plasticity models, 'Taylor' type models, and finite element crystal plasticity models. In 'Taylor' type modelling, properties such as slip systems, slip rates, rotation of lattice and deviatoric stress are calculated for individual grains independent of the behaviour of other grains, while for crystal plasticity finite element modelling (CPFEM) a finite element mesh takes into account the behaviour of other grains, considering it to be a matrix with averaged out properties of the whole polycrystalline. Thus, 'Taylor' models have much shorter calculation times and require less intensive computational loads to complete [VLSD05].

5.1.1 Multi-level Scaling

One of the primary differences between 'Taylor' type models and CPFEM models is the multiscale modelling criteria. Crystal plasticity models differ in their behavior for mesoscopic and macroscopic scales. Selection of a representative volume

element (RVE) differs for the two crystal plasticity models [VH88]. Mesoscopic representative volume elements are supposed to have homogenous properties, with uniform stress and strain distributions. For Taylor type models, a single grain is selected as the RVE, while CPFEM models, they are chosen to be smaller than a single crystallite [VKV⁺06].

CPFEM models are also statistical, and rely on the creation of a macro RVE, with a few thousand grains which suitable represent of the macroscopic RVE, large enough to have the average properties of the polycrystalline materials. CPFEM models also make use of mechanic properties (stress equilibrium and geometrical compatibility) to relate mesoscopic scale properties to macroscopic scale properties. Taylor type models may make use of local constitutive laws based on crystal plasticity theory, to relate local properties to internal processes (as the mesoscopic scale RVE is considered to be a single crystal inside which uniformity of properties is assumed) [BH51].

Local Constitutive laws

A local constitutive law establishes relationships between local mechanical parameters such as stress and strain within mesoscopic RVEs. Thus, local constitutive laws aim to model internal processes such as determination of slip systems and crystal rotation. In the case of Taylor type models, they usually include kinematic equations, and may include additional/adverse energetic assumptions (the Taylor Hill model stands as an example of the same) [BH51]. These models generally exclude elastic parameters from their purview. The kinematic tensorial equation to determine velocity gradient with slip rates is given below. The frame of the aforementioned equation is any frame which does not rotate with respect to the polycrystalline reference system.

$$I = W^L + \sum_{s=1}^N \hat{b} \times m^s \dot{\gamma}_s$$

Additionally, Taylor type models treat the above equation as an equation in which the velocity gradient tensor is a known quantity and the slip rate is unknown. Implementing the rotation criteria, $W^L = 0$, and equations given below are obtained.

$$d_{ij} = \sum_{s=1}^N M_{ij}^s \dot{\gamma}_s$$

$$\text{Where, } M_{ij}^s = \frac{1}{2} (\hat{b} \times m^s + m^s \times \hat{b})$$

As volume is assumed to remain constant and the orthogonality constraint between m^s and \hat{b} s, there are an insufficient number of equations, and would result in a non unique solution (as the number of free variable slip variables exceed the number of independent equations).

The mathematical solution of the same is carried out on the basis of inclusion of the aforementioned 'Energetic assumption', which increases the number of equations to ensure an ideal solution can be found. The most commonly implemented assumptions include those proposed by Taylor [Tay38] which states that the internal dissipated work is minimum, and that proposed by Bishop and Hill [BH51], wherein the maximum work principle is used to determine deviatoric stress corresponding to prescribed strain rate. Bishop and Hill have shown that their method is equivalent to Taylors method and is often referred to as the Taylor Bishop Hill theory.

5.1.2 Taylor model

The earliest crystal plasticity model was proposed by Taylor [Tay38], which aimed to describe the plastic deformation of a single aluminium crystal during a tensile

test, wherein the deformation of the Aluminium crystal is described as a result of shear deformation along 12 slip systems. Deformation begins when the shear stress resolved in the direction of a slip system exceeds a critical value, referred to as the critically resolved shear stress.

The analysis of polycrystalline materials using this model was first proposed by Taylor [Tay38], in which a polycrystalline was approximated to an aggregate of grains, and adapted to a continuum mechanics framework by Hill [BH51] (for the case of small strains only). The assumption made for the adaptation to polycrystalline materials is a simple one, the microscopic strain rate is equal to the macroscopic strain rate.

This satisfies one of the two boundary conditions imposed on a polycrystalline aggregate, and is commonly referred to as the ‘full constraint’ Taylor model. A variation to full constraint Taylor theory is classical relaxed constraints Taylor theory, for which one or two of the components of the local velocity gradient tensor need not be the same for all grains [VLSDo5].

It satisfies the criteria of strain compatibility between neighbouring grains. It does not however, satisfy the stress equilibrium criteria, and thus, does not completely describe material behaviour. Studies such as Lucke [RL92] illustrate how the results obtained using Taylor’s model deviate from experimentally observed results.

5.1.3 Relaxed Constraint Taylor Model

The quality of predictions for full constraint models has not been universally accurate. Texture evolution during the rolling results in elongated and flattened grains, which are not represented accurately in the full constraint Taylor model. Models implementing a lax enforcement of the strain equilibrium criteria have been proposed by Van Houtte and Kocks and Chandra [Van82][KC82].

This ‘lax enforcement’ translates to not enforcing all the 9 constraint equations of the Taylor’s model, and allowing some conditions to remain unfulfilled. This is not based on concrete physical reasonings, and models derived are limited in their scope to certain applications. Figure 5.2 below illustrates an example of the Lath model, which can be used to simulate elongated grains. In this image, the shear l_{13} is shown to be relaxed, which would result in sheared grains in this context. The pancake model is another example of the relaxed constraint theory, in which both shear l_{13} and l_{23} are relaxed [KC82]. In the lath model, the local velocity gradient l_{13} is independent of the strain equilibrium criteria, and the value of l_{13} being derived on the basis of minimum work required for plastic deformation.

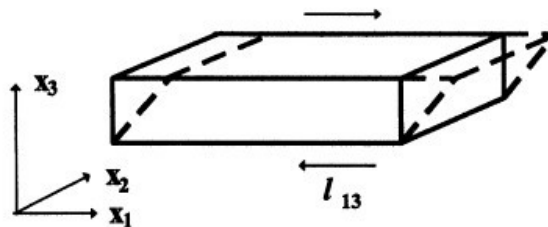


Figure 5.1: Representation of an elongated grain, with x_1 indicating rolling direction and x_3 normal direction. For lath relaxed constraint models, l_{13} is relaxed [VH88]

Van Houtte [Van82][KC82] also showed that the solutions obtained in this theory are also obtained using the ‘mixed boundary criteria’ of the aforementioned Bishop

Hill theory. The reasoning for this relationship centers around the principle that for flat elongated grains, interactions with neighbours are incapable of building the necessary stress level for enforcement of strain criteria.

5.1.4 Multigrain Relaxed Constraint models

The textures predicted by simply applying relaxed constraint equations were not found to be better than Full constraint models. Not taking into account the local interactions between grains is a suspected reason for the same. Multigrain relaxed constraint models take into account the interaction between neighbouring crystallites, though the number of neighbors that are taken into consideration depends on the specific model used. The LAMEL model takes into account the interaction between two crystallites, and the GIA model eight crystallites.

Multi grain models such as the LAMEL and ALAMEL models incorporate dual structure equations, which serve to not only relate strain and slip rates, but also stress and resolved stress in the direction of slip systems. Both LAMEL and ALAMEL models take into account interactions between neighboring grains. They also do not strictly follow the uniform field theory, but implement global average criteria, wherein global average of parameters such as average strain tensors are equal to the mean prescribed rate.

The LAMEL model was developed by Van Houtte and Delannay as a software to determine texture evolution quantitatively. It was initially developed to study cold rolled low carbon steels, which underwent rolling in room temperatures [VH88]. This model is most suitable for analysis of flat elongated grains. The limited scope of the former were adopted in the Advanced LAMEL or ALAMEL model, which overcame the limitations of scope the former has, such as the limited application of the former to only rolled samples. [VKV⁺06]

Taylor Ambiguity

The Taylor Bishop Hill model leads to multiple solutions when no degeneracy of Taylor equation occurs or when the same values are used for the critical resolved shear stresses on many slip systems. For non cubic materials, different critical shear stress values are assigned to different slip systems. Relaxed Constrained (RC) models also enforce degeneracy as a rule.

The models to differentiate between the potential slip systems are often not available, though, various physical phenomenon cause differentiation, such as strain rate sensitivity (Taylor type models such as the Taylor Bishop Hill model are strain insensitive), though these are dependent on the material and environmental parameters. Peeters et al [MH14] found that in the case of IF steels beyond 1 % plastic strain, the effect of dislocation networks overshadowed the effect of strain rate sensitivity.

5.2 LAMEL

The LAMEL model is a multigrain model that treats two grains simultaneously, and assumes they form a stack, as illustrated in figure 5.2, and are selected from the discretized input in a random manner, which are assigned to both the positions in the stack (top and bottom). Figure 5.2

The relationship criteria for deformation of grain boundary is limited to sliding along the interface, and do not allow for a distorting in the interface. Thus, in most

scenarios, only type I and type II deformation are allowed to take place, as illustrated in figure 5.2, as a result of which stress equilibrium is assured at the surface, without requiring shear stresses be equal to 0. Deformations of type III are only permitted when the shear stresses of both grains are equal, resulting in an undistorted interface. Another condition implemented relates to the strain rate, wherein the volume average of relaxation is 0, as a result of which, the average strain rate tensor is equal to the macroscopic strain rate. Thus, there is no change in macroscopic strain rate as a result of relaxation.

The LAMEL model has proven to be successful in predicting rolling textures quantitatively for steel [VH88], which is however, limited in its area of application to those involving rolling operations of materials with flat elongated grains.

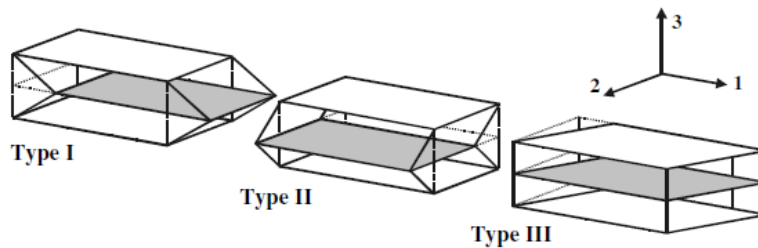


Figure 5.2: Modes of relaxation considered for the LAMEL model [VLSD05]

5.2.1 ALAMEL

The results obtained by using CPFEM models have been found to deviate sufficiently from those obtained by using the Taylor's model, with the texture predictions made using the CPFEM models being significantly better [VKV⁺06]. Van Houtte found that the partial implementation of the stress equilibrium criteria, along with a relaxation in Taylor's assumption of homogeneous deformation results in a desired result [VLSD05].

The ALAMEL model also most notably deviates from the LAMEL model and other classical relaxed constraint model in its scope of application. The ALAMEL model does not require the geometry of relaxations to be related to that of the geometry, which allows it to be used for any mode of deformation.[VKV⁺06]

Assumptions of the ALAMEL model

The ALAMEL model assumes the local strain rate is not constant throughout a crystallite, and as a result, slip rates within a crystallite are also not uniform. Figure 5.3 illustrates how interactions near grain boundaries affect their bordering regions. As a result, the deformation texture of the polycrystal can thus be represented by the orientations that are developed in this region. The equations and laws used to derive texture evolution in this model is similar to that of the LAMEL model.

The second major assumption of the ALAMEL model relates to the selection of orientations used to illustrate the material texture. While performing simulations, only a few thousand orientations are used, which are determined by taking into account the probabilities of occurrence of the grain boundary segment and orientations of bordering grains.

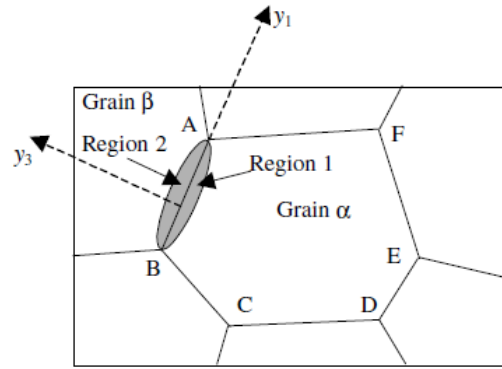


Figure 5.3: Illustration of polycrystal and grain boundary structure for ALAMEL model [VKV⁺06]

5.2.2 Implementation of the ALAMEL model

The selection of orientations is implemented by using a statistical method described by Toth and Van Houtte [TH92]. A microstructural file is used for an input, which describes the initial microstructure as an agglomeration of interface and frame orientation angles with respect to the macroscopic frame. The ALAMEL model is not restricted to elongated grains, and the microstructural file assumes equiaxed grains (unless specified by the user). The selection of pairs are created randomly from the aforementioned microstructural file.

The ALAMEL simulation is carried out as a series of consecutive reductions, with the output properties of the previous iteration serving as the input properties of the current iteration. In addition to initial texture and microstructural files, there are several parameters that determine the deformation texture, most importantly the total number of iterations, rolling reduction per iteration, rolling reduction direction and symmetry. As mentioned in previous sections, these parameters serve as global limits, valid for only infinitesimal reductions.

In addition to LAMEL variables, lattice spin is also obtained for ALAMEL simulations, which is used to calculate the orientation at the end of an iteration, while interfaces are calculated in the basis of deformation tensor. The final deformation texture is calculated by weighting of crystallite orientations using volume fraction weighting.

A crucial point to note is that ODF sample symmetry for the initial texture should not take into account sample symmetries, which would reduce the unit zone in orientation space. The ODF's specified must thus be specified in the triclinic sample symmetry. The ALAMEL model is implemented with the help of the ALTAY software suite.

5.2.3 ALTAY software system

The 'ALTAY' software system is used in the current study, and is a software system that can be used to carry out ALAMEL, Taylor and GBD simulations for plastic strains on polycrystalline materials. The model is based on literature from van houtte [VKV⁺06]. The software is written and compiled in Fortran (version 6.5), and can be run as an executable. It is run as a set of subroutines, which are called

from the main program.

The file uses as an input descriptions of possible slip systems (and twinning systems), crystallographic texture details and strain instructions. The slip system information is entered as a .PRE file, which is dependent on the crystal structure of the sample (for the current study, the BCC.PRE file is used).

The crystallographic data is entered as a set of discrete orientations, and two formats may be used, a .smt format input, which is arrived at by application of a discretization program from the MTMTAY/MTM-FHM software system, or as a .cur file, which is the format generated as an output in this software system. The strain increments are encoded within an .io1 format file, (maina1.io1) which also allows the selection of parameters such as output name, input crystallographic texture name, number of steps and reduction per step.

The outputs from the software system include .Res output files, which record the stresses, taylors factors and plastic work associated after the first strain increment, in addition to the aforementioned .CUR files that record output texture data and .LST files that record log information and average values of variables such as stress. .RAT files are also included in the output, and they detail the slip rate for each slip system.

6

DISORIENTATION REORDERING

6.1 PROBLEM DEFINITION

As discussed in earlier sections, the ALAMEL model uses as an input a textural file, in addition to a microstructural file. The textural file lists the grain orientations of ALAMEL pairs, while the microstructural file contains information about interface segments between two grains, denoting information about segment normal orientations, represented as Euler angles. The data from microstructural files are considered to allow relaxation of grains as described in earlier sections (deformation is allowed in the direction of these segment normal orientation).

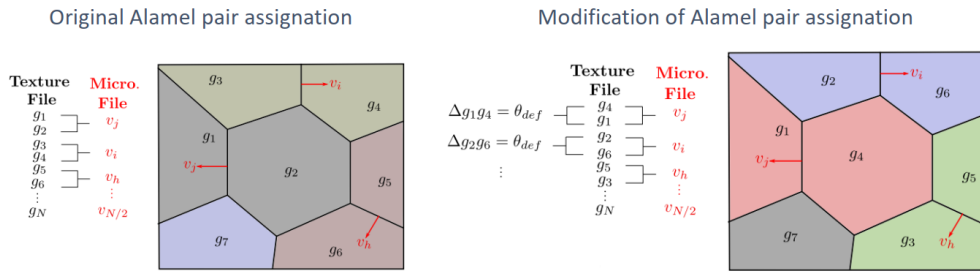


Figure 6.1: Procedure of ALAMEL pair assignment modification, illustrating the original unmodified pair assignment (left), and disorientation sorted modified pair assignment (right) —Need to include credit—

The ALAMEL model randomly assigns a microstructural file vector to texture file pairs. Each texture file pair is indicative of a pair of grains whose boundary parameters are given by the randomly assigned microstructural file vector. The grain pairs are formed from sequential texture file input entries.

The aim of this study is to determine the effect of disorientation between pairs for the textural file grain orientations. Figure 6.1 illustrates the process of ALAMEL modification used for this study. The texture file input is modified to rearrange pair disorientation values (given as $\Delta g_i g_j$) so as to obtain specific disorientation values between each pair. The textural file pairs are simply rearranged, and the microstructural input is not modified in any manner in this process, resulting in no change in input texture. Furthermore, the assignment of microstructural vectors is random for the ALAMEL model

The rearrangement of texture file input results in a change in disorientation angle between ALAMEL pairs (its disorientation 'topology') while not impacting input texture. The behaviour and impact of the disorientation topology under plastic deformation is observed in this study.

6.2 MODEL VALIDITY

Prior to the adoption of a specific model, its efficacy needs to be determined. The process of verification and validation aims to understand the same. The processes of verification and validation are distinct processes, although they are both used to analyse the efficacy of the models used. Barry Boehm described the differences between them as two simple questions, which are given below. [Boe84] Thus, the verification of the model aims to answer the question of the implementation of the model for the specified task, while validation of the model refers to the efficacy of the system as a whole with respect to the broader aims and tasks. • Verification: Are we building the product right? • Validation: Are we building the right product?

In the current context, the verification process aims to analyse the implementation of the given mathematical model in the computational domain. This relates to its architectural, database and model specification implementation, which would include the histogram and pairwise variation of disorientation angles, in addition to model specific parameters, which for the Monte Carlo method would include the dependence of results on the number of iterations, and variation of results in different runs.

The validation process for the current context would analyse the variation parameters for different orientations compared. The output parameters are expected to vary with disorientation parameters, as the distribution of disorientation angles is not even, with random orientations producing the Mckinzie distribution [?], which displays low frequencies of orientations at low and very high disorientation angles.

6.3 MONTE CARLO METHOD

Monte Carlo algorithms are a broad class of computational algorithms that rely on repeated random numerical sampling to obtain results [Les13]. This method is a probabilistic method to obtain results for deterministic problems. The use of Monte Carlo methods may be used for optimisation problem, and is the nature of its use in the current study.

The Monte Carlo method was developed in Los Alamos in the 1940s to solve multidimensional integrals and intractable numerical problems [MU49]. The name 'Monte Carlo' is also derived from the famous casinos of the area (though they are not named so because of the association of gambling with probability theory, but rather in honour of an uncle of one of its founders, who shared the ability of solving intractable problems with the method) [Les13].

The use of Monte Carlo simulations is proffered when the problem or data being optimised has many degrees of freedom. In the case of the current study, each orientation is independent of each other, and reclassification into similarly spaced results can be done using innumerable pairings. There may be more than one 'ideal' representation, and results may be based on initial ordering of data or the algorithm used. The use of Monte Carlo simulates a vast range of outcomes, including some of the more extreme possibilities. The accuracy of the use of this method is proportional to the number of Monte Carlo runs, and is described by the law of large

numbers. According to the aforementioned law, the result of a large number of random substitutions is stable [Caf98].

The current study also looks into the stability of the usage of Monte Carlo methods, by performing multiple Monte Carlo runs using the same number of steps. Five runs were performed for the optimisation of disorientation, with fixed variance in disorientation of 5° beginning with a minimum disorientation criterion, 10° of disorientation to 60° disorientation and maximum disorientation. The standard deviation for each iteration is given in figure 6.5 along with obtained results for variation of mean vs number of trials.

As illustrated in the figure 6.5, a large variation of average disorientation in the initial set of tranche of Monte Carlo runs is observed, after which there is only a minor change in average values, and average values are close to ideal values. But on observing the standard deviation of the same dataset, it becomes clear that an increasing number of Monte Carlo iterations are linked to reducing standard deviation.

6.3.1 Implementation of the Monte Carlo Model

As discussed in earlier sections, the Monte Carlo method is used to evaluate complex multi-dimensional functions. The implementation of the Monte Carlo method is performed in three steps, the definition of the problem space or function region, the definition of function variables or 'random input' and measurement and convergence of results.

The definition of function region aims to define the region within which includes the function and is a 'boundary' definition. Within this region, the second step of random input generation is performed. The generation of random inputs must take into account characteristics such as the curvature of the domain defined in the first step into account. Euler space is 'distorted' in volume, and requires an invariant transformation to accurately generate random inputs. This is illustrated in figure 6.2, which illustrates the 'random distribution' of orientations in Euler space with and without accounting for the distortion using invariant measures.

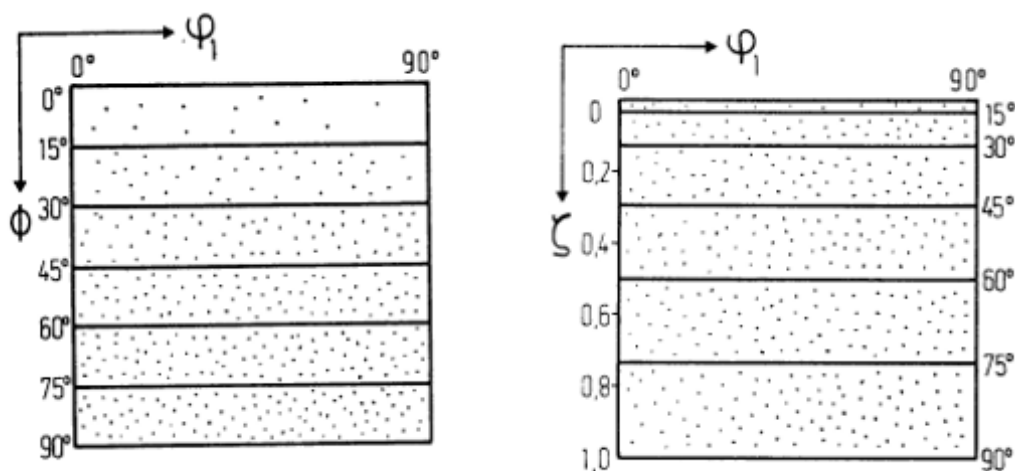


Figure 6.2: Random orientation distribution in Euler space without in-variance (left) and after invariant transformation (right) which takes into account the distortion of Euler space

[Bun13]

The last step involved measurement of output functions and convergence. The measurement of output variables is the measure of inputs that fall within the defined domains to the total number of iterations. The process of convergence indicates the arrival of a solution, and is indicated when additional iterations produce negligible changes in output.

Figure 6.3 illustrates an application of the Monte Carlo method to solve the “hanging chain” problem, where subplot 2 indicates a flexible hanging chain suspended from 2 points, with the red dotted line being the initial trial solution. The remaining subplots measure the output variables, measured against the number of iterations. Convergence can be observed, as the energy values measured do not vary significantly with number of iterations when the number of iterations closes to 200.

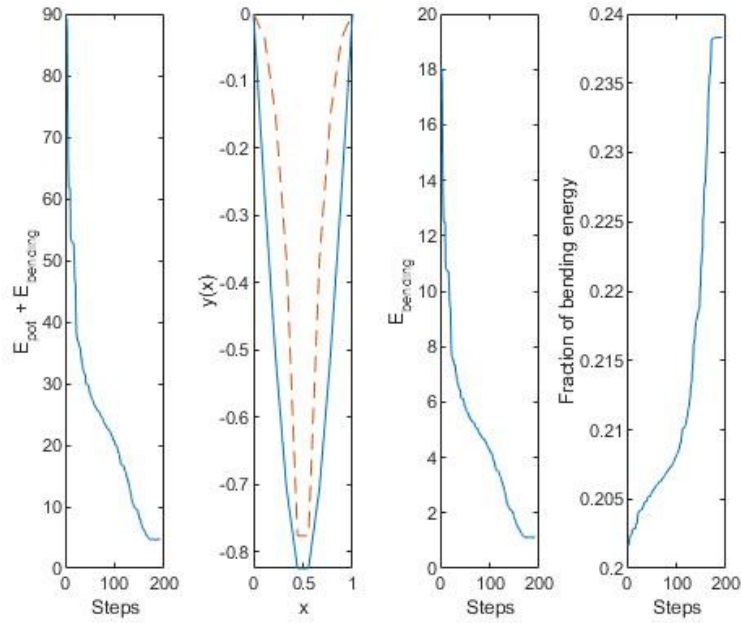


Figure 6.3: Monte Carlo convergence of the Hanging chain problem, indicating the variation in sum of potential and kinetic energy (subplot 1), bending energy (subplot 3) and fraction of bending energy (subplot 4) with number of iterations and steady state chain shape (subplot 2)

Within the context of the current study, the Monte Carlo algorithm is used to reorder pairs on the basis of pair disorientation. The function region is limited to initial disorientation pairs, bound to the aforementioned Euler Angle region. The function variables in this study are the individual vectors, whose ‘pair partners’ are used as variable for swap calculations. The criteria for swapping is simply a closer output to the ideal disorientation (given as the modulus of difference between obtained and desired disorientation’s). The convergence criteria is defined by either a (orientation volume dependant) predefined maximum number of iterations or (orientation volume dependant) trials without success. The output file is also rewritten at the end of every iterations performed.

6.3.2 Drawbacks of the current methodology

The use of Monte Carlo method for this study also poses many challenges, the foremost of which is the probabilistic nature of the method. The solution obtained by the use of this method is not ideal, as it is dependant on the number of iterations performed. The conversion criteria is also specified as a static standard deviation

value, and not perfect convergence. There is also a possibility of a 'false minima', especially as fractions of negative results are not accepted in the program used. Only 4 orientations are analysed in each iteration, which is a small number in comparison to the total number of iterations [Caf98].

The probabilistic nature of the solution also makes the result analytically untraceable, and non-repeatable. As a result, multiple trials are also conducted to observe the variation of results with a variation in Monte Carlo results. Lastly, the computational time and resources required for this method are immense. A single run involves hundreds of thousands to millions of iterations for a sample with a few thousand orientations. Each iteration involves a measurement of the desirable property, imposition of change, re-measurement, comparison of both initial and modified parameters and substitution (or lack thereof). The number of entries analysed is typically very low, and there is an ever decreasing probability of being a successful trial, in addition to ever-shrinking gains. Obtaining accurate results is accompanied by an exponential increase in computational resources [MU49](however, the degree of complexity of this algorithm is still $O(n)$ swaps).

6.3.3 Verification of Monte Carlo model

The verification process of this model involves plotting the histogram and the pairwise variation of the output disorientation texture data. This is in addition to limits on tolerances related to the mean and standard deviation of the results. Figure 6.4 illustrates the obtained histogram and pairwise variation of disorientation for target angles of 50° and 30° respectively.

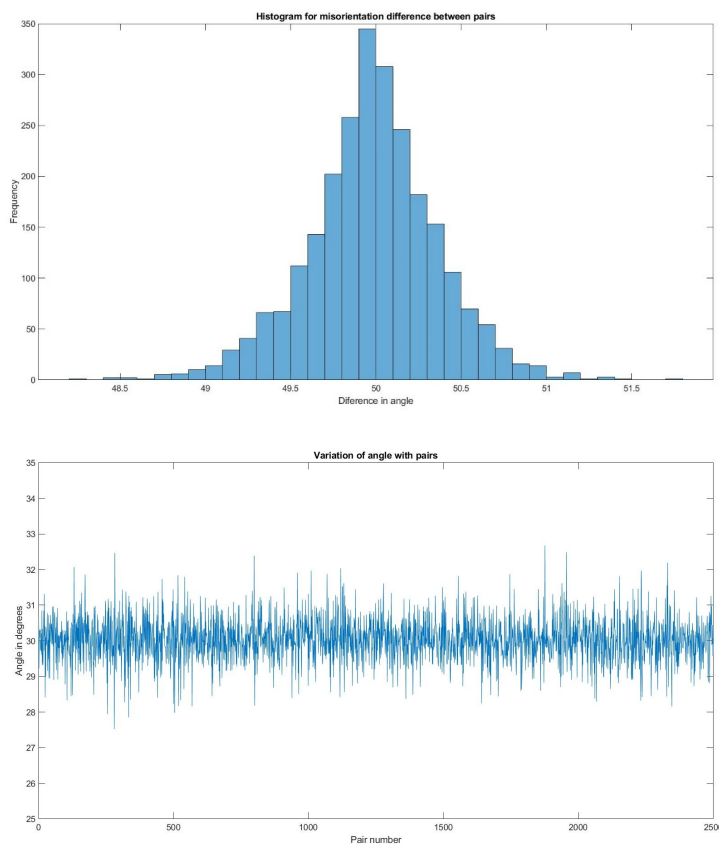


Figure 6.4: Histogram for obtained disorientation distribution and pairwise variation of disorientation

The primary model assumption in this Monte Carlo simulation results is a 'dependency' on the number of iterations performed. A large number of iterations results in a more accurate result, while being taxing computationally. The validation of this model is conducted by measuring the response of the system with respect to the number of iterations conducted. A texture file with 5000 orientations is used as an input, and after each iteration, the average disorientation of the dataset, and its standard deviation is recorded, for a large number of iterations (50000 iterations). The average disorientation data is utilised to measure the evolution of results for disorientation angles which are very different to initial averaged values (and illustrates how the average values change with number of iterations).

Figure 6.5 illustrates the obtained results, in which the variation of standard deviation for a 30° and 60° target and average disorientation for 60° and 35° are measured against the number of iterations.

The standard deviation curve displays an inverse exponential relationship for both angles measured. The convergence criteria and standard deviation properties vary with the target disorientation angle, with extreme target angles such as 60° disorientation and minimum disorientation having the highest standard deviation value and requiring the largest number of iterations to achieve convergence. This is both a result of initial disorientation pairing values (as illustrated by the average disorientation subplot for a desired disorientation of 35°, where the average obtained disorientation values at the start of the shuffling process is close to 35°), and the nature of disorientation distribution for cubic crystal geometries, where, as the Mackinzie distribution indicates, the aforementioned disorientation angles have a sparse distribution.

6.4 HUNGARIAN ALGORITHM

The Hungarian method is an assignment method first described by two Hungarian mathematicians Dénes König and Jenő Egerváry, which described the Hungarian problem in a literature paper on bipartite graph theory [Kön31]. One of the most consequential theorems from this paper illustrated the duality of this linear programming problem. For a binary input, the minimum number of lines that contain all of an input type also equals the largest number of rows and columns with that input, such that no other two inputs occupy the same row or column. Egevary described a computationally trivial method to reduce more general cases into binary problems, which together can be used to solve for a general case.

The Hungarian algorithm can be used as a deterministic method to re-order textural file pairs. Linear programming solvers present a powerful optimised method of solving the aforementioned 'textural file sorting' on the basis of disorientation problem [Bal65].

6.4.1 Definition of problem

The Hungarian problem is defined as illustrated in figure 6.6 by Kuhn [Kuh55] who first developed the Hungarian algorithm to solve the same by combining the methods of both Hungarian scientists. The problem relates to the best assignment of personnel and cost, where ranked or absolute values for each of the same is available. It aims to minimize cost or maximize ratings for a given assignment matrix (The duality of the method allow it to be used for both maximization and

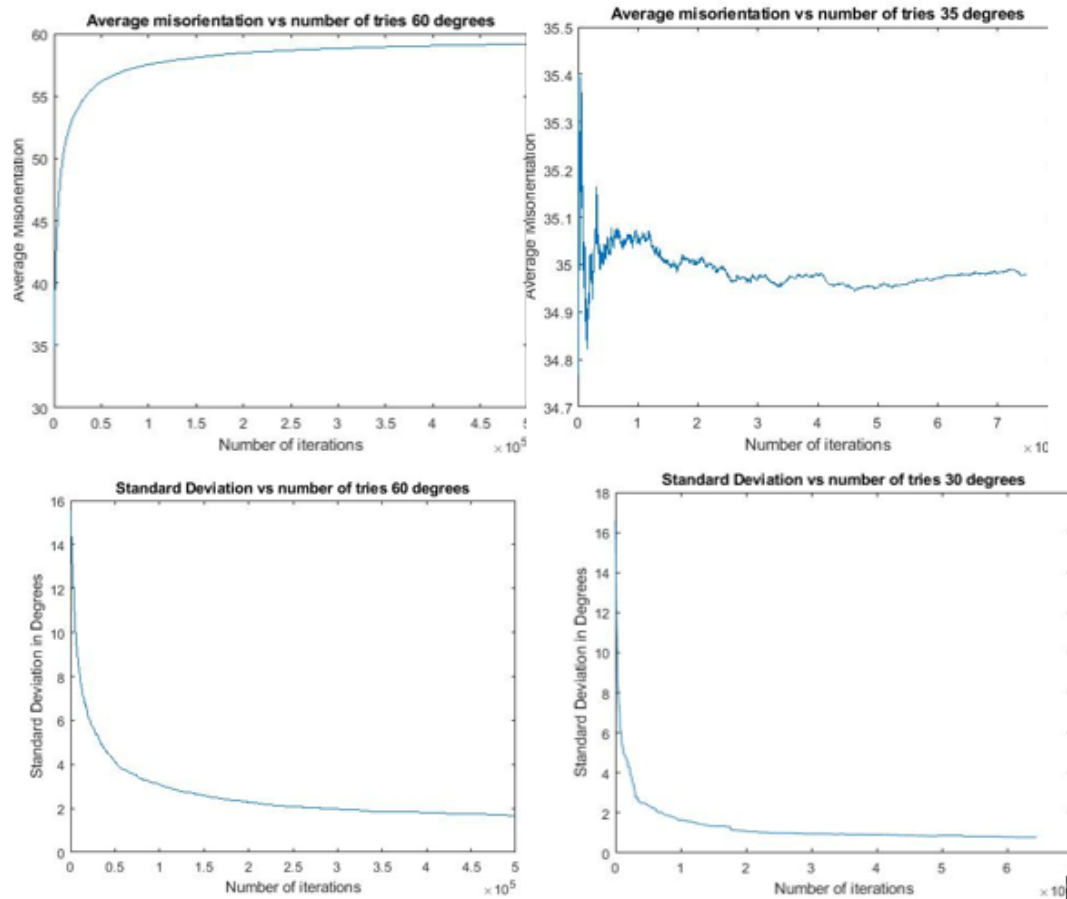


Figure 6.5: Obtained results for variation of average disorientation for target angle values of 60° disorientation (top left), 35° disorientation (top right) and standard deviation for target angles of 60° (bottom left) and 30° (bottom right) v/s number of iterations

minimization criteria). Modern algorithms can be used to solve for an m by n matrix.

6.4.2 Modes for solution

Specialised algorithms and methods have been developed to solve the aforementioned problem efficiently, in comparison to general linear programming methods. The earliest solution developed was the Hungarian method, which makes use of the theorems described by Konigs graph theory, and involves tedious steps, as the selection of minimum number of lines to cover all the zeros present, which are challenging to implement [Lot89].

There exist three general categories of solutions

- Maximum flow
- Shortest path
- Linear programming

Most algorithms are based on maximum flow, as the algorithms by Kuhn [Kuh55], Lawler [Lawo1] and Jonker [JV87]. The shortest path algorithms are solved by find-

Assuming that numerical scores are available for the performance of each of n persons on each of n jobs, the "assignment problem" is the quest for an assignment of persons to jobs so that the sum of the n scores so obtained is as large as possible. It is shown that ideas latent in the work of two Hungarian mathematicians may be exploited to yield a new method of solving this problem.

Figure 6.6: Hungarian problem definition according to Kuhn [Kuh55]

ing the shortest paths on an auxiliary graphs, akin to the minimization of cost criteria. Linear programming methods are specialized versions of the simplex method, and include algorithms such as those presented by Balinski [Bal86]. Linear programming algorithms are complex to implement and are outperformed by their peers [JV87].

Working of the Hungarian algorithm

The basis of the Hungarian algorithm is laid out in Konig graph theory [Kuh55]. The input for the algorithm is bipartite in nature, most commonly enunciated as a cost or qualification matrix. The output, as previously mentioned, is the minimum cost for assignment. The first step performed for this algorithm involves aggregation of the relevant data into a cost or qualification matrix, horizontal / row sections stand for individuals and column / section stand for jobs. The next step involves normalisation of the given entries by ensuring they have positive values. In the context of disorientation ordering, the matrix represents a disorientation matrix, with each element R_{ij} representing the disorientation between the disorientation pair made from the i^{th} and j^{th} orientation entries. Additionally, the rows and columns are made to represent odd and even values respectively, so as to generate a 'pair-wise' solution. If this action is not performed, the output solution would include each orientation being paired with two other orientations, thus not corresponding to the modified scenario.

The third step requires calculation of a set of row and column integers for which U_{ij} (row equivalent entry) and V_{ij} (column equivalent entry) are always lower than or equal to any R_{ij} (graph values). This is akin to picking the minima of each row and column, following which Marking (or qualifying) each R_{ij} position if its corresponding row or column values correspond to its R_{ij} (graph values) is performed. This corresponds to marking the minima points as specific 'qualified locations'. A set of 'marked' or 'qualified points' is noted as an 'independent', if its row and column are not home to any other 'marks'

If in the first iteration, there are 'n' independent marks, where n corresponds to the number of rows and columns, then the desired assignment is already reached. If the above is not the case, the graph theorem derived refining is carried out, using the graph theory. Refinement is carried out by drawing a set of less than n lines to improve the cover. This refinement is carried out by two routines, as shown in figure 6.7 Each iteration of Routine 1 increases the number of assignments by 1 and each iteration of Routine 2 decreases the covering sum by at least 1.

The steps followed in Routine 1 are given below, 6.8

- Row scanning for 'eligible' assignments, followed by classification of rows and columns by whether they are essential (they yield an assignment) or not. The optimality of selection is carried out by the steps detailed in the preceding figure. Optimisation is carried out in a row-wise order.

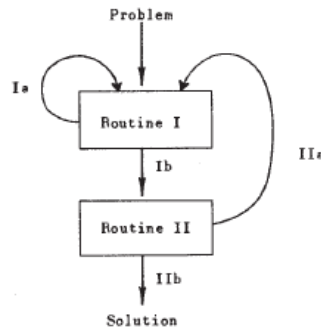


Figure 6.7: Hungarian routine for solution optimisation
[Kuh55]

- Routine 2 is carried out to increase the number of essential entries, and to complete the assignment of essential entries. The implementation of routine 2 is simple, the minima of the entire matrix is subtracted from all inessential rows and added to all essential columns (an alternative case may also be adopted when for some inessential rows i , $U_i = 0$, in which case the minimum value is added to all essential rows and subtracted from all inessential columns). This routine serves to increase eligible assignments.

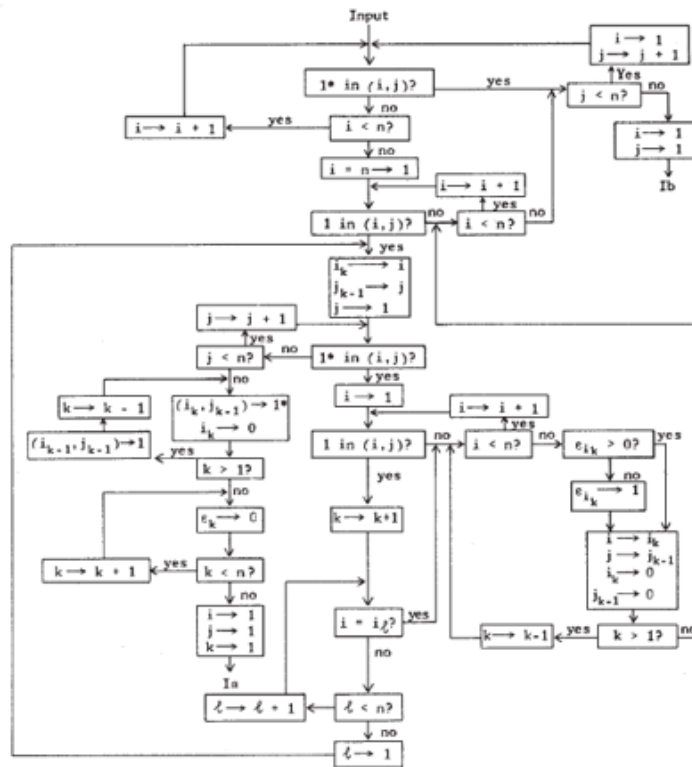
There also exist various specialised methods and techniques within the Hungarian model framework, such as the generalised interval arithmetic method [PR19], which might be used to solve more specialised problems such as the fully interval assignment problem. Additional methods of solution of this problem are simplex method based solutions and zero one integer models [JLL97].

Selection of model and algorithm used based on efficiency, complexity of associated mode and available literature and software packages. The efficiency of terms of computational load is expressed as a function of computational time complexity. The time complexity of the original Kuhn Munkres algorithm is classified as $O(n^4)$, which is defined in terms of polynomial order of initial matrix (the Hungarian algorithm is polynomial in nature) [Bal86]. The most efficient models are an order of polynomial more efficient, having a complexity factor of On^3 was first developed by Lawler [Law01] with later additions including models such as the Edmond Karp model [EK72], the dual simplex method, and [Bal86] and the Jonker-Volgenant Algorithm [JV87]

6.4.3 Implementation of Hungarian Algorithm

The simplest and fastest algorithms to implement are the maximum flow class of algorithms, further classified on the basis of computational efficiency, with On^4 algorithms such as the Kuhn-Munkres algorithm [Kuh55] and On^3 implementations such as those developed by Lawler [Law01] and Jonker-Volgenant [JV87]. The selection of the Jonker algorithm is performed on the basis of robust support and software availability [Cao13] [Trao6]. The LAPJV MATLAB code, based on the work of Jonker [JV87] and developed by Yi Cao of Cranfield University [Cao13] is used for the implementation of the solution.

The implementation of the algorithm uses as three basic inputs, which are illustrated in figure 6.9. The first is disorientation between every pair, in the format of a text file is illustrated in the top of the figure, and is a large table. As mentioned in earlier sections, in order to enforce the bipartite pairwise nature of the output, the input disorientation file pairs odd and even inputs to each other. Thus, the table is



| Symbol | Use in Routine |
|---|--|
| i | Index of rows of Q . |
| j | Index of columns of Q . |
| k | { Tally of length of sequence of 1's and 1*'s. Tally to clear essential rows in Alternative Ia. |
| l | Tally to test distinctness of i_{k+1} from i_1, \dots, i_k . |
| i_1, i_2, \dots, i_n | Record of rows in sequence of 1's and 1*'s. |
| j_0, j_1, \dots, j_{n-1} | Record of columns in sequence of 1's and 1*'s. |
| $\epsilon_1, \epsilon_2, \dots, \epsilon_n$ | Record of essential rows. |

Figure 6.8: Routine 1 or the Kuhn algorithm [Kuh55]

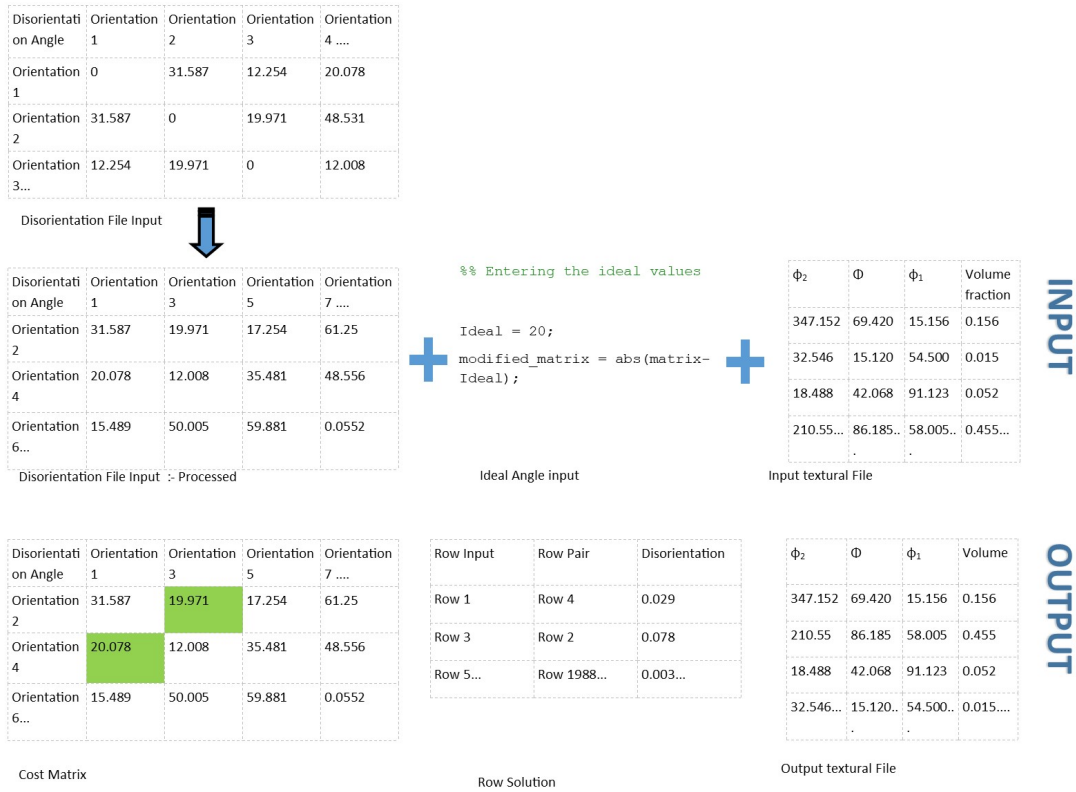


Figure 6.9: Hungarian Method Implementation visualisation with input and output files

'reformatted' (as indicated by the blue arrow) to a table which only contains disorientation angles between odd and even vector pairs. The second input (illustrated by the code entry to the right of the first processed input) is the ideal disorientation values (which indicates the target disorientation value desired). The second line of code intends to transform the first input to a 'max-min' format. The last input, textural file, includes the orientation of each grain in Euler space and its volume fraction. This input is not reshuffled, and thus, the difference between orientation vector numbers for this input are indicated in the unprocessed input number 1.

The 'cost matrix' input is then derived by taking the absolute value of the difference between the matrix element values and the ideal disorientation values. This operation results in positive 'elements' which identify the deviation from the ideal disorientation. The minimization of this 'cost matrix' thus represents the minimum deviation from ideal disorientation. For the minimum and maximum angle criteria, an ideal angle of 0 and 63 are used (as a value close to 62.9° is derived by Mackenzie [Mac58] to be the highest)

Thus, three outputs are once again derived. The first output is the aforementioned cost matrix, illustrated in figure 6.9, with highlighted entries signifying ideal solution selections. The second result, 'Row Solution' provides row-wise output assignment, and is used to 'reshuffle' the input texture file. It additionally details the deviation from Ideal values for each entry. The final output is the reshuffled textural file, generated by rewriting the rows in the order prescribed by the row solution output.

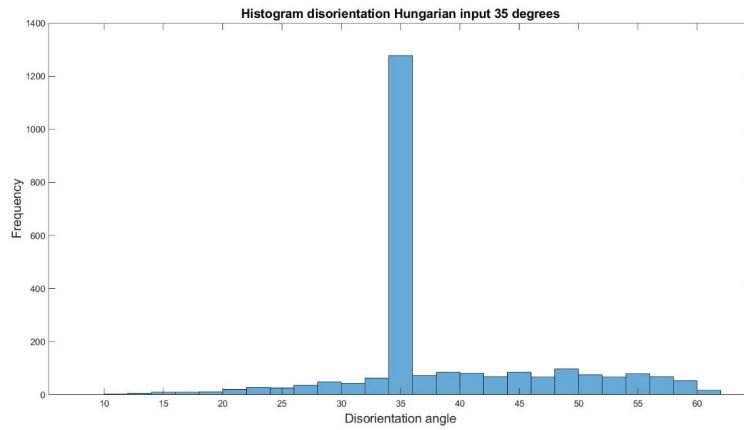


Figure 6.10: Histogram for obtained disorientation, using the LAPJV algorithm with a 35° disorientation goal

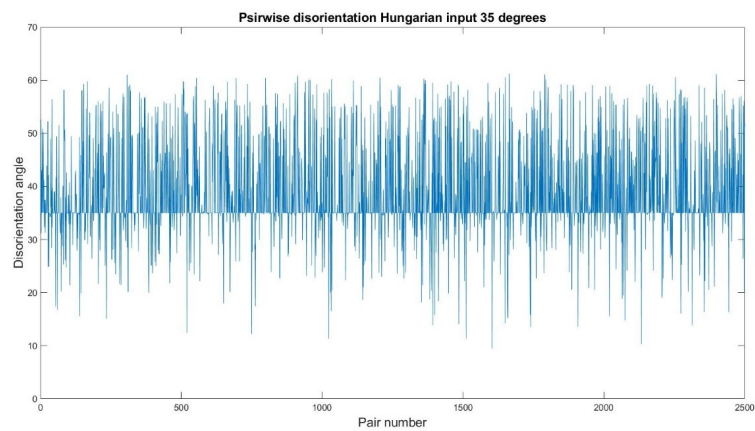


Figure 6.11: Pairwise disorientation obtained, using the LAPJV algorithm with a 35° disorientation goal

6.4.4 Verification of Hungarian Algorithm

The verification of the Hungarian method implementation is carried out by analysing the disorientation distribution of output orientation pairs. The efficacy of the model and its step-wise evolution is not tested, as no modifications have been made to the Jonker algorithm steps.

Figures 6.10 and 6.11 illustrate the distribution of obtained disorientation for the Hungarian derived output for a disorientation target of 35° . In contrast to the Monte carlo results, which show a normal distribution around ideal values, the Hungarian results more closely resemble 'digital inputs', with sharp peaks and distinct frequencies present throughout nearly the entire spectrum of possible disorientation values.

6.4.5 Validation of Hungarian Algorithm

The validation process of the Hungarian algorithm is carried out by analyzing the variation of the mean, standard deviation and variance of disorientation outputs for different disorientation values, as illustrated by figures 6.12 6.13 6.14

(which illustrate obtained values only and exclude the original experimental results). As illustrated in the aforementioned diagrams, the disorientation angle ob-

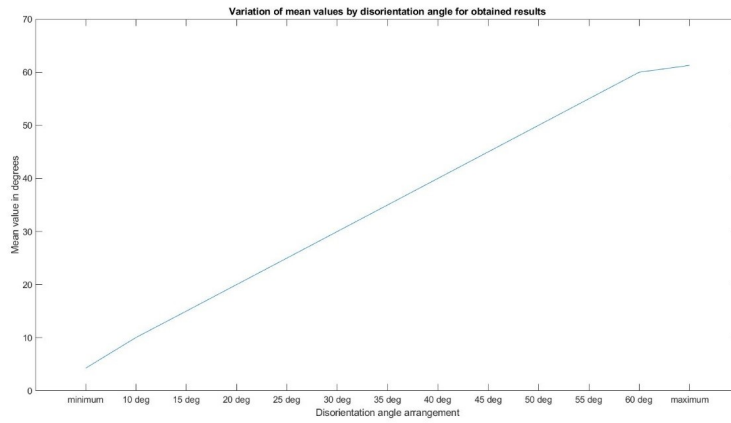


Figure 6.12: Variation of obtained mean disorientation value with input disorientation specification

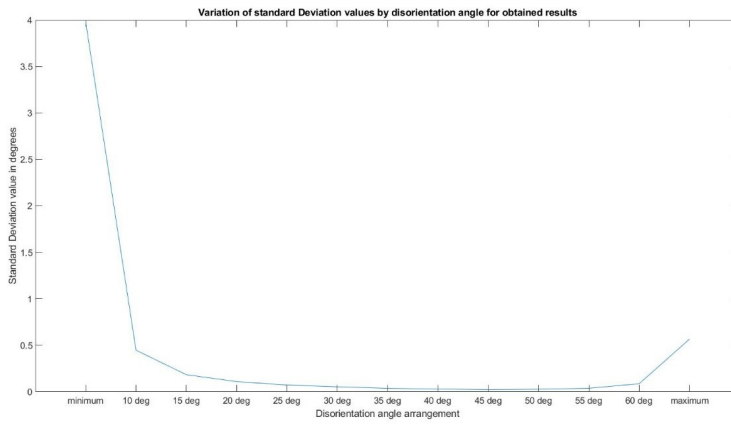


Figure 6.13: Variation of obtained disorientation standard deviation values with input disorientation specification

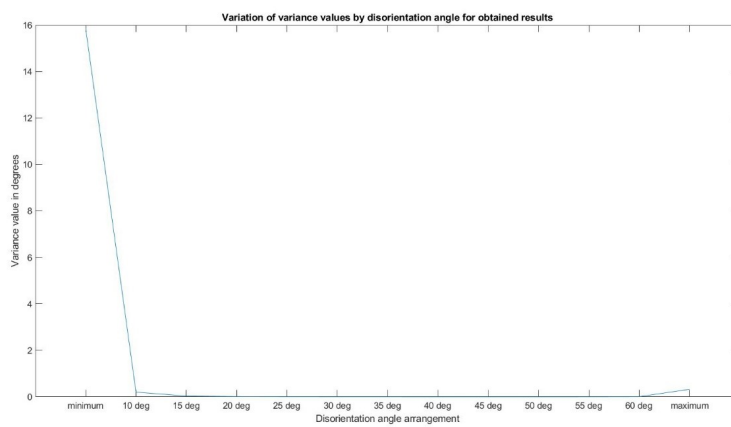


Figure 6.14: Variation of obtained disorientation variance with input disorientation specification

tained follows a linear trajectory (though a deviation is seen for the maximum disorientation scenario, whence a disorientation value higher than 63° is not possible). The standard deviation and variance figures display an apogee at minimum disorientation, for which a possible explanation is the nature of disorientation distribution for cubic symmetries. Additionally, the standard deviation results follow a U shaped curve, with the lowest values being reported at 45° .

The mean values obtained are within a margin of 0.05° of target angles (this excludes the minimum and maximum data files) with multiple results being accurate to the 4th decimal, and a standard deviation value of less than 0.5° for all but the minimum disorientation results, with a similar trend being seen in the case of variance as well. The lowest standard deviation is recorded for the 45° disorientation file, for which the standard deviation is 0.0234

7

RESULTS

The qualitative and quantitative comparison of the large set of output results requires characterisation parameters to highlight important results and trends. Output results are compared to experimental results, in addition to results obtained using different runs (in the case of Monte Carlo inputs) or methodologies and require the use of a comparative parameter. Additionally, the texture evolution properties also need to be highlighted using texture characterisation parameters.

7.1 TEXTURE INDEX

The characterisation of texture properties can be captured by the coefficients of its series expansion in generalised spherical harmonics. The complete characterisation of these coefficients is needed for a complete characterisation of texture. The value of each coefficient describes the sharpness characterisation, while the distribution of coefficients describes the distribution characteristics. The C coefficients of a texture file can be obtained by using the MTMTAY software suite, using a host of input options.

While C – coefficients are useful in carrying out limited qualitative analysis, it becomes a cumbersome and complex tool for carrying out a large scale quantitative analysis. The use of a more general texture index parameter (which is an indicator of texture severity without considering its distribution details) would better serve this need. The texture index parameter is thus a single parameter that describes the sharpness of a texture

The texture parameter is obtained by integrating the square of the texture parameter function, which is given by

$$t = \int f(g)^2 dg$$

. On expanding the equation, we get the following

$$J = \sum_{l,\mu,\nu} \frac{1}{2l+1} |C_l^{\mu\nu}|^2$$

. For random textures, all C coefficient values except for C_0^{11} are 0, which results in $J_r = 1$, while for ideal crystals

$$C_i^{\mu,\nu} = (2l+1) T_l^{*\mu\nu} g_0$$

For which $J_{ideal} \rightarrow \infty$ [Bun13].

7.2 ERROR INDEX

The texture index results cannot be used to effectively compare textures with close sharpness values, or to other ODF results. Many of the outputs derived vary only

marginally or display significant differences in sharpness. The approximation error function calculates the difference between sharpness concentration in Euler space.

$$\delta = \left| \frac{v_A - v_E}{v_E} \right| \times 100\%$$

where v_A represents actual value/obtained value and v_E represents expected value or standard value. δ represents obtained percent difference. This is performed by using a Fourier based algorithm, which analyses the difference in Fourier coefficient concentration in predefined quadrature nodes [Too].

7.3 MONTE CARLO AND EXPERIMENTAL RESULT VARIANCE

The Monte Carlo method is a probabilistic method, which yields a distinct order each time it is run, though the difference in input texture characteristics for each run is small. This study makes use of 5 Monte Carlo runs to definitively draw a better idea about the relevance of disorientation angle in output texture properties. Thus, within this section an analysis of the Monte Carlo results is carried out using the aforementioned Error Index Value (EIV) and Texture index (TI) parameters. For the case of EIV, the comparison of Monte Carlo results is performed against the experimentally obtained 55 and 83 % rolling samples.

7.3.1 Error Index values and Rolling reduction curve variations of Monte Carlo results

The first two results, Figures 7.1 and 7.2 compare output Monte Carlo results to obtained experimental results using the Error Index parameters. Figure 7.3 displays the texture index values for all Monte Carlo runs. All results are presented by their mean values, with error bars indicating the span of the curves across all the runs (the maximum and minimum values over five separate Monte Carlo runs is used to define the error bars). The run-wise data is included in the Appendix.

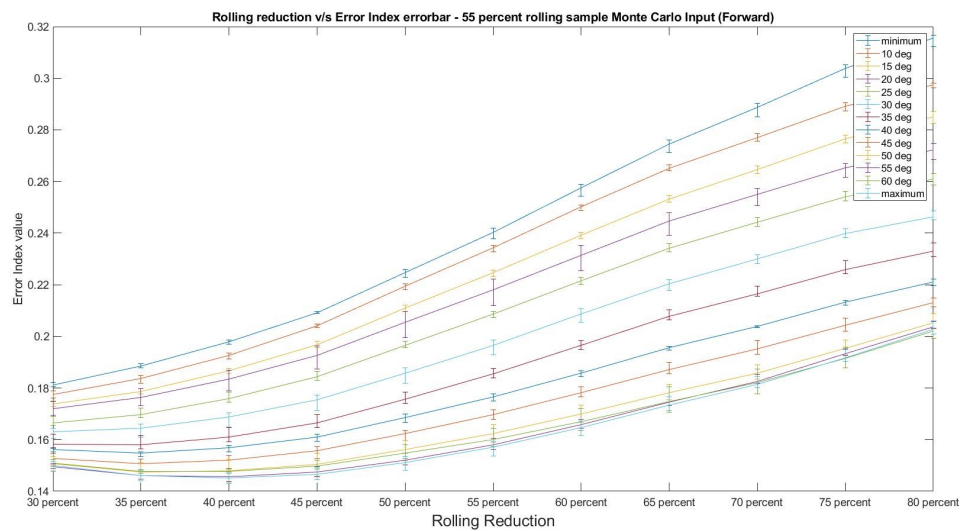


Figure 7.1: Rolling Reduction v/s Error Index, comparison between 55 % rolled experimental samples and Monte Carlo evolved texture, with Error bars

The shape of the obtained results for the Error Index Value (EIV) curves (Figures 7.1 and 7.2) is upward sloping with increase in rolling reduction. The obtained error graphs list the minimum disorientation value curves to have the highest Error Index values (EIV) for every specified rolling reduction percent. Every consequent increase in disorientation angle results in a curve with lower Error Index Values. Additionally, the distinction of curves (and thus non-overlap of obtained Monte Carlo results) for disorientation angle values of 45° and below. This separation is most apparent for high rolling reduction values, but persists even for low rolling percent values.

For the most part, both Figures 7.1 and 7.2 follow the same general trajectory across rolling reduction. A slight reduction of EIV is observed, following which a steady increase is recorded. The steady increase after the minima appears to be characterised as parabolic growth.

The rolling reduction characteristic with minimum EIV values is different for both figures, and for each figure, this value is different for each disorientation curve. The rolling reduction associated with minimum EIV values for a curve is lower for smaller disorientation angle curves and higher for larger disorientation angle curves. In the case of figure 7.1, for the largest disorientation curves, this is found to be at 40 % rolling reduction, corresponding to an EIV of just over 0.14. In the case of figure 7.2, for the largest disorientation curves, this is found to be at 50 % rolling reduction, corresponding to an EIV of just under 0.2.

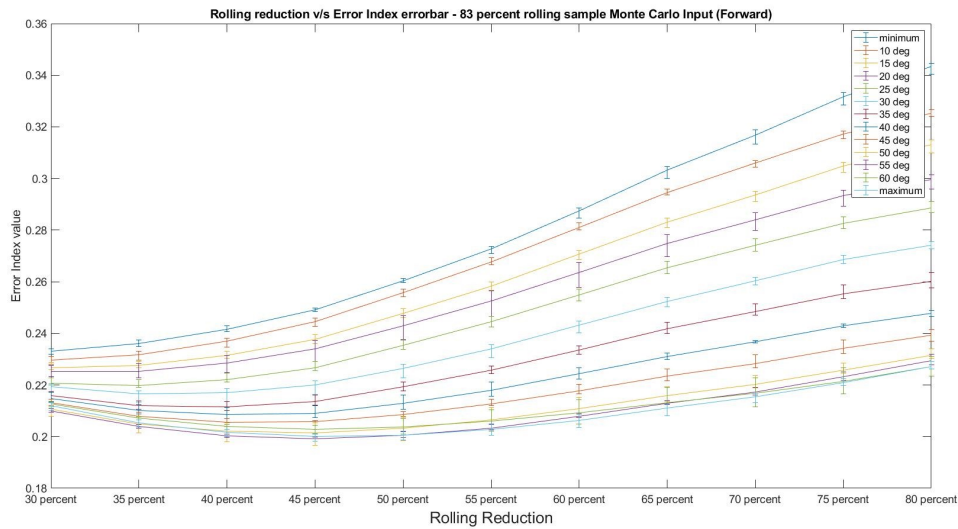


Figure 7.2: Rolling Reduction v/s Error Index, comparison between 83 % rolled experimental samples and Monte Carlo evolved texture, with Error bars

The overlap angle for the two Error index v/s disorientation graphs can also be accurately determined to be 20° disorientation between 30 % and 35 % adjacent curved when the 83 % rolled reduction sample is observed, and 35° disorientation for the 83 % rolling reduction sample. Interestingly, in the instance of the latter, the highest adjacent pair overlapping is the 30 % and 35 % rolling reduction pair, while in the instance of the former is 50 % and 55 % rolling reduction (55 % and 60 % if the results are rounded to three decimals).

7.3.2 Texture Index values and Rolling reduction curve variations of Monte Carlo results

The texture index variation with rolling reduction is represented in figure 7.3, and follows the same illustration methodology as the EIV results of the previous section, with mean values displayed alongside error bars indicative of the span of results obtained over 5 runs. The run-wise data for this set of results is available in the appendix.

The shape of the Texture Index variation with rolling reduction, figure 7.3 appears to indicate that the relationship between texture index and rolling reduction closely resembles a linear function. The arrangement of each disorientation curve comprising the result is also very simple, with the curves being ordered on the basis of their disorientation angle, with the minimum disorientation curve having the highest and maximum disorientation curve having one of the lowest values across all rolling reductions. Each disorientation curve making up this result appears to follow a marginal difference in slope values (following the same ordering as arrangement, with minimum disorientation curves having the highest slope and maximum disorientation curve having one of the lowest slope), resulting in a mild divergence for the aggregate set of curves.

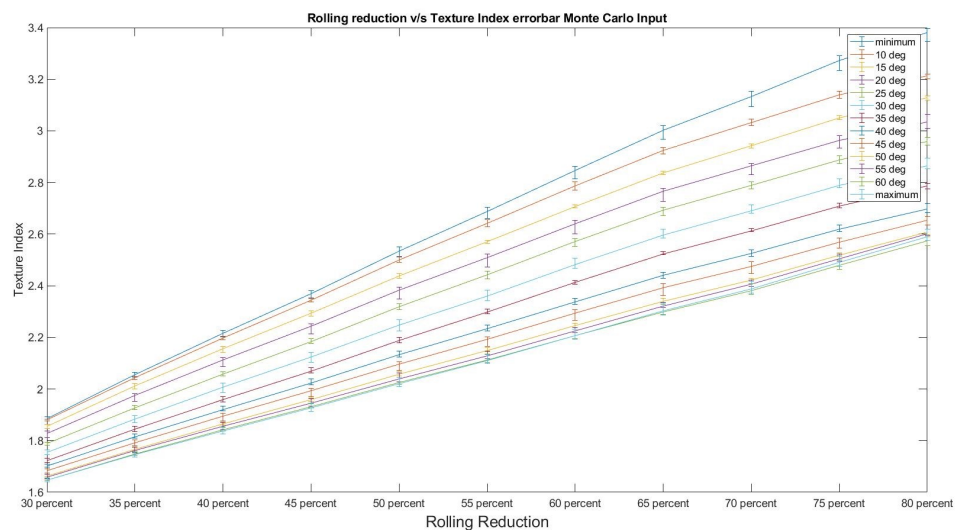


Figure 7.3: Rolling Reduction v/s Texture Index, Monte Carlo evolved texture, with Error bars

The aforementioned results (given by figure 7.3) indicate that a smaller disorientation results in a stronger texture than a larger disorientation value. Another observation that can be made is that the results for all disorientation curves with disorientation above 45° strongly overlap. Thus, an increase in disorientation beyond 45° does not change the obtained results significantly, and texture sharpness.

A large variance in ALAMEL texture results for the same input texture disorientation suggests that factors unrelated to the disorientation values play a role in texture evolution in the ALAMEL model. Consequently, a distinct set of curves with a large separation between sequential is indicative of the strong role played by disorientation ordering in the evolved texture.

Non Overlap ODF behaviour

As described in this section, there is scarce overlap in the Error Index and Texture Index for low disorientation high rolling reduction simulations. Figure 7.4 depicts the ODF plot of the 5th set of Monte Carlo input simulations, with an input disorientation of 10° , and a rolling reduction of 70 %. Figure 7.5 looks at another run from the same set of simulations, the only difference between the two being the disorientation angle. While figure 7.4 has an input disorientation angle of 10° , figure 7.5 is obtained using a minimum input disorientation criteria. While the ODF figures resemble each other closely, the texture sharpness of figure 7.5 is clearly observed to be greater. A higher sharpness in ODF figures translates to an increased Texture Index value.

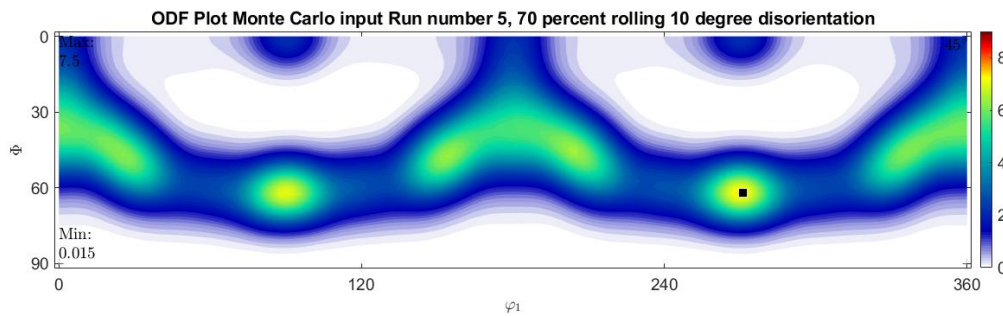


Figure 7.4: ODF plot for Run Number 5, Monte Carlo simulation, with an input disorientation of 10° and rolling reduction of 70 %

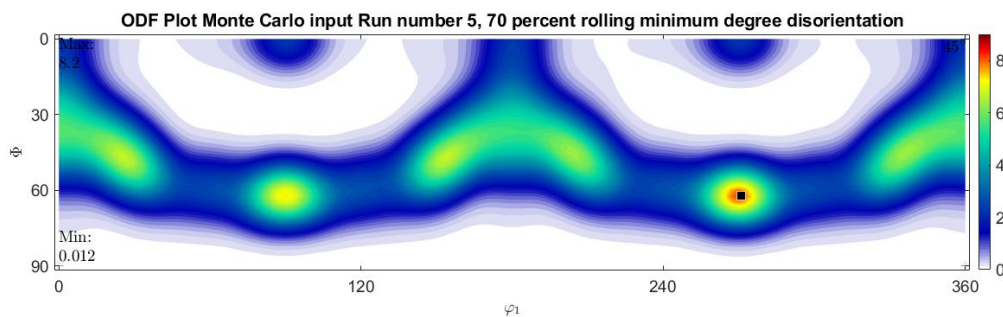


Figure 7.5: ODF plot for Run Number 5, Monte Carlo simulation, with a minimum input disorientation and rolling reduction of 70 %

Interestingly, the effect of this increased texture sharpness is minimal while comparing Error Index values. Figure 7.6 and figure 7.7 highlight the ODF difference between the aforementioned ODF graphs and the experimentally obtained results. This ODF difference chart is obtained by subtracting the ODF concentrations of its component units, and is thus similar in methodology to Error Index Value calculations (which is performed by quadrature concentration difference between its component units). The aforementioned ODF difference charts do not show a large deviation in terms of shape or concentration, with the maximum concentration between the two being $5.4 \times$ Random intensity and $4.7 \times$ Random intensity. Even so, a clear distinction can be made between the two ODF difference figures in terms of sharpness.

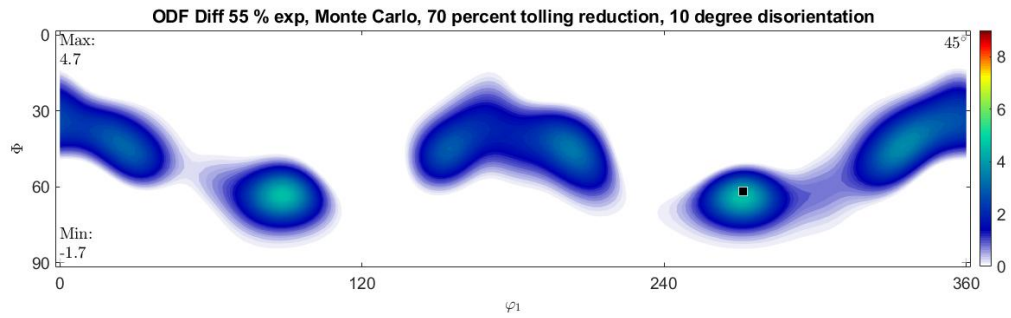


Figure 7.6: ODF difference plot between obtained experimental 55 % rolling reduction and Run Number 5, Monte Carlo simulation, with an input disorientation of 10° and rolling reduction of 70 %

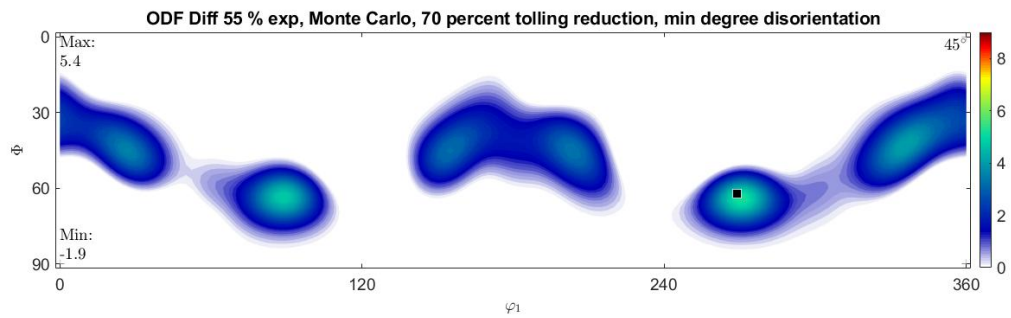


Figure 7.7: ODF difference plot between obtained experimental 55 % rolling reduction and Run Number 5, Monte Carlo simulation, with minimum input disorientation and rolling reduction of 70 %

7.3.3 Error Index values and Rolling reduction curve variations of Monte Carlo results

The Error Index curves results can also be illustrated in comparison to disorientation angle values. Figures 7.8, 7.10 and 7.9 The second set of images. These results compare the same data-set as the earlier section, but differ in the sorting and selection of outputs to be measured. The results in this section are measured against disorientation angle in the X-axis, and are meant to highlight the observations of the earlier sections.

The curves illustrating error index variations with rolling reduction include Figures 7.8 and 7.9. While the shape of the aggregate set of curves is not similar for the two sets of results, they follow the same trend. The maximum error of both these curves is close to each other (at close to 0.32). The minimum disorientation values have the highest errors, which show a near linear reduction in Error Index Values (EIV) in response to increases in disorientation angles unto disorientation values between 45° and 50° . Above these disorientation values, the Error Index Value shows little variation and levels off.

The rolling reduction curves are also prominently ranked on the order of decreasing rolling reductions (high EIVs associated with high rolling reductions). Each rolling reduction curve also has a different slope, resulting in overlap with curves of a sequentially higher rolling reduction values. This probability of overlap is increasingly prevalent at higher disorientation angles, and for the EIVs compared to 83 % rolling reduction experimental samples (given in figure 7.9). Lastly, this overlap is significantly more common for low rolling reduction curves than for high

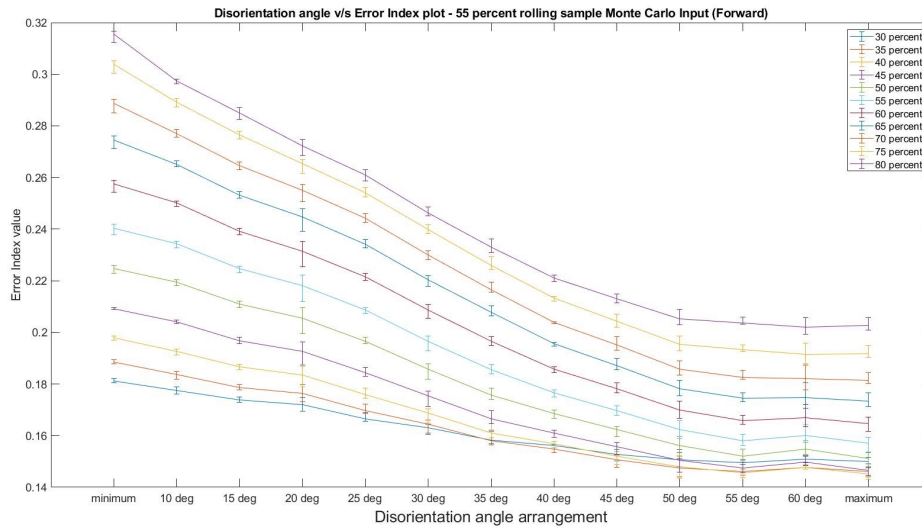


Figure 7.8: Rolling Reduction v/s Error Index, comparison between 55 % rolled experimental samples and Monte Carlo evolved texture, with Error bars

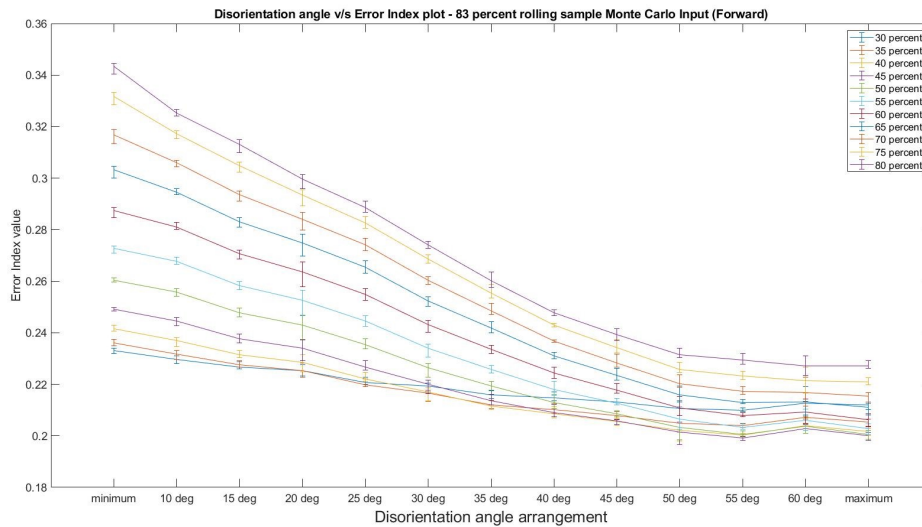


Figure 7.9: Rolling Reduction v/s Error Index, comparison between 83 % rolled experimental samples and Monte Carlo evolved texture, with Error bars

rolling reduction curves.

There is also a slight deviation observed between the Error Index Value curves for the two experimentally obtained comparisons, where the error index compared with the 83 % reduction displays a narrower spread of 0.12 for the lowest disorientation (highest spread section) and 0.04 for the highest disorientation (narrowest spread section). In comparison, the 55 % rolling reduction Error index spreads of 0.14 and 0.06 respectively. This is interesting as the mean convergence values, minima and maxima values of the Error Index are lower for the 55 % rolling reduction experimental comparison. Thus, the overlap disorientation for adjacent rolling reduction curves takes place at smaller disorientation values for the 83 % rolling reduction experimental curves, when compared to the 55 % rolling reduction experimental curves.

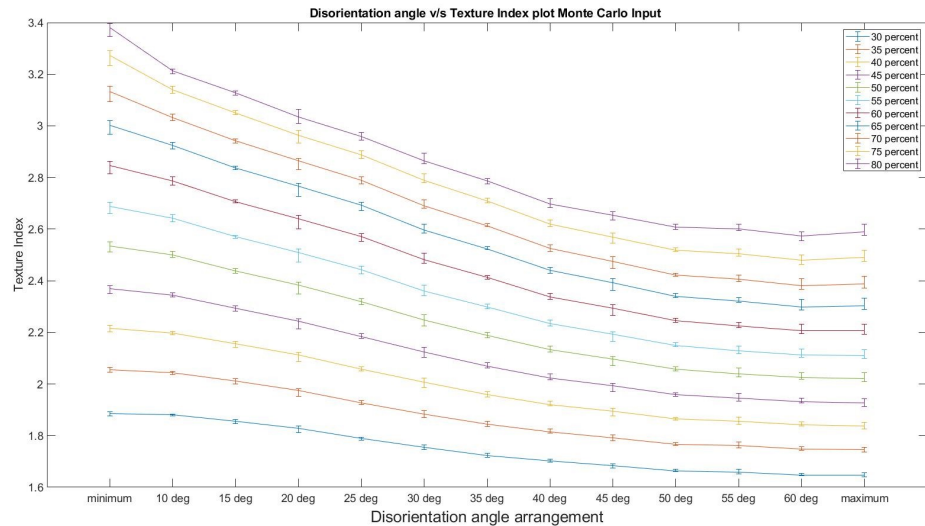


Figure 7.10: Rolling Reduction v/s Texture Index, Monte Carlo evolved texture, with Error bars

The texture Index results, given by figure 7.10 illustrates the effect of rolling. It is marked by distinct close to evenly spaced out parallel rolling reduction curves, whose error bars do not overlap with one another. Instead, the slopes of the curves flatten out with increasing disorientation values.

As expected, the texture index of smaller rolling reductions is the least, progressing to the highest values for the largest reduction. An interesting feature concerns the space between adjacent curves, which can be seen to reduce with increasing rolling reduction, i.e. the distance between the aforementioned parallel rolling reduction texture index curves is largest for the smallest rolling reduction pairs, with the gap reducing with an increase in rolling reduction of the pairs.

The variation of texture index curves is interesting as it illustrates the magnitude of impact of disorientation value. The texture index of an 83 % rolling reduction texture reordered for maximum disorientation is similar to that of a 55 % rolling reduction minimum disorientation sample

Overlap ODF behaviour

The preceding sections describe an 'overlap' between certain high disorientation curves, even at high rolling reduction values. Figure 7.11 and figure 7.12 below display a pair of results that represent such an 'overlapping' pair. These ODF figures are obtained from the third Monte Carlo simulation set, and describe simulations with rolling reductions of 70 % (similar to the results from the 7.3.2 section). Figure 7.11 illustrates a simulation with an input disorientation angle of 55° , while figure 7.12 illustrates a simulation with a maximum input disorientation angle. Interestingly, the difference in input angle for the set of ODFs described in section 7.3.2 and the current set are similar, at about 7° , but they occupy polar opposite sequential spaces.

Both the aforementioned ODF figures have a very similar shape, with a near exact minima and maxima. This is in sharp contrast to the results of section 7.3.2, which display a much sharper texture (both results describe simulations performed with the same rolling reductions). This trend carries on while comparing ODF differences to experimentally obtained results, given in figure 7.13 and 7.14, which describe the 55° disorientation and maximum disorientation respectively. Interest-

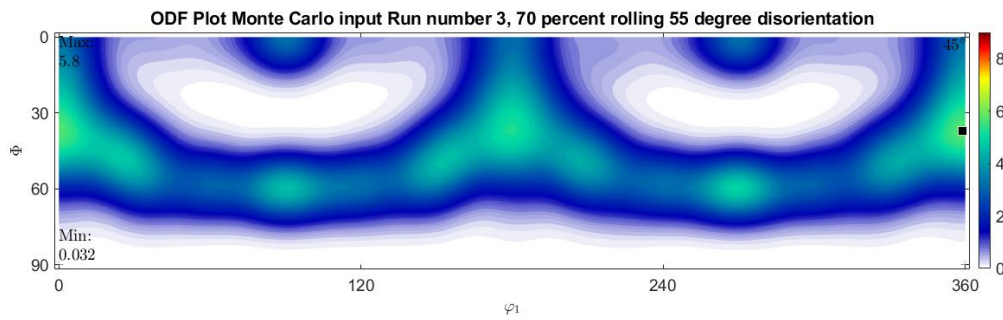


Figure 7.11: ODF plot for Run Number 3, Monte Carlo simulation, with an input disorientation of 55° and rolling reduction of 70 %

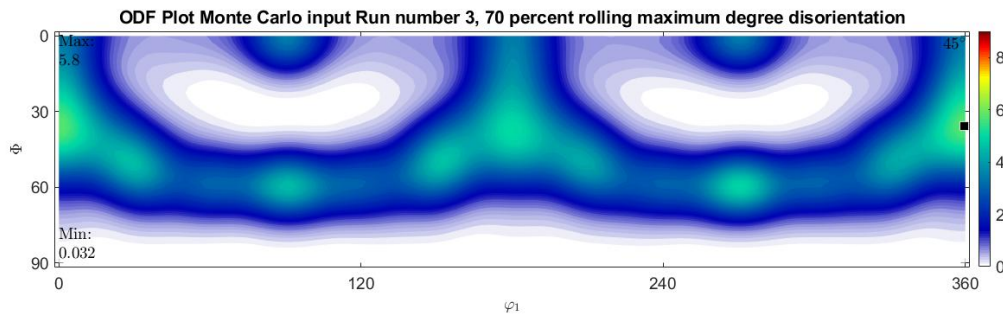


Figure 7.12: ODF plot for Run Number 3, Monte Carlo simulation, with a maximum input disorientation and rolling reduction of 70 %

ingly, the difference is ever so slightly sharper for figure 7.14, which describes a higher disorientation angle (and runs contrary to the established trend at lower rolling reductions).

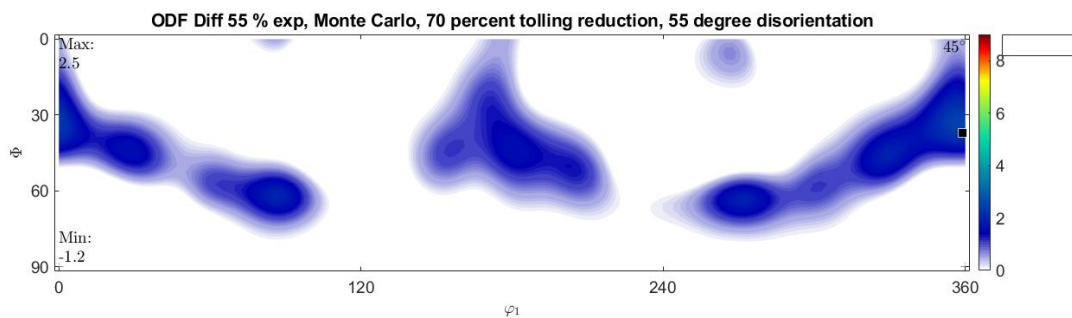


Figure 7.13: ODF difference plot between obtained experimental 55 % rolling reduction and Run Number 3, Monte Carlo simulation, with an input disorientation of 55° and rolling reduction of 70 %

7.4 STANDARD DEVIATION PROPERTIES OF MONTE CARLO RESULTS

As discussed in earlier chapters, the Monte Carlo method of obtaining disorientation ordered shuffling is a probabilistic method, and returns a slightly different result for each instance it is run. This sections aims to compare the standard deviation properties of results, for Error Index Values and Texture Index results. As

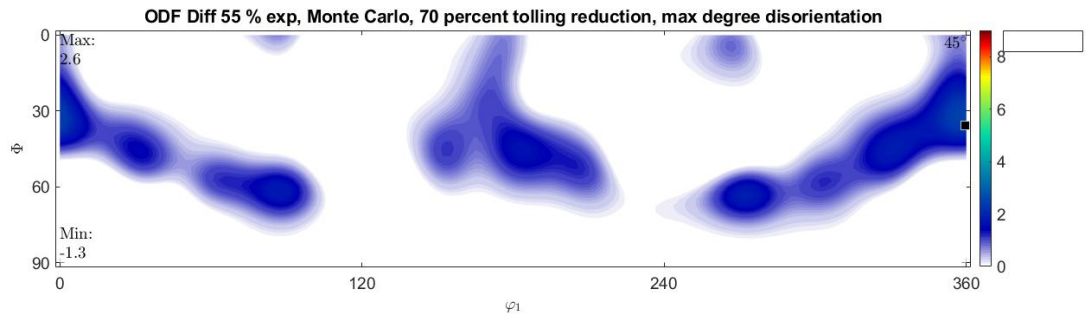


Figure 7.14: ODF difference plot between obtained experimental 55 % rolling reduction and Run Number 3, Monte Carlo simulation, with maximum input disorientation and rolling reduction of 70 %

with earlier sections, these results are also measured against rolling reduction and disorientation angle.

7.4.1 Standard deviation properties of Monte Carlo Error Index Value results, plotted against disorientation angle

The spread within the various Monte Carlo input runs is characterised in this section as a variation of the Error index value standard deviation for the family. The standard deviation variation for the standard deviation graphs plotted against disorientation angle include Figures 7.15 and 7.16.

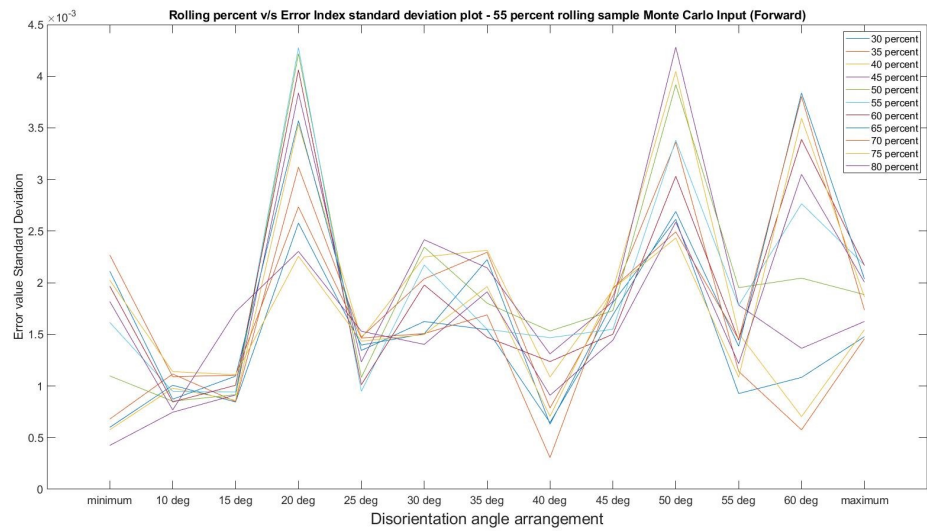


Figure 7.15: Disorientation Angle v/s Error Index Standard deviation, comparison between 55 % rolled experimental samples and Monte Carlo evolved texture

The standard deviation curves are influenced by both selection and simulation parameters. The disorientation angle is associated with a standard deviation value, as illustrated in figure 6.13 from the validation of the Hungarian model section. The minimum and maximum disorientation scenarios result in higher standard deviation than the median values. The low volatility band suggests corresponds with the sections with lower disorientation standard deviation.

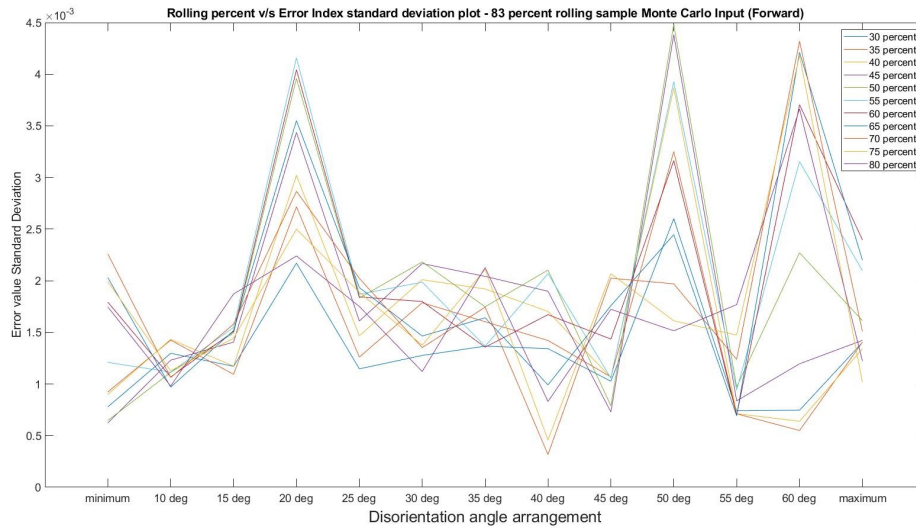


Figure 7.16: Disorientation Angle v/s Error Index Standard deviation, comparison between 83 % rolled experimental samples and Monte Carlo evolved texture

7.4.2 Standard deviation properties of Monte Carlo Texture Index Value results, plotted against disorientation angle

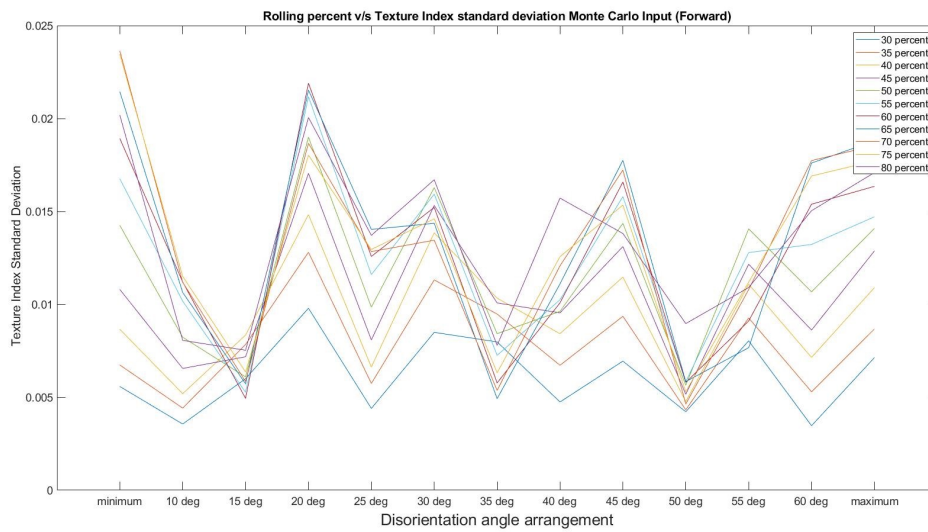


Figure 7.17: Disorientation Angle v/s Texture Index Standard deviation, Monte Carlo evolved texture

The texture index standard deviation results, illustrated in figure Figure 7.20, also display a sharp increase in texture index values at the 20° disorientation mark. The standard deviation at a disorientation value of 20° varies from 1.5 times its preceding value to over 4 times as high. This is preceded by a largely sustained reduction that culminates in a local minima. This higher than normal texture index variation may be a result of the changing nature of grain boundary interaction, with the associated disorientation being slightly above the low angle to high angle grain boundary transition.

Additional observations made on this set of results include the range of distribution of standard deviation values, which is slight, and the nature of distribution

of the same with respect to rolling reduction values. The range of distribution of error index standard deviations are narrow, between 0.005 and 0.025. On the other hand, the nature of distribution for lower rolling reduction seems to be proportional to rolling reductions, with distinct parallel curves being the norm, but for higher rolling reductions, this relationship seems doesn't seem to hold.

7.4.3 Standard deviation properties of Monte Carlo Error Index Value results, plotted against rolling reduction

The results illustrating the standard deviation properties of the Monte Carlo Error Index value are given in figures 7.18 and 7.18. These are collated from the same dataset as the previous section in this section.

On observing the standard deviation variation with rolling reduction, the most striking feature of the standard deviation curve is its seemingly periodic, almost sinusoidal nature. The mean value shows a significant proportional relationship with increasing rolling reduction, and earlier graphs illustrating overlap at higher rolling reductions. The same trend is not reflective in the standard deviation graphs, indicating overlap relates not to increased statistical divergence with increasing rolling reduction, but rather the converging nature of simulations. This fact can be further confirmed upon observing the corresponding mean value graphs.

There is also much variation in the 'amplitude' and 'mean' and 'period' of the periodic variations. In the set of results illustrated by figure 7.18. The disorientation values of 20° and 50° have a higher standard deviation when compared to the remaining dataset, with a 'period' difference in maxima being observed. The 20° disorientation curve reaches this value at 45% rolling reduction while the 50° disorientation curve reaches this value at a rolling reduction of 55%. At very high rolling reduction values, the 60° disorientation curve seems to have the highest standard deviation, but seems to have lower mean but higher 'amplitude' than the aforementioned curves.

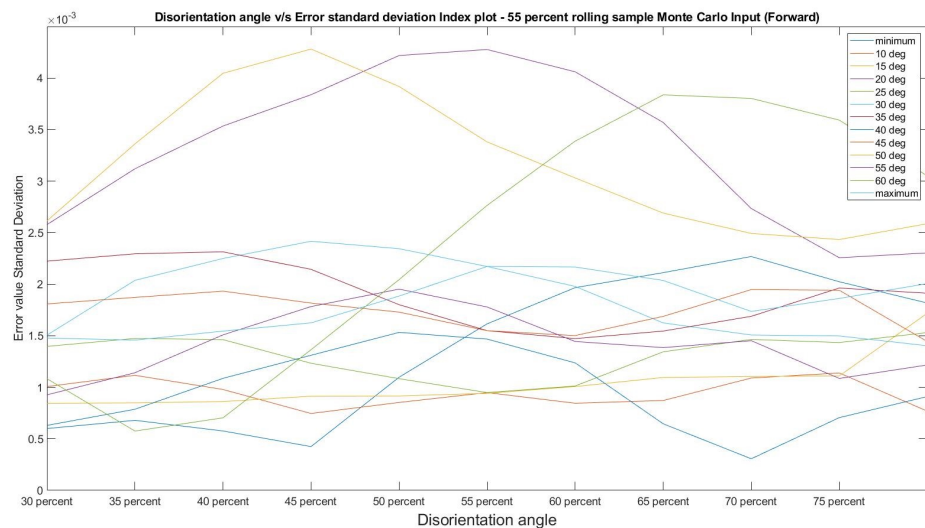


Figure 7.18: Rolling Reduction v/s Error Index Standard deviation, comparison between 55 % rolled experimental samples and Monte Carlo evolved texture

The curves represented by figures 7.19 also return similar results. The standard deviation scale observed is also similar to the aforementioned experimental com-

parison, the 55 % rolling reduction results.

7.4.4 Standard deviation properties of Monte Carlo texture index results, plotted against rolling reduction

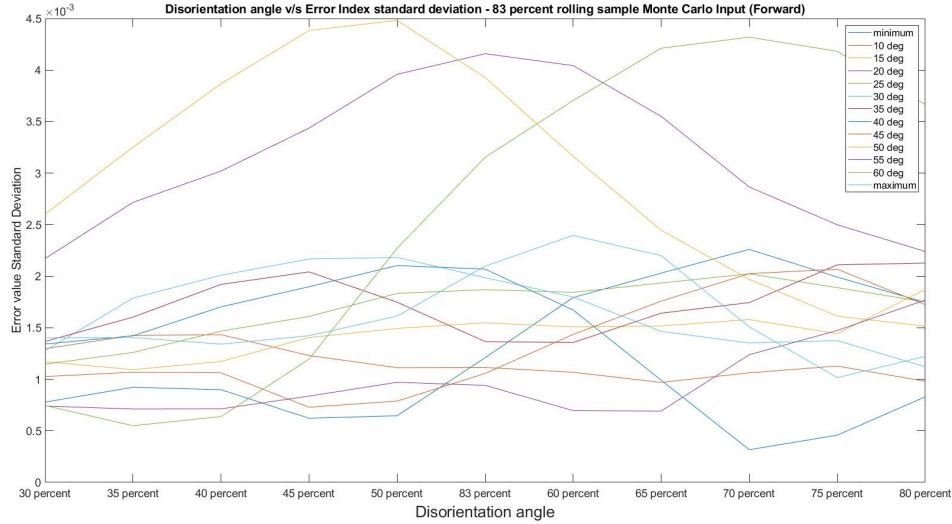


Figure 7.19: Rolling Reduction v/s Error Index Standard deviation, comparison between 83 % rolled experimental samples and Monte Carlo evolved texture

The texture index standard deviation curve, given by figure 7.20 shows a stronger standard deviation, while also following a more general growth trend with increasing rolling reductions. Interestingly, the 20° disorientation curve is also the maxima for lower rolling reductions, though for higher rolling reductions the curve with the highest standard deviation values is the minimum disorientation curve, and the 50° disorientation curve is a low mean curve. For higher disorientations, the curves resemble a 'periodic' 'sinusoidal' nature.

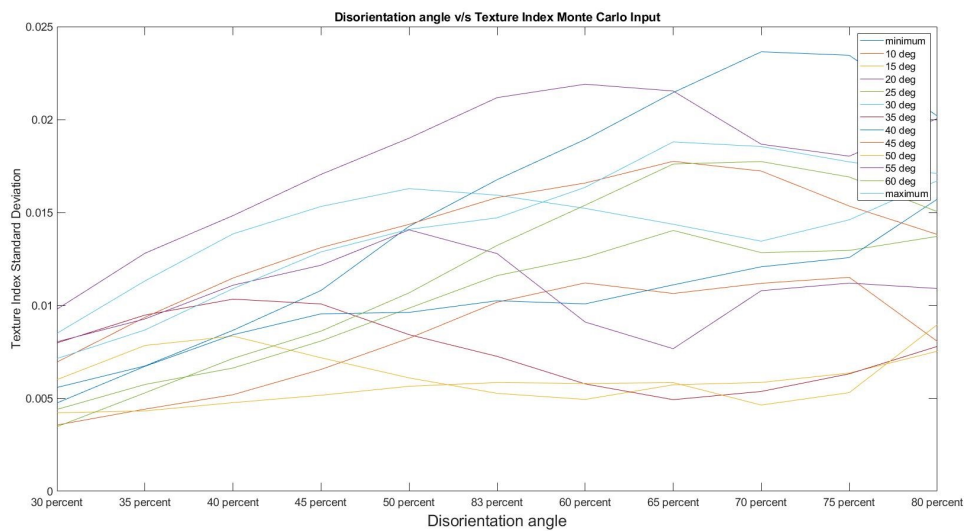


Figure 7.20: Rolling Reduction v/s Texture Index Standard deviation, Monte Carlo evolved texture

ODF behaviour for multiple runs

The standard deviation properties described in this section are a reflection of the variations between multiple Monte Carlo simulation runs. Each set of Monte Carlo runs has very similar disorientation distribution, but vastly different input order. A small standard deviation value and low overlap between sequential simulations is indicative of a strong relationship between input characteristics and evolved texture, and vice versa.

Figures 7.21, 7.22, 7.23, 7.24 and 7.25 illustrate the obtained simulation results for each of the 5 Monte Carlo runs with an input disorientation angle of 20° and rolling reduction of 45 %. As expected, the simulations are very similar to each other, but they do display very minor differences (the sharpest texture has a sharpness of $5.5 \times$ Random Intensity, while the least sharp texture has an intensity of $5.4 \times$ Random Intensity), which in turn, influence outputs. The appendix of this study includes the obtained ODF figures for a range of standard deviation scenarios

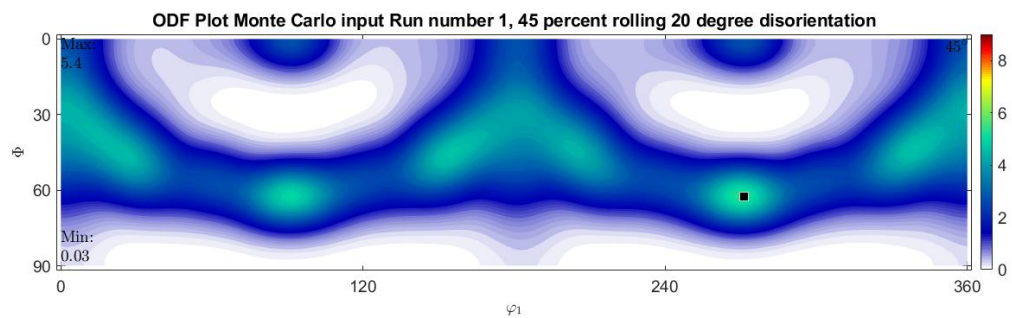


Figure 7.21: ODF plot for Run Number 1, Monte Carlo simulation, with a 20° input disorientation and rolling reduction of 45 %

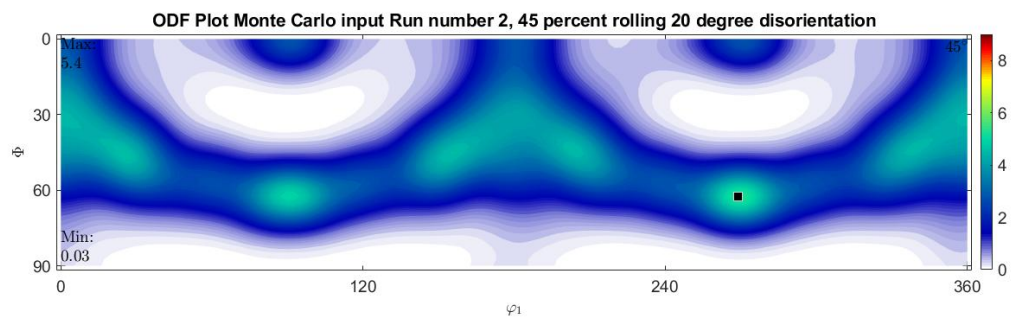


Figure 7.22: ODF plot for Run Number 2, Monte Carlo simulation, with a 20° input disorientation and rolling reduction of 45 %

7.5 MONTE CARLO RESULTS COMPARED TO DEFAULT EVOLVED TEXTURE

While comparing simulated textures and experimental outputs is helpful in determining the practical implications of disorientation, it may not describe the behaviour of the ALAMEL model accurately. This section aims to compare two simulated textures, those simulated by performing rolling reduction operations on the experimental input texture, and Monte Carlo reshuffled inputs. This comparison will illustrate the impact of disorientation angle on the ALAMEL software suite

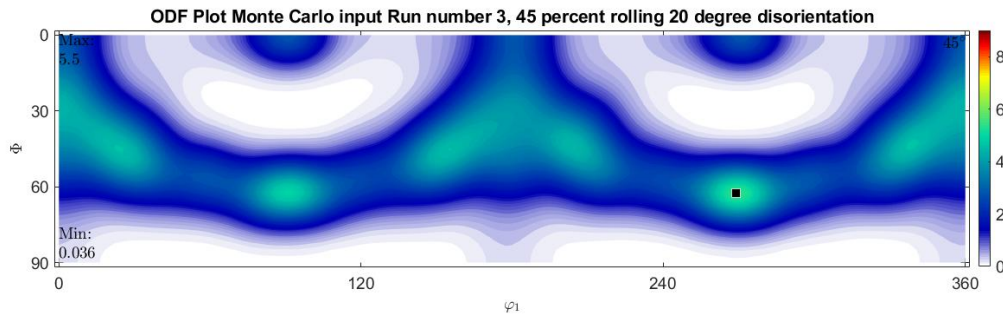


Figure 7.23: ODF plot for Run Number 3, Monte Carlo simulation, with a 20° input disorientation and rolling reduction of 45 %

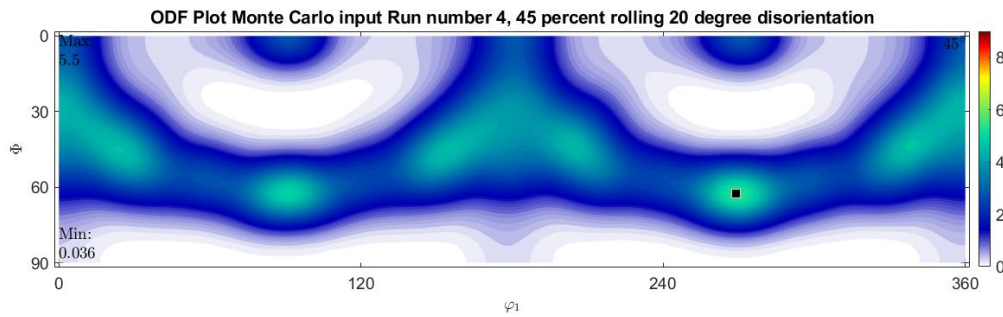


Figure 7.24: ODF plot for Run Number 4, Monte Carlo simulation, with a 20° input disorientation and rolling reduction of 45 %

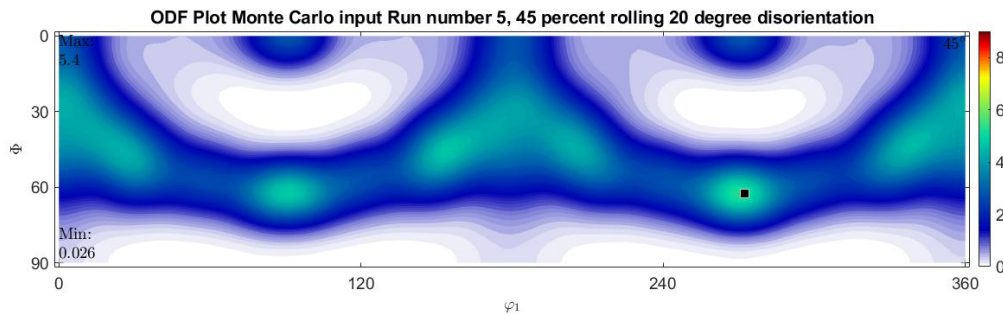


Figure 7.25: ODF plot for Run Number 5, Monte Carlo simulation, with a 20° input disorientation and rolling reduction of 45 %

and model.

The obtained results are given in Figures 7.26, 7.27, 7.28 and 7.29. The graphs plotted include mean error graphs and their standard deviation with respect to disorientation angle variation and rolling percent variation.

Figure 7.26 represents the Error Index Value and disorientation angle results. The curves comprising the result display a distinct and evenly spread out error index values for the lowest disorientation, arranged in a descending order of rolling reduction. An increase in disorientation angle sees a consistent convergence at the minima, taking place at a disorientation of 40° , where the spread across all the curves is reduced to lower than 0.005 EIV. This results in not just a sequential overlap, but a convergence of all component curves to a near point. This convergence is followed by a divergence, where higher rolling reduction curves see an increase in

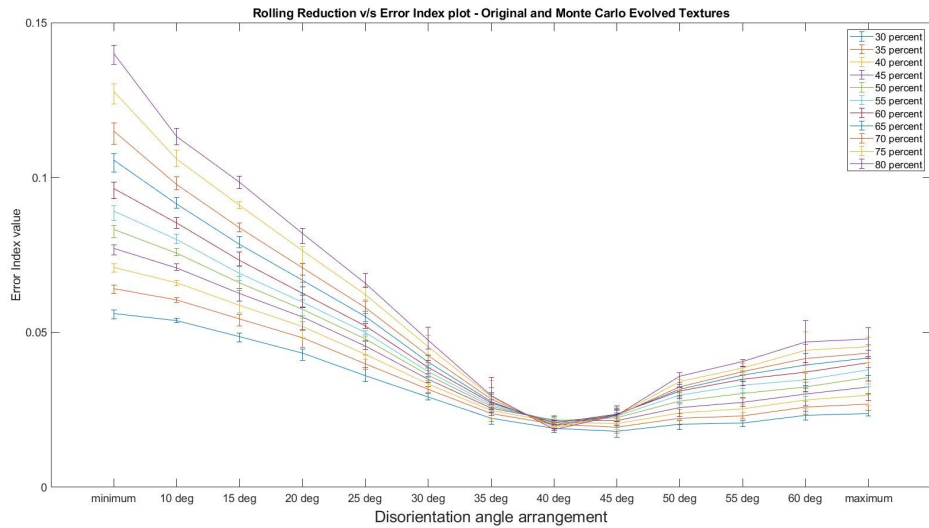


Figure 7.26: Disorientation Angle v/s Error Index, comparison between Original evolved texture and Monte Carlo evolved texture, with Error bars

EIV, while the lowest rolling reduction curves see little change.

The observed error value is far lower than the aforementioned error compared to experimental results, with the highest error obtained for the present set of graphs being just shy of the global minima of the former. The minimum error of the present set of results meanwhile, is less than a fifth that of the former set of results. This result is in line with expectations, as the ALAMEL model is not a perfect representation of experimental processes, and the former set of results include the errors. The average disorientation value for the original texture is a tad higher than 36° , and the obtained results reflect the same.

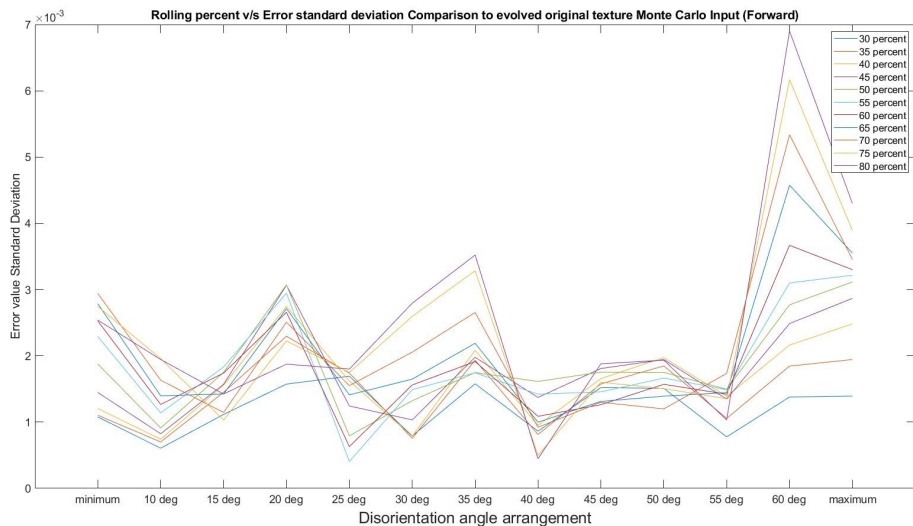


Figure 7.27: Disorientation Angle v/s Error Index Standard deviation, comparison between Original evolved texture and Monte Carlo evolved texture

The sequential overlap during convergence process is observed to take place at values closer to the minima than observed during the divergence process. This tepid 'rebound' after the minimum disorientation value illustrates that disorienta-

tion values higher than that associated with the minima see little impact comparatively. This is also confirmed by the standard deviation results during the process, given by figure 7.27 as a low standard deviation (with less volatility) is found at disorientation values higher than the minima. Interestingly, the standard deviation value rises to its maxima for a disorientation value of 60° , and sees a high value for maximum disorientation as well. This results in an overlap of curves at high disorientation values. Thus, the relatively tepid rebound and high standard deviation at very high disorientation values sees the general trend of distinct curves not being held for disorientation angles higher than the minima.

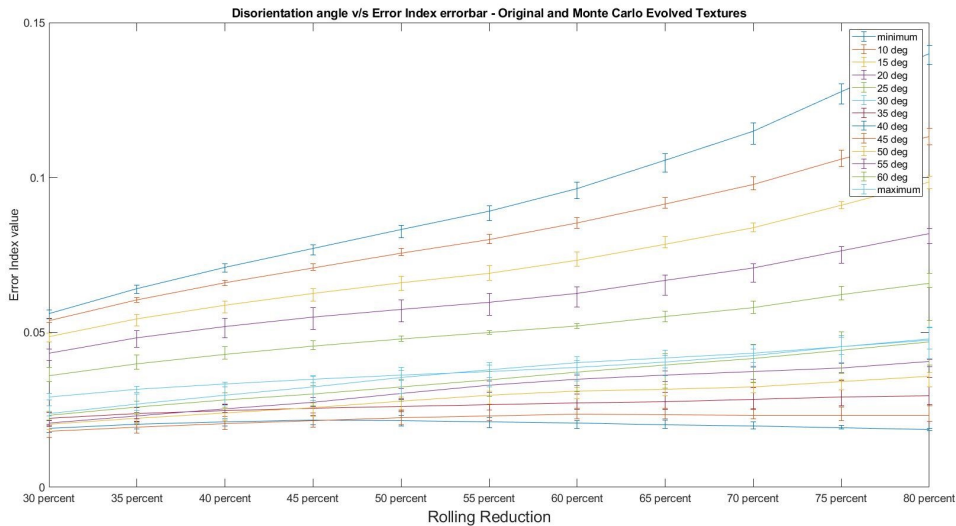


Figure 7.28: Rolling Reduction v/s Error Index, comparison between Original evolved texture and Monte Carlo evolved texture, with Error Index

Figure 7.28 illustrates results representing the relationship between error and rolling reduction percent, comparing Monte Carlo results and default texture simulations.

The resulting curves are roughly ranked in order of increasing disorientation values, with a visible distinction between two tranches of results, those curves with a disorientation angle lower than 25° , and those over. The disorientation curve grouping lower than 25° show no sequential overlap between curves, and they display a resemblance to the Sigmoid function shape. The higher disorientation curves overlap at lower rolling reductions, though they separate at higher rolling reductions. The error curves record lower error values and limited to a small error band, with increasing rolling reductions resulting in a relatively marginal increase in error index.

The standard deviation results, given by figure 7.29 also does not follow any clearly discernible pattern. The standard deviation of the results is interestingly higher than the standard deviation values for the error index comparison with experimental results, even as the error index values obtained for these set of results is lower than the minima of the previous set.

7.5.1 Monte Carlo and Default texture ODFs, variation with rolling reduction

The aforementioned section describes an interesting scenario, for which at 0° disorientation, the difference between Monte Carlo evolved textures, and textures evolved from non-shuffled inputs are at the minimum. There is also scant difference in error

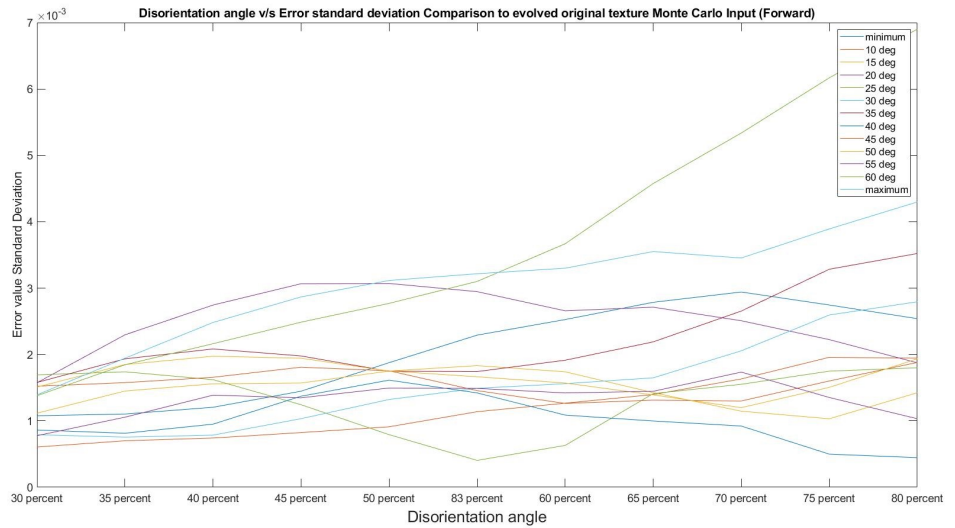


Figure 7.29: Rolling Reduction v/s Error Index Standard Deviation, comparison between Original evolved texture and Monte Carlo evolved texture

for all the rolling reduction curves. Figure 7.30 and 7.31 illustrate the ODFs of 30 % rolling reduction and 80 % rolling reduction for the fourth simulation set, with a disorientation value of 40 degrees. A sharp contrast can be observed between the two images, as their rolling reductions are vastly different.

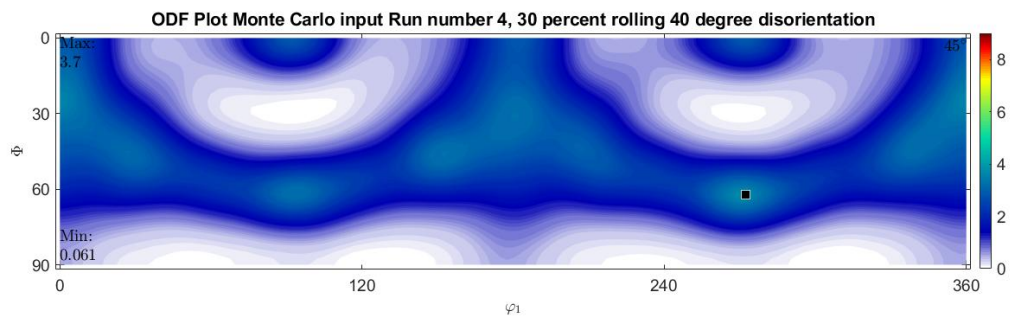


Figure 7.30: ODF plot for Run Number 4, Monte Carlo simulation, with a 40° input disorientation and rolling reduction of 30 %

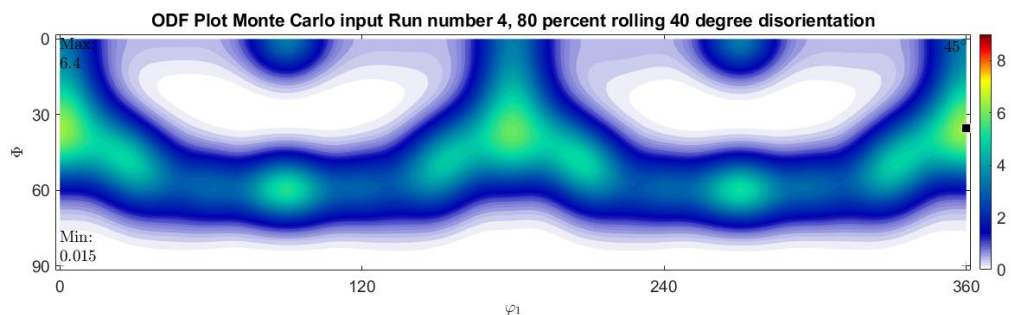


Figure 7.31: ODF plot for Run Number 4, Monte Carlo simulation, with a 40° input disorientation and rolling reduction of 80 %

The difference in ODF figures for the 30 % rolled reduction and 80 % rolled reduction textures are illustrated in figures 7.32 and 7.33 respectively. Both figures have a maximum texture difference intensity of close to $0.3 \times$ Random Intensity. In-

terestingly, the difference in ODF images is not similar for both rolling reduction values.

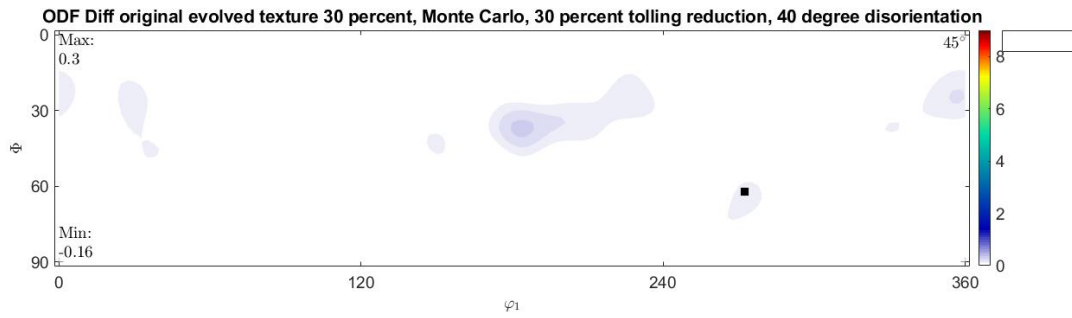


Figure 7.32: ODF difference plot between obtained experimental 83 % rolling reduction and Run Number 4, Monte Carlo simulation, with an input disorientation of 40° and rolling reduction of 30 %

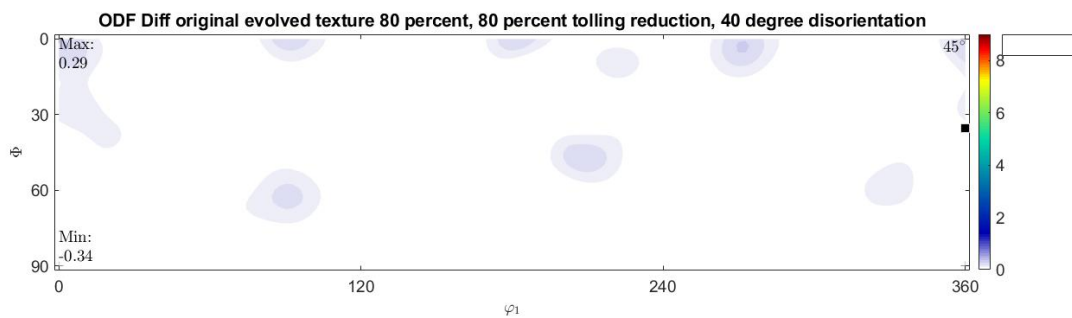


Figure 7.33: ODF difference plot between obtained experimental 83 % rolling reduction and Run Number 4, Monte Carlo simulation, with an input disorientation of 40° and rolling reduction of 80 %

7.6 HUNGARIAN RESULTS AND EXPERIMENTAL TEXTURE COMPARISON

Hungarian outputs are deterministic in nature, and not probabilistic. Thus, only a single input texture is generated for every disorientation entry, and the result values obtained do not have any standard deviation output or error bars. The obtained results in this section include error index results, for comparison with experimentally obtained values which are illustrated in Figures 7.34 , 7.35 , 7.36 and 7.37.

7.6.1 Hungarian Output rolling reduction results

The Hungarian output comparison to experimental textures are further illustrated as variations with rolling reduction, and variation with disorientation angle. The illustration of the results illustrating the relationship between Error Index Value (EIV) and rolling reduction is given in figures 7.34 and 7.35, which illustrate the relationship with experimentally obtained specimen with rolling reductions of 55 % and 83 % respectively.

The illustration of the results illustrating the relationship between Error Index Value (EIV) and disorientation angle is given in figures 7.36 and 7.37, which illus-

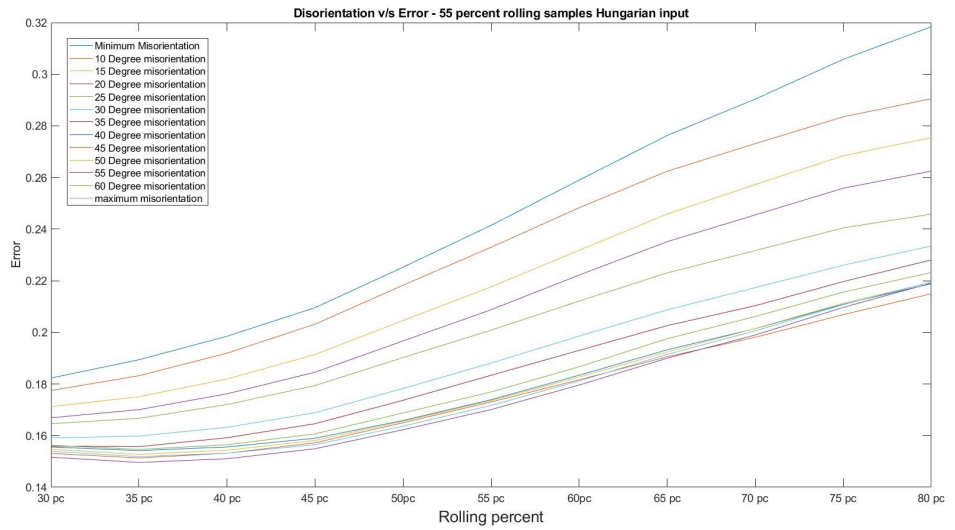


Figure 7.34: Rolling Reduction v/s Error Index, comparison between 55 % rolled experimental samples and Hungarian evolved texture

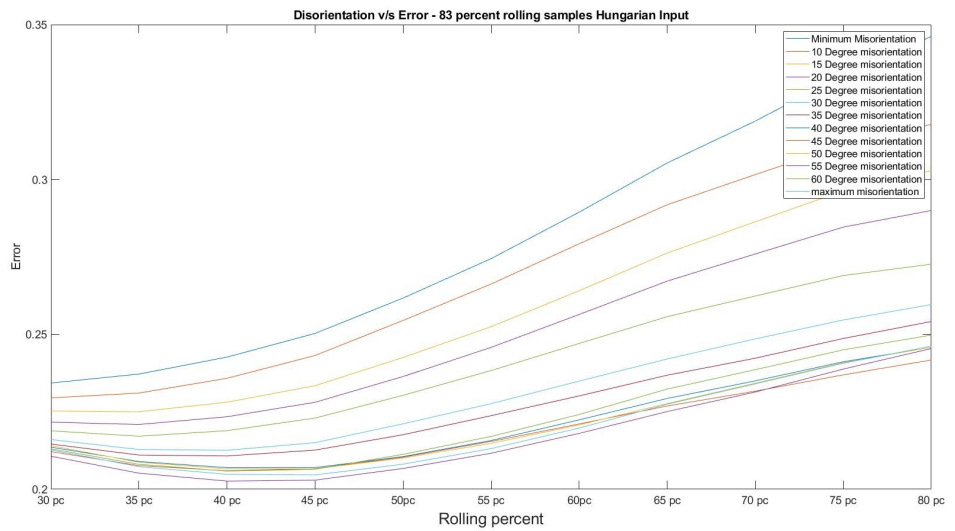


Figure 7.35: Rolling Reduction v/s Error Index, comparison between 83 % rolled experimental samples and Hungarian evolved texture

trate the relationship with experimentally obtained specimen with rolling reductions of 55 % and 83 % respectively

The Hungarian error index comparison with experimental results closely resemble the results obtained from the comparison between Monte Carlo and experimentally obtained inputs, with two key differences. The first difference being minima values, and second, the degree of convergence of Error Index curves. The overall minima of the error index curves are found to be higher for the Hungarian result set, when compared to the Monte Carlo results, even though the difference between is marginal. The trend of convergence of these curves meanwhile, is stronger for the Hungarian results, with a marginally narrower range and overlaps between adjacent curves being observed for one pair of curves more than for the Monte Carlo results.

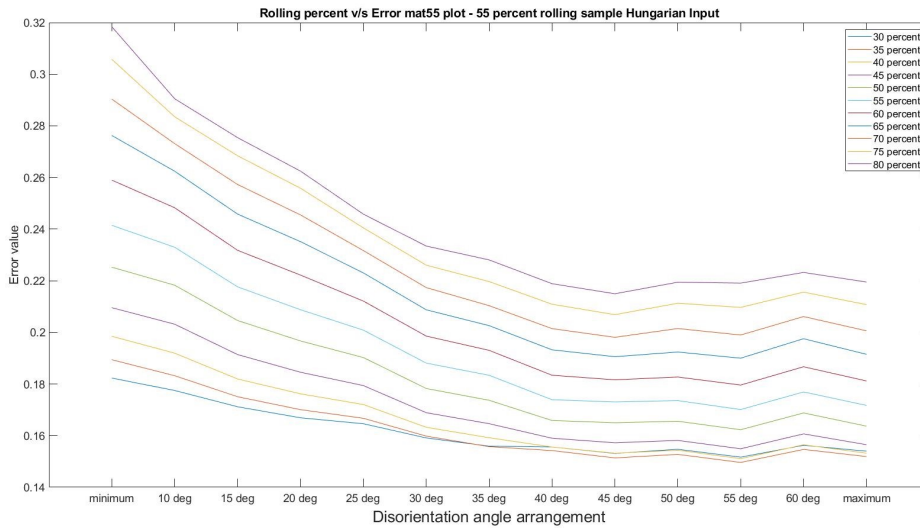


Figure 7.36: Disorientation Angle v/s Error Index, comparison between 55 % rolled experimental samples and Hungarian evolved texture

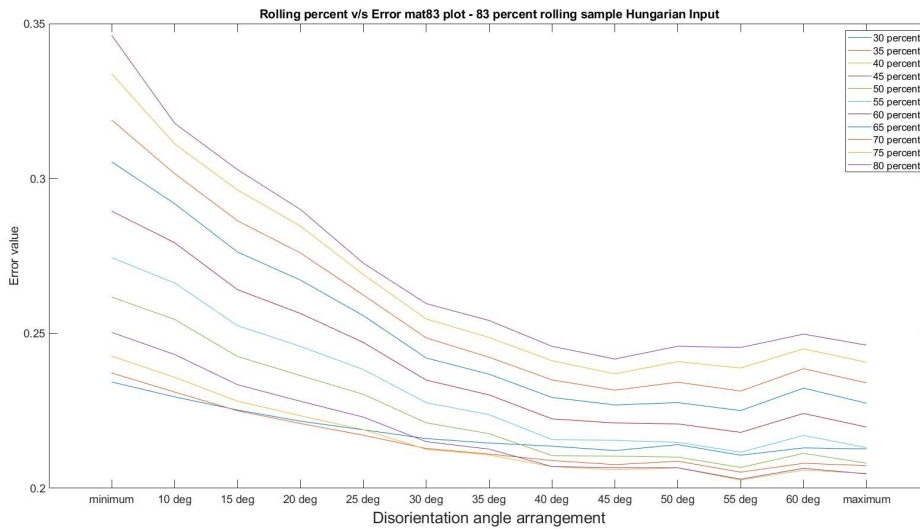


Figure 7.37: Disorientation Angle v/s Error Index, comparison between 83 % rolled experimental samples and Hungarian evolved texture

7.6.2 Hungarian Texture index Result

The variation of texture index with disorientation angle and rolling reduction are given in figures 7.38 and 7.39 respectively. There is a clear and distinctive trend following the variation of texture index with rolling reduction, where an increase in rolling reduction results in a higher texture index, characterized by evenly spaced curves. The rate of increase in texture index also reduced marginally with increasing rolling reduction. In comparison with the Monte Carlo results, the current results exhibit a marginally stronger texture index, supported by more adjacent curves overlapping (curves with disorientation of 40° and greater overlap in this case, as compared to 50° and greater for the Monte Carlo results).

This difference, however, is marginal, and falls within the error bars of the former. Another slight difference between the two is the texture index comparison results for the maximum and minimum disorientation values. For the maximum

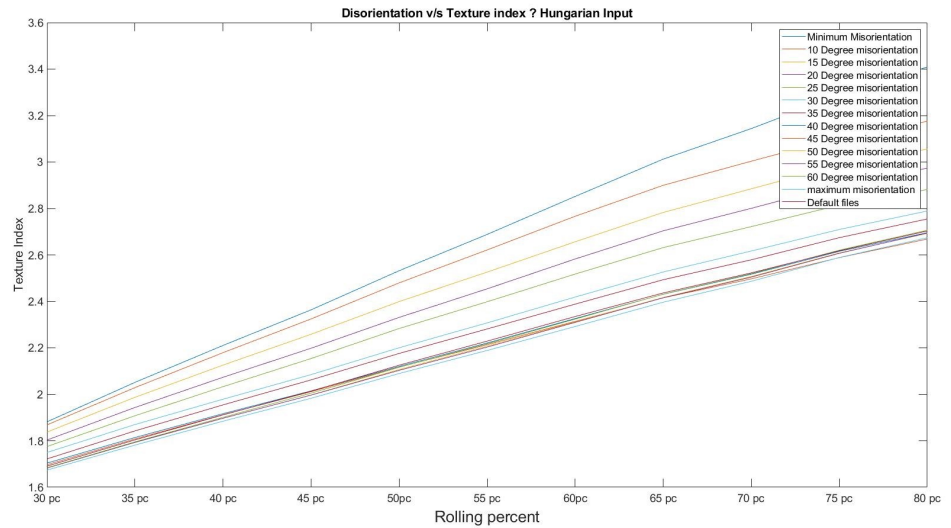


Figure 7.38: Disorientation Angle v/s Texture Index, Hungarian evolved texture

disorientation values, on a comparison between maximum disorientation and 60° disorientation values, the Hungarian results show a decline for the maximum disorientation values vis a vis the 60° disorientation, while the opposite is true for the Monte Carlo results. The minimum disorientation results also show a higher texture index value for minimum disorientation values (interestingly, this is the cause of the marginal difference in maxima between the two).

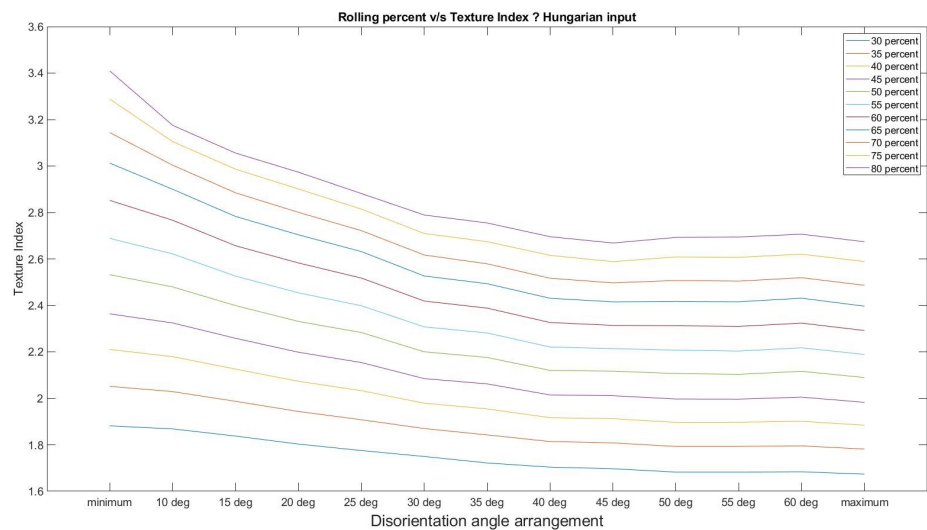


Figure 7.39: Rolling Reduction v/s Texture Index, Hungarian evolved texture

7.7 COMPARISON BETWEEN HUNGARIAN RESULTS AND ORIGINAL TEXTURE EVOLUTION

The comparison of the obtained Hungarian evolved texture and evolved texture from original input are given in Figures 7.41 and 7.41. The lowest disorientation values exhibit even stratification based on rolling reductions, with convergence be-

ing observed with increasing disorientation data. In comparison with the Monte Carlo results, the current results exhibit a stronger convergence, with overlaps being observed at 30° disorientation (the figure is 35 for the Monte Carlo results). Additionally, with increased disorientation angles, stratification is once more observed for the Monte Carlo results, and is not observed in the case of the current results, with overlap for the highest rolling reductions being observed for all disorientation values above the minima.

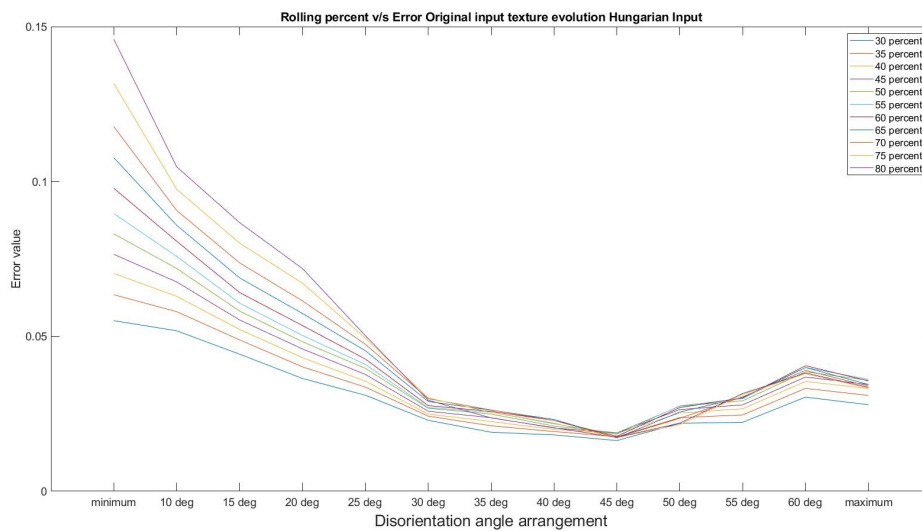


Figure 7.40: Rolling Reduction v/s Error Index, comparison between original evolved texture and Hungarian evolved texture

Additionally, the minimum disorientation error is also higher. These results may help in the arguments of original texture results being similar to higher angle disorientation values, and the influence of minutae differences in pair shuffling. The current set of results has a low error index value, and thus, reflects the minute variations in ordering properties. The Hungarian algorithm results have a lower disorientation mean for minimum disorientation solutions, which may be the cause for the slightly higher error index value.

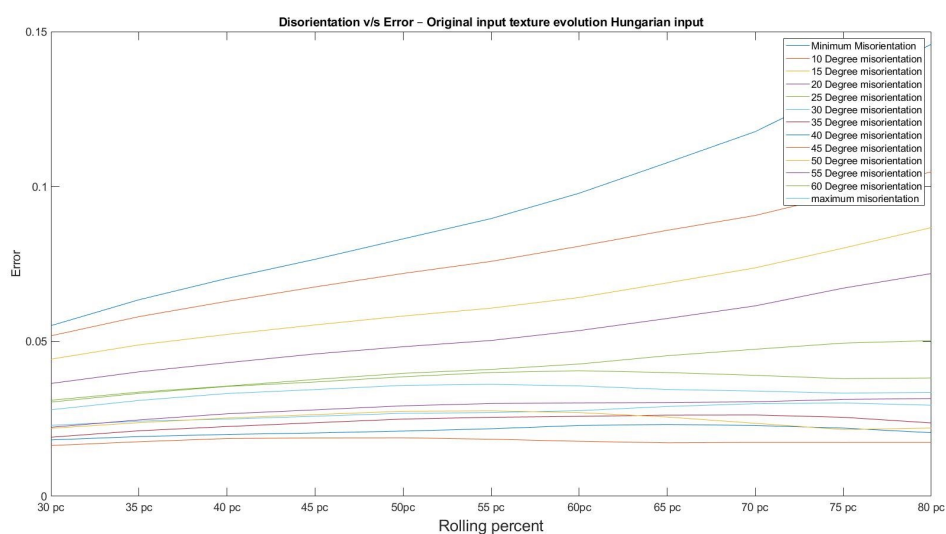


Figure 7.41: Disorientation Angle v/s Error Index, comparison between original evolved texture and Hungarian evolved texture

7.8 COMPARISON OF ORDERING METHODOLOGY

The two ordering algorithms used in this study are based on different mathematical principles, and the resulting texture as a result is different. The Monte Carlo results are probabilistic, and multiple runs of the same are conducted to obtain a mean value. On the other hand, the Hungarian method relies on a deterministic model, and thus, only a single ideal solution is obtained. The result of a comparison between the two is illustrated in figures 7.42 and 7.43.

The most striking details of the result relates to the low error observed, which is close to 0.01 (a negligible error) for minimum disorientation values. This error increases manifold with an increase in disorientation angle, though the increase does not follow a proportional pattern. The maxima is observed at a disorientation of 60° , which also holds the highest standard deviation. Interestingly, the difference between error observed for a disorientation of 60° and maximum disorientation is significant (with error index values and standard deviation decreasing), as the difference in disorientation between 60° and maximum disorientation is less than 3° , the least amongst the measured range.

The disorientation variation is striking, as the sharpest textures are observed for minimum disorientation values. Additionally, the largest differences between Monte Carlo and Hungarian results also take place at minimum disorientations. Additionally the error index for higher disorientation values closely resembles error index curves of Hungarian error index comparisons to original texture evolution. These suggest that the methodology of texture evolution for low angle pairs follows a different relationship with disorientation angles when compared to that of high angle pairs.

The error index variation between the 55° and 60° disorientation and that of the minimum and 10° disorientation are also remarkable as they are the only two pairs that do not overlap in this series. The variation of results with rolling reduction is slight, with a marginal increase in error index and error index standard deviation being observed with increasing rolling reduction. These coincide with the largest differences in reshuffled texture mean and standard deviation values.

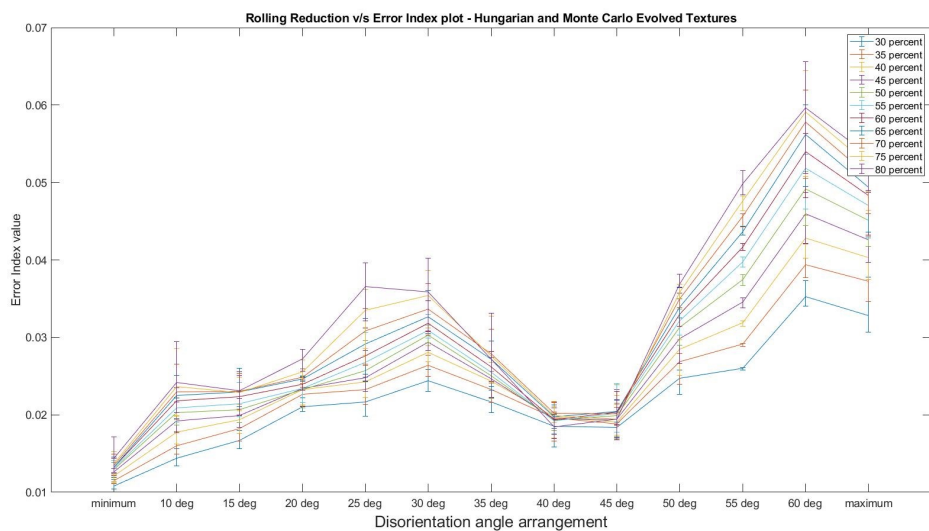


Figure 7.42: Disorientation Angle v/s Error Index, comparison between Hungarian evolved texture and Monte Carlo evolved texture, with Error bars

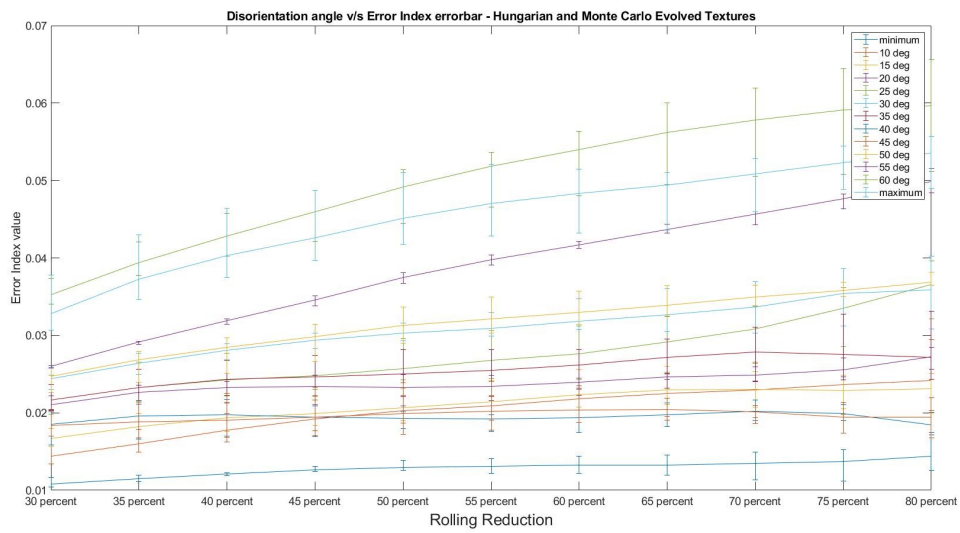


Figure 7.43: Rolling Reduction v/s Error Index, comparison between Hungarian evolved texture and Monte Carlo evolved texture, with Error bars

8

CONCLUSIONS

This study aimed to investigate the effect of initial orientation on plastically deformed texture. To that effect, the following conclusions can be drawn.

- There is a clear and non-negligible effect of disorientation angle on obtained ALAMEL texture.
- The behaviour of high disorientation angles is close to that obtained by original texture evolution.
- The texture evolution of low disorientation values is more likely to be 'disorientation dependent' with slight or no overlap of texture and error index values for reshuffled disorientation values separated by 5° , while that of higher disorientation angle is more likely to be independent of disorientation angle, with a higher likelihood of overlap between disorientation angles of 5° .

Additionally, a comparison between the Hungarian and Monte Carlo algorithms is performed, for which the conclusions are listed below.

- The deterministic Hungarian algorithm provides results that are closer to ideal, in comparison to probabilistic methods such as the Monte Carlo method (though the latter has a higher span for outlier values).
- The difference between the texture evolution of Monte Carlo and Hungarian results is close to negligible, and most noticeable at large disorientations and high rolling reductions.

Lastly, the process of commercialisation of the technology discussed in this study, for which the conclusions drawn are listed below

- Low disorientations are observed to have a sharper texture evolution, which may be helpful in the manufacturing processes of specialized low carbon steels such as electrical steels, whose performance strongly correlates to texture sharpness.
- The domain is analysed to fall under level 2 on the technology readiness level, requiring joint development programs to avoid the 'valley of death' for future technologies
- Critical partnerships and integration, along with leadership in materials development and manufacturing technology development are the important factors in the 'way to market' strategy to enter the beachhead market of DC converters for 'more electrical aircraft'.

BIBLIOGRAPHY

- Neil W Ashcroft, N David Mermin, et al. Solid state physics [by] neil w. ashcroft [and] n. david mermin., 1976.
- Jemimah Akiror, A. Merkhouf, Claude Hudon, and P. Pillay. Consideration of design and operation on rotational flux density distributions in hydrogenerator stators. *IEEE Transactions on Energy Conversion*, 30:1–10, 07 2015.
- J. Bourdon, P. Asfaux, and A. M. Etayo. Review of power electronics opportunities to integrate in the more electrical aircraft. In *2015 International Conference on Electrical Systems for Aircraft, Railway, Ship Propulsion and Road Vehicles (ESARS)*, pages 1–6, 2015.
- Michel Louis Balinski. Integer programming: methods, uses, computations. *Management science*, 12(3):253–313, 1965.
- M L Balinski. A competitive (dual) simplex method for the assignment problem. *Mathematical Programming*, 34(2):125–141, 1986.
- Philip Beckley. *Electrical Steels for Rotating Machines*. Energy Engineering. Institution of Engineering and Technology, 2002.
- J.F.W. Bishop and R. Hill. Xlvi. a theory of the plastic distortion of a polycrystalline aggregate under combined stresses. *The London, Edinburgh, and Dublin Philosophical Magazine and Journal of Science*, 42(327):414–427, 1951.
- Barry W. Boehm. Verifying and validating software requirements and design specifications. *IEEE software*, 1(1):75, 1984.
- Benoît Beausir, László S. Tóth, and Kenneth W. Neale. Ideal orientations and persistence characteristics of hexagonal close packed crystals in simple shear. *Acta Materialia*, 55(8):2695 – 2705, 2007.
- H-J Bunge. *Texture analysis in materials science: mathematical methods*. Elsevier, 2013.
- Aaron David Brooker, Jacob Ward, and Lijuan Wang. Lightweighting impacts on fuel economy, cost, and component losses. Technical report, SAE Technical Paper, 2013.
- Russel E. Caflisch. Monte carlo and quasi-monte carlo methods. *Acta Numerica*, 7:1–49, 1998.
- Yi Cao. Lapjv - jonker-volgenant algorithm for linear assignment problem v3.0 - file exchange - matlab central. <https://nl.mathworks.com/matlabcentral/fileexchange/26836-lapjv-jonker-volgenant-algorithm-for-linear-assignment-problem-v3-0?focused=3782516&tab=function>, 04 2013. (Accessed on 09/30/2020).
- S. Chen, J. Butler, and S. Melzer. Effect of asymmetric hot rolling on texture, microstructure and magnetic properties in a non-grain oriented electrical steel. *Journal of Magnetism and Magnetic Materials*, 368:342–352, 2014.
- Chih-Wen Chen. *Magnetism and metallurgy of soft magnetic materials*. Courier Corporation, 2013.

- C. W Chem. *Magnetism And Metallurgy Of Soft Magnetic Materials*. Elsevier Science, 2014.
- Asim Chaudhury, R Khatirkar, NN Viswanathan, Vivek Singal, A Ingle, S Joshi, and I Samajdar. Low silicon non-grain-oriented electrical steel: Linking magnetic properties with metallurgical factors. *Journal of magnetism and magnetic materials*, 313(1):21–28, 2007.
- C. H. Crawford and E. J. Thomas. Silicon steel in communication equipment. *Transactions of the American Institute of Electrical Engineers*, 54(12):1348–1353, 1935.
- Bhavya Dilipkumar. India's top steelmakers may invest in making crgo electrical steel to cut import dependence, 2020.
- Voestalpine Steel Division. Electrical Industry. Technical report, 2014.
- Nicolò Daina, Aruna Sivakumar, and John W. Polak. Electric vehicle charging choices: Modelling and implications for smart charging services. *Transportation Research Part C: Emerging Technologies*, 81:36 – 56, 2017.
- Jack Edmonds and Richard M. Karp. Theoretical improvements in algorithmic efficiency for network flow problems. *J. ACM*, 19(2):248–264, April 1972.
- Electrical steel market - global forecast to 2021 - increasing urban population proliferate the demand for electrical steel — markets insider. <https://bit.ly/2LZ5BoJ>. (Accessed on 12/26/2019).
- Olaf Engler and Valerie Randle. *Introduction to texture analysis: microtexture, microtexture, and orientation mapping*. CRC press, 2009.
- M. Frommert, C. Zobrist, L. Lahn, A. Böttcher, D. Raabe, and S. Zaefferer. Texture measurement of grain-oriented electrical steels after secondary recrystallization. *Journal of Magnetism and Magnetic Materials*, 320(20):e657–e660, 2008.
- Peter Fajfar, Alenka Šalej Lah, Jakob Kraner, and Goran Kugler. Asymmetric rolling process. *Materials and Geoenvironment*, 64(3):151 – 160, 2017.
- Klaus Günther, Giuseppe Abbruzzese, Stefano Fortunati, and Guy Ligi. Recent technology developments in the production of grain-oriented electrical steel. *steel research international*, 76(6):413–421, 2005.
- Pampa Ghosh, Richard R. Chromik, Babak Vaseghi, and Andrew M. Knight. Effect of crystallographic texture on the bulk magnetic properties of non-oriented electrical steels. *Journal of Magnetism and Magnetic Materials*, 365:14 – 22, 2014.
- M.I. Ghobrial. A photoelastic investigation on the contact stresses developed in rolls during asymmetrical flat rolling. *International Journal of Mechanical Sciences*, 31(10):751 – 764, 1989.
- Norman P Goss. Electrical sheet and method and apparatus for its manufacture and test, July 3 1934. US Patent 1,965,559.
- Nippon Group. Electrical steel sheets—investments for capacity and quality improvement. https://www.nipponsteel.com/en/news/20201106_100.html, November 2020. (Accessed on 01/18/2021).
- Donald Galler and George Slenski. Causes of aircraft electrical failures. *IEEE Aerospace and Electronic Systems Magazine*, 6(8):3–8, 1991.
- Karen Elizabeth Gulbrandsen. Bridging the valley of death: The rhetoric of technology transfer. 2009.
- Patrick Haddad. Tata to shut newport steelworks — power transformer news, 2019.

- Yasuyuki Hayakawa. Mechanism of secondary recrystallization of Goss grains in grain-oriented electrical steel. *Science and Technology of Advanced Materials*, 18(1):480–497, 2017.
- Sheuli Hore and Suchandan K. Das. Computer simulation of microstructure evolution in strip-cast silicon steel with cube and fibre texture. *Philosophical Magazine*, 99(22):2841–2857, 2019.
- C. C. Heath. The market for distributed power systems. In *[Proceedings] APEC '91: Sixth Annual Applied Power Electronics Conference and Exhibition*, pages 225–229, 1991.
- Jan Hensen, Roel Loonen, Maria Archontiki, and Michalis Kanellis. Using building simulation for moving innovations across the “valley of death”. *REHVA Journal*, 52:58–62, 05 2015.
- Nile W. Hatch and David C. Mowery. Process innovation and learning by doing in semiconductor manufacturing. *Management Science*, 44(11-part-1):1461–1477, 1998.
- Hotaka Homma, Shuichi Nakamura, and Naoki Yoshinaga. On $h_{1,1,1}/h_{1,1,2}$, the recrystallisation texture of heavily cold rolled bcc steel. In *Recrystallization and Grain Growth*, volume 467 of *Materials Science Forum*, pages 269–274. Trans Tech Publications Ltd, 8 2004.
- Martin Hölscher, Dierk Raabe, and Kurt Lücke. Rolling and recrystallization textures of bcc steels. *Steel Research*, 62(12):567–575, 1991.
- J. Harase and R. Shimizu. Texture evolution by grain growth in the presence of mns and ain precipitates in fe-3. *Acta Metallurgica et Materialia*, 38(8):1395 – 1403, 1990.
- Yeong-Maw Hwang and Gow-Yi Tzou. Analytical and experimental study on asymmetrical sheet rolling. *International Journal of Mechanical Sciences*, 39(3):289 – 303, 1997.
- Voestalpine Inc. voestalpine and automotive electrical steel - voestalpine. <https://www.voestalpine.com/blog/en/mobility/voestalpine-and-automotive/>, March 2020. (Accessed on 01/14/2021).
- Dow Jones Sustainability Indices. Tsmc sustainability outline. https://csr.tsmc.com/download/csr/2011_tsmc_csr_e/pdf_e/e.2.4.pdf, 05 2011. (Accessed on 02/05/2021).
- T. Iuchi, S. Yamaguchi, T. Ichiyama, M. Nakamura, T. Ishimoto, and K. Kuroki. Laser processing for reducing core loss of grain oriented silicon steel. *Journal of Applied Physics*, 53(3):2410–2412, 1982.
- Andreas Janson. The energy transition with powercore trade mark electrical steel — thyssenkrupp steel. <https://www.thyssenkrupp-steel.com/en/newsroom/highlights/renewable-energy-grid.html>, November 2018. (Accessed on 01/09/2021).
- Ping Ji, W.B. Lee, and Hongyu Li. A new algorithm for the assignment problem: An alternative to the hungarian method. *Computers Operations Research*, 24(11):1017 – 1023, 1997.
- Werner Jara, Pia Lindh, Juan Tapia, Ilya Petrov, Anna-Kaisa Repo, and J. Pyrhönen. Rotor eddy current losses reduction in an axial flux permanent magnet machine. *IEEE Transactions on Industrial Electronics*, 63:1–1, 08 2016.

- Beatriz Junquera, Blanca Moreno, and Roberto Álvarez. Analyzing consumer attitudes towards electric vehicle purchasing intentions in Spain: Technological limitations and vehicle confidence. *Technological Forecasting and Social Change*, 109:6 – 14, 2016.
- Roy Jonker and Anton Volgenant. A shortest augmenting path algorithm for dense and sparse linear assignment problems. *Computing*, 38(4):325–340, 1987.
- U.F Kocks and H Chandra. Slip geometry in partially constrained deformation. *Acta Metallurgica*, 30(3):695 – 709, 1982.
- John Keller. The squeeze is on for smaller and more rugged aircraft power electronics — military & aerospace electronics. <https://www.militaryaerospace.com/power/article/16710659/the-squeeze-is-on-for-smaller-and-more-rugged-aircraft-power-electronics>, July 2001. (Accessed on 02/06/2021).
- Leo Kestens and Sigrud Jacobs. Texture control during the manufacturing of nonoriented electrical steels. *Texture, Stress, and Microstructure*, 2008, 2008.
- Dénes König. Graphok és matrixok. *Mat. Fiz. Lapok*, 38:116–119, 1931.
- Andreas Krings and Juliette Soulard. Overview and comparison of iron loss models for electrical machines. *Journal of Electrical Engineering*, 10(3):162–169, 2010.
- UF Kocks, CN Tomé, and HR Wenk. Texture and anisotropy Cambridge university press. *Cambridge, UK*, 1998.
- H. W. Kuhn. The Hungarian method for the assignment problem. *Naval Research Logistics Quarterly*, 2(1-2):83–97, 1955.
- Markus Kaufmann, Dan Zenkert, and Per Wennhage. *Integrated cost/weight optimization of aircraft structures*, volume 41. 2010.
- Eugene L Lawler. *Combinatorial optimization: networks and matroids*. Courier Corporation, 2001.
- R Lesar. *Computational materials science. fundamentals to applications*, 2013.
- Yin Li. State, market, and business enterprise: development of the Chinese integrated circuit foundries. *China as an innovation nation*, pages 192–214, 2016.
- Sang Heon Lee and Dong Nyung Lee. Analysis of deformation textures of asymmetrically rolled steel sheets. *International Journal of Mechanical Sciences*, 43(9):1997 – 2015, 2001. Selected Papers from AEPA 2000.
- Sang Heon Lee and Dong Nyung Lee. Analysis of deformation textures of asymmetrically rolled steel sheets. *International Journal of Mechanical Sciences*, 43(9):1997–2015, 2001.
- Research Ltd and Markets. Electrical steel market by type (grain-oriented and non grain-oriented), application (transformers, motors, inductors), end-use industry (energy, automobile, manufacturing, household appliances), and region - global forecast to 2021, 2019. https://www.researchandmarkets.com/research/5s7llt/electrical_steel.
- Vahid Lotfi. A labeling algorithm to solve the assignment problem. *Computers Operations Research*, 16(5):397 – 408, 1989.
- Grigory Lyudkovsky, P K Rastogi, and M Bala. Nonoriented Electrical Steels. *JOM*, 38(1):18–26, 1986.

- Hai Tao Liu, Sheng Jie Yao, Yu Sun, Fei Gao, Hong Yu Song, Guo Huai Liu, Lei Li, Dian Qiao Geng, Zhen Yu Liu, and Guo Dong Wang. Evolution of microstructure, texture and inhibitor along the processing route for grain-oriented electrical steels using strip casting. *Materials Characterization*, 106:273–282, 2015.
- J. K. Mackenzie. Second paper on statistics associated with the random disorientation of cubes. *Biometrika*, 45(1/2):229–240, 1958.
- Marketwatch. grain oriented electrical steel market 2019. <https://on.mktw.net/36IcAfv>. (Accessed on 12/20/2019).
- M.E. McHenry. *Encyclopedia of Materials : Science and Technology*, 2001.
- Colonel William T McLyman. *Transformer and inductor design handbook*. Dekker New York,, USA, 1988.
- B V Molotilov, G N Eremin, A E Cheglov, and V I Parahin. Some Fundamental Issues of the Development of Electrical Steel Production Technology in Russia. *Steel in Translation*, 49(8):574–579, 2019.
- Tomáš Mánik and Bjørn Holmedal. Review of the taylor ambiguity and the relationship between rate-independent and rate-dependent full-constraints taylor models. *International Journal of Plasticity*, 55:152 – 181, 2014.
- Farhan H. Malik and Matti Lehtonen. A review: Agents in smart grids. *Electric Power Systems Research*, 131:71 – 79, 2016.
- Esther Majerowicz and Carlos Aguiar de Medeiros. Chinese industrial policy in the geopolitics of the information age: the case of semiconductors. *Revista de Economia Contemporânea*, 22(1), 2018.
- Market and Markets. Dc-dc converter market — size, share, industry analysis and market forecast to 2025. <https://www.marketsandmarkets.com/Market-Reports/global-dc-dc-converter-market-17565254.html>, 05 2018. (Accessed on 02/07/2021).
- Markets and Markets. Electrical steel market global forecast to 2025. <https://www.marketsandmarkets.com/Market-Reports/electrical-steel-market-96179524.html>, December 2020. (Accessed on 01/18/2021).
- AJ Moses. Electrical steels: past, present and future developments. *IEE Proceedings A (Physical Science, Measurement and Instrumentation, Management and Education)*, 137(5):233–245, 1990.
- A J Moses. Importance of rotational losses in rotating machines and transformers. *Journal of Materials Engineering and Performance*, 1(2):235–244, 1992.
- Tony Moses. Opportunities for exploitation of magnetic materials in an energy conscious world. *Interdisciplinary Science Reviews*, 27(2):100–113, 2002.
- Anthony John Moses. Energy efficient electrical steels: Magnetic performance prediction and optimization. *Scripta Materialia*, 67(6):560 – 565, 2012. Viewpoint Set No. 51: Magnetic Materials for Energy.
- Phillip T. Meade and Luis Rabelo. The technology adoption life cycle attractor: Understanding the dynamics of high-tech markets. *Technological Forecasting and Social Change*, 71(7):667 – 684, 2004.
- J. K. Mackenzie and M. J. Thomson. Some statistics associated with the random disorientation of cubes. *Biometrika*, 44(1/2):205–210, 1957.
- Nicholas Metropolis and S. Ulam. The monte carlo method. *Journal of the American Statistical Association*, 44(247):335–341, 1949. PMID: 18139350.

- Dominique Patton Min Zhang. China's steel industry fragmentation worsening: official, 2019.
- J. S. Ngoua Teu Magambo, R. Bakri, X. Margueron, P. Le Moigne, A. Mahe, S. Guguen, and T. Bensalah. Planar magnetic components in more electric aircraft: Review of technology and key parameters for dc–dc power electronic converter. *IEEE Transactions on Transportation Electrification*, 3(4):831–842, 2017.
- Sandro Notargiacomo and Stefano Fortunati. Evaluating Electrical Steels for Electric Vehicles Electrical Steel Rina Consulting - Centro Sviluppo Materiali Introduction.
- nippon steel raises investment to nearly 1billionto boost production of electrical steel sheets for transformers. *magneticsmagazine2020*, 2020.
- Tadao Nozawa, Masato Mizogami, Hisasi Mogi, and Yukio Matsuo. Domain structures and magnetic properties of advanced grain-oriented silicon steel. *Journal of Magnetism and Magnetic Materials*, 133(1):115 – 122, 1994.
- Z. Ouyang and M. A. E. Andersen. Overview of planar magnetic technology—fundamental properties. *IEEE Transactions on Power Electronics*, 29(9):4888–4900, 2014.
- OECD. Focus on green recovery. <https://www.oecd.org/coronavirus/en/themes/green-recovery>. (Accessed on 01/19/2021).
- Darja Steiner Petrovic. Institute of metals and Technology. Non-oriented electrical steel sheets, ISSN : 0371411X, 2010.
- Gobernado P, Roumen Petrov, Ruiz D, Leunis E, and Leo Kestens. Texture Evolution in Si-Alloyed Ultra Low-Carbon Steels after Severe Plastic Deformation. *Advanced Engineering Materials*, 12(10):1076–1081, 2010.
- D Priya and G Ramesh. The hungarian method for the assignment problem, with generalized interval arithmetic and its applications. *Journal of Physics: Conference Series*, 1377:012046, nov 2019.
- R. H. Pry. Development of metallurgical structures and magnetic properties in iron silicon alloys. *Journal of Applied Physics*, 30(4):S189–S193, 1959.
- Wei Pei, Y.H. Sha, H.P. Yang, F. Zhang, and Liang Zuo. Through-thickness texture variation in non-oriented electrical steel sheet produced by asymmetric rolling. In *Multi-Functional Materials and Structures II*, volume 79 of *Advanced Materials Research*, pages 1947–1950. Trans Tech Publications Ltd, 11 2009.
- Valerie Randle. Origins of misorientation texture (mesotexture). *Textures and Microstructures*, 14, 1970.
- Valerie Randle. Microtexture investigation of the relationship between strain and anomalous grain growth. 8610, 2006.
- Ann Bettina Richelsen. Elastic-plastic analysis of the stress and strain distributions in asymmetric rolling. *International Journal of Mechanical Sciences*, 39(11):1199–1211, 1997.
- D. Raabe and K. Lücke. Texture and microstructure of hot rolled steel. *Scripta Metallurgica et Materialia*, 26(8):1221 – 1226, 1992.
- X. Roboam, B. Sareni, and A. D. Andrade. More electricity in the air: Toward optimized electrical networks embedded in more-electrical aircraft. *IEEE Industrial Electronics Magazine*, 6(4):6–17, 2012.

- Carbon Steel, Satyaveer Singh Dhinwal, Laszlo S Toth, Rimma Lapovok, and Peter Damian Hodgson. Tailoring One-Pass Asymmetric Rolling of Extra Low. 2019.
- L Seidel, M Hölscher, and K Lücke. Rolling and recrystallization textures in iron–3% silicon. *Texture, Stress, and Microstructure*, 11(2-4):171–185, 1989.
- Wei Shong. Hsmc promised china’s first 7 nm chips. it didn’t go well. <https://technode.com/2020/09/09/hsmc-promised-chinaa-first-7-nm-chips-it-didnt-go-well/>, September 2020. (Accessed on 02/05/2021).
- Big River Steel. Big river sees expansion, electrical steel in its future - steel market update. <https://bigriversteel.com/wp-content/uploads/2018/03/Big-River-Sees-Expansion-Electrical-Steel-in-its-Future-Steel-Market-Update.pdf>, March 2018. (Accessed on 01/18/2021).
- Kunihiko Senda, Masanori Uesaka, Soichiro Yoshizaki, and Yoshihiko Oda. Electrical steels and their evaluation for automobile motors. *31st International Electric Vehicle Symposium and Exhibition, EVS 2018 and International Electric Vehicle Technology Conference 2018, EVTeC 2018*, 2018.
- Jurij J. Sidor, Kim Verbeken, Edgar Gomes, Juergen Schneider, Pablo Rodriguez Calvillo, and Leo A.I. Kestens. Through process texture evolution and magnetic properties of high si non-oriented electrical steels. *Materials Characterization*, 71:49 – 57, 2012.
- Gregory M. Spencer, Tara Vinodrai, Meric S. Gertler, and David A. Wolfe. Do clusters make a difference? defining and assessing their economic performance. *Regional Studies*, 44(6):697–715, 2010.
- Peter J. Sher and Phil Y. Yang. The effects of innovative capabilities and rd clustering on firm performance: the evidence of taiwan’s semiconductor industry. *Technovation*, 25(1):33–43, 2005.
- Geoffrey Ingram Taylor. Plastic strain in metals. *J. Inst. Metals*, 62:307–324, 1938.
- László Tóth and Paul Houtte. Discretization techniques for orientation distribution functions. *Textures and Microstructures*, 19, 01 1992.
- V.J. Thomas and Elicia Maine. Market entry strategies for electric vehicle start-ups in the automotive industry – lessons from tesla motors. *Journal of Cleaner Production*, 235:653–663, 2019.
- MTEX Toolbox. calcerror function— mtex. <https://mtex-toolbox.github.io/ODF.calcError.html>. (Accessed on 08/09/2020).
- Eric Trautmann. Faster jonker-volgenant assignment algorithm - file exchange - matlab central. <https://nl.mathworks.com/matlabcentral/fileexchange/30838-faster-jonker-volgenant-assignment-algorithm?focused=5234907&tab=function>, 2012 06. (Accessed on 09/30/2020).
- Yoshiyuki Ushigami, Masato Mizokami, Masahiro Fujikura, Takeshi Kubota, Hiroyasu Fujii, and Kenichi Murakami. Recent development of low-loss grain-oriented silicon steel. *Journal of Magnetism and Magnetic Materials*, 254-255:307–314, 2003.
- P. Van Houtte. On the equivalence of the relaxed taylor theory and the bishop-hill theory for partially constrained plastic deformation of crystals. *Materials Science and Engineering*, 55(1):69 – 77, 1982.
- P Van Houtte. A comprehensive mathematical formulation of an extended taylor–bishop–hill model featuring relaxed constraints, the renouard–wintemberger theory and a strain rate sensitivity model. *Texture, Stress, and Microstructure*, 8:313–350, 1988.

- Paul Van Houtte, Anand Krishna Kanjarla, Albert Van Bael, Marc Seefeldt, and Laurent Delannay. Multiscale modelling of the plastic anisotropy and deformation texture of polycrystalline materials. *European Journal of Mechanics, A/Solids*, 25(4):634–648, 2006.
- Paul Van Houtte, Saiyi Li, Marc Seefeldt, and Laurent Delannay. Deformation texture prediction: from the Taylor model to the advanced lamel model. *International Journal of Plasticity*, 21(3):589 – 624, 2005.
- A R De Vos. *The effects of protectionist trade measures : An Empirical Study on the Steel Sector*. PhD thesis, UVA.
- K. Verbeken, J. Schneider, J. Verstraete, H. Hermann, and Y. Houbaert. Effect of hot and cold rolling on grain size and texture in Fe-2.4wt pct Si strips. *IEEE Transactions on Magnetics*, 44(11):3820–3823, 2008.
- Frédéric Wurtz and Benoît Delinchant. “smart buildings” integrated in “smart grids”: A key challenge for the energy transition by using physical models and optimization with a “human-in-the-loop” approach. *Comptes Rendus Physique*, 18(7):428 – 444, 2017. Demain l’énergie.
- Nicholas Williard, Wei He, Christopher Hendricks, and Michael Pecht. Lessons learned from the 787 dreamliner issue on lithium-ion battery reliability. *Energies*, 6(9):4682–4695, 2013.
- David Wyatt and Mike Tooley. *Aircraft electrical and electronic systems*. Routledge, 2018.
- S. Wronski, M. Wrobel, A. Baczmanski, and K. Wierzbanski. Effects of cross-rolling on residual stress, texture and plastic anisotropy in f.c.c. and b.c.c. metals. *Materials Characterization*, 77:116 – 126, 2013.
- Zhaosuo Xia, Yonglin Kang, and Quanli Wang. Developments in the production of grain-oriented electrical steel. *Journal of Magnetism and Magnetic Materials*, 320(23):3229–3233, 2008.
- Hiroshi Yasuda and Junichi Iijima. Linkage between strategic alliances and firm’s business strategy: the case of semiconductor industry. *Technovation*, 25(5):513–521, 2005.
- J.H. Yu, J.S. Shin, J.S. Bae, Z.-H. Lee, T.D. Lee, H.M. Lee, and E.J. Lavernia. The effect of heat treatments and Si contents on B₂ ordering reaction in high-silicon steels. *Materials Science Engineering A*, 307(1-2):29–34, 2001.



ERROR INDEX VARIATION WITH EXPERIMENTAL RESULTS

A.1 SERIES 1: MONTE CARLO ROLLING REDUCTION VS ERROR INDEX FOR 55 PERCENT SAMPLE

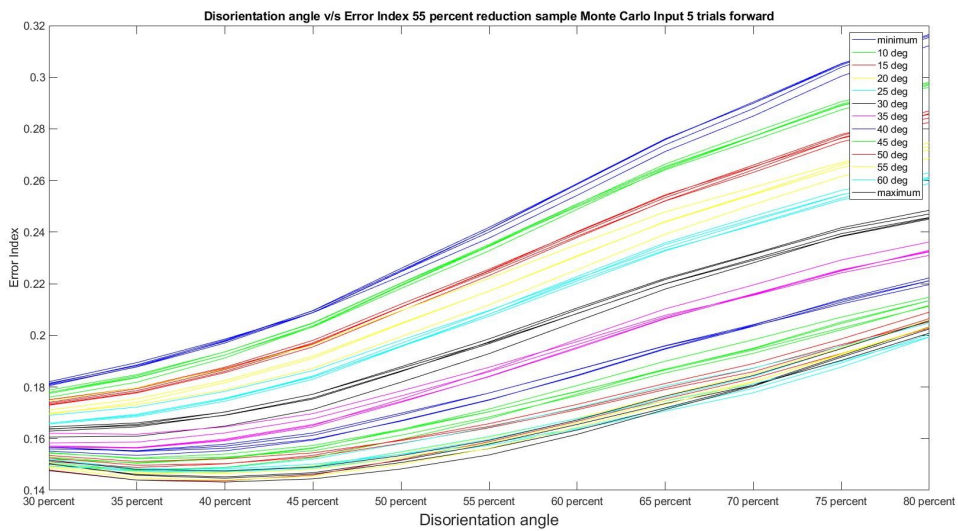


Figure A.1: Disorientation Angle v/s Error Index : 55 percent reduction sample, Monte Carlo, 5 trials

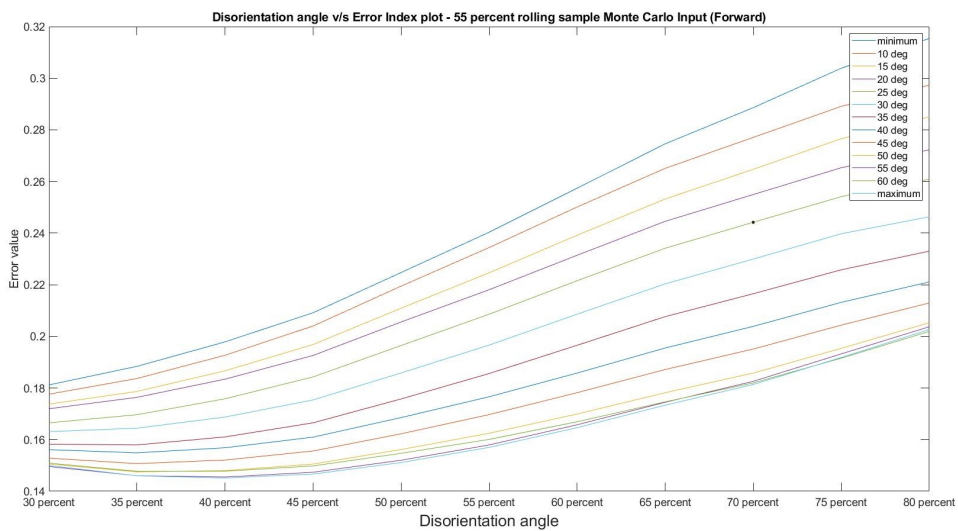


Figure A.2: Disorientation Angle v/s Error Index mean : 55 percent reduction sample, Monte Carlo

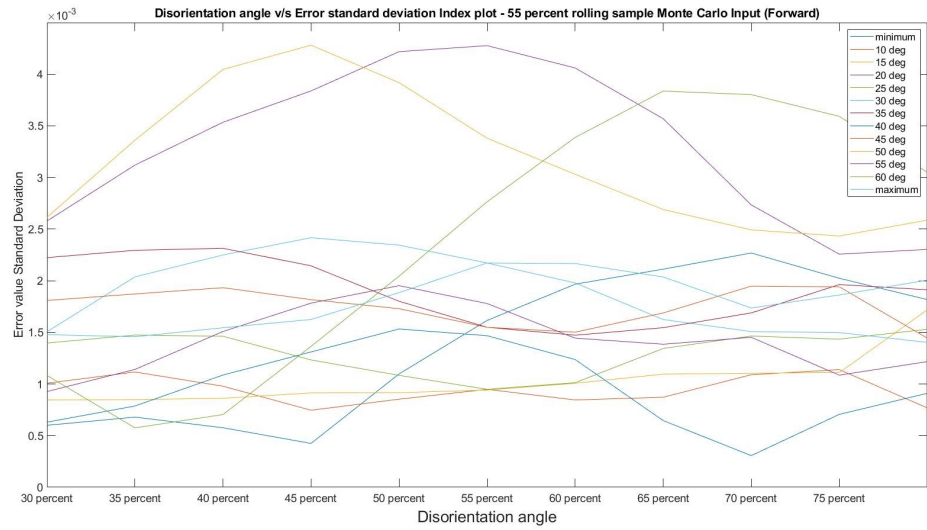


Figure A.3: Disorientation Angle v/s Error Index Standard Deviation : 55 percent reduction sample, Monte Carlo

A.2 SERIES 2. MONTE CARLO DISORIENTATION ANGLE VS ERROR INDEX FOR 55 PERCENT EXPERIMENTAL SAMPLE

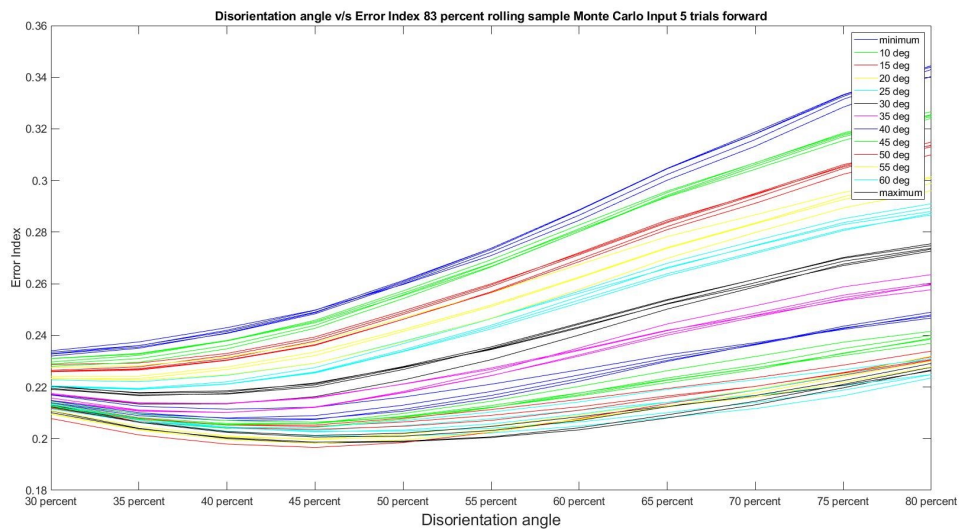


Figure A.4: Disorientation Angle v/s Error Index : 83 percent reduction sample, Monte Carlo, 5 trials

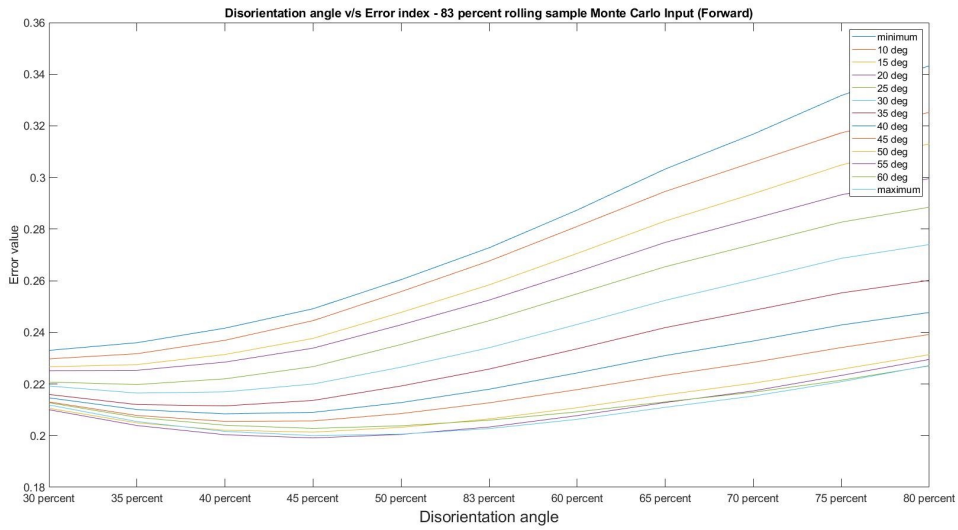


Figure A.5: Disorientation Angle v/s Error Index mean : 83 percent reduction sample, Monte Carlo

A.3 SERIES 3. MONTE CARLO ROLLING REDUCTION VS ERROR INDEX FOR 83 PERCENT EXPERIMENTAL SAMPLE

A.4 SERIES 4. MONTE CARLO DISORIENTATION ANGLE VS ERROR INDEX FOR 83 PERCENT EXPERIMENTAL SAMPLE

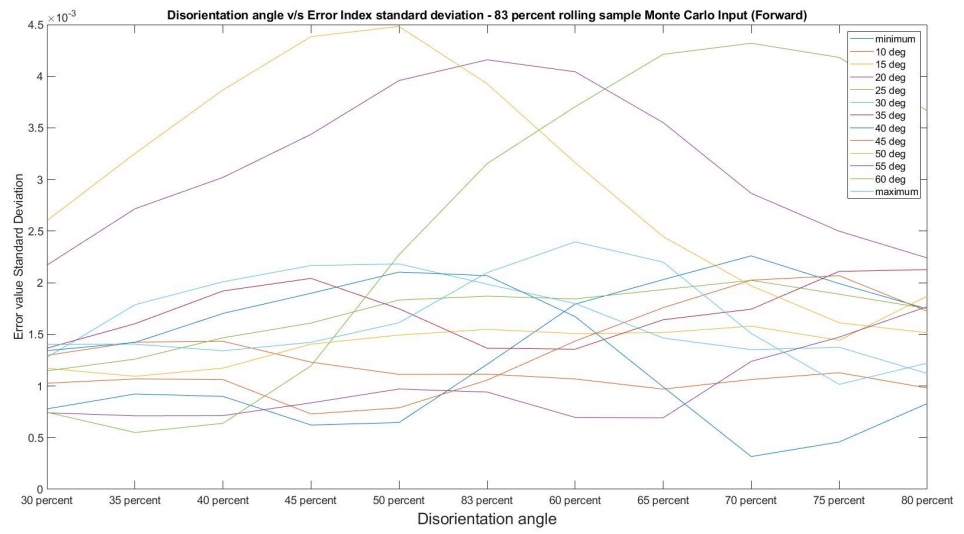


Figure A.6: Disorientation Angle v/s Error Index Standard Deviation : 83 percent reduction sample, Monte Carlo

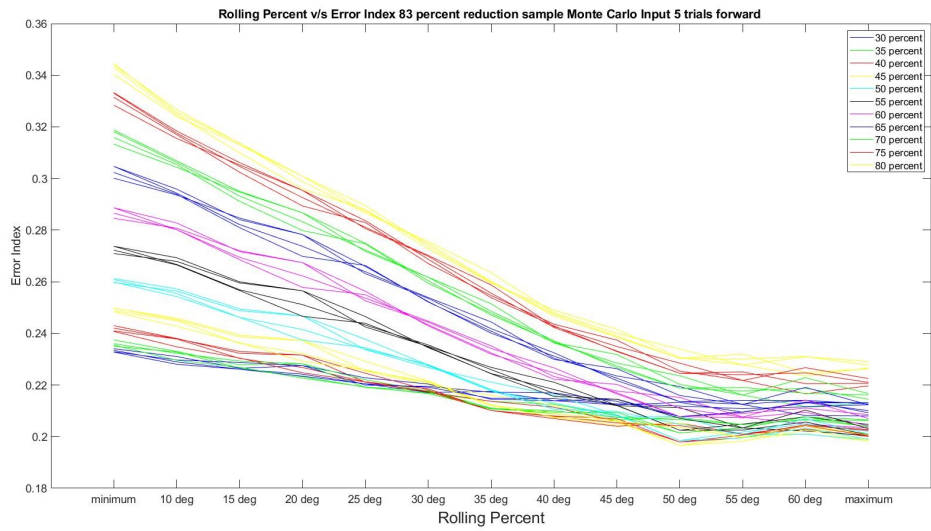


Figure A.7: Rolling Reduction v/s Error Index : 83 percent reduction sample, Monte Carlo, 5 trials

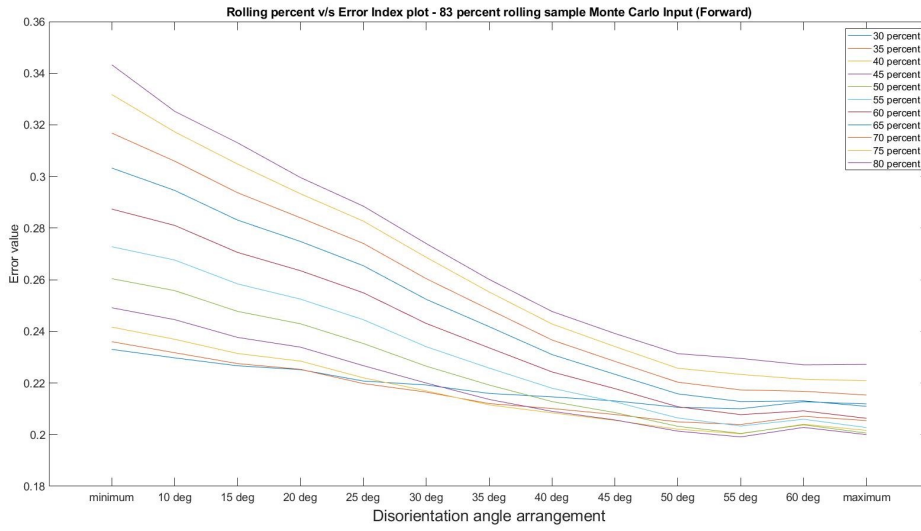


Figure A.8: Rolling Reduction v/s Error Index mean : 83 percent reduction sample, Monte Carlo

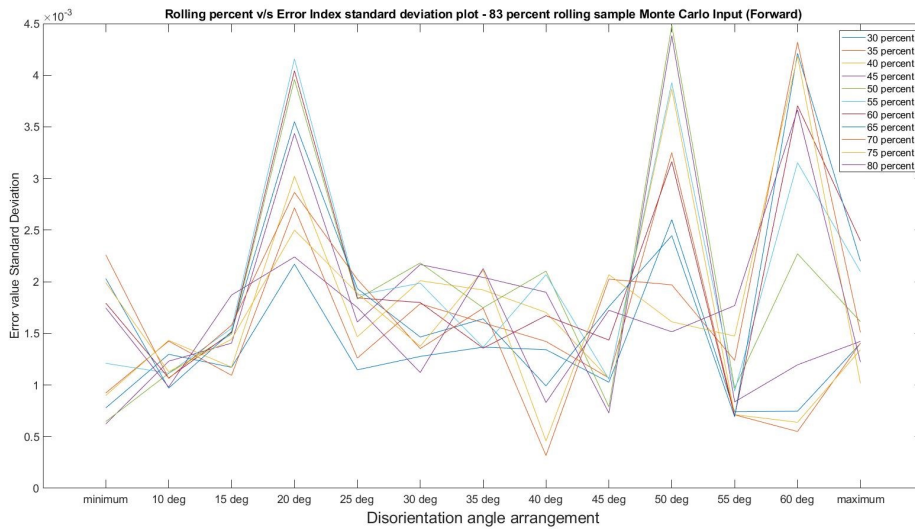


Figure A.9: Rolling Reduction v/s Error Index Standard Deviation : 83 percent reduction sample, Monte Carlo

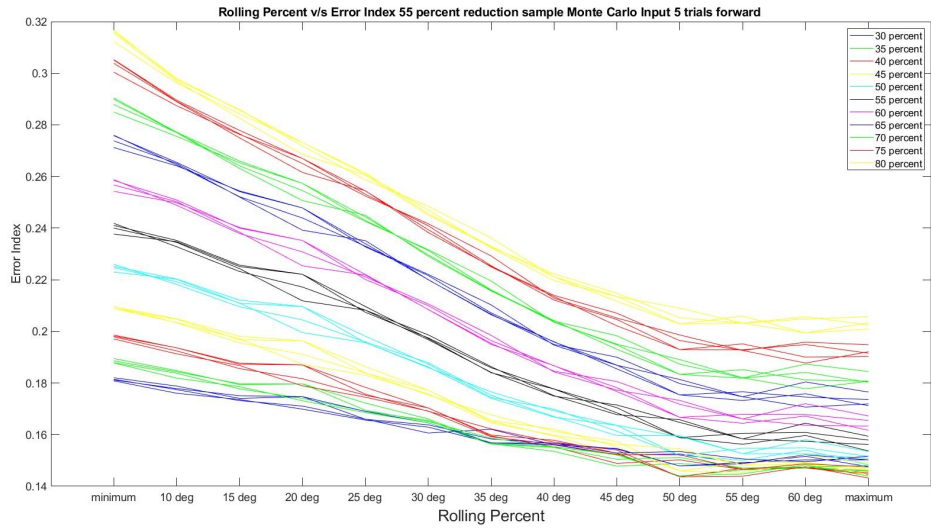


Figure A.10: Rolling Reduction v/s Error Index : 55 percent reduction sample, Monte Carlo, 5 trials

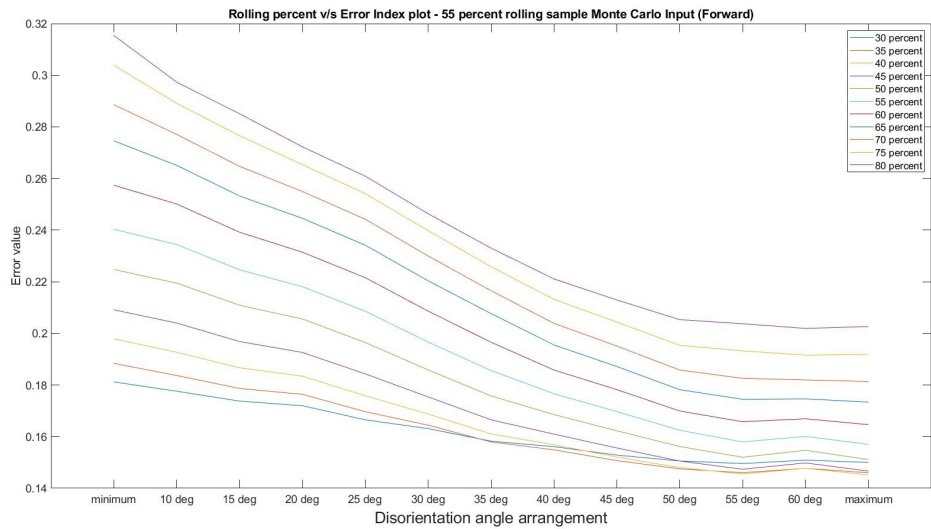


Figure A.11: Rolling Reduction v/s Error Index mean : 55 percent reduction sample, Monte Carlo

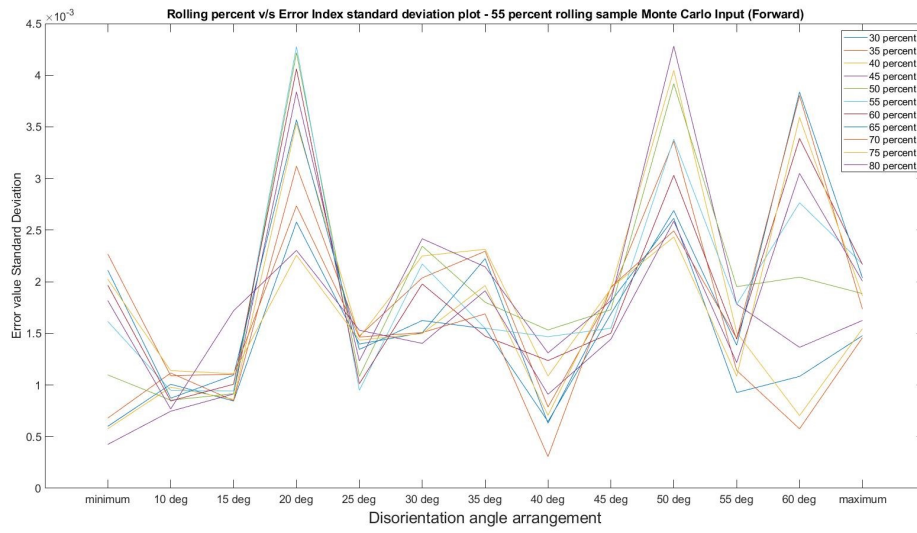


Figure A.12: Rolling Reduction v/s Error Index Standard Deviation : 55 percent reduction sample, Monte Carlo

B | TEXTURE INDEX VALUES OF MONTE CARLO SAMPLES

B.1 SERIES 1. MONTE CARLO DISORIENTATION VS TEXTURE INDEX

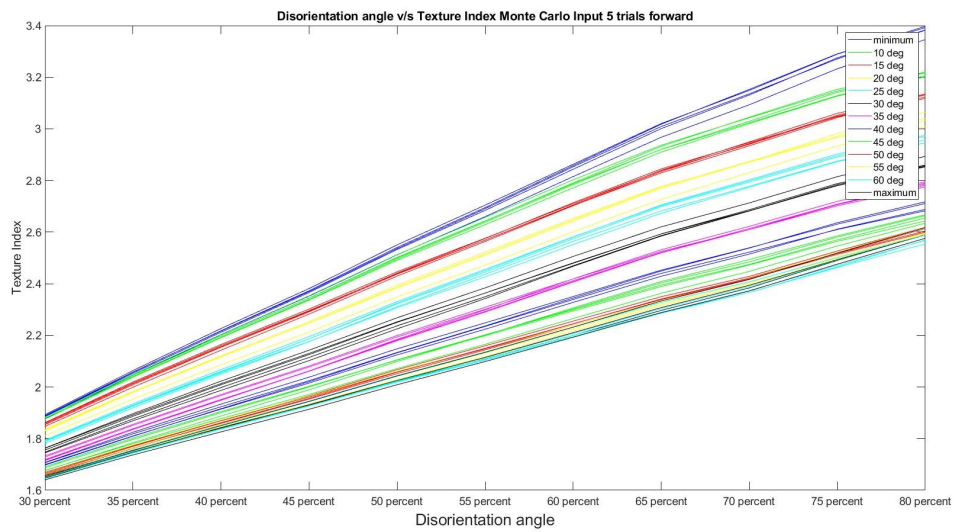


Figure B.1: Disorientation Angle v/s Texture Index : Monte Carlo All runs

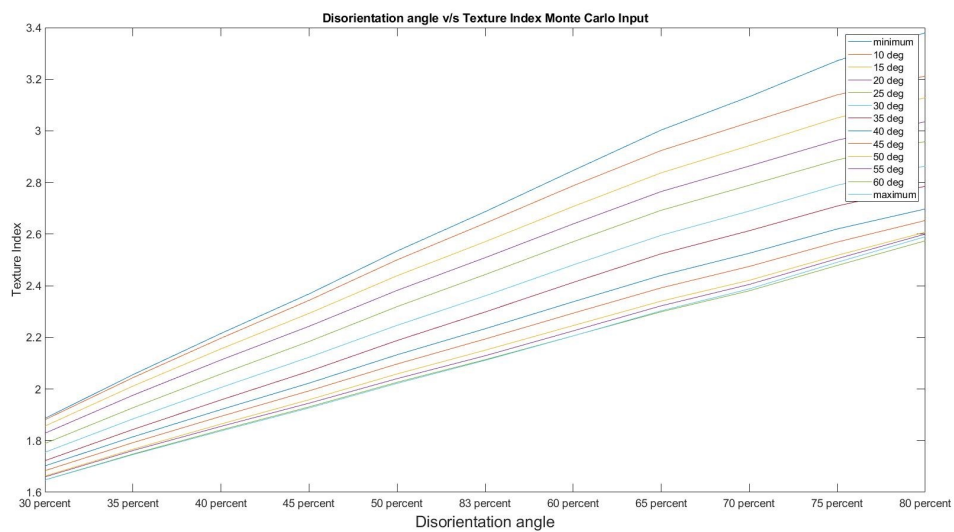


Figure B.2: Disorientation Angle v/s Texture Index : Monte Carlo, mean value

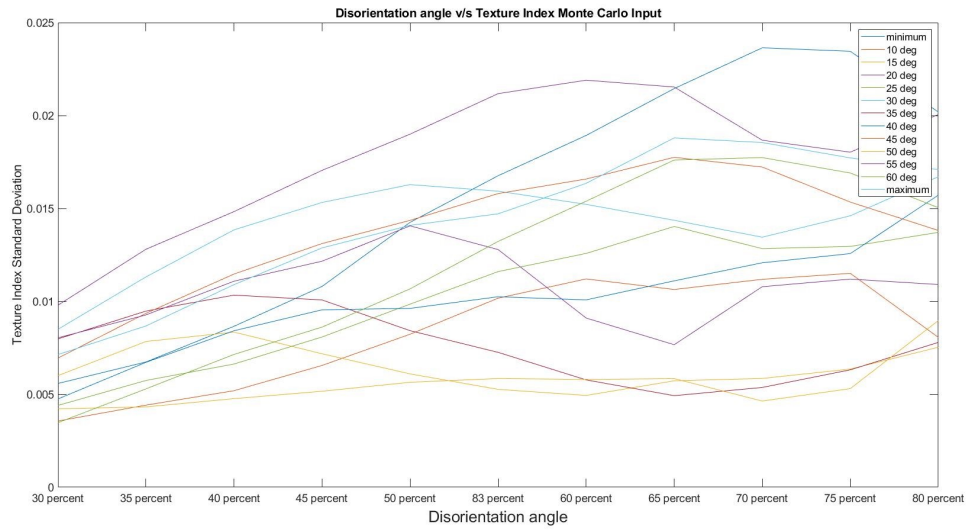


Figure B.3: Disorientation Angle v/s Texture Index : Monte Carlo, standard deviation value

B.2 SERIES 2. MONTE CARLO ROLLING REDUCTION VS TEXTURE INDEX

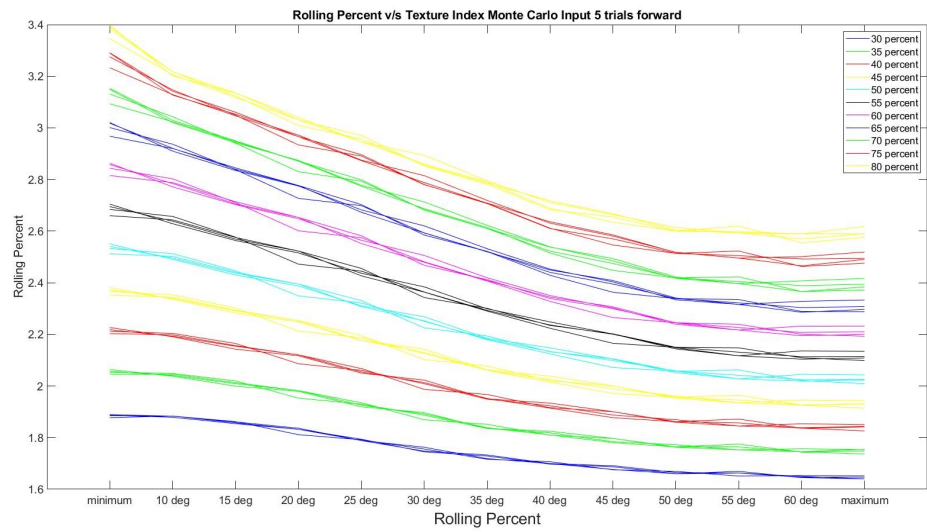


Figure B.4: Rolling Reduction v/s Texture Index : Monte Carlo All runs

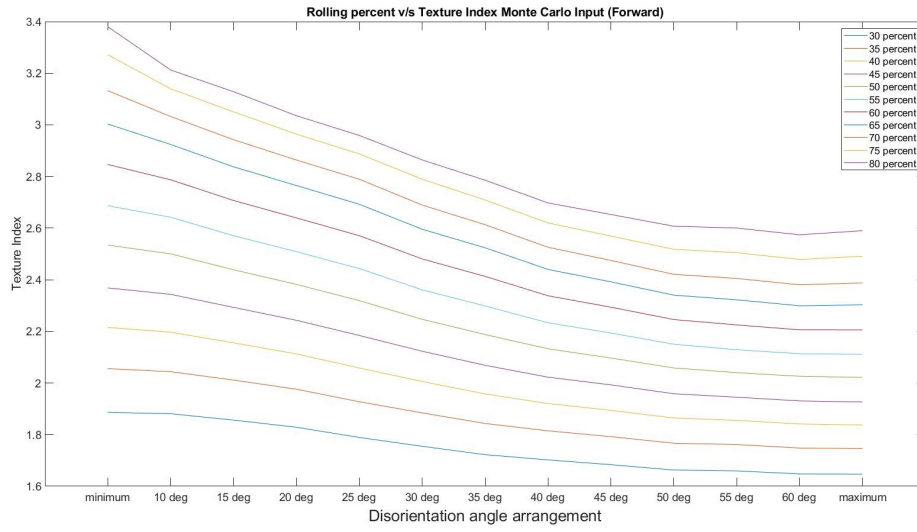


Figure B.5: Rolling Reduction v/s Texture Index : Monte Carlo, mean value

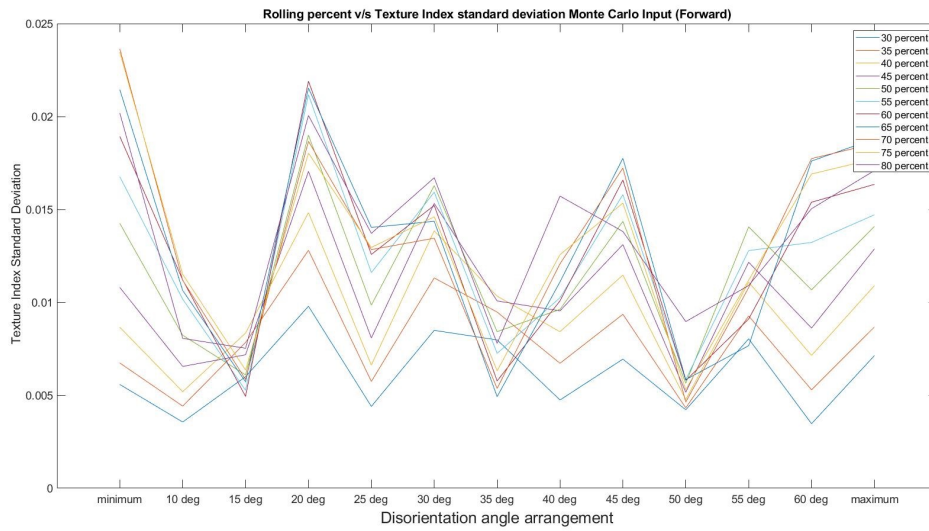


Figure B.6: Rolling Reduction v/s Texture Index : Monte Carlo, standard deviation value

C

MONTE CARLO ERROR INDEX VARIATION WITH SIMULATED ORIGINAL TEXTURE RESULTS

C.1 SERIES 1. MONTE CARLO ROLLING REDUCTION VS ERROR INDEX

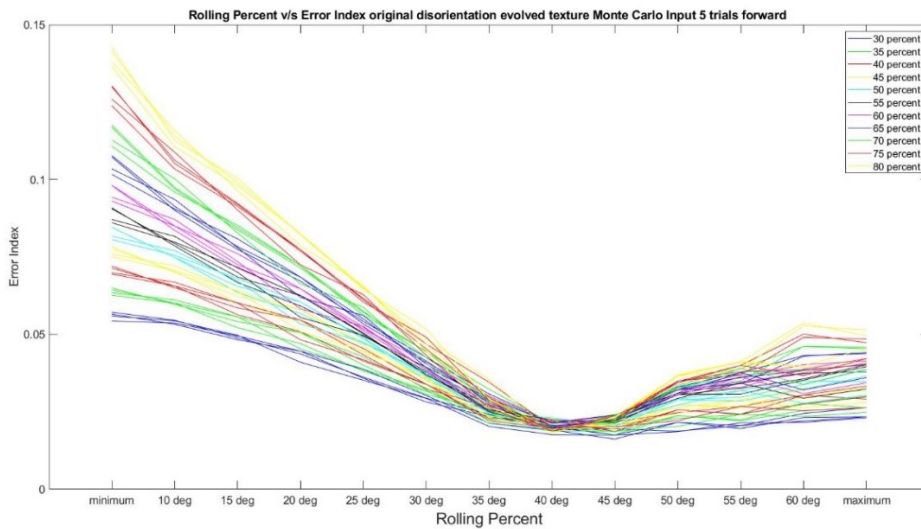


Figure C.1: Rolling Reduction v/s Error Index between Monte Carlo and original simulated results, All trials

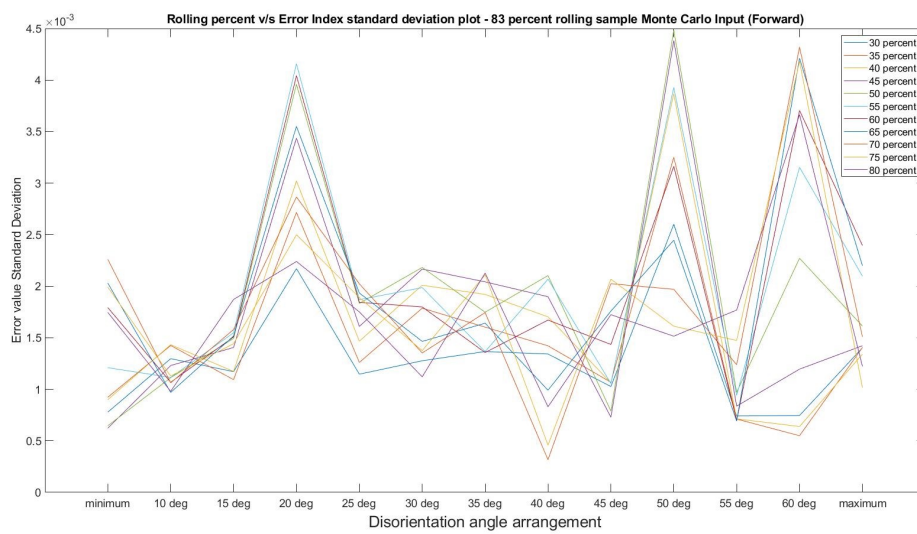


Figure C.2: Rolling Reduction v/s Error Index between Monte Carlo and original simulated results, mean values

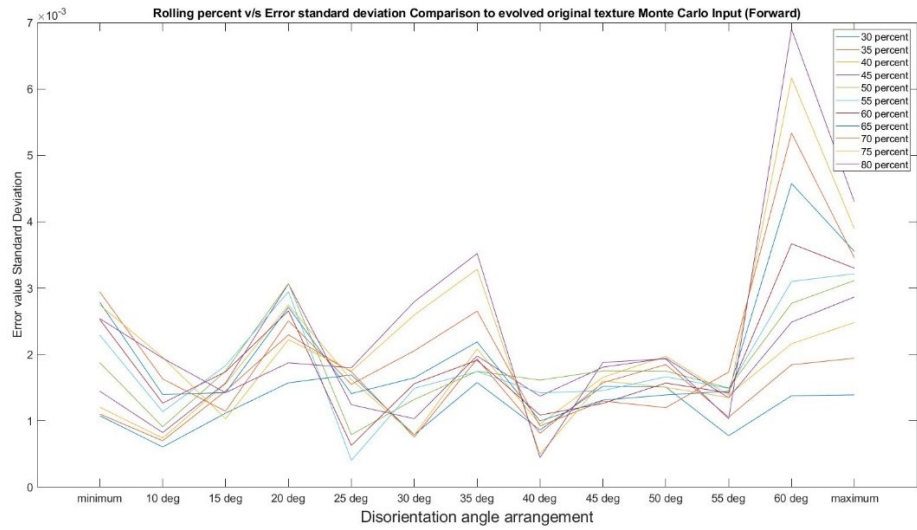


Figure C.3: Rolling Reduction v/s Error Index between Monte Carlo and original simulated results, Standard deviation values

C.2 SERIES 2. MONTE CARLO DISORIENTATION ANGLE VS ERROR INDEX

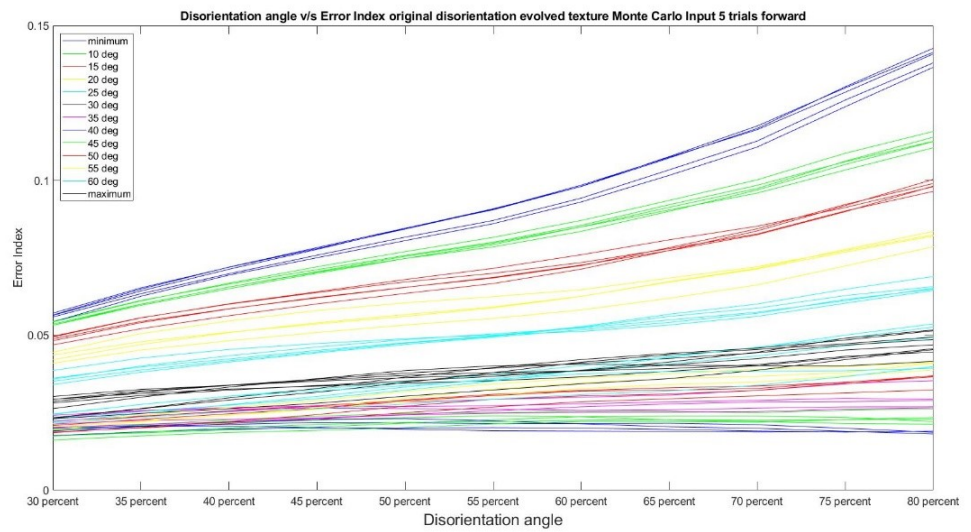


Figure C.4: Disorientation Angle v/s Error Index between Monte Carlo and original simulated results, All trials

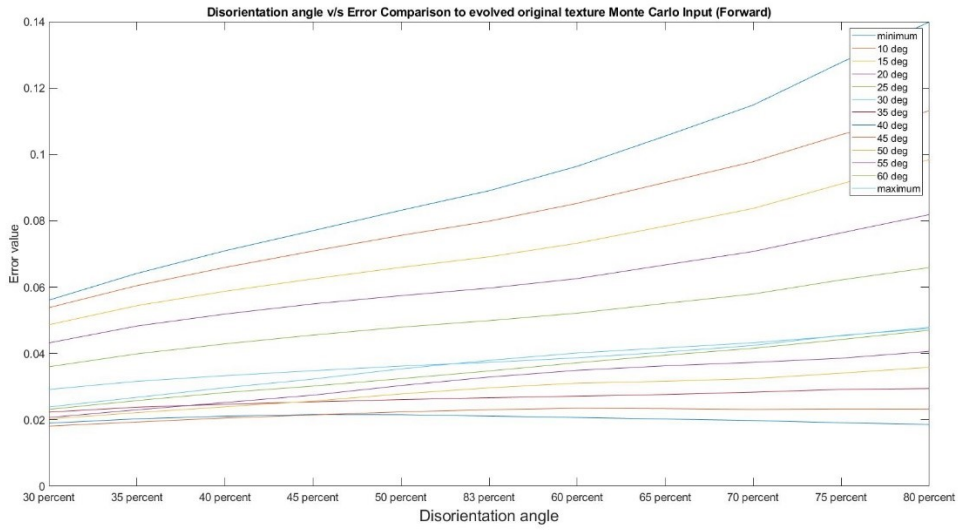


Figure C.5: Disorientation Angle v/s Error Index between Monte Carlo and original simulated results, mean values

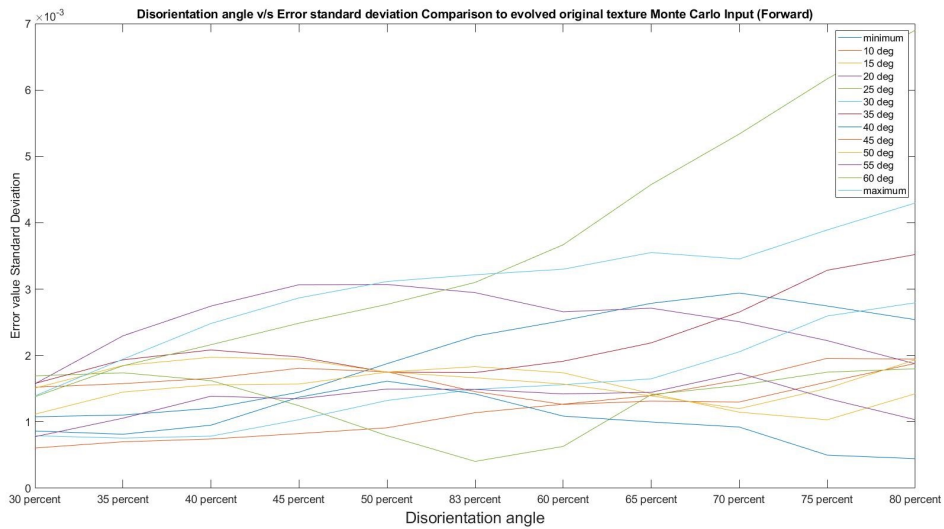


Figure C.6: Disorientation Angle v/s Error Index between Monte Carlo and original simulated results, Standard deviation values

D

HUNGARIAN ERROR INDEX VARIATION WITH EXPERIMENTALLY OBTAINED 55 PERCENT REDUCTION RESULTS

D.1 SERIES 1. ERROR INDEX VARIATION FOR 55 PERCENT SAMPLE

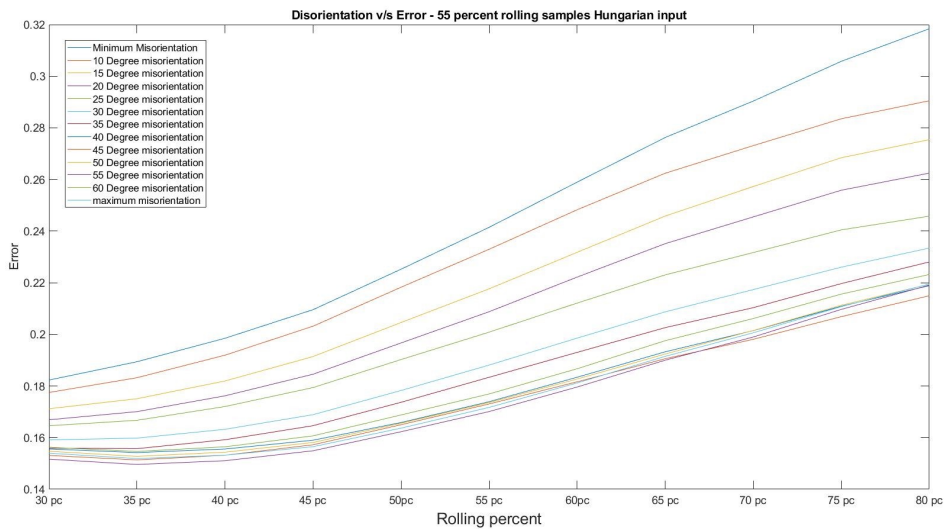


Figure D.1: Disorientation Angle v/s Error Index between 55 Percent Experimental Texture and Hungarian Result

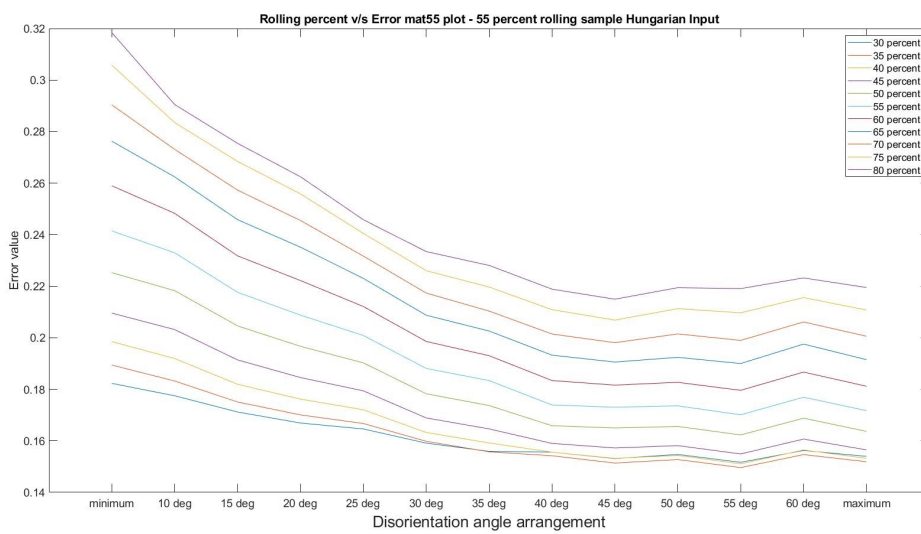


Figure D.2: Rolling Reduction v/s Error Index between 55 Percent Experimental Texture and Hungarian Result

D.2 SERIES 2. ERROR INDEX VARIATION FOR 83 PERCENT SAMPLE

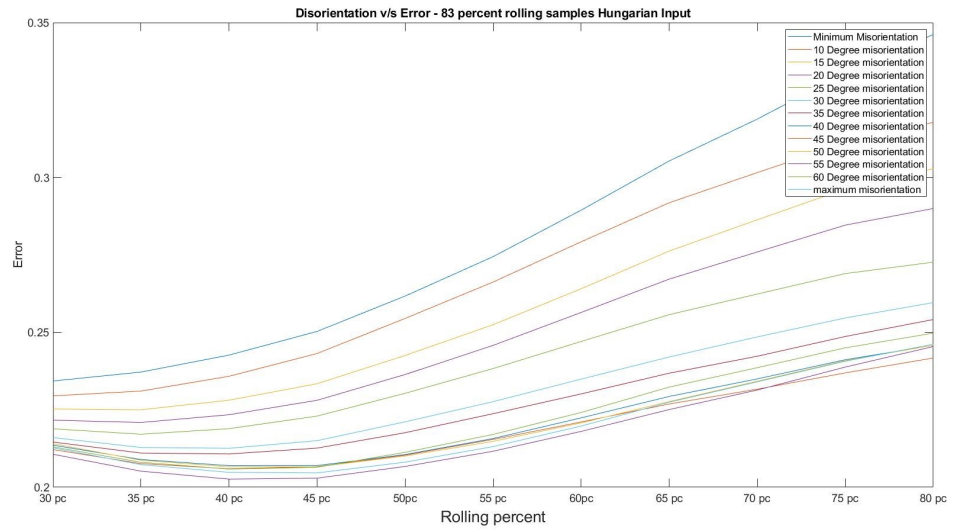


Figure D.3: Disorientation Angle v/s Error Index between 83 Percent Experimental Texture and Hungarian Result

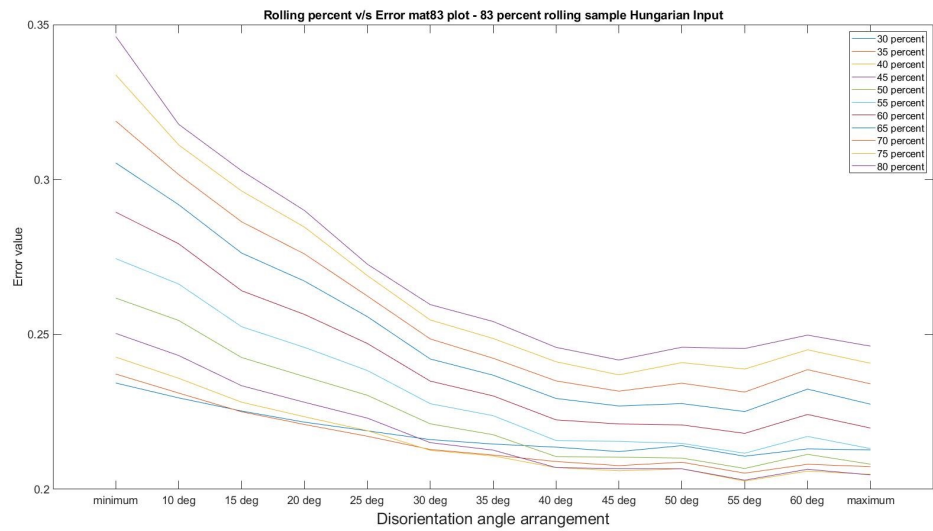


Figure D.4: Rolling Reduction v/s Error Index between 83 Percent Experimental Texture and Hungarian Result

E | HUNGARIAN ALGORITHM TEXTURE INDEX VARIATION

E.1 SERIES 1. ERROR INDEX VARIATION FOR 55 PERCENT SAMPLE

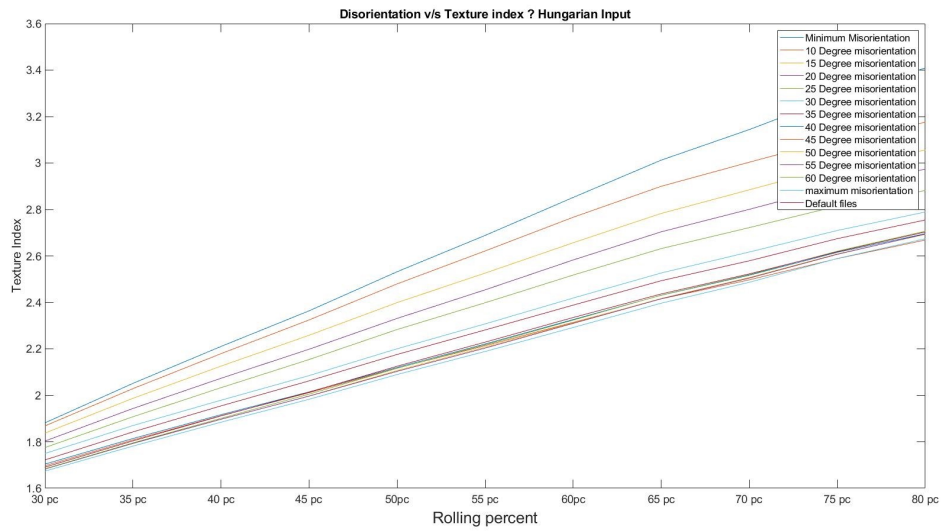


Figure E.1: Disorientation Angle v/s Texture Index, Hungarian Algorithm

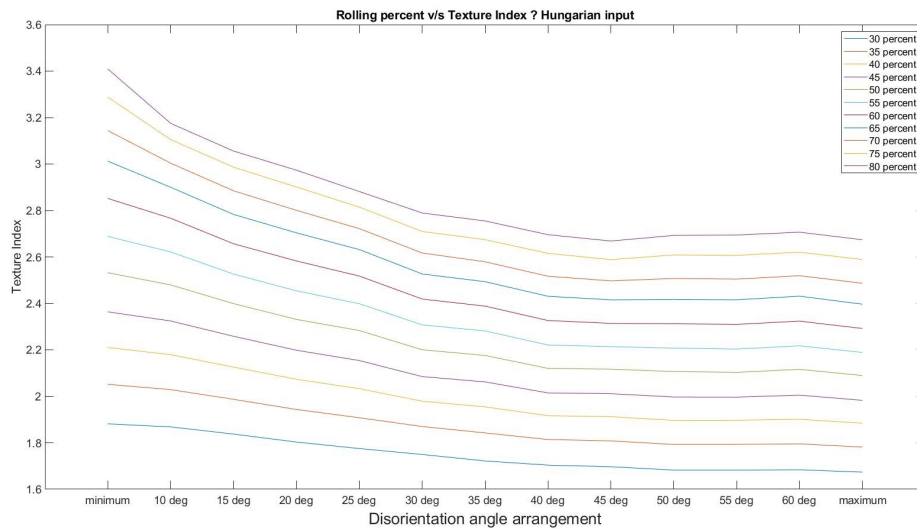


Figure E.2: Rolling Reduction v/s Texture Index, Hungarian Algorithm

F

HUNGARIAN ERROR INDEX VARIATION WITH SIMULATED ORIGINAL TEXTURE SOLUTION

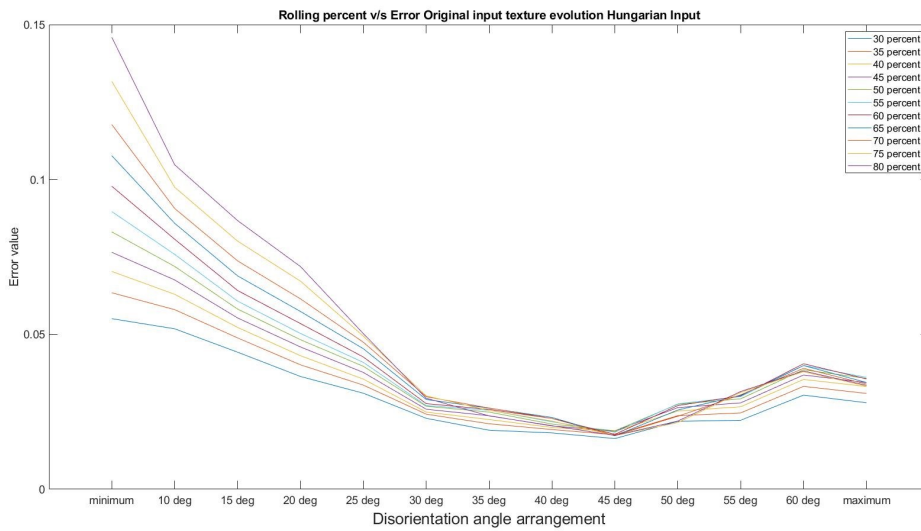


Figure F.1: Rolling Reduction v/s Error Index for difference between original texture evolution and Hungarian Evolution

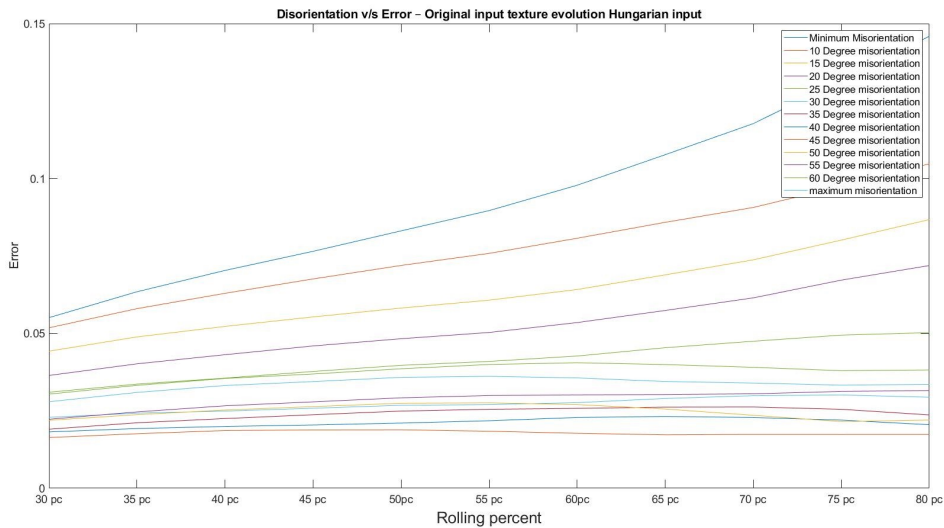


Figure F.2: Disorientation Angle v/s Error Index for difference between original texture evolution and Hungarian Evolution

G

ERROR INDEX COMPARISON BETWEEN HUNGARIAN AND MONTE CARLO SOLUTIONS

G.1 SERIES 1. ROLLING REDUCTION VS ERROR INDEX COMPARISON

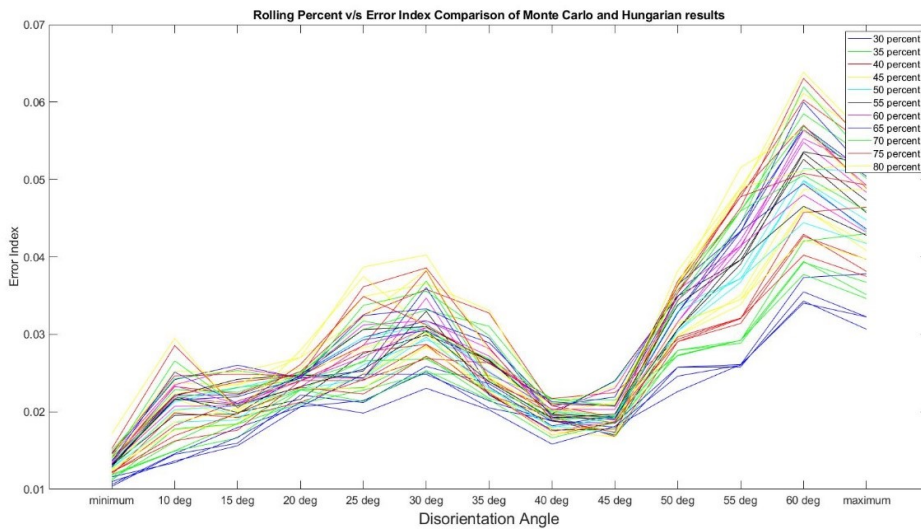


Figure G.1: Rolling Reduction v/s Error Index comparison between Hungarian and Monte Carlo results, All runs

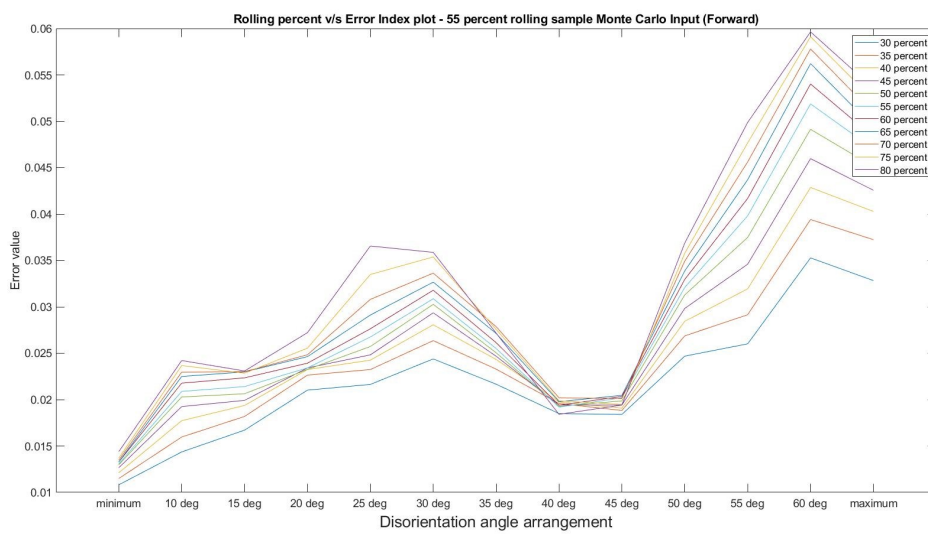


Figure G.2: Rolling Reduction v/s Error Index comparison between Hungarian and Monte Carlo results, Mean value

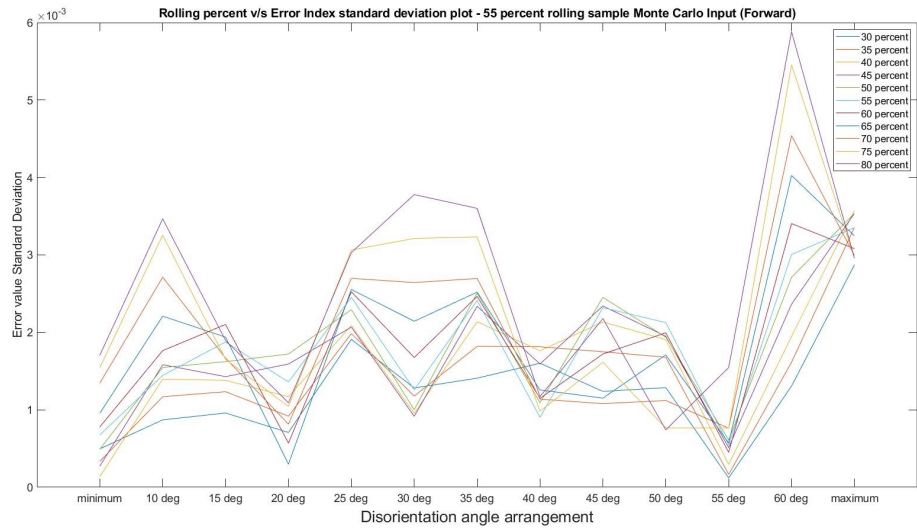


Figure G.3: Rolling Reduction v/s Error Index comparison between Hungarian and Monte Carlo results, Standard Deviation

G.2 SERIES 2. DISORIENTATION ANGLE VS ERROR INDEX COMPARISON

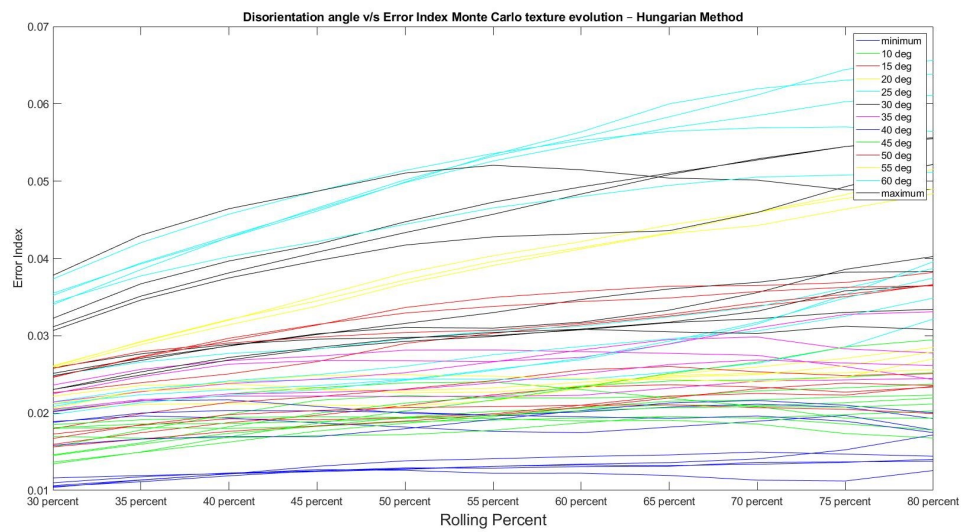


Figure G.4: Disorientation Angle v/s Error Index comparison between Hungarian and Monte Carlo results, All runs

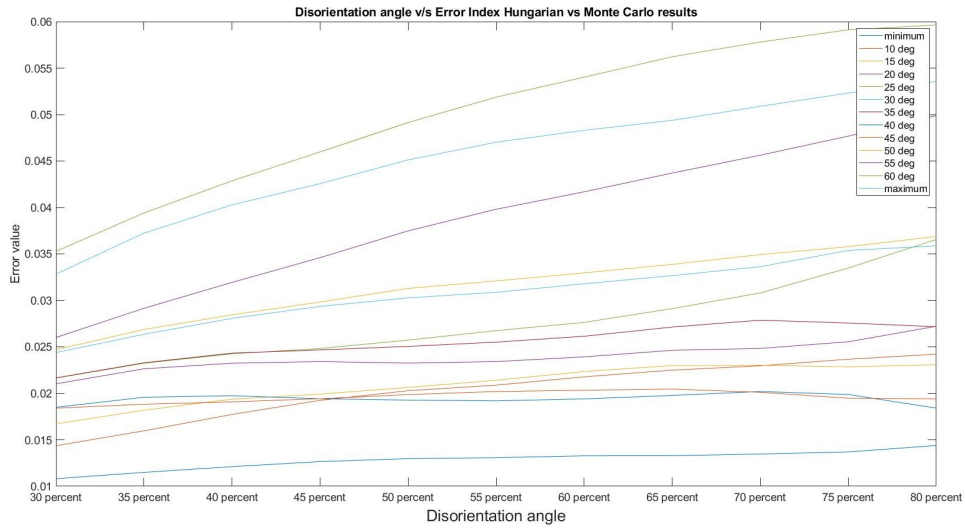


Figure G.5: Disorientation Angle v/s Error Index comparison between Hungarian and Monte Carlo results, mean value

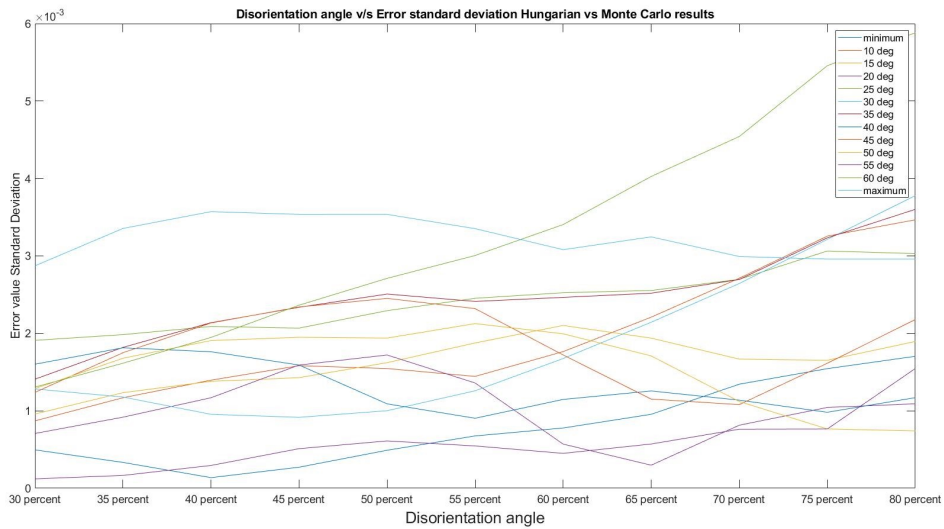


Figure G.6: Disorientation Angle v/s Error Index comparison between Hungarian and Monte Carlo results, Standard Deviation

H

MONTE CARLO ODF FIGURES FOR MAXIMUM STANDARD DEVIATION, 50 DEGREE DISORIENTATION AND 50 PERCENT ROLLING REDUCTION

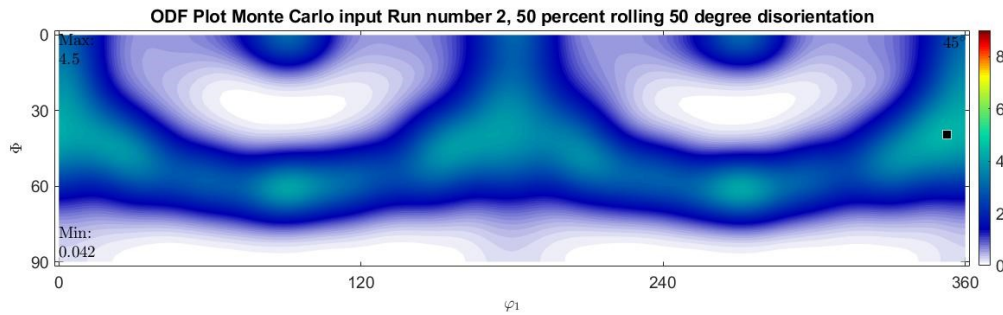


Figure H.1: ODF 50 degree disorientation and 50 percent rolling reduction Run 1

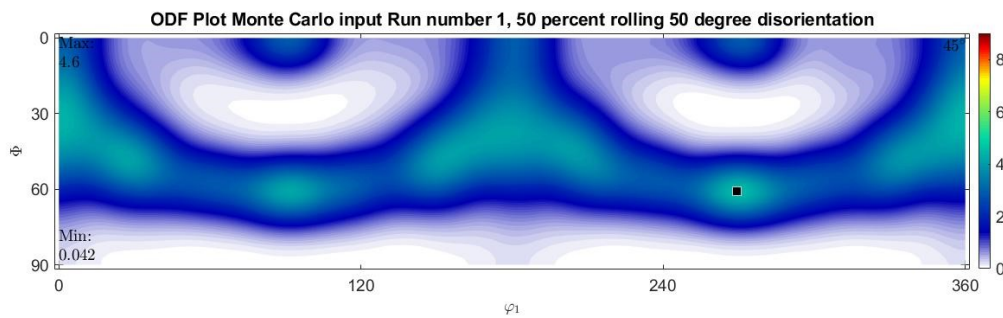


Figure H.2: ODF 50 degree disorientation and 50 percent rolling reduction Run 2

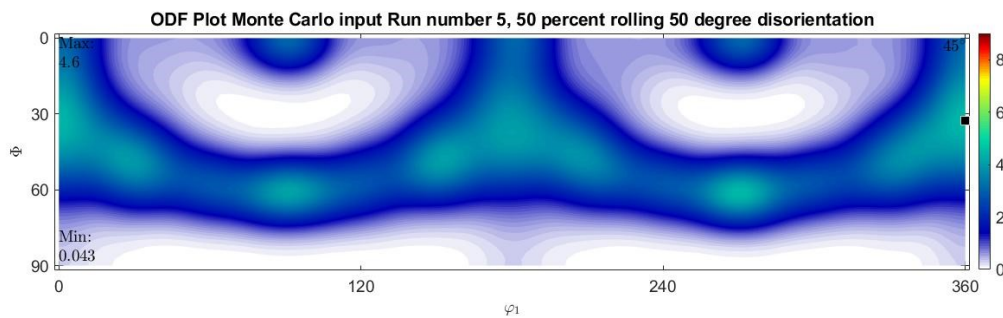


Figure H.3: ODF 50 degree disorientation and 50 percent rolling reduction Run 3

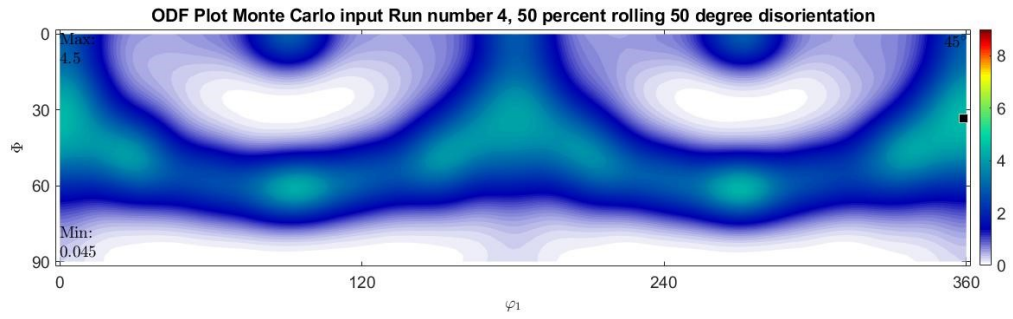


Figure H.4: ODF 50 degree disorientation and 50 percent rolling reduction Run 4

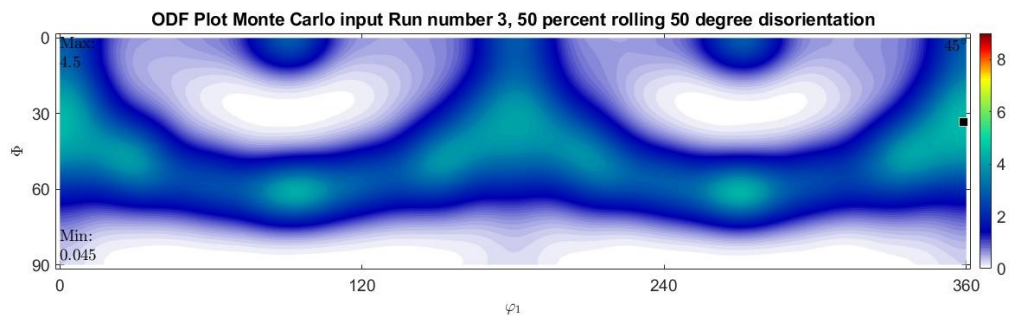


Figure H.5: ODF 50 degree disorientation and 50 percent rolling reduction Run 5

I

VARIATION OF ODF WITH ROLLING REDUCTION WITH DISORIENTATION ANGLE

I.1 SERIES 1. 30 PERCENT ROLLING

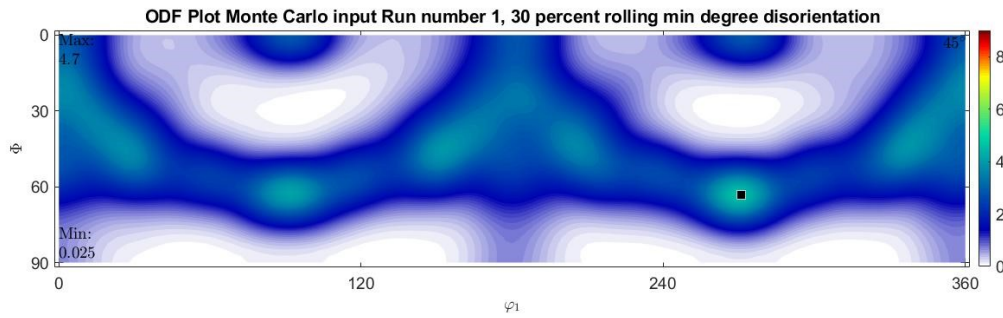


Figure I.1: ODF Plot, Monte Carlo Run 1 30 percent rolling, min disorientation

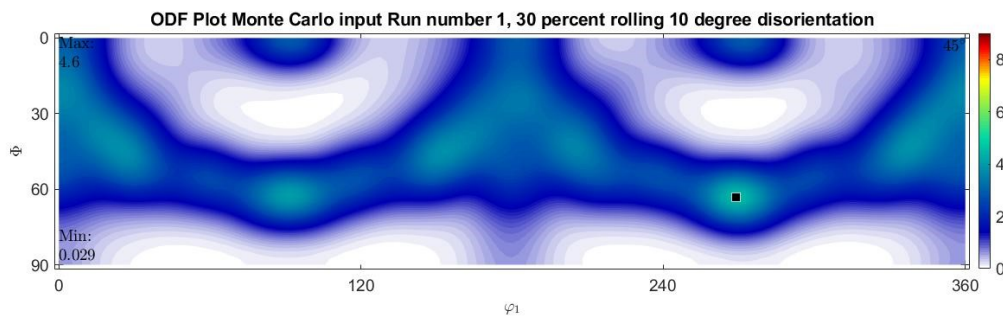


Figure I.2: ODF Plot, Monte Carlo Run 1 30 percent rolling, 10 degree disorientation

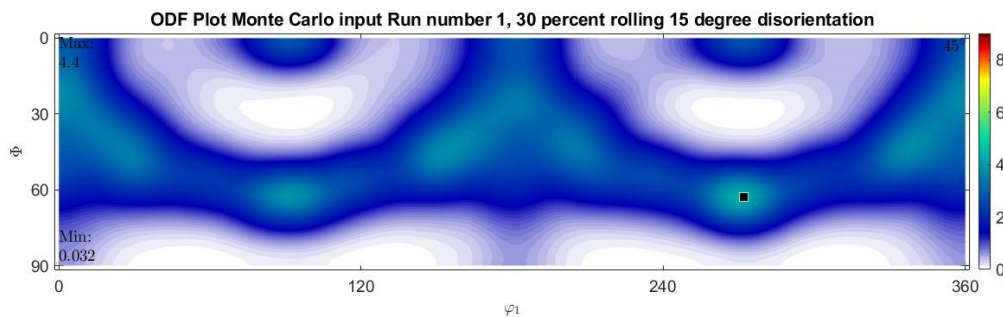


Figure I.3: ODF Plot, Monte Carlo Run 1 30 percent rolling, 15 degree disorientation

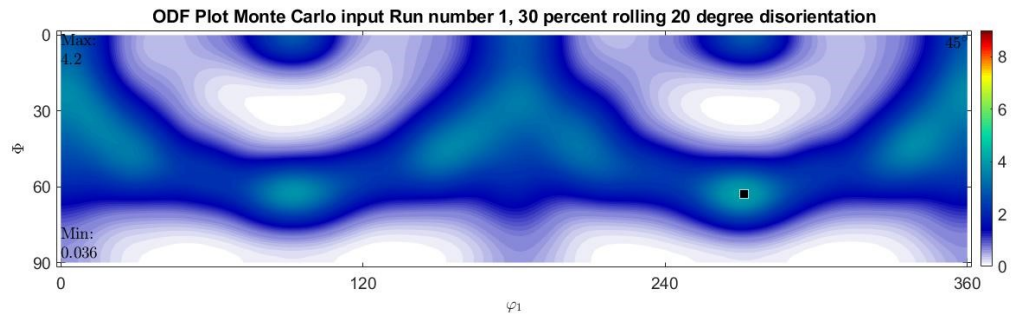


Figure I.4: ODF Plot, Monte Carlo Run 1 30 percent rolling, 20 degree disorientation

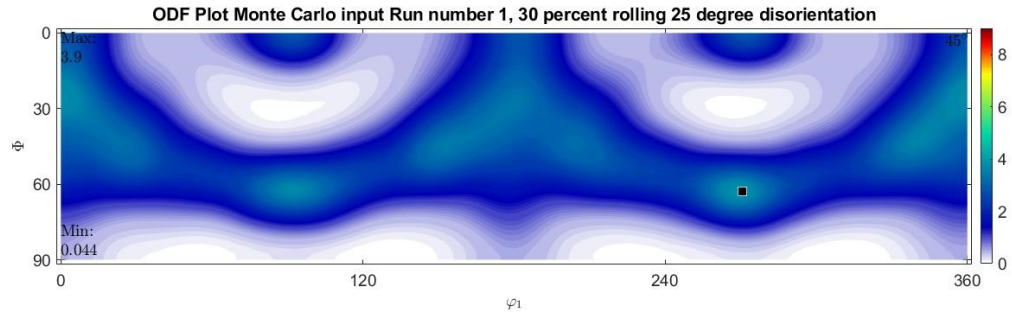


Figure I.5: ODF Plot, Monte Carlo Run 1 30 percent rolling, 25 degree disorientation

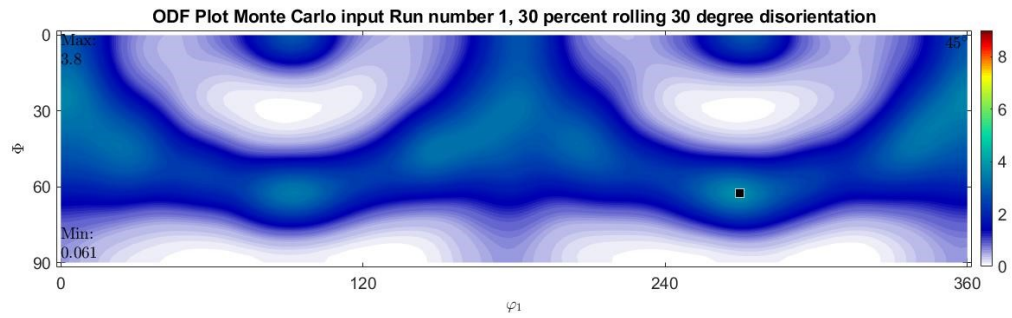


Figure I.6: ODF Plot, Monte Carlo Run 1 30 percent rolling, 30 degree disorientation

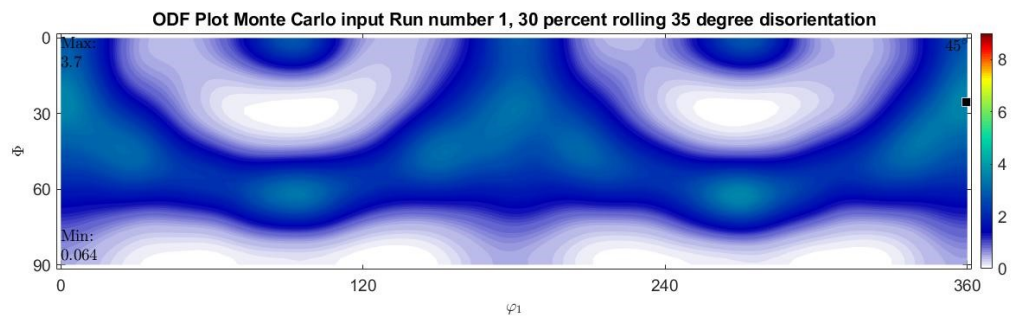


Figure I.7: ODF Plot, Monte Carlo Run 1 30 percent rolling, 35 degree disorientation

1.2 SERIES 2. 50 PERCENT ROLLING

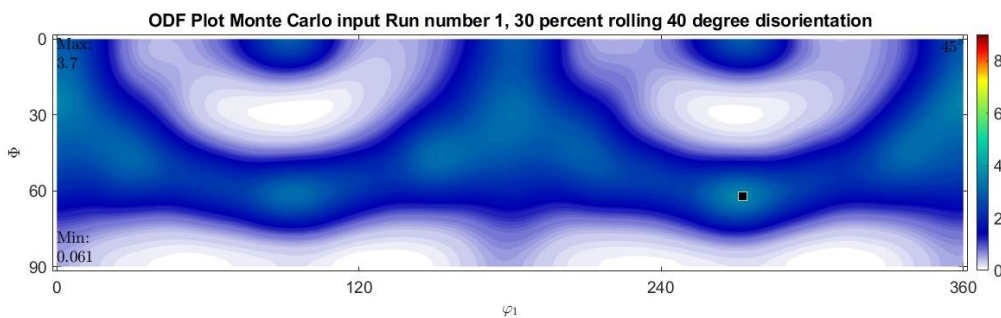


Figure I.8: ODF Plot, Monte Carlo Run 1 30 percent rolling, 40 degree disorientation

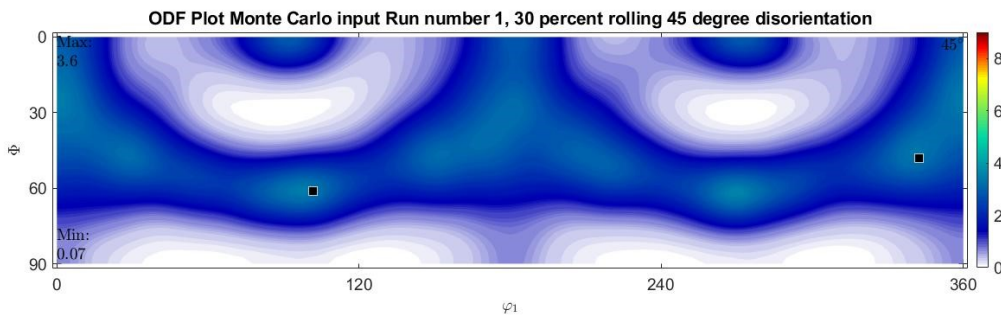


Figure I.9: ODF Plot, Monte Carlo Run 1 30 percent rolling, 45 degree disorientation

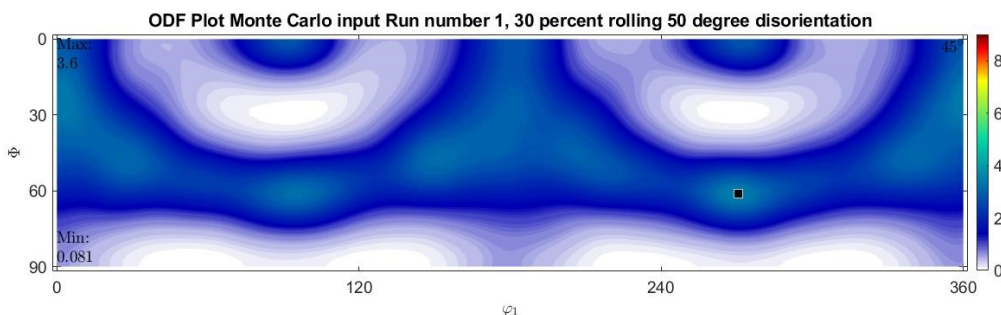


Figure I.10: ODF Plot, Monte Carlo Run 1 30 percent rolling, 50 degree disorientation

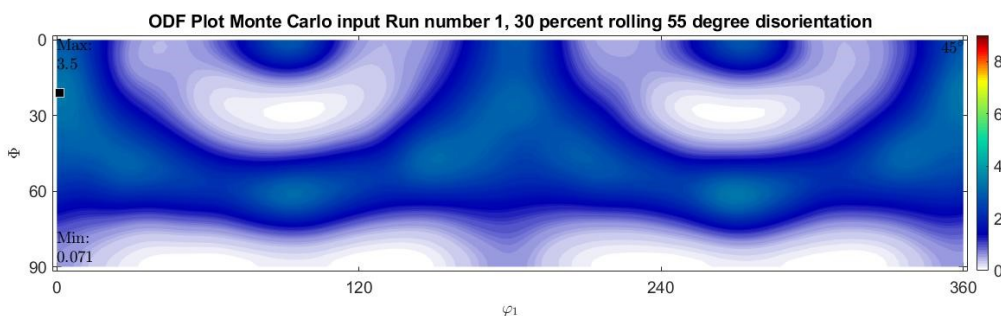


Figure I.11: ODF Plot, Monte Carlo Run 1 30 percent rolling, 55 degree disorientation

I.3 SERIES 3. 80 PERCENT ROLLING

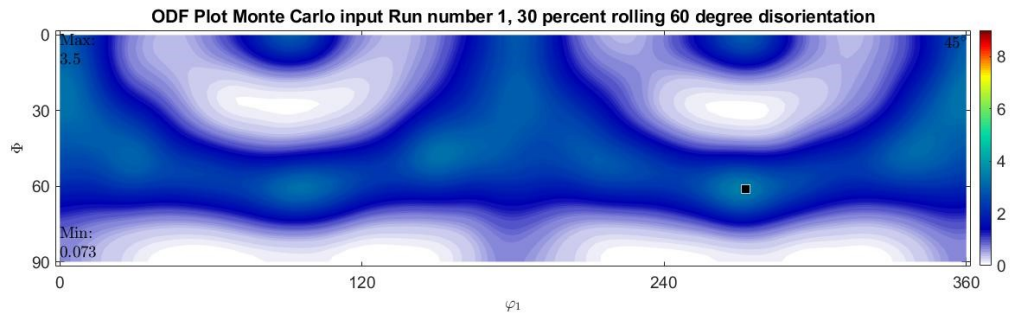


Figure I.12: ODF Plot, Monte Carlo Run 1 30 percent rolling, 60 degree disorientation

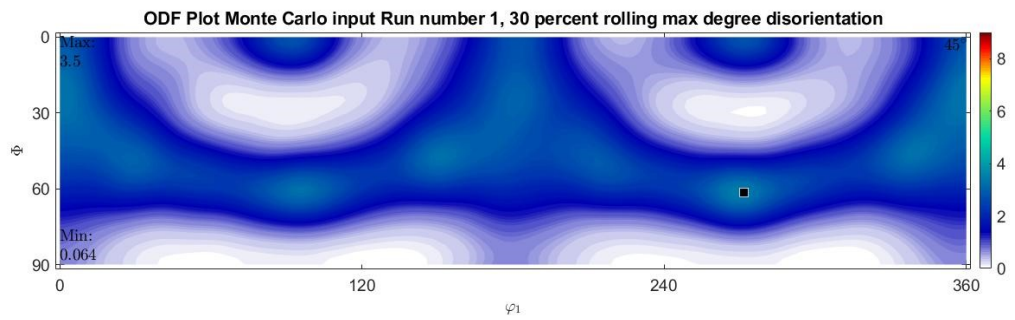


Figure I.13: ODF Plot, Monte Carlo Run 1 30 percent rolling, max disorientation

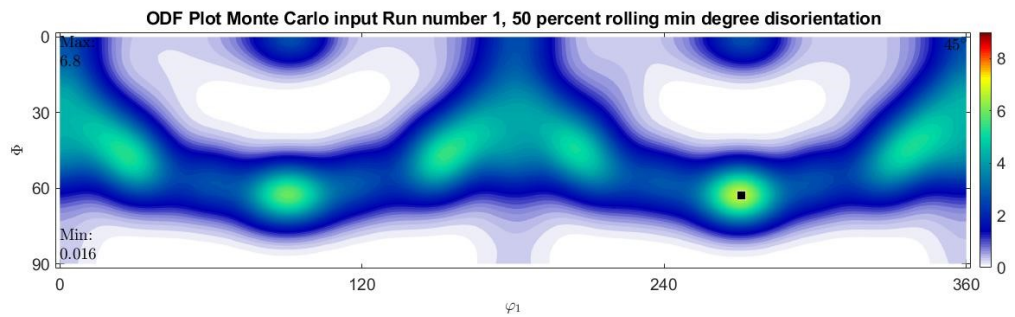


Figure I.14: ODF Plot, Monte Carlo Run 1 50 percent rolling, min disorientation

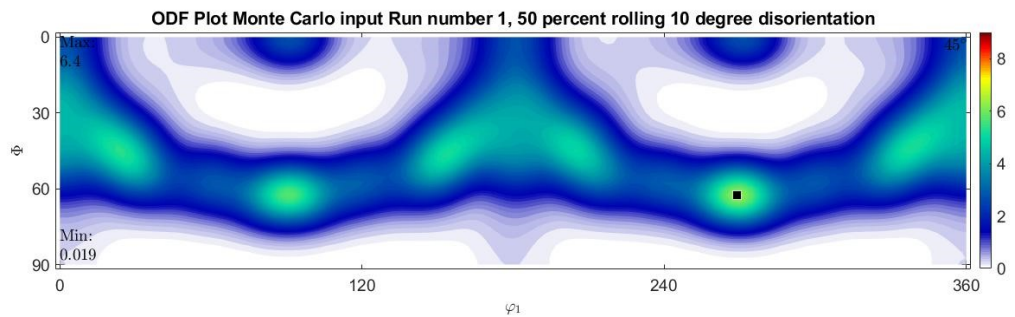


Figure I.15: ODF Plot, Monte Carlo Run 1 50 percent rolling, 10 degree disorientation

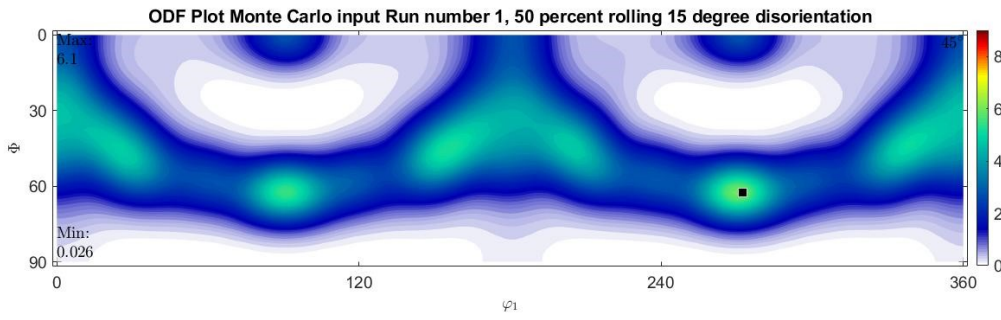


Figure I.16: ODF Plot, Monte Carlo Run 1 50 percent rolling, 15 degree disorientation

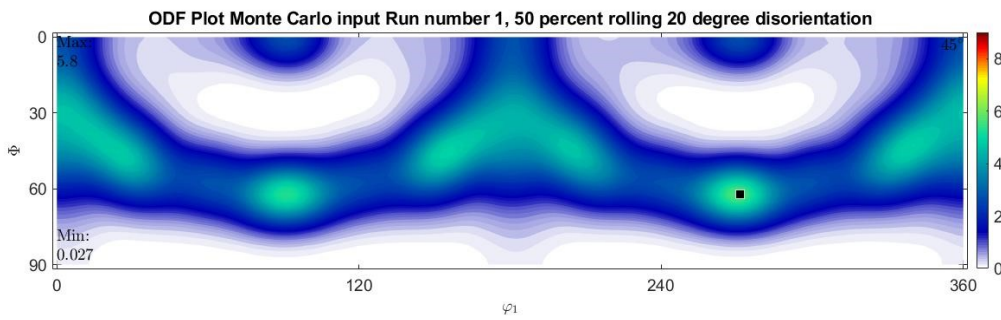


Figure I.17: ODF Plot, Monte Carlo Run 1 50 percent rolling, 20 degree disorientation

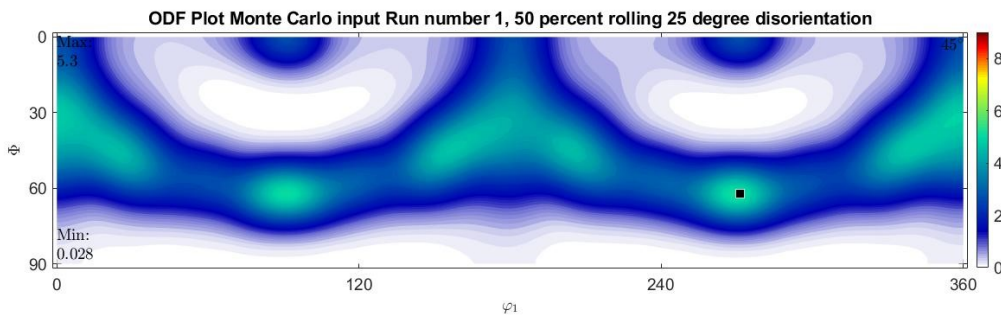


Figure I.18: ODF Plot, Monte Carlo Run 1 50 percent rolling, 25 degree disorientation

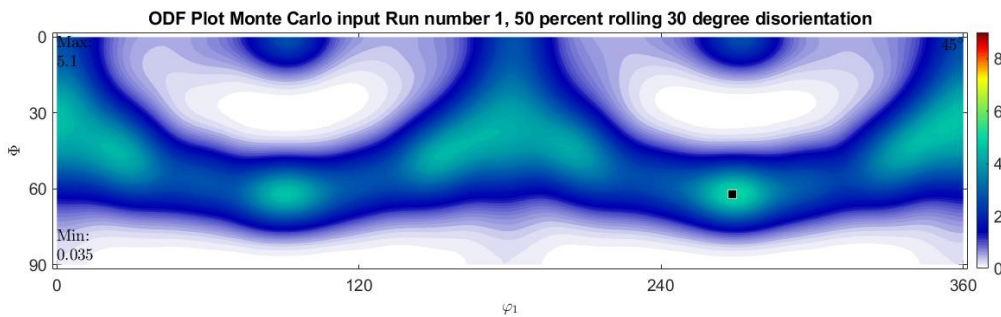


Figure I.19: ODF Plot, Monte Carlo Run 1 50 percent rolling, 30 degree disorientation

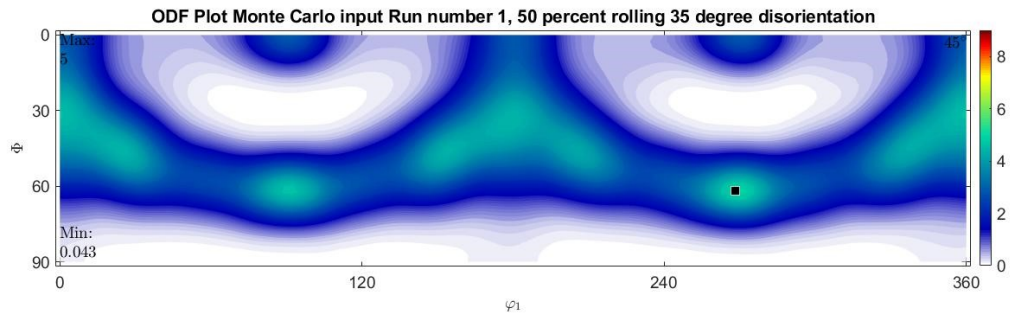


Figure 1.20: ODF Plot, Monte Carlo Run 1 50 percent rolling, 35 degree disorientation

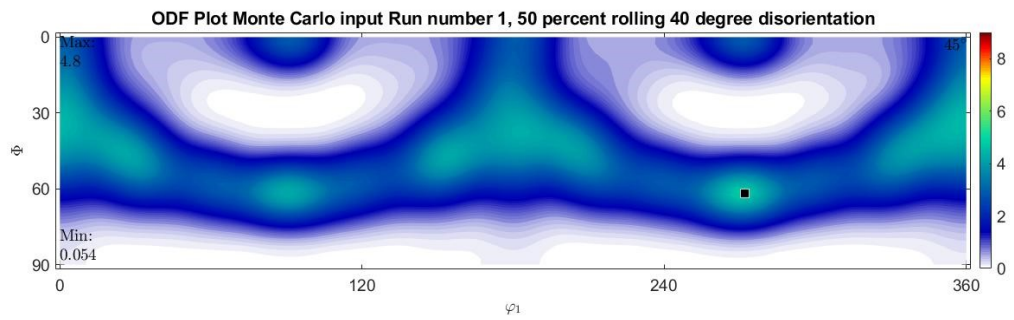


Figure 1.21: ODF Plot, Monte Carlo Run 1 50 percent rolling, 40 degree disorientation

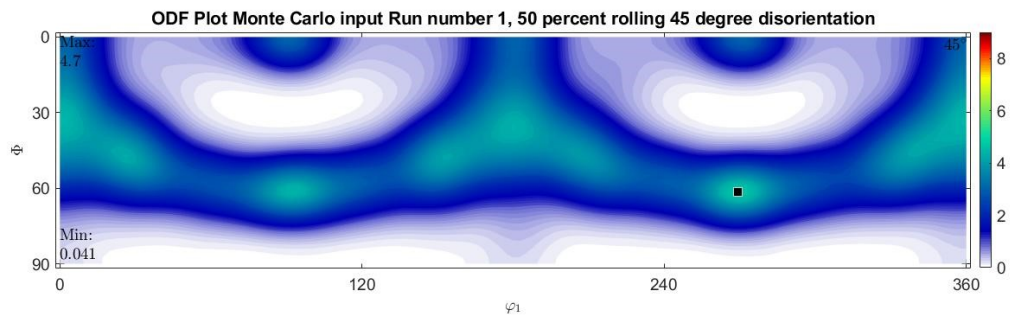


Figure 1.22: ODF Plot, Monte Carlo Run 1 50 percent rolling, 45 degree disorientation

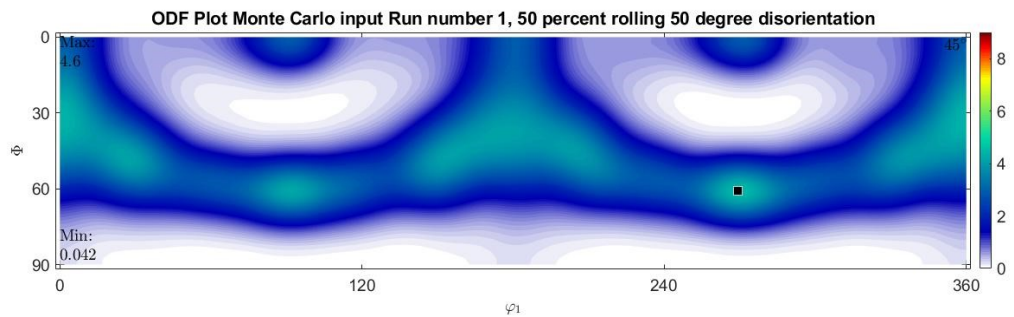


Figure 1.23: ODF Plot, Monte Carlo Run 1 50 percent rolling, 50 degree disorientation

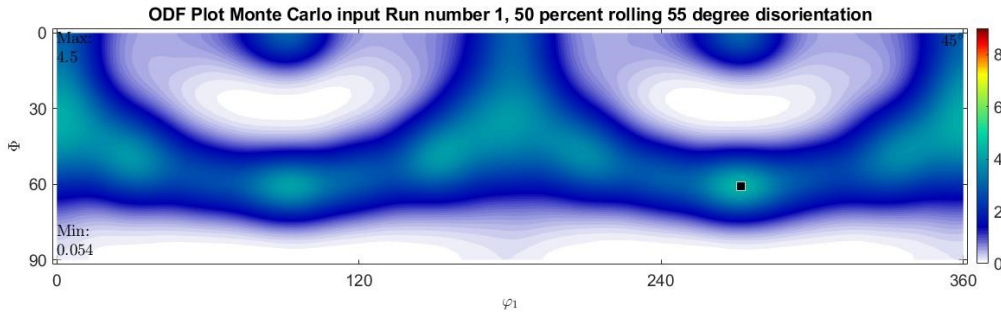


Figure I.24: ODF Plot, Monte Carlo Run 1 50 percent rolling, 55 degree disorientation

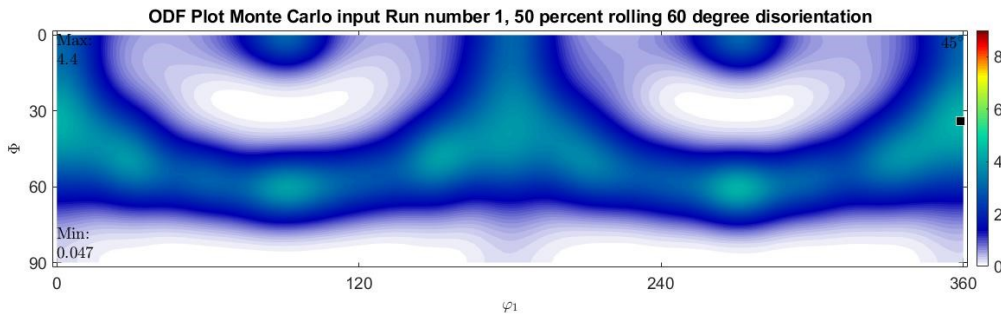


Figure I.25: ODF Plot, Monte Carlo Run 1 50 percent rolling, 60 degree disorientation

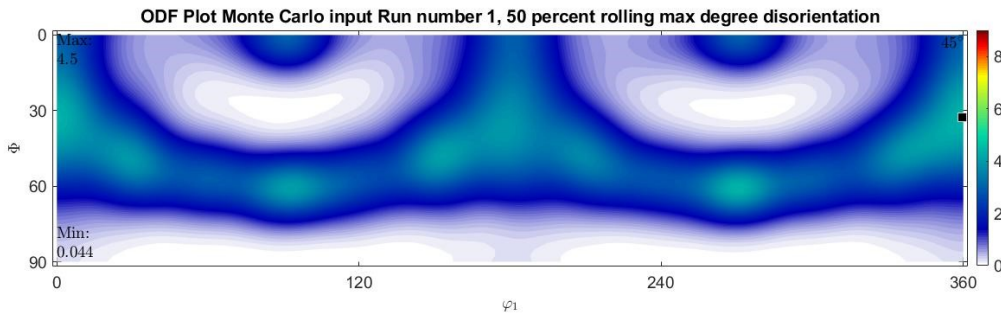


Figure I.26: ODF Plot, Monte Carlo Run 1 50 percent rolling, max disorientation

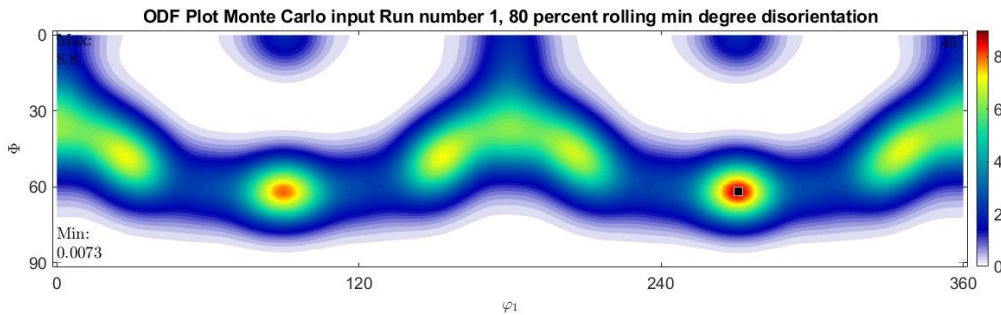


Figure I.27: ODF Plot, Monte Carlo Run 1 80 percent rolling, min disorientation

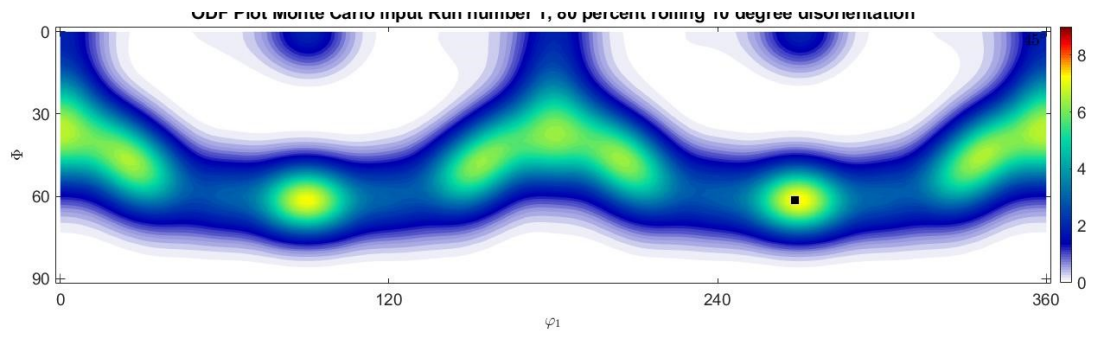


Figure I.28: ODF Plot, Monte Carlo Run 1 80 percent rolling, 10 degree disorientation

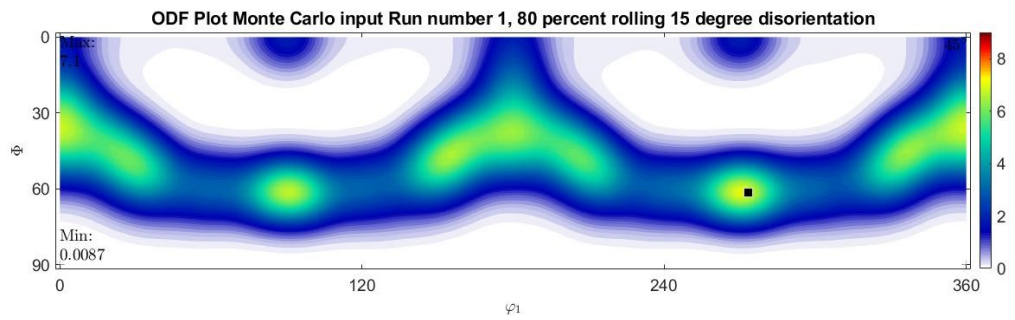


Figure I.29: ODF Plot, Monte Carlo Run 1 80 percent rolling, 15 degree disorientation

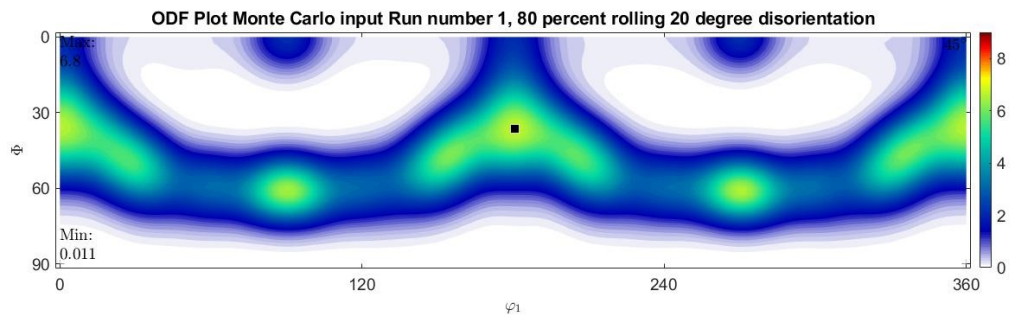


Figure I.30: ODF Plot, Monte Carlo Run 1 80 percent rolling, 20 degree disorientation

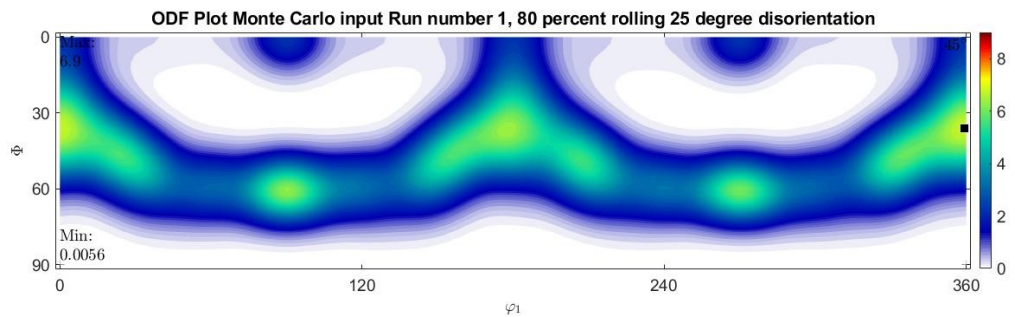


Figure I.31: ODF Plot, Monte Carlo Run 1 80 percent rolling, 25 degree disorientation

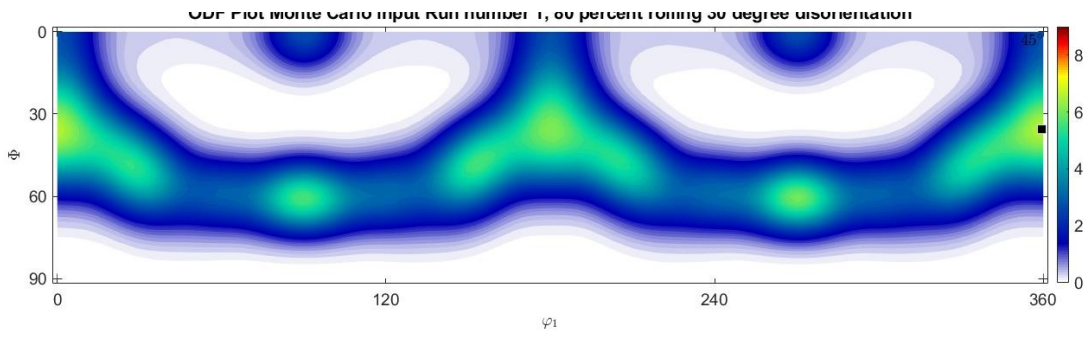


Figure I.32: ODF Plot, Monte Carlo Run 1 80 percent rolling, 30 degree disorientation

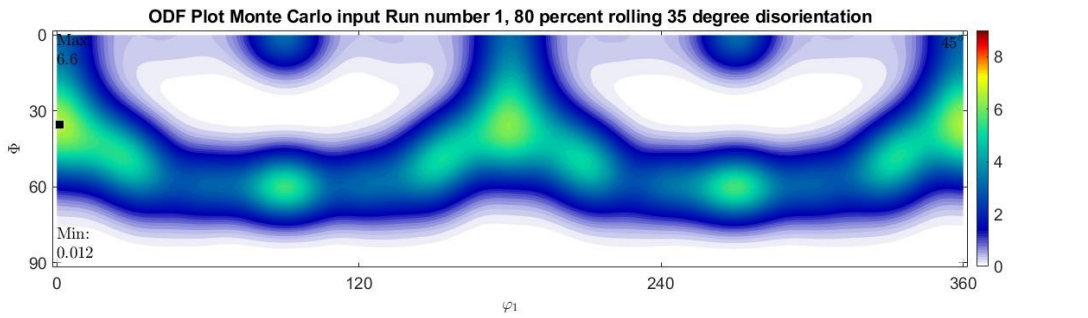


Figure I.33: ODF Plot, Monte Carlo Run 1 80 percent rolling, 35 degree disorientation

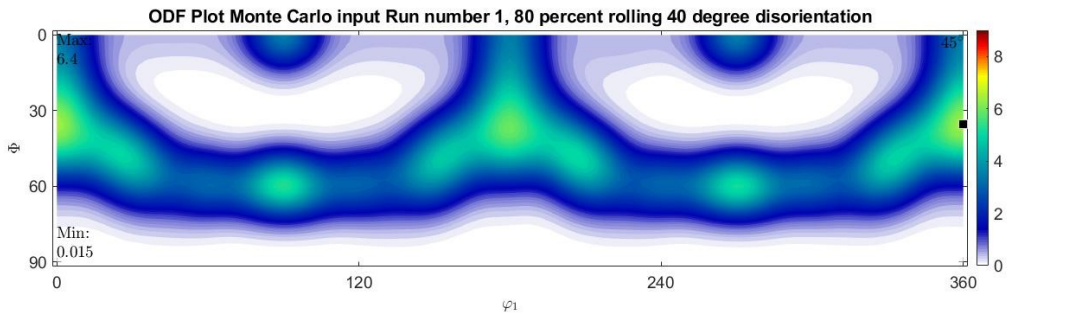


Figure I.34: ODF Plot, Monte Carlo Run 1 80 percent rolling, 40 degree disorientation

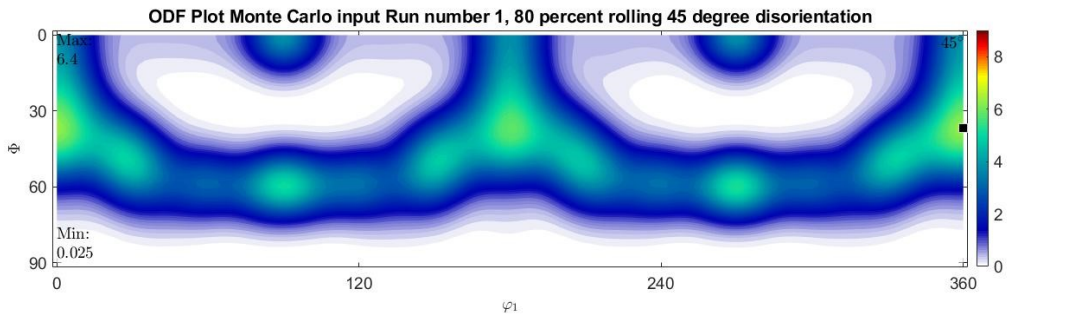


Figure I.35: ODF Plot, Monte Carlo Run 1 80 percent rolling, 45 degree disorientation

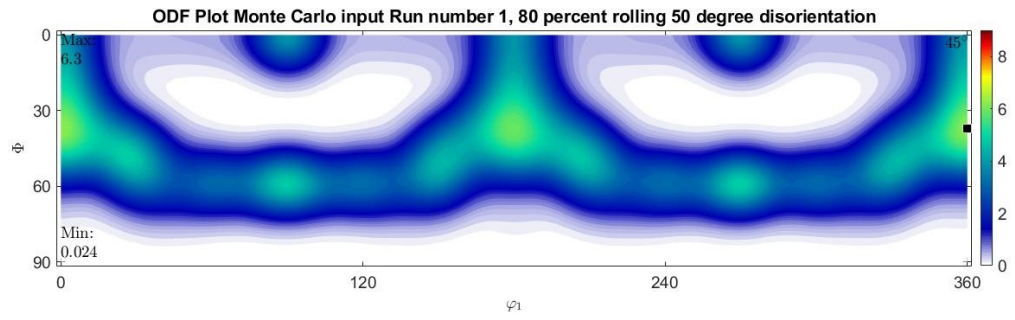


Figure I.36: ODF Plot, Monte Carlo Run 1 80 percent rolling, 50 degree disorientation

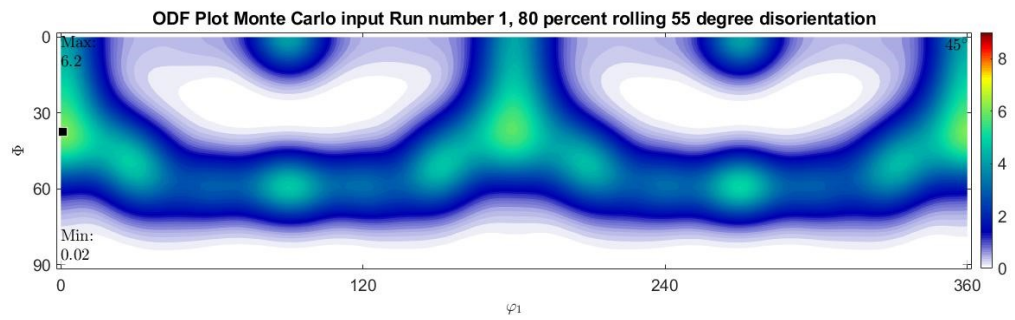


Figure I.37: ODF Plot, Monte Carlo Run 1 80 percent rolling, 55 degree disorientation

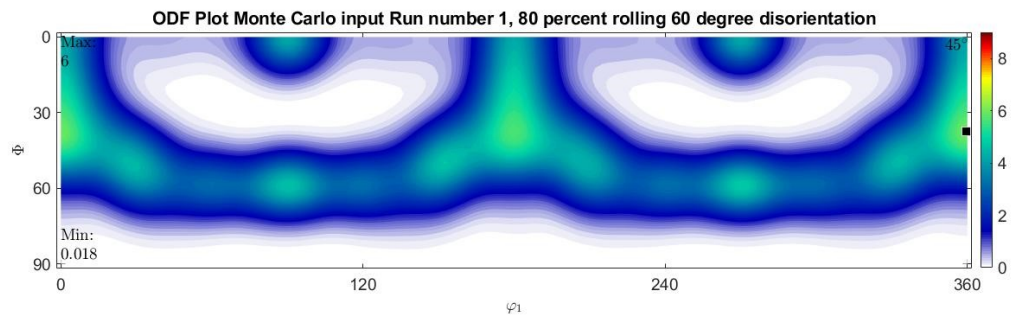


Figure I.38: ODF Plot, Monte Carlo Run 1 80 percent rolling, 60 degree disorientation

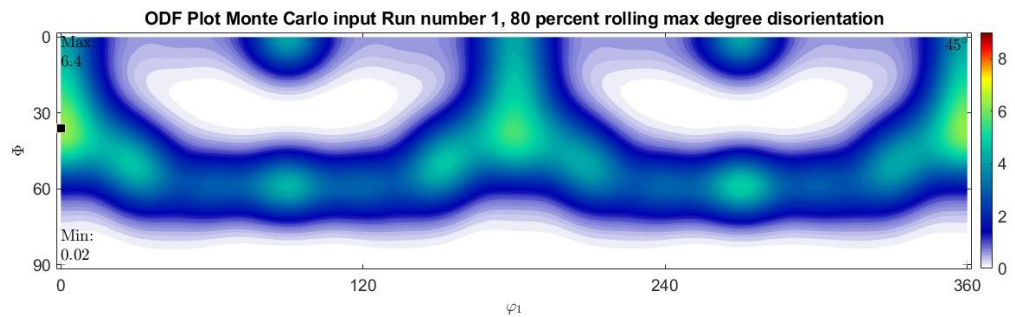


Figure I.39: ODF Plot, Monte Carlo Run 1 80 percent rolling, max disorientation

J | VARIATION OF ODF WITH DISORIENTATION ANGLE

J.1 SERIES 1: MINIMUM DISORIENTATION ANGLE

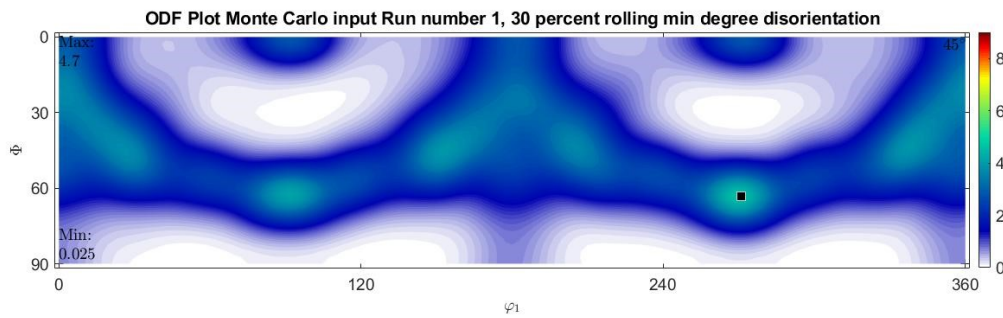


Figure J.1: ODF Plot, Monte Carlo Run 1 30 percent rolling, min disorientation

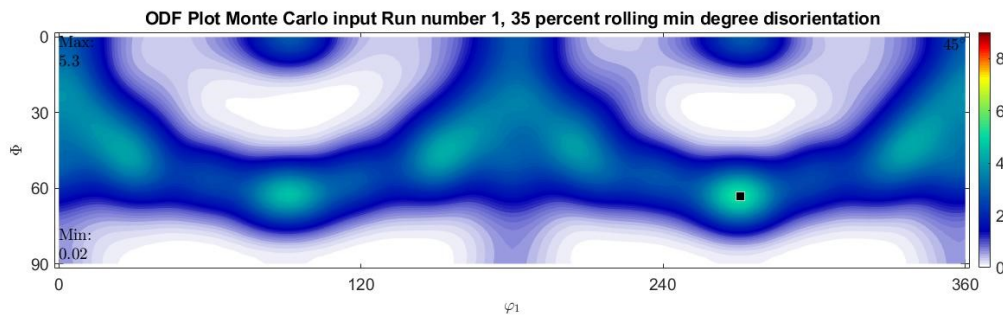


Figure J.2: ODF Plot, Monte Carlo Run 1 35 percent rolling, min disorientation

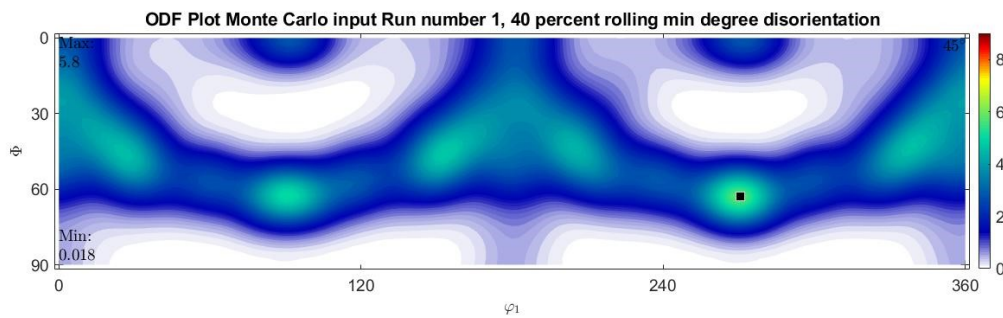


Figure J.3: ODF Plot, Monte Carlo Run 1 40 percent rolling, min disorientation

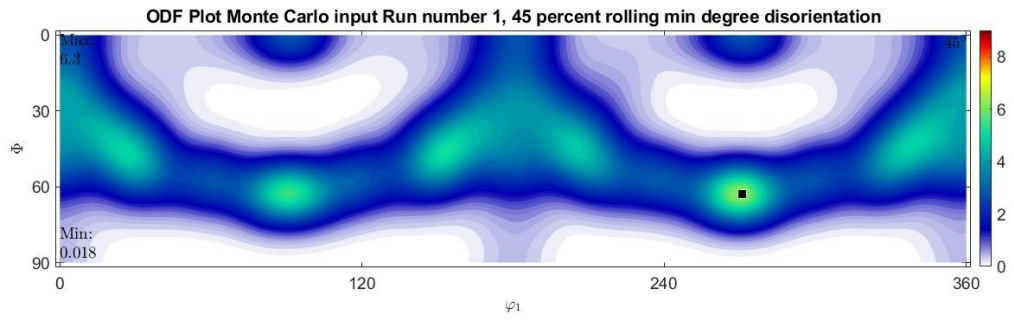


Figure J.4: ODF Plot, Monte Carlo Run 1 45 percent rolling, min disorientation

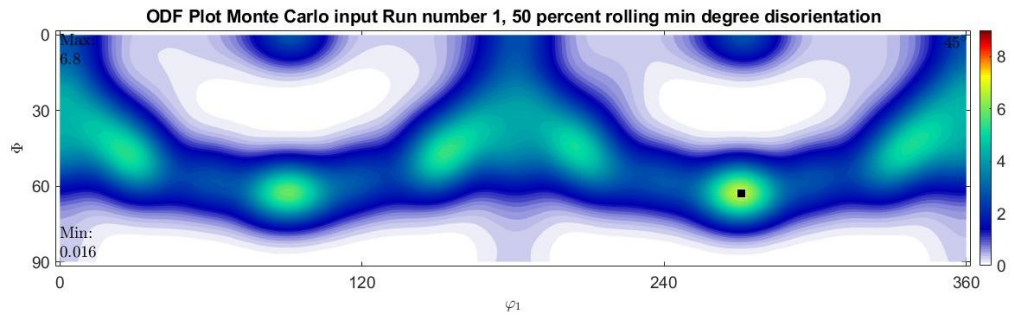


Figure J.5: ODF Plot, Monte Carlo Run 1 50 percent rolling, min disorientation

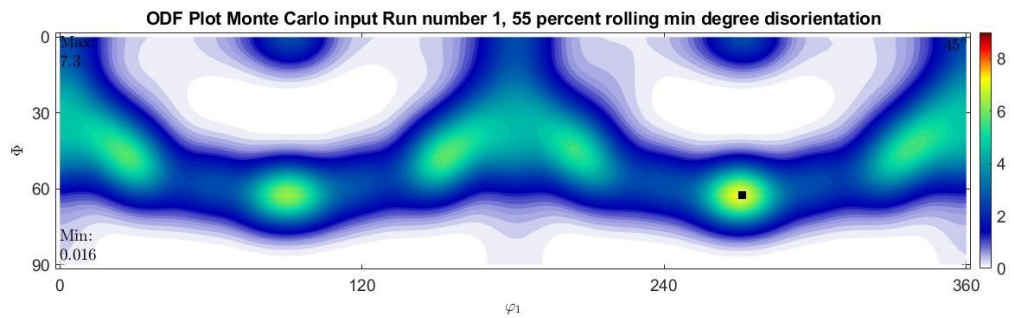


Figure J.6: ODF Plot, Monte Carlo Run 1 55 percent rolling, min disorientation

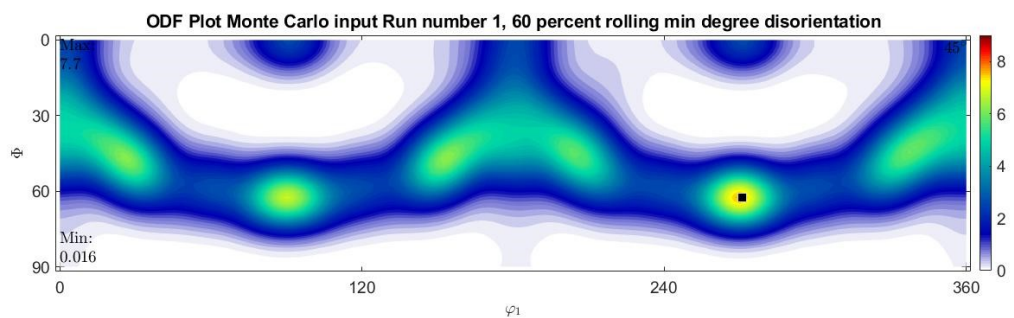


Figure J.7: ODF Plot, Monte Carlo Run 1 60 percent rolling, min disorientation

J.2 SERIES 1: 20 DEGREE DISORIENTATION ANGLE

J.3 SECTION 3 : 55 DEGREE DISORIENTATION

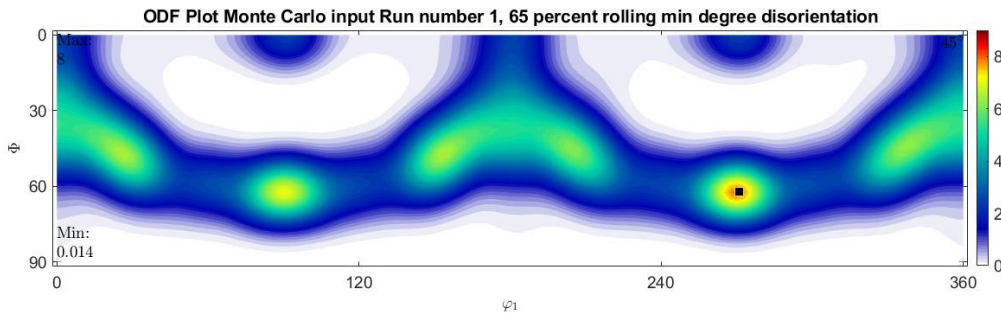


Figure J.8: ODF Plot, Monte Carlo Run 1 65 percent rolling, min disorientation

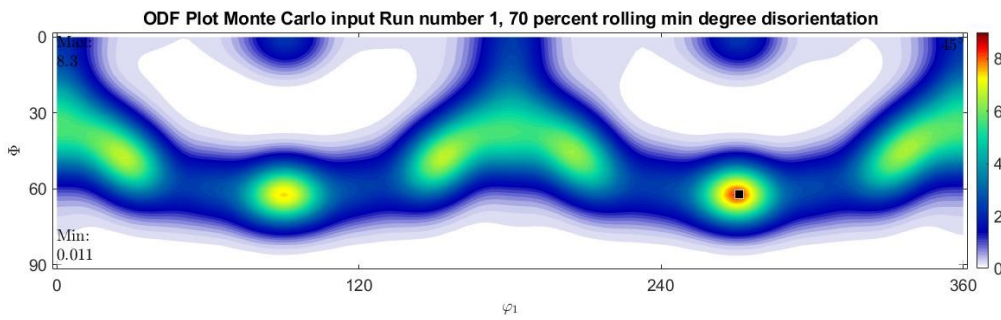


Figure J.9: ODF Plot, Monte Carlo Run 1 70 percent rolling, min disorientation

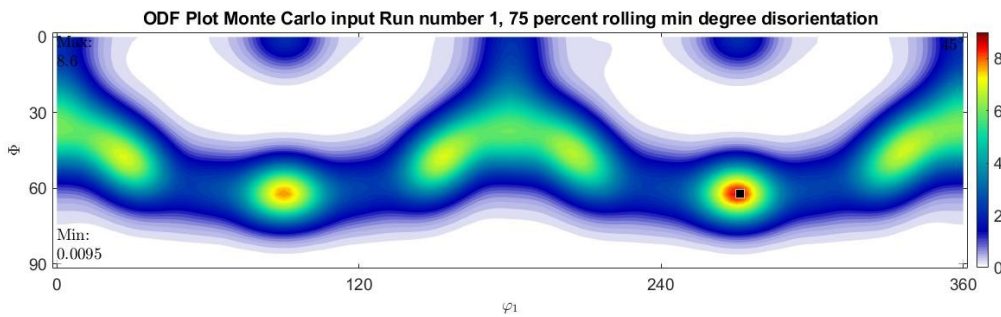


Figure J.10: ODF Plot, Monte Carlo Run 1 75 percent rolling, min disorientation

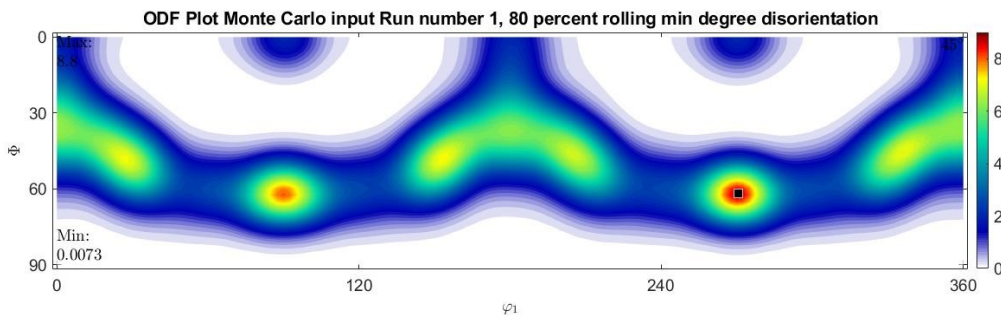


Figure J.11: ODF Plot, Monte Carlo Run 1 80 percent rolling, min disorientation

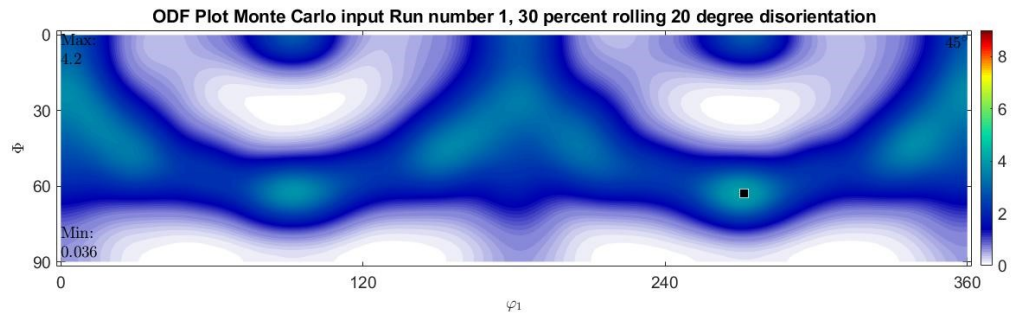


Figure J.12: ODF Plot, Monte Carlo Run 1 30 percent rolling, 20 degree disorientation

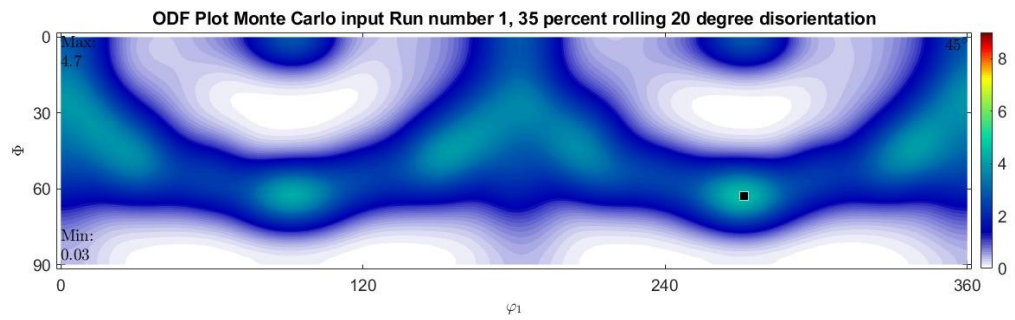


Figure J.13: ODF Plot, Monte Carlo Run 1 35 percent rolling, 20 degree disorientation

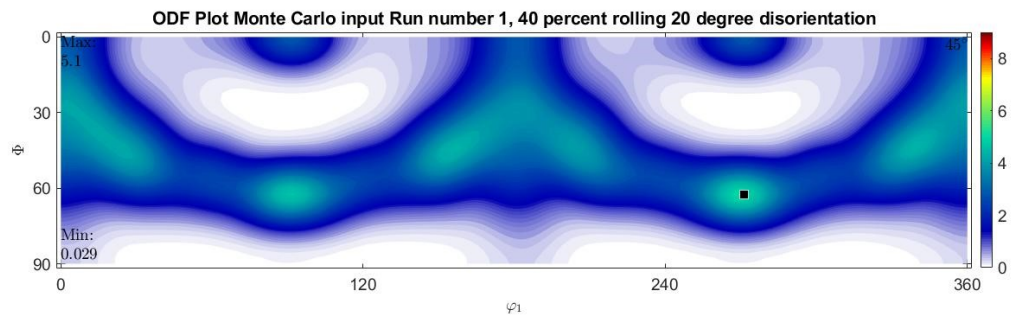


Figure J.14: ODF Plot, Monte Carlo Run 1 40 percent rolling, 20 degree disorientation

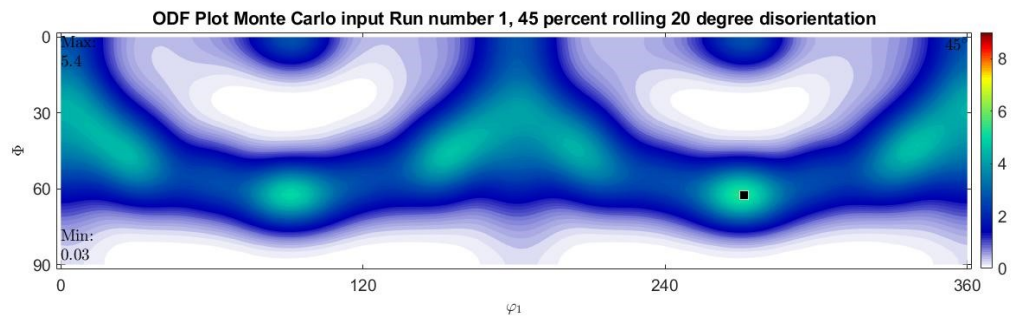


Figure J.15: ODF Plot, Monte Carlo Run 1 45 percent rolling, 20 degree disorientation

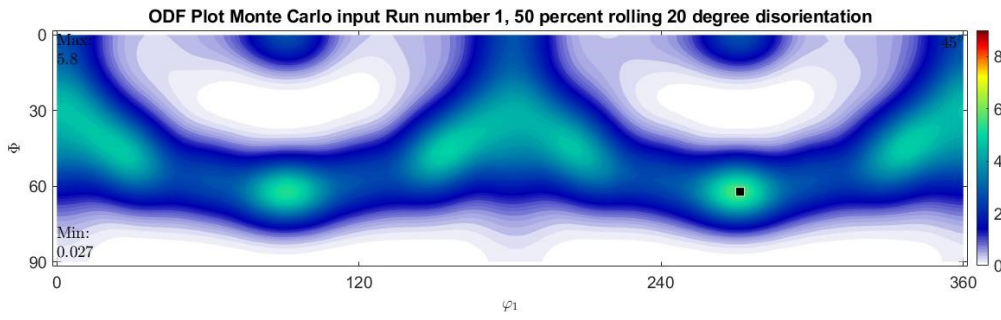


Figure J.16: ODF Plot, Monte Carlo Run 1 50 percent rolling, 20 degree disorientation

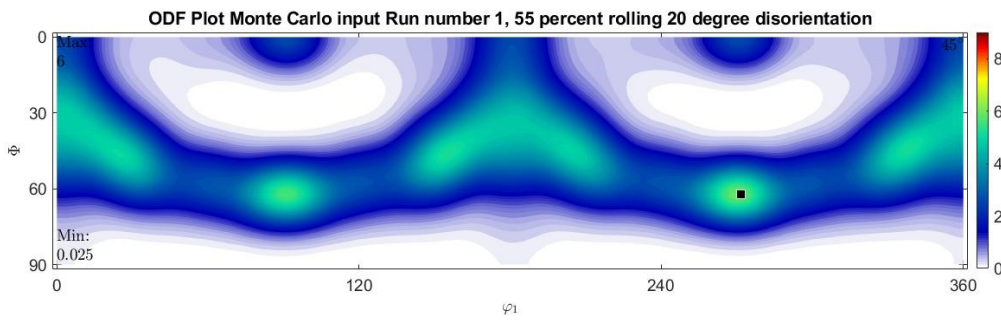


Figure J.17: ODF Plot, Monte Carlo Run 1 55 percent rolling, 20 degree disorientation

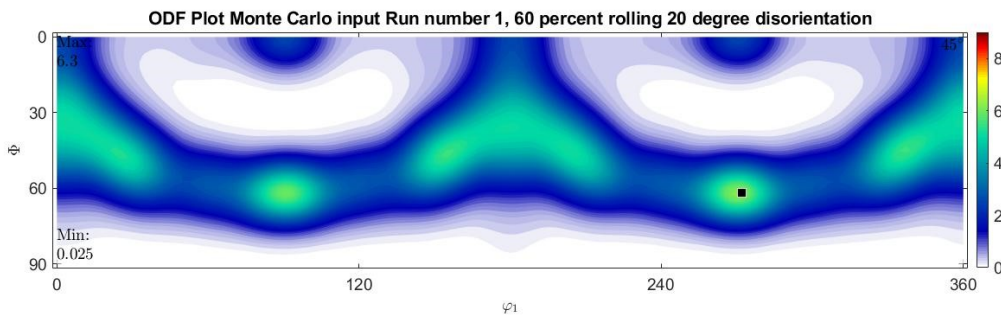


Figure J.18: ODF Plot, Monte Carlo Run 1 60 percent rolling, 20 degree disorientation

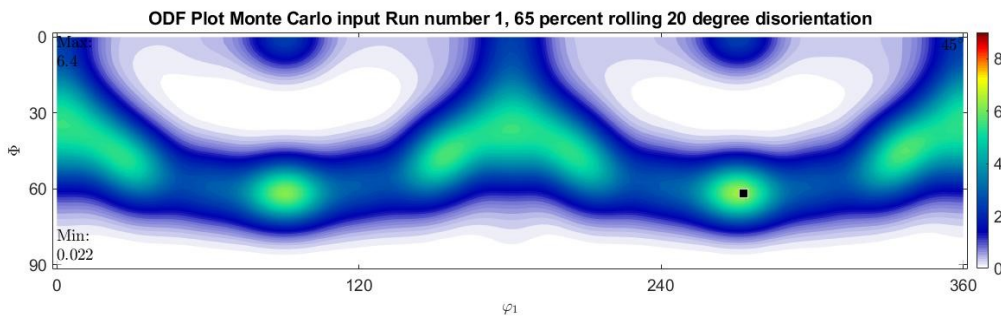


Figure J.19: ODF Plot, Monte Carlo Run 1 65 percent rolling, 20 degree disorientation

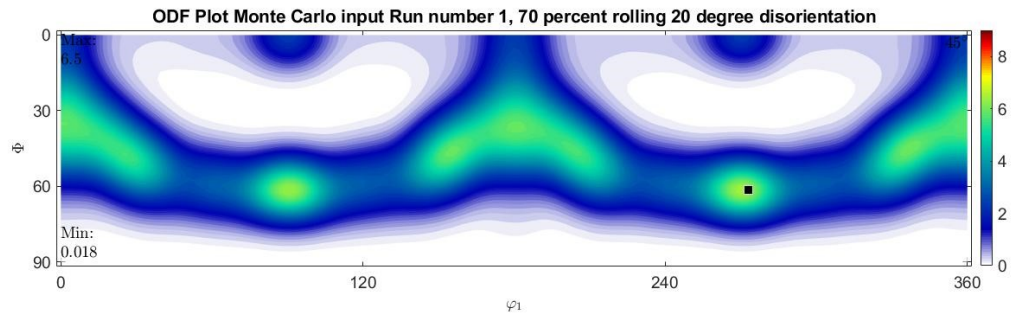


Figure J.20: ODF Plot, Monte Carlo Run 1 70 percent rolling, 20 degree disorientation

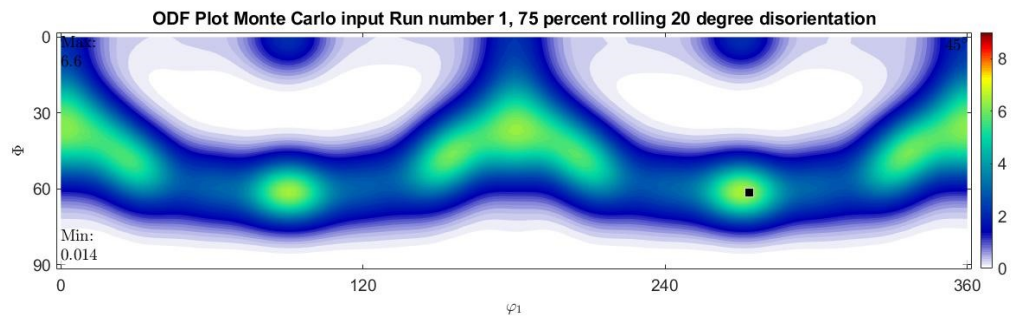


Figure J.21: ODF Plot, Monte Carlo Run 1 75 percent rolling, 20 degree disorientation

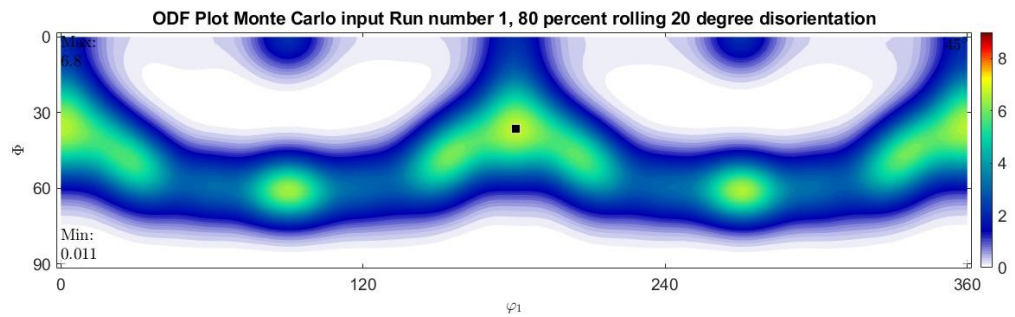


Figure J.22: ODF Plot, Monte Carlo Run 1 80 percent rolling, 20 degree disorientation

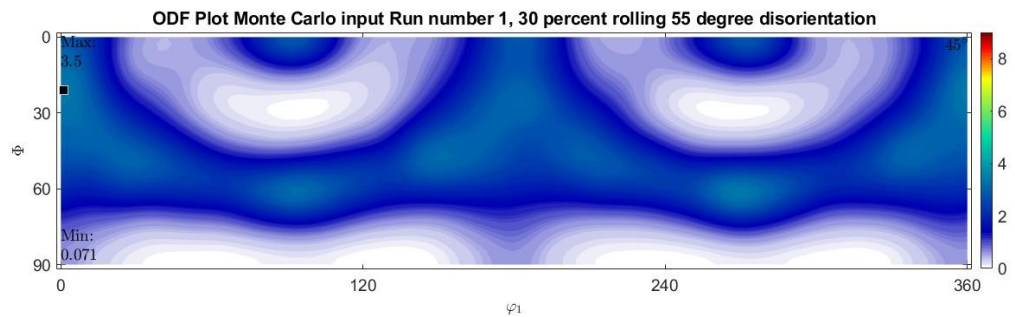


Figure J.23: ODF Plot, Monte Carlo Run 1 30 percent rolling, 55 degree disorientation

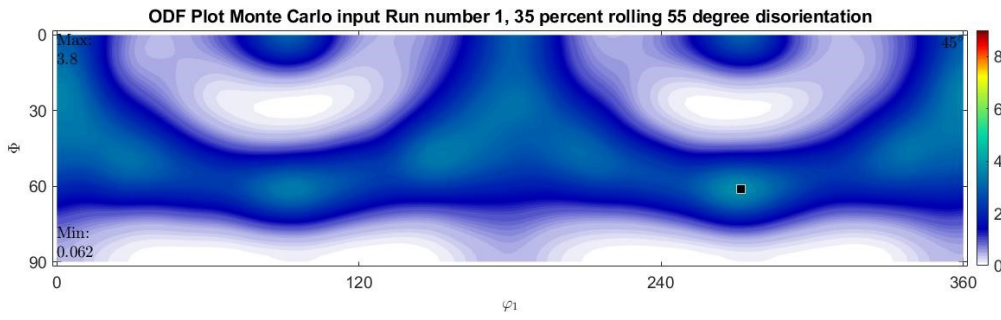


Figure J.24: ODF Plot, Monte Carlo Run 1 35 percent rolling, 55 degree disorientation

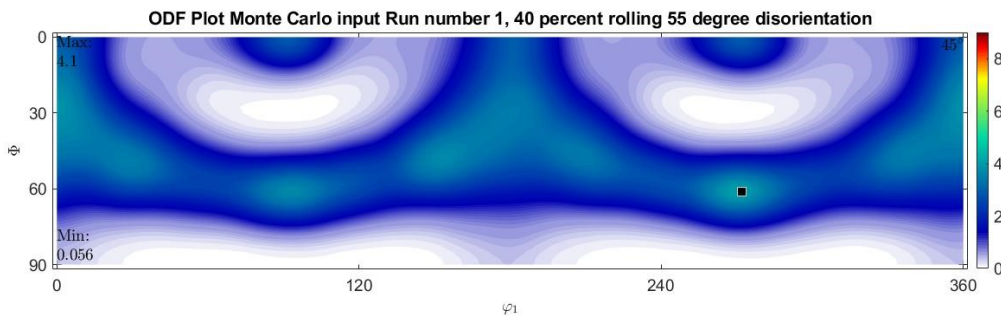


Figure J.25: ODF Plot, Monte Carlo Run 1 40 percent rolling, 55 degree disorientation

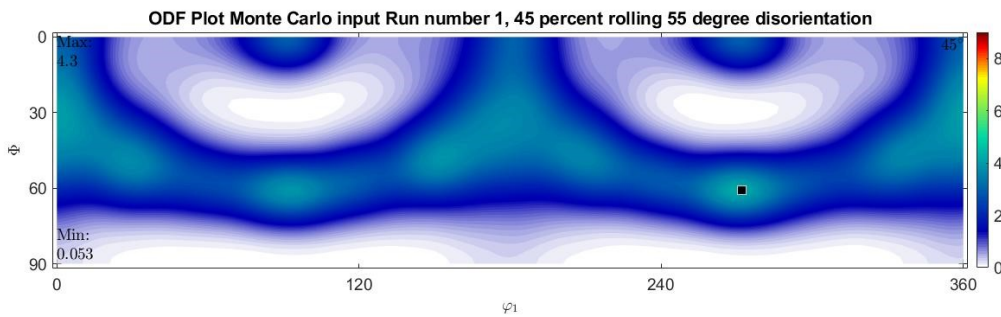


Figure J.26: ODF Plot, Monte Carlo Run 1 45 percent rolling, 55 degree disorientation

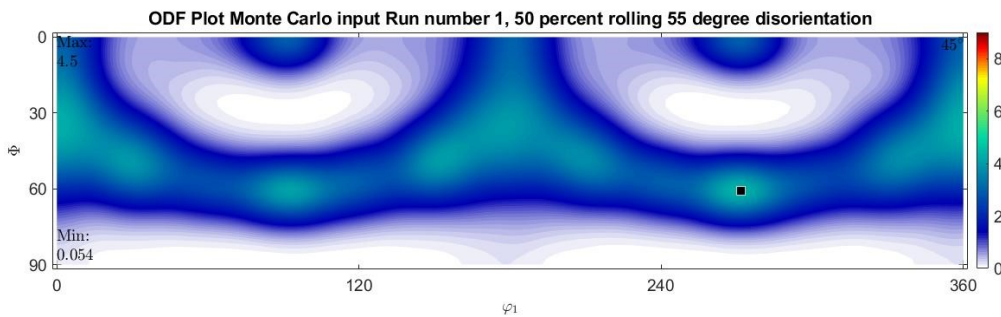


Figure J.27: ODF Plot, Monte Carlo Run 1 50 percent rolling, 55 degree disorientation

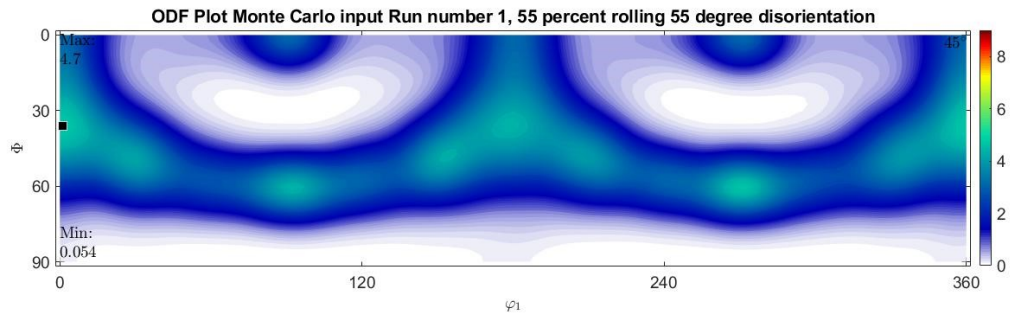


Figure J.28: ODF Plot, Monte Carlo Run 1 55 percent rolling, 55 degree disorientation

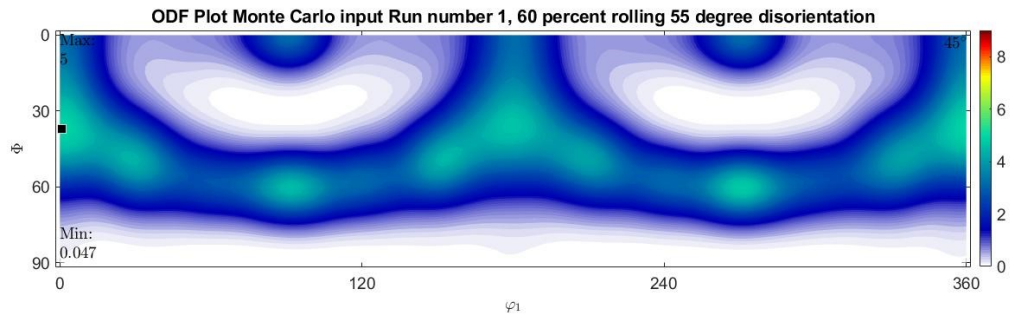


Figure J.29: ODF Plot, Monte Carlo Run 1 60 percent rolling, 55 degree disorientation

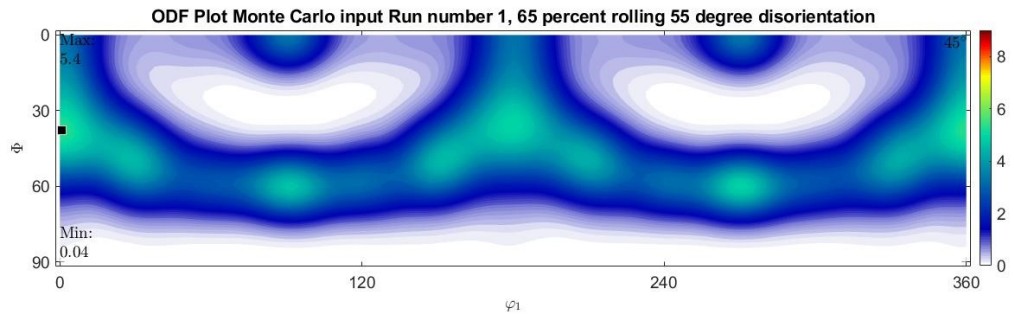


Figure J.30: ODF Plot, Monte Carlo Run 1 65 percent rolling, 55 degree disorientation

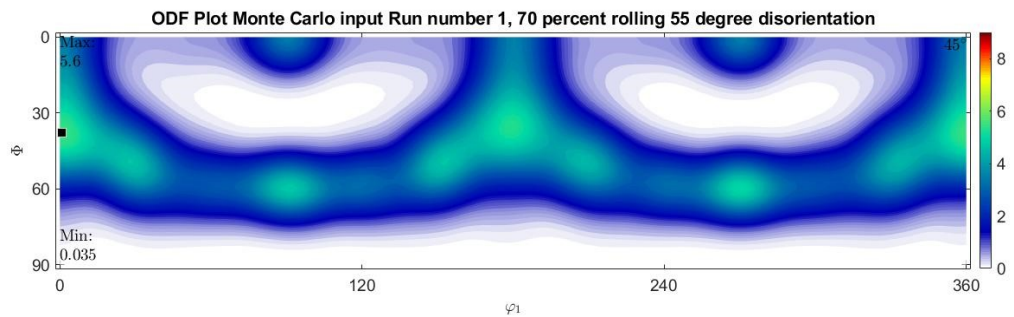


Figure J.31: ODF Plot, Monte Carlo Run 1 70 percent rolling, 55 degree disorientation

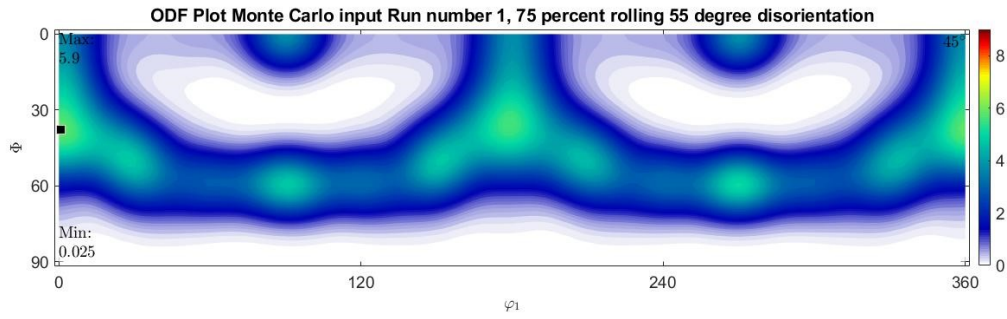


Figure J.32: ODF Plot, Monte Carlo Run 1 75 percent rolling, 55 degree disorientation

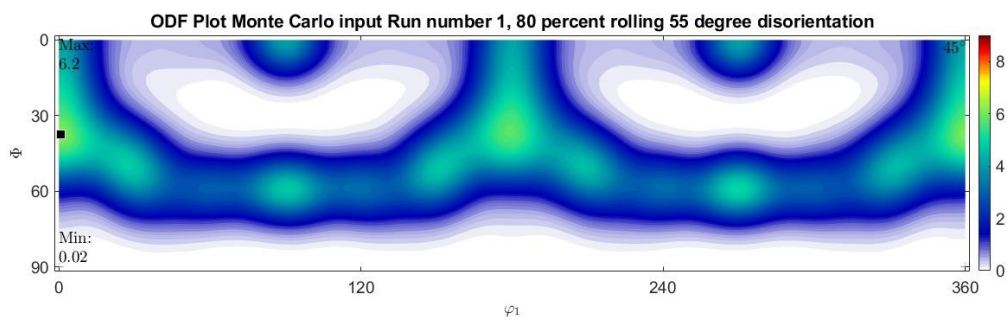


Figure J.33: ODF Plot, Monte Carlo Run 1 80 percent rolling, 55 degree disorientation

COLOPHON

This document was typeset using \LaTeX . The document layout was generated using the `arsclassica` package by Lorenzo Pantieri, which is an adaption of the original `classithesis` package from André Miede.

